

Année 2016

N° d'ordre : 42054

UNIVERSITE LILLE 1 - SCIENCES ET TECHNOLOGIES

**ECOLE DOCTORALE-SCIENCE DE LA MATIERE, DU
RAYONNEMENT ET DE L'ENVIRONNEMENT**

Doctorat

Molécules et Matière Condensée

Nassim EL ACHI

**PHOTOCHEMICAL AND PHOTOREDOX REACTIONS IN
CONTINUOUS MICROREACTORS: APPLICATION TO
CYCLOADDITION, CONTROLLED POLYMERIZATION AND
RADICAL CHEMISTRY**

Qui a été soutenue publiquement le 16 juin 2016

Dr Christian ROLANDO	Directeur de recherche au CNRS, Université de Lille	Directeur de thèse
Dr Maël PENHOAT	Maître de conférences, Université de Lille	Co-directeur de thèse
Pr Samir ZARD	Professeur, Ecole Polytechnique	Président de Jury
Dr Éric CLOUTET	Directeur de recherche au CNRS, Université de Bordeaux	Rapporteur
Pr Timothy NOEL	Professeur, Eindhoven University of Technology	Rapporteur
Pr Youssef BAKKOUR	Professeur, Université Libanaise	Examineur
Dr Laetitia CHAUSSET- BOISSARIE	Chargée de recherche au CNRS, Université de Lille	Examineur

OUTLINE

The aim of this work is to study the impact of miniaturization on different types of photochemical reactions. Kinetics studies were performed to compare the results in flow to those of batch reactors.

Chapter 1 introduces briefly both concepts of photochemistry and microflow technology. It emphasizes on the factors rendering miniaturization a key point in improving the productivity and selectivity of photochemical reactions.

Chapter 2 includes actinometric numerical and experimental assessments that measure the quantity of light that is supplied to the reaction mixture when working in the Mikrogas® Dwell Device under different concentrations, solvents and LEDs' powers

Chapter 3 focuses on the intramolecular [2+2] photocycloaddition reaction in chip reactor using two different conditions. The first condition includes sensitization and performed under UV whereas the second is using photoredox catalysis and blue irradiation.

Chapter 4 targets controlled photopolymerization of methyl methacrylate in a tubing reactor using the organocatalyst Eosin Y and green LEDs. Characterization of the formed polymer is done using GPC, and NMR spectroscopy.

The C-C and C-O bond formation in flow under UV are tested using photoredox catalysis in **chapter 5**. A detailed kinetic study is performed to plot the Hammett curve for the C-O bond formation from benzylic trifluoroborates.

ACKNOWLEDGMENTS

On a sunny day in my hometown Tripoli, I was watching TV when I ran through a French movie “Bienvenue chez les Ch’tis”. Ironically in less than two months I was on my way to Lille! After around three years of cloudy and super busy days I can truly say that it was one of the best experiences one could ever have.... But of course this would have never been possible without the amazing people that I met and worked with at the MSAP lab.

So first I would like to thank my supervisor, the *Big Boss*, Dr. Christian Rolando for all his guidance and support. It was such a pleasure working with such a devoted and hardworking scientist as you. I really appreciate all of your efforts in making me a better chemist.

Special thanks also goes to my co-supervisor Dr. Maël Penhoat. I am grateful for your continuous support and advice. Thank you for giving me all the time and chemistry chats that I needed to get a better understanding of Organic chemistry.

I am deeply grateful to have the external jury members Dr. Eric Cloutet (University of Bordeaux), Pr. Timothy Noël (Eindhoven University of Technology) and Pr. Samir Zard (Ecole Polytechnique). Thank you for giving this work some of your precious time. Having the “elites” in chemistry as members of my dissertation committee is such a great honor.

My supervisor during my MSc studies and the reason why I made it to the MSAP Lab, Pr. Youssef Bakkour, thanks for everything. I am truly indebted to you.

Laetitia (Dr. Chausset-Boissarie), though we only worked together for about 7 months, I am truly happy that I had the chance to meet such an amazing person/researcher as you. We made a great team. A side note: I was relieved to finally have another “Louis Vuitton” Fan! One step closer to outnumber “Star wars” fans at MSAP!

Pr. Caroline Tokarski, the MSAP lab director, thanks for your encouragement and support. Your efforts are and will always be highly appreciated.

I would like also to thank Dr. Séverine Le Gac for giving me the chance to join her group at the University of Twente for 1 month. You are truly a walking “guidelines of successful female researcher”.

Special thanks to Dr. Nathalie Azaroual, Dr. Vincent Darcos and Dr. Benjamin Nottelet for their input in the polymer chemistry section.

I would also like to thank all past and present members of the MSAP group: Adrien, Amra, Fabien, Fabrice, Karine, Nicolas C, Nicolas S and Stephanie.

Christophe Penverne, I always called you the superman of the day as you always managed to solve the complications I faced in the lab... though you are a Star wars fan... thanks for everything!

The Lebanese “dudes” Mireille, Sara, Diaa, Khalil and Serge. You guys ROCK.... I am really grateful to have you in my life... you always managed to share with me the precious Lebanese spices, fun and talks.

Enschede felt much better with Renée, Jean-Baptiste, Adithya, Josh, Hai and Miguel... I had a great time with you guys... *Dank je wel*.

Reem, Salim, Tarek and the “too cool to care” Ayman.... You are the best siblings ever. Thank you for giving me the support in the tough times... I love you to the moon and back and I am super proud of you.

Mom and Dad also known by *Nahnouh* and *Ashi Pascha*: just the idea of writing your names gets me emotional... words can never explain how much I am blessed to have you in my life. You are the ultimate definition of unconditional love... I love you so much and to you I dedicate this work... We did it!

To my Family

TABLE OF CONTENTS

OUTLINE	ii
ACKNOWLEDGEMENTS	iii
TABLE OF CONTENTS	vi
LIST OF ABBREVIATIONS	xii
LIST OF TABLES	xv
LIST OF FIGURES	xviii
CHAPTER 1: INTRODUCTION	1
1.1 Photochemistry	1
<i>1.1.1 Bohr's Model:</i>	1
<i>1.1.2 Franck-Condon Principle</i>	2
<i>1.1.3 Jablonski Diagram</i>	3
<u>1.1.3.1 Internal conversion</u>	4
<u>1.1.3.2 Vibrational relaxation</u>	4
<u>1.1.3.3 Intersystem crossing</u>	4
<u>1.1.3.4 Fluorescence and phosphorescence</u>	5
<u>1.1.3.5 Quenching and sensitization</u>	5
<i>1.1.4 Excitations and Transitions that Induce Photochemical Reactions</i>	6
<u>1.1.2.1 Transitions of π, σ and n electrons</u>	7
<u>1.1.2.2 d-d transitions</u>	8
<u>1.1.2.3 Transitions involving charge transfer</u>	10
1.1.2.3.1 LMCT	10
1.1.2.3.2 MLCT	11
<u>1.1.2.4 Implication of transitions on photochemistry</u>	11
1.2 Photochemistry for Organic Synthesis	12
<i>1.2.1 Conventional Techniques & Equipment</i>	13
<u>1.2.1.1 Lamps</u>	13
<u>1.2.1.2 Photoreactors</u>	15
<u>1.2.1.3 Glassware</u>	17
<u>1.2.1.4 Solvent</u>	18
<i>1.2.2 Limitations</i>	18
1.3 Microreactor Technology	19

<i>1.3.1 Why to Use Photochemistry in Flow?</i>	22
<u>1.3.1.1 Photon flux</u>	22
<u>1.3.1.2 Photonic efficiency</u>	22
<u>1.3.1.3 Path length</u>	23
<i>1.3.2 Continuous Flow Microreactor Design for Photochemistry</i>	24
<u>1.3.2.1 Reactor's material</u>	25
<u>1.3.2.2 Injection system</u>	27
<u>1.3.2.3 Light sources</u>	27
<u>1.3.2.4 Mixing systems</u>	28
<u>1.3.2.5 Purification apparatus and analytical systems</u>	30
<u>1.3.2.6 Material and solvent constraints</u>	30
<i>1.3.3 Types of Flow systems used in Photochemistry</i>	30
<u>1.3.3.1 Tubing devices</u>	31
<u>1.3.3.2 Chip devices</u>	32
<i>1.3.4 Examples of Photochemical Reactions Performed in Continuous Flow</i>	34
<i>1.3.5 Advantages and Limitations</i>	37
CHAPTER TWO: CHEMICAL ACTINOMETRY	40
2.1 Introduction	40
2.1.1 <i>Chemical Actinometers</i>	41
<u>2.1.1.1 Effect of refraction on the photon flux emitted by the light source</u>	42
<u>2.1.1.2 Temperature</u>	43
2.1.2 <i>Examples of Chemical Actinometers</i>	43
<u>2.1.2.1 Uranyl oxalate actinometer</u>	43
<u>2.1.2.2 Ferrioxalate actinometer</u>	43
<u>2.1.2.3 Reinecke's salt actinometer</u>	44
<u>2.1.2.4 Photochromic actinometers</u>	44
2.1.3 <i>Azobenzene</i>	45
<u>2.1.3.1 Photochemistry of azobenzene</u>	46
<u>2.1.3.2 Mechanism of photoisomerization of azobenzene</u>	48
<u>2.1.3.3 Mechanism of thermal isomerization of azobenzene</u>	50
<u>2.1.3.4 Azobenzene as an actinometer</u>	50
2.1.4 <i>Kinetic Studies of Azobenzene</i>	52

<u>2.1.4.1 Thermal isomerization</u>	52
<u>2.1.4.2 Photoisomerization</u>	52
2.1.4.2.1 Rate law of the reversible isomerization of azobenzene	55
2.2 Experimental Actinometric Measurements	57
2.2.1 Determination of the ϵ of azobenzene (<i>E</i>) and total transmittance <i>T</i> of the reactor	59
2.3 Results	60
2.3.1 Calculation of Photon Flux emitted by the UV LEDs	61
2.3.2 The variation of <i>Z</i> and <i>E</i> Isomers with Time	62
2.3.3 Thermal Isomerization	64
2.4 Discussion	64
2.5 Conclusion	66
CHAPTER THREE: CYCLOADDITION	68
3.1 Introduction	68
3.1.1 Diels- Alder Addition	68
3.1.2 Frontier Molecular Orbital Theory	69
3.2 Photocycloaddition	72
3.2.1 [2+2] Cycloaddition using UV Irradiation	73
<u>3.2.1.1 Sensitization</u>	73
<u>3.2.1.2 [2+2] photocycloaddition model experiment</u>	74
3.2.2 Visible Light Photoredox Catalysis	76
3.2.2.1 Photochemistry of Ru(bpy) ₃ ²⁺	78
<u>3.2.2.2 Intramolecular [2+2] photocycloaddition</u>	80
<u>3.2.2.3 Photoinduced reductive cyclization</u>	82
3.3 Results and Discussion	84
3.3.1 Synthesis of starting material	84
3.3.2 [2+2] cycloaddition via sensitization under UV irradiation in flow	85
3.3.3 Kinetics of [2+2] Cycloaddition using Sensitization	93
<u>3.3.1.1 Determination of reaction order of pinacolization</u>	94
<u>3.3.1.2 Determination of reaction order of [2+2] cycloaddition</u>	97
<u>3.3.1.3 Kinetic studies of the other substrates</u>	104
3.3.4 Limitations of the sensitized Reaction	105
3.3.5 Visible Light Induced Intramolecular [2+2] Cycloaddition using Ru(bipy) ₃ Cl ₂	105

3.3.5.1 Kinetics of parallel reactions	110
3.4 Conclusion	114
CHAPTER FOUR: PHOTO-INDUCED ATRP USING EOSIN Y	117
4.1 Introduction	117
4.2 Ionic Polymerization	118
4.2.1 Anionic Polymerization	118
4.2.2 Cationic Polymerization	119
4.3 Radical Polymerization	119
4.3.1 Nitroxide Mediated CRP	121
4.3.2 RAFT/MADIX Polymerization	122
4.3.3 Atom Transfer Radical Polymerization (ATRP)	123
4.4 Characterization of Polymers	125
4.4.1 Degree of Conversion	125
4.4.2 Kinetics	125
4.4.3 Molecular Weight	125
4.4.3.1 Number average molecular weight M_n	126
4.4.3.2 Weight average molecular weight M_w	126
4.4.3.3 Polydispersity index	126
4.4.4 Tacticity	128
4.5 Components of ATRP	130
4.5.1 Monomers	130
4.5.2 Initiators	130
4.5.3 Catalysts	131
4.6 Limitations of ATRP	132
4.7 Photoinduced ATRP	133
4.7.1 ATRP by Photoredox Catalysis	134
4.7.1.1 Copper mediated	134
4.7.1.2 Other metals mediated	136
4.7.1.3 Metal-free photoredox catalysis	137
4.8 Continuous -Flow Photopolymerization	138
4.9 Eosin Y	139
4.10 Plan of Work	141
4.11 Results and Discussion	142

4.11.1 Batch vs. flow	142
4.11.2 Metal vs. metal free ATRP under visible light irradiation	145
4.11.3 Kinetic study	148
<u>4.11.3.1 EBPA</u>	149
<u>4.11.3.2 EBiB</u>	151
<u>4.11.3.3 (p-OMe)-EBPA</u>	153
4.11.4 Controlled “on-off” light switching regulation of polymerization	155
4.11.5 Macroinitiator	158
4.11.6 Mechanism	160
4.11.7 Determination of M_w by Diffusion Ordered Spectroscopy (DOSY)	161
4.11.8 Tacticity	163
4.12 Conclusion	164
CHAPTER FIVE: C-C AND C-O BOND FORMATION VIA PHOTOREDOX CATALYSIS	167
5.1 Introduction	167
5.1.1 Synthesis of the Starting Trifluoroborates	168
5.1.2 Generation of carbon-centered radicals from organoboron derivatives via oxidation	169
5.1.3 Generation of carbon-centered radicals from organoboron derivatives via visible light photoredox catalysis	170
5.2 Objective	178
5.3 Results and Discussion	179
5.3.1 Preparation of Trifluoroborates	179
5.3.2 C-O bond formation from potassium trifluoroborates in batch and in flow	180
<u>5.3.2.1 Optimization of the metal photocatalyzed C-O bond formation</u>	180
5.3.2.1.1 Influence of the metal catalyst	180
5.3.2.1.2 Influence of the wavelength of irradiation	181
5.3.2.1.3 Metal free photocatalyzed C-O bond formation	183
<u>5.3.2.2 Scope of the metal photocatalyzed reaction in flow by UV irradiation</u>	184
5.3.3 Hammett correlation for the C-O bond formation from substituted benzylic trifluoroborates	187
<u>5.3.3.1 Benzyl trifluoroborate</u>	190
<u>5.3.3.2 p-methoxybenzyl trifluoroborate</u>	191

<u>5.3.3.3 <i>p</i>-methylbenzyl trifluoroborate</u>	193
<u>5.3.3.4 <i>p</i>-chlorobenzyl trifluoroborate</u>	195
<u>5.3.3.5 <i>p</i>-Fluorobenzyl trifluoroborate</u>	196
<u>5.3.3.6 <i>m</i>-methylbenzyl trifluoroborate</u>	198
<u>5.3.3.7 <i>m</i>-methoxybenzyl trifluoroborate</u>	199
<u>5.3.3.8 Hammett plot</u>	201
<i>5.3.4 C-C bond formation from potassium trifluoroborates under UV in flow</i>	204
5.4 Conclusion	206
CHAPTER SIX: CONCLUSION	208
CHAPTER SEVEN: EXPERIMENTAL PART	211
LIST OF REFERENCES	247

LIST OF ABBREVIATIONS

ATRP	Atom Transfer Radical Polymerization
BET	Back Electron Transfer
BnMA	Benzyl MethAcrylate
BP	BenzoPhenone
CRP	Controlled/living Radical polymerization
D	Diffusion
\bar{D}	PolyDispersity Index
DMAEA	N,N-DiMethylAminoEthyl Acrylamide
DMBP	4,4 DiMethoxyBenzoPhenone
DMF	DiMethylFormamide
DOSY	Diffusion Ordered SpectroscopY
DP	Degree of Polymerization
EBiB	Ethyl 2- BromoisoButyrate,
EBMPA/ (<i>p</i> -OMe)EBPA	Ethyl 2-Bromo-2-(4-MethoxyPhenyl) Acetate
EBPA	Ethyl α - BromoPhenylAcetate
EDTA	EthyleneDiamineTetraacetic Acid
Eq.	Equivalent
FEP	Fluorinated Ethylene Propylene
FL	Fluorescein
FMO	Frontier Molecular Orbital
GC	Gas Chromatography
GPC	Gel Permeation Chromatography

HOMO	Highest Occupied Molecular Orbital
HPLC	High Performance-Liquid Chromatography
IC	Internal Conversion
ID	Internal Diameter
i-Pr ₂ NEt	N,N-Diisopropyl EthylAmine
ISC	Intersystem Crossing
LC-MS	Liquid Chromatography-Mass Spectrometry
LEDs	Light Emitting Diodes
LMCT	Ligand to Metal Charge Transfer
LUMO	Lowest Unoccupied Molecular Orbital
MA	Methyl Acrylate
MADIX	Macromolecular Design via the Interchange of Xanthates
Me-PTH	10-MethylPhenoThiazine
MLCT	Metal to Ligand Charge Transfer
MMA	Methyl MethAcrylate
nBA	Butyl Acrylate
NMP	Nitroxide-Mediated Radical Polymerization
PDMS	PolyDiMethylSiloxane
PET	Photoinduced Electron Transfer
PFA	PerFluoroalkoxyAlkane
PMDETA	N,N,N',N'',N'''-PentaMethylDiEthyleneTriAmine
PMMA	Polymethyl Methacrylate
PSS	Photo Stationary State

PS	Poly Styrene
RAFT	Reversible Addition Fragmentation Chain Transfer Radical Polymerization
SCE	Saturated Calomel Electrode
SET	Single Electron Transfer
TEA	TriEthylAmine
TFA	TriFluoroAcetic acid
TLC	Thin Layer Chromatography
TMDPO	(2,4,6-TriMethylbenzoyl) DiPhenylphosphine Oxide
TPMA	Tris(2-PyridylMethyl)Amine
TPMA*	Tris((4-Methoxy-3,5-dimethylPyridin-2-yl)Amine)
VAc	Vinyl Acetate

LIST OF TABLES

Table 2.1	Summary of the experiments done for the chemical actinometric assessment.	59
Table 2.2	Values of ϵ of azobenzene in different solvents	60
Table 2.3	The total transmittance of light in the used solvents	60
Table 2.4	The % of the Z isomer vs the irradiation time	61
Table 2.5	Physical constants used for calculations	61
Table 2.6	Results of actinometric measurements	63
Table 2.7	Results of kinetic measurements	63
Table 2.8	Thermal isomerization of (Z) azobenzene to (E) azobenzene after PSS	63
Table 3.1	Screening of conditions for the photosensitized reaction of 1a in a Dwell device microreactor irradiated with HP UV-LEDs A (365 nm)	87
Table 3.2	Scope of photosensitized intramolecular [2+2] cycloaddition reaction	91
Table 3.3	Results of pinacolization reaction in flow for $[B]_0 = 0.074 \text{ M}$	95
Table 3.4	Results of pinacolization reaction in flow for $[B]_0 = 0.037 \text{ M}$	96
Table 3.5	Results of sensitized [2+2] cycloaddition in flow where $[S]_0 = 0.037 \text{ M}$	97
Table 3.6	Results of sensitized [2+2] cycloaddition in flow where $[S]_0 = 0.01 \text{ M}$	99
Table 3.7	Results of sensitized [2+2] cycloaddition in flow where $[S]_0 = 0.02 \text{ M}$	100
Table 3.8	Results of sensitized [2+2] cycloaddition in flow where $[S]_0 = 0.08 \text{ M}$	101
Table 3.9	Summary of the kinetic results for the variation of $[S]_0$.	103
Table 3.10	Summary of the kinetic results for photosensitized intramolecular [2+2] cycloaddition of substrates 1a-1d in flow	104

Table 3.11	Screening of conditions for the intramolecular [2+2] cycloaddition reaction of 1f in a Mikroglas ® Dwell device irradiated with white LEDs and catalyzed by Ru(bpy) ₃ Cl ₂	107
Table 3.12	Intramolecular [2+2] cycloaddition reaction of 1f in a Mikroglas ® Dwell device irradiated for 1 hour with different visible LEDs	108
Table 3.13	Screening of conditions for the intramolecular [2+2] cycloaddition reaction of 1f in a Mikroglas ® Dwell device irradiated with visible LEDs	109
Table 3.14	Summary of the photoredox induced cyclization of bisenone in flow using blue LEDs	110
Table 4.1	Cu-catalyzed ATRP in batch and flow conditions	144
Table 4.2	Visible light induced ATRP in batch and flow conditions	146
Table 4.3	Eosin Y catalyzed ATRP of MMA using EBPA as an initiator in flow	151
Table 4.4	Eosin Y catalyzed ATRP of MMA using EBiB as an initiator in flow	152
Table 4.5	Eosin Y catalyzed ATRP of MMA using (<i>p</i> -OMe)-EBPA as an initiator in flow	154
Table 4.6	Effect of visible light irradiation on the yield and PDI value of Eosin Y mediated ATRP of MMA with EBPA as initiator	157
Table 4.7	Mw measurements of PMMA synthesized in flow by DOSY NMR and GPC	163
Table 4.8	Tacticity of PMMA formed by eosin Y catalysis in flow	164
Table 5.1	Redox potentials of the possible transitions of Ir(III)/ L ₁	173
Table 5.2	Yields of the preparation of the trifluoroborate salts (1h-1t)	179
Table 5.3	Results of C-O bond formation in flow via metal based photoredox catalysis	181
Table 5.4	Results of C-O bond formation in flow catalyzed by eosin Y in flow	183

Table 5.5	Results of the C-O bond formation of various trifluoroborates in flow using Ir(III)/ L ₁ at 365 nm.	185
Table 5.6	The substituted benzyl trifluoroborates used in this study	189
Table 5.7	Results of the flow reaction of benzyl trifluoroborate with TEMPO	190
Table 5.8	Results of the flow reaction of <i>p</i> -methoxybenzyl trifluoroborate with TEMPO	192
Table 5.9	Results of the flow reaction of <i>p</i> -methylbenzyl trifluoroborate with TEMPO	194
Table 5.10	Results of the flow reaction of <i>p</i> -chlorobenzyl trifluoroborate with TEMPO	195
Table 5.11	Results of the flow reaction of <i>p</i> -fluorobenzyl trifluoroborate with TEMPO	197
Table 5.12	Results of the flow reaction of <i>m</i> -methylbenzyl trifluoroborate with TEMPO	198
Table 5.13	Results of the flow reaction of <i>m</i> -methoxybenzyl trifluoroborate with TEMPO	200
Table 5.14	Summary of the rate constants, σ and σ^+ values of each of the tested substituted benzyl trifluoroborates	201
Table 5.15	Results of the C-C bond formation in flow using Ir(III) */ L ₁ as a photocatalyst at 365 nm wavelength	205

LIST OF FIGURES

Figure 1.1	Franck-Condon energy model of diatomic molecules	3
Figure 1.2	Jablonski diagram	5
Figure 1.3	n- π^* and π - π^* transitions in an excited molecule	8
Figure 1.4	d-d splitting in octahedral and tetrahedral geometries	9
Figure 1.5	Colors of some Cr ³⁺ complexes	10
Figure 1.6	MLCT and LMCT	11
Figure 1.7	Emission spectrum of low -pressure Hg lamp	14
Figure 1.8	Emission spectrum of high- pressure Hg lamp	15
Figure 1.9	An immersion-well batch reactor with medium -pressure Hg lamp	16
Figure 1.10	Rayonet reactor	16
Figure 1.11	Falling film reactor	17
Figure 1.12	Variation of the transmittance of light vs. the distance for benzophenone and Ru(bpy) ₃ Cl ₂	24
Figure 1.13	Set-up of a photomicroreactor assembly	25
Figure 1.14	Examples of microreactors fabricated from: (a) glass; (b) ceramic; (c) metal and (d) silicon	26
Figure 1.15	Mechanical pumps: (a) syringe pump; (b) peristaltic pump; (c) HPLC pump	27
Figure 1.16	Types of flow: (a) Laminar flow (b) turbulent flow	29
Figure 1.17	(a) Scheme of FEP flow reactor, (b) image of the system	31
Figure 1.18	(a) Microfluidic glass reactor; (b) same reactor illuminated by UV LEDs	32
Figure 1.19	Corning® Advanced-Flow™ G1 photo reactor	33
Figure 1.20	[2+2] Photocycloaddition of cyclohexenone and vinyl Acetate	34
Figure 1.21	[2+2] Photocycloaddition of maleimide with an alkene	35
Figure 1.22	Photoisomerization of nitrones to amides	35
Figure 1.23	Photocyclization of stilbenes to phenanthrenes	35
Figure 1.24	Formation of imidazoles from secondary amines and vinyl azides by photoredox catalysis	36
Figure 1.25	Oxidation of thiols to disulfides using eosin Y	36
Figure 2.1	Uranyl oxalate actinometry reaction	43

Figure 2.2	Ferrioxalate actinometry reaction	44
Figure 2.3	Fulgide aberchrome 540 actinometry reaction	45
Figure 2.4	The trans (E) & cis (Z) isomers of azobenzene	46
Figure 2.5	The isomerization reaction of azobenzene	46
Figure 2.6	The absorption spectrum of azobenzene upon irradiation with 320 nm light	47
Figure 2.7	Mechanisms of azobenzene isomerization	49
Figure 2.8	The Isomerization reaction of azobenzene	52
Figure 2.9	The setup of the photoisomerization of azobenzene under flow conditions using lab assembled UV LEDs	58
Figure 2.10	Mikroglas Dwell device illuminated by HP LEDs B	58
Figure 2.11	Graph of $\ln(Z_{PSS}-Z_t)$ vs. time (s)	61
Figure 2.12	Rate Law	62
Figure 2.13	Kinetic graph of the thermal isomerization of azobenzene after PSS	64
Figure 3.1	Diels Alder addition	68
Figure 3.2	Examples of natural products prepared by cycloaddition	69
Figure 3.3	FMO representation of ethene	70
Figure 3.4	(a): FMO of diene, (b): Overlapping of orbitals in [4+2] cycloaddition	71
Figure 3.5	FMO of ethene following irradiation	71
Figure 3.6	Sensitization	73
Figure 3.7	Absorption spectrum of DMBP in acetonitrile	74
Figure 3.8	[2+2] intramolecular photocycloaddition of 3-oxa-1,5-hexadienones	74
Figure 3.9	The straight and crossed [2+2] cycloadducts	75
Figure 3.10	Proposed mechanism for the [2+2] photocycloaddition of 3-oxa-1,5-hexadienones	76
Figure 3.11	Simplified molecular orbital depiction of $\text{Ru}(\text{bpy})_3^{2+}$	78
Figure 3.12	Structure and major properties of $\text{Ru}(\text{bpy})_3^{2+}$	79
Figure 3.13	Mechanism of intramolecular [2+2] cycloaddition of a bisenone	81
Figure 3.14	Reductive cyclization of a bisenone using a Brønsted acid	83
Figure 3.15	Mechanism of reductive cyclization of bisenone	83

Figure 3.16	Preparation of 1a-1d	84
Figure 3.17	Preparation of 1g	85
Figure 3.18	Preparation of 1f	85
Figure 3.19	Mikroglas Dwell Device illuminated by HP UV LEDs 365 nm	85
Figure 3.20	Intramolecular [2+2] cycloaddition of 3-oxa-1,5-hexadienones using UV irradiation	86
Figure 3.21	Pinacolization	94
Figure 3.22	Graph of $1/[B]_0 - [P]$ vs. t where $[B]_0 = 0.074$ M	95
Figure 3.23	Graph of $1/[B]_0 - [P]$ vs. t where $[B]_0 = 0.037$ M	96
Figure 3.24	Plot of $\ln([S]_0 - [C]t)$ vs. t (min) with $[S]_0 = 0.037$ M	98
Figure 3.25	Plot of $1/[B]t$ vs. t (min) with $[S]_0 = 0.037$ M	98
Figure 3.26	Plot of $\ln([S]_0 - [C]t)$ vs. t (min) with $[S]_0 = 0.01$ M	99
Figure 3.27	Plot of $1/[B]t$ vs. t (min) with $[S]_0 = 0.01$ M	99
Figure 3.28	Plot of $\ln([S]_0 - [C]t)$ vs. t (min) with $[S]_0 = 0.02$ M	100
Figure 3.29	Plot of $1/[B]t$ vs. t (min) with $[S]_0 = 0.02$ M	101
Figure 3.30	Plot of $\ln([S]_0 - [C]t)$ vs. t (min) with $[S]_0 = 0.08$ M	102
Figure 3.31	Plot of $1/[B]t$ vs. t (min) with $[S]_0 = 0.08$ M	102
Figure 3.32	Visible light induced intramolecular cycloaddition of bisenone in flow using $\text{Ru}(\text{bpy})_3\text{Cl}_2$	105
Figure 3.33	Set up for the photocycloaddition in flow using $\text{Ru}(\text{bpy})_3\text{Cl}_2$ and blue LEDs	105
Figure 3.34	Representation of parallel reactions	110
Figure 3.35	Variation of $\ln[\text{Biseneone}]$ with respect to irradiation time (min)	112
Figure 3.36	Variation of Bisenone (blue), [2+2] cycloadduct (red) & reductive adduct (green) vs. irradiation time (min) in a competitive reaction	113
Figure 3.37	Method of preparation of SBA 15 grafted with benzophenone by click chemistry	115
Figure 4.1	Initiation of Anionic Polymerization	118
Figure 4.2	Initiation of Cationic Polymerization: A^+ is the active species like aqueous aluminum chloride	119
Figure 4.3	Nitroxide Mediated CRP	122
Figure 4.4	RAFT/MADIX agents	122
Figure 4.5	RAFT/MADIX Polymerization	123

Figure 4.6	Mechanism of ATRP	124
Figure 4.7	The three possible arrangements in PMMA	128
Figure 4.8	Determination of the three triads by ¹ H NMR	129
Figure 4.9	Structures of Common ATRP Monomers	130
Figure 4.10	Activities of various alkyl halide initiators used in ATRP	131
Figure 4.11	Structure of eosin Y	140
Figure 4.12	Absorption spectra of eosin Y at different concentrations	140
Figure 4.13	The redox potentials of eosin Y in the ground and excited states	141
Figure 4.14	Cu II/Ligand mediated ATRP of MMA	142
Figure 4.15	ATRP of MMA using: a: Ru(bpy) ₃ Cl ₂ and blue LEDs, b: Eosin Y and green LEDs in both batch and flow conditions	145
Figure 4.16	a: Eosin Y mediated ATRP of MMA using different initiators; b: composition of the different initiators used	148
Figure 4.17	A plot of ln([M] ₀ /[M] _t) vs. irradiation time for polymerization using EBPA as an initiator	150
Figure 4.18	M _n of PMMA as a function of monomer conversion using EBPA as an initiator	150
Figure 4.19	A plot of ln([M] ₀ /[M] _t) vs. irradiation time for polymerization using EBiB as an initiator	152
Figure 4.20	M _n of PMMA as a function of monomer conversion using EBiB as an initiator	153
Figure 4.21	A plot of ln([M] ₀ /[M] _t) vs. irradiation time for polymerization using (<i>p</i> -OMe)-EBPA as an initiator	154
Figure 4.22	M _n of PMMA vs. monomer conversion using (<i>p</i> -OMe)EBPA as an initiator.	155
Figure 4.23	Plot of monomer conversion vs. time using EBPA as an initiator in “on-off” cycling of irradiation	156
Figure 4.24	ln([M] ₀ /[M]) as a function of exposure time during an “on-off” irradiation cycles	157
Figure 4.25	Eosin Y mediated ATRP of styrene using PMMA as a macroinitiator	158
Figure 4.26	GPC trace of PMMA-Br (green) and PMMA-PS (blue)	159
Figure 4.27	¹ H NMR trace of PMMA-PSt	160

Figure 4.28	Proposed mechanism of ATRP using eosin Y	161
Figure 4.29	PMMA calibration curve in CDCl ₃ used for M _w prediction	162
Figure 5.1	Synthesis of the potassium trifluoroborates	168
Figure 5.2	Generation of radicals from trifluoroborates using oxidants	169
Figure 5.3	Alkylation of heteroaryls following radical formation using oxidants	170
Figure 5.4	Heck reaction using oxidants and Cu(OTf) ₂	170
Figure 5.5	C-O bond formation via photoredox catalysis	171
Figure 5.6	Structure of Ir(dF(CF ₃)ppy) ₂ (dtbbpy) ⁺	172
Figure 5.7	Mechanism of C-O bond formation <i>via</i> photoredox catalysis	173
Figure 5.8	C-C bond formation via photoredox catalysis	174
Figure 5.9	Mechanism of C-C bond formation <i>via</i> photoredox catalysis	174
Figure 5.10	Alkoxy trifluoroborates for C-C bond formation <i>via</i> photoredox catalysis	175
Figure 5.11	C-C bond formation using amino alkyl trifluoroborates <i>via</i> photoredox catalysis	175
Figure 5.12	C-C bond formation using thio alkyl trifluoroborates <i>via</i> photoredox catalysis	176
Figure 5.13	Addition of alkyl radical to vinyl carboxylic acid <i>via</i> photoredox catalysis	176
Figure 5.14	Dual catalysis for cross coupling	177
Figure 5.15	Dual catalysis for cross coupling using secondary alkyl trifluoroborates	177
Figure 5.16	Dual catalysis for the synthesis of benzylic ethers by cross coupling	178
Figure 5.17	C-O bond formation in flow <i>via</i> photoredox catalysis	180
Figure 5.18	Absorption spectrum of [Ir(dF(CF ₃)ppy) ₂ (dtbbpy)](PF ₆)	182
Figure 5.19	C-O bond formation of various trifluoroborates in flow using Ir(III)/ L ₁ at 365 nm	185
Figure 5.20	Benzyl trifluoroborates of different substitutions for C-O bond formation in flow <i>via</i> photoredox catalysis	187
Figure 5.21	Reaction of benzyl trifluoroborate with TEMPO in flow <i>via</i> Ir(III)/ L ₁ catalysis in UV	190

Figure 5.22	Kinetic plot of the flow reaction of benzyl trifluoroborate with TEMPO	191
Figure 5.23	Reaction of <i>p</i> -methoxybenzyl trifluoroborate with TEMPO in flow via Ir(III)/ L ₁ catalysis in UV	191
Figure 5.24	Kinetic plot of the flow reaction of <i>p</i> -methoxybenzyl trifluoroborate with TEMPO	193
Figure 5.25	Reaction of <i>p</i> -methylbenzyl trifluoroborate with TEMPO in flow via Ir(III)/ L ₁ catalysis in UV	193
Figure 5.26	Kinetic plot of the flow reaction of <i>p</i> -methylbenzyl trifluoroborate with TEMPO	194
Figure 5.27	Reaction of <i>p</i> -chlorobenzyl trifluoroborate with TEMPO in flow via Ir(III)/ L ₁ catalysis in UV	195
Figure 5.28	Kinetic plot of the flow reaction of <i>p</i> -chlorobenzyl trifluoroborate with TEMPO	196
Figure 5.29	Reaction of <i>p</i> -fluorobenzyl trifluoroborate with TEMPO in flow via Ir(III)/ L ₁ catalysis in UV	196
Figure 5.30	Kinetic plot of the flow reaction of <i>p</i> -fluoro benzyl trifluoroborate with TEMPO	197
Figure 5.31	Reaction of <i>m</i> -methylbenzyl trifluoroborate with TEMPO in flow via Ir(III)/ L ₁ catalysis in UV	198
Figure 5.32	Kinetic plot of the flow reaction of <i>m</i> -methylbenzyl trifluoroborate with TEMPO	199
Figure 5.33	Reaction of <i>m</i> -methoxybenzyl trifluoroborate with TEMPO in flow via Ir(III)/ L ₁ catalysis in UV	199
Figure 5.34	Kinetic plot of the flow reaction of <i>m</i> -methoxybenzyl trifluoroborate with TEMPO	200
Figure 5.35	Hammett plot using σ (red) and σ^+ (blue) values	204
Figure 5.36	C-C bond formation in flow <i>via</i> photoredox catalysis in UV	204

CHAPTER ONE

INTRODUCTION

1.1 Photochemistry

Photochemistry is the study of the chemical changes that take place in response to light. It is based on the Grotthus-Draper 1st law of photochemistry that states that a photochemical reaction occurs only when light is absorbed by a compound [1]. In other words, such chemical changes are the result of the usage of photons in an attempt to overcome the activation barrier. Photochemistry affords a wide range of reactions that are not feasible using the thermochemical or electrochemical pathways. Along with providing routes for the synthesis of advanced complex structures, its intervention led to the shortening of other synthetic routes by replacing several steps with a one-step photoreaction making it popular in total synthesis and material science fields [2].

The following section includes a brief summary of the science behind the chemical transformations that take place following photon absorption, i.e. excitation of the organic molecule.

1.1.1 Bohr's Model

Bohr's model demonstrated that protons and neutrons occupy a dense central region, the nucleus, whereas electrons travel in certain orbits around the nucleus. In this model, the energy of these orbitals was quantized and restricted to certain discrete values or energy levels. The electrons can move from one energy level to the other if the amount of energy absorbed or released is equal to the energy difference of the levels as stated in the Planck relation (Equation 1.1) [3]

$$\Delta E = h \nu$$

Equation 1.1

Where ΔE is the energy difference of levels, h is the Planck's constant and ν is the frequency of the emitted or absorbed irradiation.

When relaxed, the electron occupies the ground level ($n = 1$). Upon excitation, the electron moves to one of the higher energy levels depending on the energy absorbed. The Bohr model successfully predicted the energies for the hydrogen atom and has been extended later to other atoms using Schrödinger model based on quantum mechanics.

1.1.2 Franck-Condon Principle

A more advanced energy model for diatomic molecules was done by J. Frank and R. Condon. In this model, both the ground and the excited states include sub vibrational levels. Franck and Condon have assumed that since the nucleus is much heavier than the electrons, the promotion of the electron from the lowest vibrational level of the ground state to a higher vibrational level within the excited state in a molecule is much more rapid than any nuclear response. As a result, the nuclei preserve their position during this electronic transition but acquire some vibrational energy. This excitation will be followed by an instant energy dissipation in the form of heat. Thus the excited electron reaches the least vibrational sublevel of the excited state (Figure 1.1). The relaxation to the ground state is accompanied by photon emission i.e. fluorescence. The Franck –Condon Principle gave an interpretation to the experimental observation of the difference between the absorption and emission spectra, known as Stokes' shift. [4]

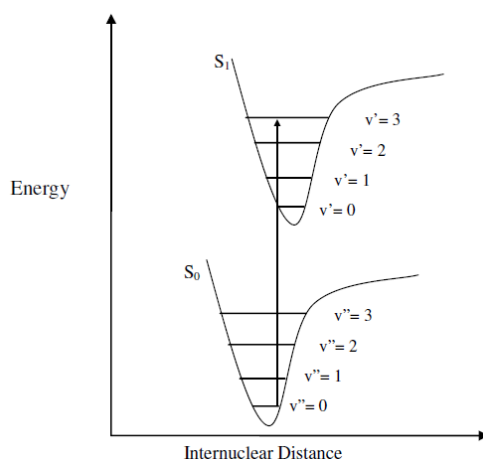


Figure 1.1: Franck-Condon energy model of diatomic molecules

1.1.3 Jablonski Diagram

Since the model for diatomic molecules is not applicable to organic compounds that mostly have more than two atoms, the Jablonski diagram is more general module as it shows the various relaxation routes an excited molecule can take to lose its excess energy. Following Franck-Condon principle, excitation occurs to higher vibrational levels. However, the molecule also has multiple excited states and there are rotational and vibrational sub-levels [3, 4].

The different excited states can also be classified into triplet and singlet states based on their electron spin angular momentum. According to Pauli principle, electrons usually pair in opposite spins when occupying bonding and nonbonding orbitals. This will lead to a diamagnetic molecule having a ground state with a net zero spin. As a result, such a state will exhibit a single energy state “singlet” in an applied magnetic field. In contrast, in some cases like O₂, single electrons of the same spin occupy different orbitals: the Pauli Exclusion Principle. In such cases, the molecule will be paramagnetic and its ground state will have a net spin of 1. When placed in a magnetic field, such a ground state will have three energy levels or “triplets” (-1, 0, +1). This shows that each molecule has its set of excited states that depend on the nature of the bonding that takes place among its atoms. [3, 4]

Since most of the organic molecules possess singlet ground states, the excitation of these molecules will lead to an electronic transition to singlet excited states as only excitations within the same multiplicity are allowed. Following the excitation from the ground singlet state S_0 to the excited singlet state S_n , the following relaxation routes may take place: [3, 4] (Figure 1.2)

1.1.3.1 Internal conversion

Internal conversion (IC) is a non-radiative transition from one excited state to a lower excited state of the same multiplicity so the spin state will be conserved during this transition. The excess of the vibrational energy after this transition will be released through vibrational relaxation.

1.1.3.2 Vibrational relaxation

Vibrational relaxation, is the process by which the excited molecule loses its excess vibrational energy very quickly by collisions with other particles or by a loss of heat energy. This phenomenon takes place within the same electronic state.

1.1.3.3 Intersystem crossing

Intersystem crossing (ISC) is a non-radiative transition from an electronic state to a lower electronic state of different multiplicity. In this case, the spin of the electron inverts during the transition. Though this transition is forbidden, and thus slower, it takes place due to the spin-orbit coupling. This coupling allows the change in the spin of the electron and thus favors this type of transition.

1.1.3.4 Fluorescence and phosphorescence

Fluorescence is the radiative relaxation from the excited state to the ground state of the same multiplicity (mostly singlet). Relaxations from triplet excited state to singlet ground state are termed phosphorescence. Usually, the radiative energy is not exactly equal to that absorbed due to energy loss by vibrational relaxation which is in agreement with Stokes' Shift.

1.1.3.5 Quenching and sensitization

Other forms of non-radiative relaxation include the intermolecular energy transfer to a different molecule leading to the excitation of the latter. This form of relaxation is very significant in liquid phase due to frequent collisions.

This exchange of energy is considered quenching when taking into consideration the relaxation of the excited molecule to the ground state. It is termed sensitization when focusing on the new molecule which is now excited. Note that the energy transferred is not enough to induce electronic excitation in most cases. So this energy will be then liberated as vibrational or rotational energies.

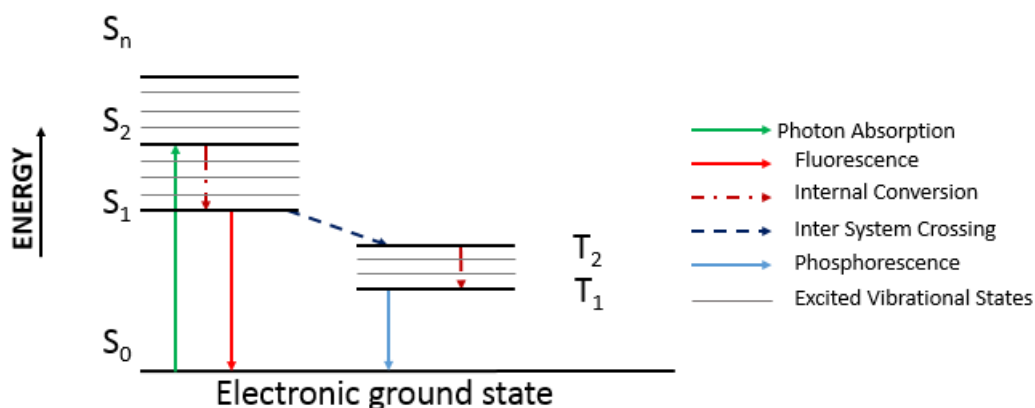


Figure 1.2: Jablonski diagram

1.1.4 Excitations and Transitions that Induce Photochemical Reactions

It is good to mention that not every photon can lead to the formation of a product. The 2nd law of photochemistry, known by the Stark-Einstein law, states that each photon absorbed is capable of activating, *at most*, one molecule for subsequent reactions [4]. There are cases where the excess of energy is liberated solely in the form of a radiative or a non-radiative process leading to the return to the ground state. As a result, the quantum yield is used to describe the efficiency of the photochemical reaction.

The *quantum yield* (ϕ) is the ratio of the number of molecules reacted to the number of photons absorbed, [4]. (Equation 1.2)

$$\phi = \frac{\# \text{ molecules reacted}}{\# \text{ photons absorbed}} \quad \text{Equation 1.2}$$

Its value lies between 0 and 1 for non-chain reactions. The closer its value to unity, the more efficient the process will be. In cases like photoredox catalysis and polymerizations that involve chain reactions, the value of the quantum yield exceeds 1. For example in photopolymerization, the irradiation will lead to the generation of a radical (initiation) that will be involved in further propagation steps until termination.[5]

By referring to the previous section, it is clear that for a photochemical transformation to take place, two factors should be taken into consideration: the energy of the supplied irradiation and the nature of the starting molecule itself. If the starting molecule includes a chromophore, direct excitation can be attainable as the molecule can undergo the electronic transitions that induce the photochemical reaction. However, this is only true for a limited number of molecules as most of the organic molecules are transparent to visible and long wave UV-A irradiation. In most cases, the starting material is excited indirectly following the transfer of electrons or energy from a sensitizer or a catalyst thus triggering the desired transformation within the sensitized molecule.

Following a UV/Vis irradiation, transitions involving π , σ and n electrons take place within the excited organic molecule/ sensitizer. As for the metal/ligand catalyst, there are three possibilities:

- Transitions within the ligand which are similar to those observed in an organic molecule.
- d-d transitions within the metal ion.
- A charge transfer between the metal and the ligand in both senses [4].

1.1.4.1 Transitions of π , σ and n electrons

An energetically favored electron transition is the one that takes place from the HOMO (highest occupied molecular orbital) to the LUMO (lowest unoccupied molecular orbital). For organic molecules including groups having valence electrons of low excitation energy, the UV/Vis absorbance will not be a series of lines, as in the hydrogen atom, but rather a continuous absorption band due to overlapping [4].

$\sigma \rightarrow \sigma^*$ is when an electron of the σ orbital is excited to the corresponding antibonding orbital σ^* . These transitions are not usually seen since they need high energies (125 nm for methane) which don't fall in the range of a typical UV/Vis spectrum (200-700nm).

$n \rightarrow \sigma^*$ is a rare form of transition that takes place when having saturated molecules with nonbonding electrons. This transition isn't very common due to the limited number of groups having this type of transition. However, it requires less energy than the $\sigma \rightarrow \sigma^*$ to be initiated (150-250 nm).

$\pi \rightarrow \pi^*$ & $n \rightarrow \pi^*$ are the most common transitions that are detected by UV/Vis spectroscopy as they can take place due to the excitation within the corresponding range of wavelengths. These transitions are exhibited by organic compounds having unsaturated groups providing the π orbital. Usually the $n \rightarrow \pi^*$ transitions show weak absorptions ($\epsilon \approx 10$ -

100 M⁻¹cm⁻¹). On the contrary, $\pi \rightarrow \pi^*$ transitions have stronger absorptions ($\epsilon \approx 100\text{-}4000$ M⁻¹cm⁻¹) that increase remarkably in conjugated systems ($\epsilon \approx 10000 - 20000$ M⁻¹cm⁻¹) [4] (Figure 1.3). The sensitizer benzophenone and the actinometer azobenzene which are used in chapter 2 and chapter 3 are examples of molecules that possess both transitions.

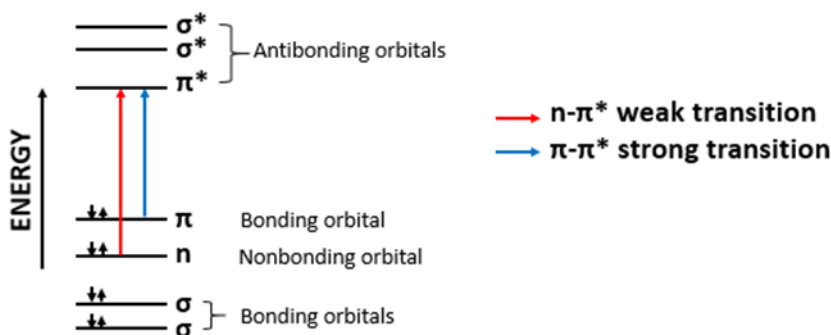


Figure 1.3: n- π^* and π - π^* transitions in an excited molecule

1.1.4.2 d-d transitions [6]

This type of transitions takes place in metal complexes. Complexes usually have a central transition metal bonded to a group of molecules known as ligands. The metal-ligand bond is formed between the Lewis acid metal having empty orbitals and the Lewis base ligand that has nonbonding electrons. The number of the metal-ligand bonds represent the coordination number which is mostly 4 or 6. Based on the coordination number, the geometry of the complex is determined. For coordination number 4, the geometry can be either tetrahedral or square planar. The most encountered geometry for coordination number 6 is octahedral.

The ligand can be monodentate, bidentate and polydentate depending on the number of donor atoms present in that ligand. Ammonia or chloride ions are considered to be monodentates, bipyridine and carbonate are bidentates by having two donor atoms and triphosphate ion and EDTA ion are polydentates.

The interaction between the metal and the ligand leads to the splitting of the d orbitals as the ligand will interact with some of the d orbitals more than the others based on the orientation (geometry). This will lead to an energy difference between the two different groups of the d orbitals (Δ). The value of this energy Δ depends on the type of the ligand attached. The placement of the two different d groups, e and t_2 , depends on the geometry of the complex. The figure below shows the d-splitting in the octahedral complexes. The position of the groups will be reversed when having a tetrahedral geometry (Figure 1.4).

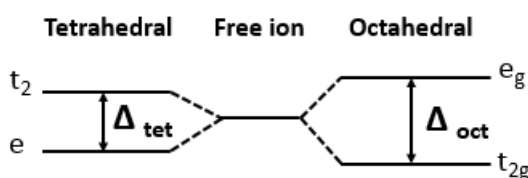


Figure 1.4: d-d splitting in octahedral and tetrahedral geometries

Note that the color of metallic complexes can be attributed to the d-d transitions. The color observed from the complex ion is the complementary color to that being absorbed and is not the result of an emitted irradiation. For example $[\text{CrF}_6]^{3-}$ needs red light (Δ is small) to allow the transition of one of the t electrons to the e group. Thus, the complex absorbs this color so the complementary color, i.e. green is the observed color of this complex. In contrary, $[\text{Cr}(\text{CN})_6]^{3-}$ has a large Δ value, so it absorbs in the violet region so that the observed complementary color of this complex is yellow (Figure 1.5)

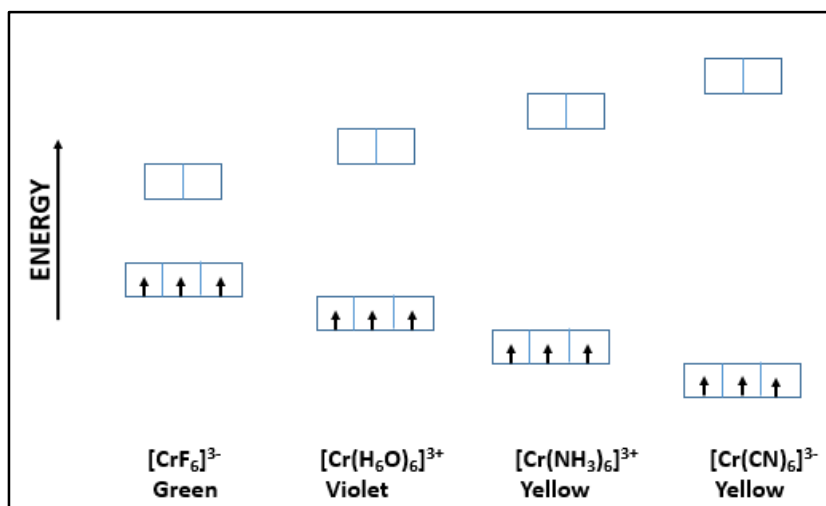


Figure 1.5: Colors of some Cr^{3+} complexes

1.1.4.3 Transitions involving charge transfer [4, 7]

d-d transitions are not always behind the color of a complex. Metal ions having d^0 or d^{10} don't have these transitions. Those having d^5 will have a forbidden d-d transition due to the change in the spin of the excited electron. However, there are complexes like MnO_4^- and $\text{Cr}_2\text{O}_7^{2-}$ that have no d-d transition but have intense colors. This is due to the change in the electronic distribution between the metal and the ligand that leads to charge transfer. It can be either a Ligand to Metal Charge Transfer (LMCT) or Metal to Ligand Charge Transfer (MLCT). Note that the MLCT and LMCT transitions result in intense bands in the UV/vis spectrum, which are much more significant than those obtained by d-d transitions (Figure 1.6).

1.1.4.3.1 LMCT

For the charge to be transferred from the ligand to the metal, the metal should be at a higher oxidation state and the ligand should be with low ionization potentials or with electron donating groups for organic ligands. In this case the energy gap will be relatively small enough for a visible irradiation to induce this transfer. Thus, the energy needed for this

transfer is absorbed by the molecule and the complementary color is observed. A typical example is MnO_4^- . The Mn is at a high oxidation state and the oxygen is a strong electron donor. The LMCT is the reason behind the intense purple color of MnO_4^- .

1.1.4.3.2 MLCT

Conversely, other metallic complexes will get their colors due to a charge transfer from a metal based d-orbital to a ligand based orbital forming the MLCT. This usually takes place when having ligands with low-lying π^* orbitals. The absorption of light energy will lead to the excitation of a d-orbital electron to the anti-bonding π^* orbital of the ligand. The color observed will be the complementary of that absorbed by the complex. The intense color of $\text{Ru}(\text{bpy})_3\text{Cl}_2$ complex, described later, is due to MLCT [8].

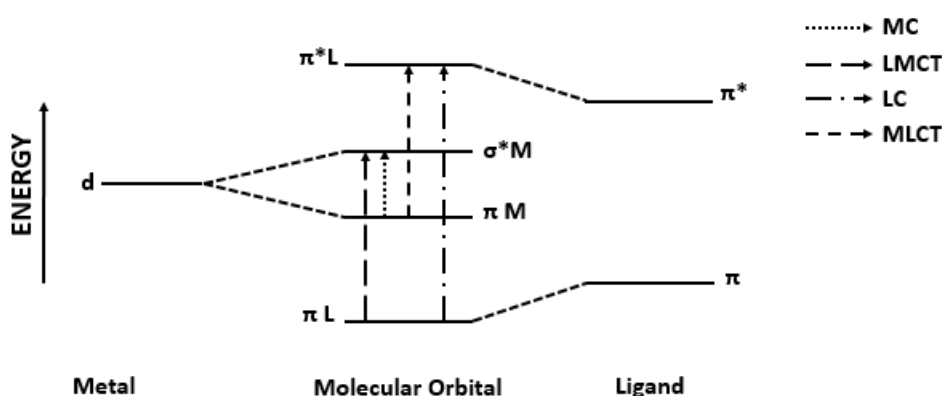


Figure 1.6: MLCT and LMCT

1.1.4.4 Implication of transitions on photochemistry

The electronic excitations $\pi \rightarrow \pi^*$ & $n \rightarrow \pi^*$ are the main contributors to photochemical reactions. For example, the excitation of the benzophenone, bearing a carbonyl group, will lead to $n \rightarrow \pi^*$ excitation that promotes H abstraction, cleavage type I and type II and addition depending on the surrounding environment. In our work, benzophenone and analogs have

been used as photosensitizers along energy transfers for the intramolecular [2+2] cycloaddition in the UV region which is discussed more in chapter 3.

Similarly, the significance of MLCT and LMCT is not only limited to providing colors to complexes. Charge transfer excitation results usually in the oxidation or reduction of the metal involved in the presence of oxidant (electron acceptor) / reductant (electron donor) species. Thus, these complexes can be used in photoredox catalysis by which the metal, upon excitation, will induce a single electron transfer to/from the starting molecules thus activating a chemical change. The photoredox catalysis of $[\text{Ir}(\text{dF}(\text{CF}_3)\text{ppy})_2(\text{dtbbpy})](\text{PF}_6)$, $\text{Ru}(\text{bpy})_3\text{Cl}_2$ and the metal free eosin Y will be discussed in details in chapters 3, 4 and 5. These catalysts are the main players for the [2+2] cycloaddition, the chemistry of trifluoroborate salts and photoinduced ATRP conducted in this work.

1.2 Photochemistry for Organic Synthesis

The beginning of organic photochemistry dates to the mid-19th century when Trommsdorf recorded the outburst of sesquiterpene santonin when exposed to sunlight [9]. This observation was further explained by Cannizzaro and Sestini in 1883 who stated that the irradiation of santonin leads to the formation of photosantonin acid [10]. However, the fundamentals of modern synthetic photochemistry were attributed to Ciamician and Silber in the early 20th century. Singlet and triplet states, $n \rightarrow \pi^*$ and $\pi \rightarrow \pi^*$ excited states, ketone photochemistry and intramolecular [2+2] cycloaddition were all first reported by this group [11].

Starting from the mid of the 20th century, photochemistry was reported to be used in the synthesis of thousands of molecules like cubane [12], caryophyllene alcohol [13] and cedrene [14]. At the industrial scale, the irradiation of cyclohexane with NOCl and HCl is

used for the synthesis of caprolactam in the Toray process [15] that is used later for making Nylon.

The current global trend toward greener synthetic approaches favors extensive research on alternative photochemical pathways as light, especially visible, is obtained from a renewable resource (the sun), is non-toxic and produces no waste. For example, until recently, the main form of polymerization was thermal. However, photopolymerization appeared ten years ago and is starting to compete with the thermal activation process since the quality of the formed polymers are the same, if not better [16]. In the same course, visible light photoredox catalysis that was rediscovered by Stephenson and Mc Millan groups is the topic of research for a lot of research groups around the world [17-21]

1.2.1 Conventional Techniques & Equipment

The parameters that are taken into consideration in a photochemical reaction are the light source, the photoreactor, the solvent and the glassware. The following section includes the equipment which is classically used in photochemical processes [2, 5, 22]

1.2.1.1 Lamps

The commercial availability of the mercury-discharge lamps made them the main type of UV source used by photochemists. A mercury vapor is placed inside a glass vacuum tube that includes electrical discharges. Electric supply will lead to the excitation of the mercury atoms that will then emit UV irradiation upon relaxation. High, medium and low pressure Hg lamps are commercially available and provide different ranges of irradiations. Medium and low pressure Hg lamps are more preferred due to their reliable lifetimes [2, 5, 22].

- Low-pressure (LP): These cost effective mercury lamps emit their irradiation mostly at 254 nm (Figure 1.7); however adding phosphors can shift the emission spectra to

the UV-A and UV-B regions in the hybrid LPUV lamp known as the fluorescent lamp.

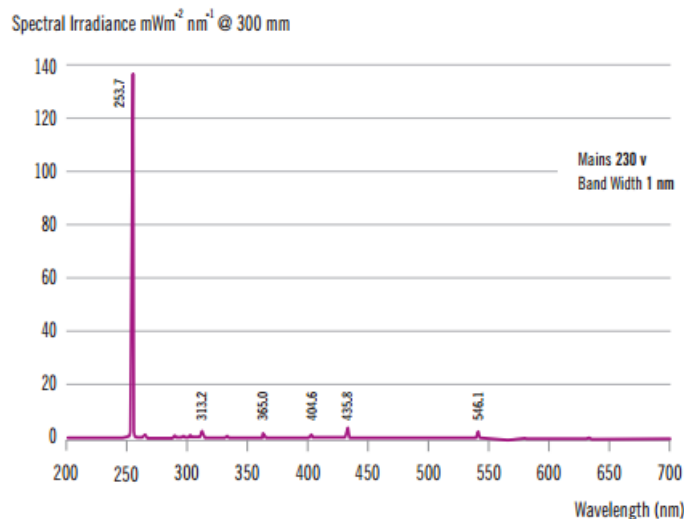


Figure 1.7: Emission spectrum of low-pressure Hg lamp[23]

- Medium- pressure (MP) are broadband emitters in the 300–370 nm region. They are used when working with chromophores that absorb between 290 and 400 nm. However, these lamps heat up so they must be coupled with proper water cooling systems.
- High-pressure (HP) lamp provides maximum emission at 365 nm with substantial radiations at 435, 313, 254, 405 and 546 and 570 nm (Figure 1.8).

In most cases, photochemists use filters to get the desired irradiation wavelength when using MPUV and HPUV lamps that emit polychromatic radiations.

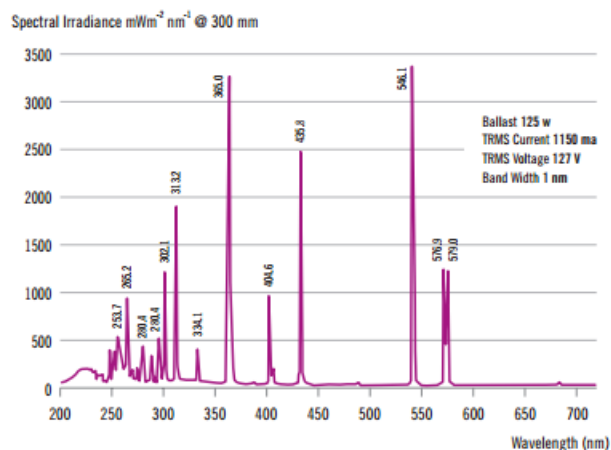


Figure 1.8: Emission spectrum of high- pressure Hg lamp [23]

1.2.1.2 Photoreactors

- Immersion well reactor is the most commonly used photoreactor for organic photochemistry in conjunction with mercury-vapor discharge lamps (Figure 1.9). This assembly was used to produce chemicals in the range of mg to g. The photoactive substrate is placed in a classical Pyrex flask. The irradiation system is composed of a lamp which is surrounded by a water- cooled immersion well. This system is then immersed within the Pyrex flask. Covering the whole set with aluminum foil can be done to prevent any illumination other than that provided by the photoreactor's light source. The reaction mixture can be degassed to prevent any side reaction that might take place due to oxygen. Once the reaction is started, classical methods of monitoring (TLC, GC, LC-MS), workup and extraction are applied [22].

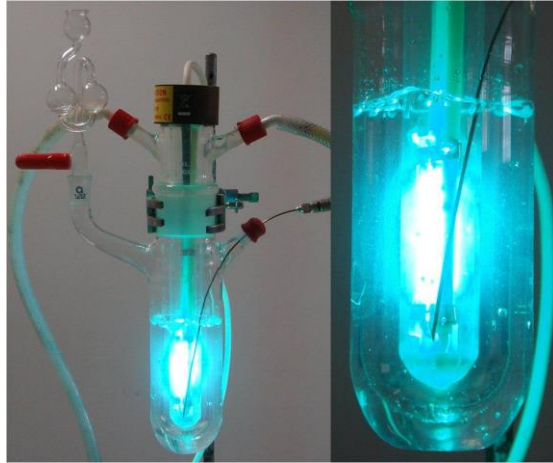


Figure 1.9: An immersion-well batch reactor with medium -pressure Hg lamp [22].

- In a Rayonet reactor, the sample is placed at the center of a cabinet surrounded by 16 lamps. Such reactors are usually accompanied by a cooling fan for temperature control [22] (Figure 1.10).



Figure 1.10: Rayonet reactor [24]

- A Falling film reactor is composed of a tube whose outer wall is surrounded by the temperature control system. Its inner wall is in contact with the liquid film containing the reactant. The irradiation source is inserted to be in proximity with the liquid film (Figure 1.11). This short distance between the light source and the reaction mixture

makes it an efficient photoreactor. However, the main drawback of such a system is the short irradiation time thus the reaction mixture should be recirculated for several times to get the optimum irradiation time thus increasing the risk of side reactions [2, 5, 22].

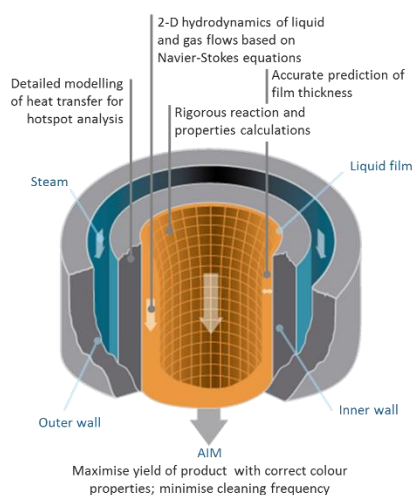


Figure 1.11: Falling film reactor [25]

1.2.1.3 Glassware

The choice of the glassware to be used in photoreactors depends mainly on the desired wavelength of irradiation. In such cases, the glassware has a dual role as a container and as a filter that can cut off all of the undesired irradiations that are emitted from an HPUV. For instance, Quartz is transparent starting from 170 nm whereas the cut-off of Pyrex is 275 nm. Moreover, placing a piece of Pyrex glass in the middle way between the reaction mixture and the irradiation source is also used for filtering out all of the irradiation which is below 275 nm [2, 5, 22].

1.2.1.4 Solvent

Another key factor in photochemistry is the choice of the solvent. Other than being able to dissolve the reagents added, the solvent in photochemical reactions should be checked for its transparency and reactivity at the chosen irradiation. Under specific conditions, the solvent might undergo modifications in response to irradiation (a side reaction) that hinder the reaction in concern. Acetonitrile was shown to be a convenient solvent as it doesn't absorb above 200 nm, dissolves a wide range of substrates, has no detrimental effects on the walls of the reactor, easy to handle and economical [2, 5, 22].

1.2.2 Limitations

However, one might ask why such technology is still limited to small scale production after around two centuries of development and research on photochemical reactions' kinetics and mechanisms. Industries still prefer using routes other than photochemical due to multiple complications.

The knowledge and numerical models which are gathered about thermochemical reactors cannot be applied to photoreactors. This is due to the fact that photons are the major players in such reactions; thus, additional considerations should be taken to optimize the conditions of a reaction. This includes the choice of the light source, its distance from the photoreactor, the uniformity of the photoreactor's illumination, the geometry of the photoreactor and even the material the reactor is composed of. In addition, cooling systems should be adjusted to the photoreactor to prevent its damage and the solvent should be chosen in a way that it neither damages the walls of the reactor nor absorbs light at the chosen wavelength nor hinders in any way the photochemical process. All of this complicates the shift to the photochemical routes. More importantly, scaling up of a photochemical reaction to the industrial scale faces a lot of challenges as the efficiency of the mixing, heat transfer

and light illumination are at their best on the laboratory scale. Not to mention the safety precautions that should be taken due to the dangerous emitted irradiations. This has made a lot of synthetic chemists avoid the photosynthetic pathways and prefer the classical routes [2, 22].

1.3 Microreactor Technology

Most of the limitations listed above (solvent, glassware, reactor's material, cooling system...) are already overcome and optimized on the lab scale and thus can be directly implemented on the industrial scale. However, the only real problem that hinders the up scaling of photoreactions lies in the significant difference in the performance between lab scale and industrial scale batch reactors. Fortunately, the microreactor technology can be a solution for this problem as it is considered to be one of the most efficient technologies used for process intensification. It started gaining interest among synthetic chemists during the last 15 years in response to the work done by Ley [26, 27] that demonstrated the possibility of synthesizing complex organic molecules using this technology. It is now believed that almost all of the common batch reactions can be easily performed in flow reactors [28].

A microreactor is a miniaturized confined space upon which a reaction takes place. It is made up mostly of a tubular system with microscale dimensions [29]. It operates by the continuous feeding of reactants and collection of products in a highly controlled manner. There exist a wide range of microreactors with various volumes. Those whose volumes are 5 mL and above are called mesoscale reactors [5].

Based on the reaction conditions, the flow generated inside these microreactors can be classified by single phase or segmented phase. Single phase flow is applicable when the reaction is taking place in homogeneous-liquid phase reactions. Segmented flow however

corresponds to cases where a reaction takes place under heterogeneous phase conditions as in gas- liquid or immiscible liquids reaction conditions [30].

When working with flow microreactors, one must distinguish between the residence time and the reaction time. The residence time is the time that every molecule of the reaction mixture stays within the microreactor. It corresponds to the irradiation time for photochemical reactions. This parameter depends on two factors, the volume of the microreactor (that is exposed to the irradiation) and the flow rate of the reaction mixture (Equation 1.3).

$$\tau = \frac{V}{q} \quad \text{Equation 1.3}$$

τ (residence time); V (reactor volume); q (flow rate).

In some cases, as when using tubing as the microreactor, the volume of the reactor can be modified. However, in cases where designed microchips are used, the volume of the reactor is fixed. As a result, the change in the irradiation time can be established by changing the flow rate of the reaction mixture: smaller flow rates for longer residence times and vice versa.

In contrary, the reaction time depends on the volume of the reaction mixture to be purged within the microreactor and the flow rate (Equation 1.4). This factor can be modified by changing both the volume injected and the flow rate. For a given flow rate, the reaction time will be more than the irradiation time if the volume of the reactor is less than the volume of the reaction mixture. Since this is the case when working with micro-scale reactors, this can be considered a drawback in flow chemistry.

$$\tau = \frac{V_{sample}}{q} \quad \text{Equation 1.4}$$

τ (reaction time); V (volume injected); q (flow rate).

To determine the efficiency of a microreactor, the throughput of a reaction is usually determined. It corresponds to the number of moles of product produced per minute of irradiation. This factor is usually used to compare the performance of microreactors to those of batch reactors.

Microreactor technology can exhibit a good control over all of the implications encountered in a photochemical reaction. Its high surface area to volume ratio favors high mass and heat transfer leading to improved yields and temperature regulation. The simultaneous injection of the reactant and collection of the product also enhances the yield in the continuous flow operation. Side reactions and photodecomposition of light sensitive products are limited as they are not subjected to prolonged irradiation times. Safety hazards are minimized as it is less likely to have an accumulation of potentially hazardous materials or pressure when working with relatively smaller quantities at a time. Even scaling up can be done by simply numbering up the microreactors. Another advantage that favors the usage of microreactor technology for photochemistry is the microscopic dimensions of the microfluidic system. Such systems are characterized by small dimensions, mainly the path length, that provide efficient penetration of light and thus ensures homogeneous irradiation of the reaction mixture. In this case, better selectivity and productivity along with the decrease in reaction times and catalyst/sensitizer loading are achieved due to the significant increase in the quantum efficiency. In addition, as previously noted, photochemistry provides simple and easy routes of synthesis for complex molecules. Thus, the combination of microreactor technology with photochemistry provides the perfect scenario for green and sustainable synthetic pathways [31].

1.3.1 Why to Use Photochemistry in Flow?

1.3.1.1 Photon flux

The Photon flux is the number of photons that is provided to the reaction mixture in a setup per unit of time. It can be used to determine the quantum yield of a reaction [5]. The photon flux can be determined by chemical actinometry (described in chapter 2) as the amount of photons delivered by the irradiation system might not be fully transmitted to the reaction mixture due to refraction and to the incompatibility between the dimensions and geometries of the reactor and the light source.

Knowing that the photon flux has a very important factor on the reaction kinetics, Loubière and co-workers made a comparison between the photon flux received by a batch reactor and a flow reactor [32]. The former received a photon flux of 4.44×10^{-4} Einstein.min⁻¹ whereas the latter, i.e. the microreactor, received a photon flux of 2.46×10^{-4} Einstein.min⁻¹

The photon flux density is obtained by dividing the value of the photon flux over the volume of the reactor. In that case the microreactor had 301 Einstein.m⁻³.min⁻¹ vs. 1.98 Einstein.m⁻³.min⁻¹ for the batch reactor showing that the amount of photons delivered to the microreactor is 150 times more than that delivered to the batch reactor. This explains the reason behind the acceleration in the reaction kinetics in flow reactors [5, 32].

1.3.1.2 Photonic efficiency

The photonic efficiency is also another factor that can define a photochemical process. It corresponds to the ratio of the reaction rate to the photon flux Q (Equation 1.6) [5].

$$\xi = \frac{\text{reaction rate}}{Q} \qquad \text{Equation 1.6}$$

In batch reactors, this value was reported to range between 0.0086 and 0.0042 [33]. A recent study done by Noël and co-workers showed that when using microscale irradiation sources like LEDs, this value can be improved up to 0.66 [34].

1.3.1.3 Path length

The impact of the small path length on the photochemical reaction can be explained by using Beer-Lambert's Law (Equation 1.7).

$$\log \frac{I_0}{I} = \Delta A = \varepsilon c l \quad \text{Equation 1.7}$$

This shows that for a given concentration c (mol.L^{-1}) and molar extinction coefficient ε ($\text{L.mol}^{-1}.\text{cm}^{-1}$), the absorption of light by a specific chromophore increases with the distance l (cm). An absorbance of 2 means that 99% of the light is absorbed by the substrate and only 1 % of the light is transmitted after a given length l ($I = 0.01 I_0$). For example, consider the sensitizer 4,4 dimethoxybenzophenone (DMBP) that has a molar extinction coefficient $\varepsilon = 135 \text{ M}^{-1}.\text{cm}^{-1}$ at $\lambda = 365 \text{ nm}$. By applying the law above for $c = 0.05 \text{ M}$, 99% of the light will be absorbed after only a distance of 3 mm (Figure 1.12). This value is by far less than the path length of a typical batch reactor that is in the range of few centimeters. In other words, after only 3 mm no light is capable of penetrating so that only a limited portion of the reaction mixture is illuminated. This problem is more intensified with the increase in the value of the molar extinction coefficient ε . For instance, the catalyst $\text{Ru}(\text{bpy})_3\text{Cl}_2$ has a very strong absorption at $\lambda = 450 \text{ nm}$ due to MLCT. The corresponding molar extinction coefficient ε is $14600 \text{ M}^{-1}.\text{cm}^{-1}$ so a concentration of 1 mM will be enough to absorb almost 90 % of the irradiation after only 685 μm ! (Figure 1.12). Note that a typical $\pi \rightarrow \pi^*$ will have ε values between 10000 and 20000 hence having similar results for those of $\text{Ru}(\text{bpy})_3\text{Cl}_2$ [4].

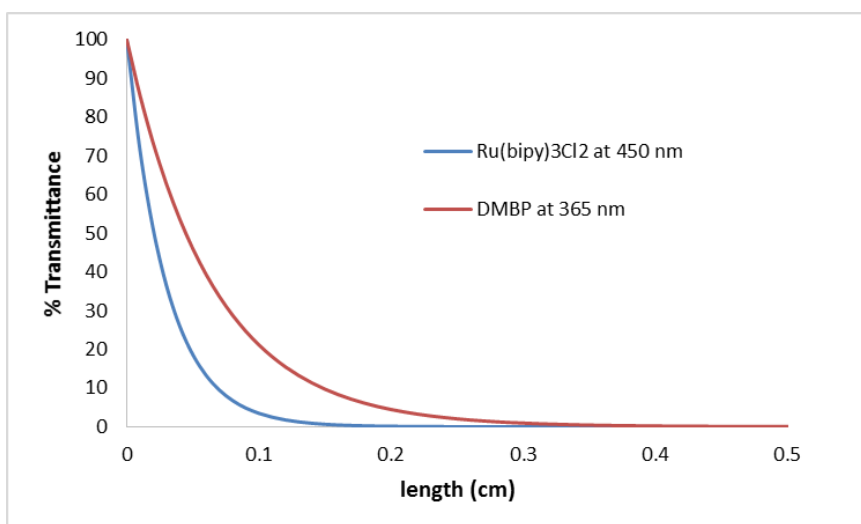


Figure 1.12: Variation of the transmittance of light vs. the distance (path length) for benzophenone (0.05 M, $\epsilon = 135 \text{ M}^{-1}\cdot\text{cm}^{-1}$, $\lambda = 365 \text{ nm}$) and Ru(bpy)₃Cl₂ (0.001 M, $\epsilon = 14600 \text{ M}^{-1}\cdot\text{cm}^{-1}$, $\lambda = 450 \text{ nm}$).

The variation in the illumination within the same reaction mixture will lead to having side products due to over irradiation on one hand and a decrease in the productivity in response to under irradiation on the other. This problem in batch reactors is overcome by using microreactors whose path lengths are less than 1 mm. As a result, the reaction mixture in continuous flow systems is more likely to be fully illuminated.

1.3.2 Continuous Flow Microreactor Design for Photochemistry

The usage of the flow technology for photochemistry was restricted to few reports during the 20th century. Vitamin D synthesis was reported to be assessed in a spiral glass reactor in 1959 (Doede & Walker, 1959). During the synthesis of methyl chloride in 1971, coiled Teflon tubing was used as a gas phase reactor [35]. The integration of the microreactor technology within photochemistry started to grow rapidly starting from the beginning of the 21st century [22].

Photochemical reactions like addition, cyclization and decarboxylation were assessed using microflow conditions. The microfluidic systems excelled over the batch reactors even

though the latter was supplied with triple the number of lamps (16 lamps vs. 5 lamps). In all cases, better yields and selectivities along with the decrease in the irradiation times and side reactions were observed. This has also provided an additional advantage: limiting the side reactions gave almost pure products thus further purification steps were excluded.

Since the microreactors can be pre-designed and engineered, it is important to understand the nature and the implications of the reactions to be run in the reactor for the optimization of the latter to the conditions of these reactions. Whether simple or complex a photomicroreactor assembly should be composed of three main parts: The flow reactor, an injection system and a light source. In some cases, mixing, online analytical or purification systems can also be included within this assembly (Figure 1.13).

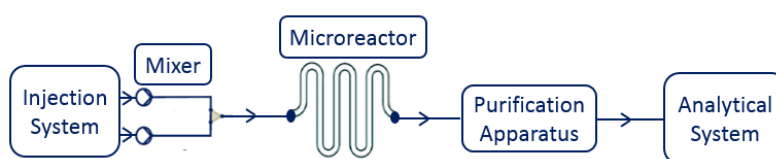


Figure 1.13: Set-up of a photomicroreactor assembly

1.3.2.1 Reactor's material

Reactors with microscale dimensions can be fabricated from a wide range of material. There exist various methods of fabrication like hot embossing, wet and dry etching, lithography, injection molding ... that can provide the desired dimensions with very high precision [29]. For photoreactors, it is very important for the material used to be transparent to the desired irradiation wavelength. This limits the choice of the optimum material to certain types of polymers, glass, silicon and ceramics (Figure 1.14).

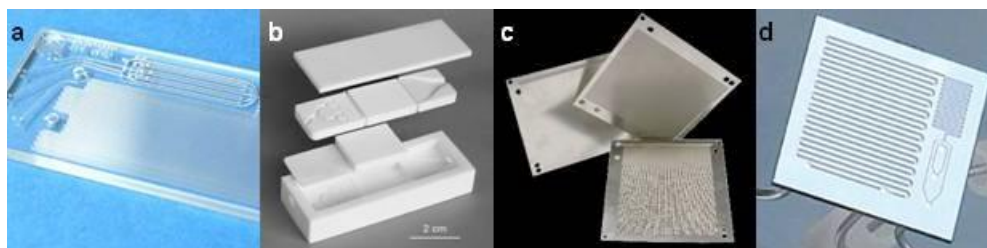


Figure 1.14: Examples of microreactors fabricated from: (a) glass; (b) ceramic; (c) metal and (d) silicon[2].

Polymers are the cheapest and easiest to be fabricated of all. Polymethyl methacrylate (PMMA), polydimethylsiloxane (PDMS), perfluoroalkoxyalkane (PFA), and fluorinated ethylene propylene (FEP) polymers are used for photomicroreactors due to their elevated light transmissions. However, organic solvents lead to the swelling of PMMA and PDMS thus limiting the usage of these polymers to only aqueous reactions. FEP and PFA are on the contrary inert to most reagents and solvents even under high acidic and alkaline conditions. They have high flexibility and also high transparency to UV (PFA, T=77-91%) and visible light (PFA, T= 91–96%) making them favored for fabricating tubing used as photoreactors (wrapped around a lamp) [31].

Quartz (cut off < 170 nm), Pyrex (< 275 nm), Corex (< 260 nm) and Vycor (< 220 nm) are types of glass that are used in the fabrication of photomicroreactor due to their light transparency. They can also be used as filters to remove the undesired wavelength emitted from a polychromatic light source. Though they are the most chemically inert among all other types of material, their fabrication is difficult to handle. Similarly, ceramic are chemically inert but also hard to handle. Silicon's manufacturing cost is very high and it is incompatible with alkaline conditions [31].

1.3.2.2 Injection system

The continuous flow is controlled by injection systems that function based on mechanical or non-mechanical pumps. The former is more commonly used in the form of syringe pumps, peristaltic pumps and High Performance-Liquid Chromatography (HPLC) pumps (Figure 1.15).

Syringes require the storage of the reaction mixture within. Peristaltic pumps use flexible tubes that host the reaction mixture. The rotation of the rotor compresses the tube thus forcing the mixture to be expelled out of it [36]. The piston inside HPLC pumps force the liquid to flow through the tubing at specific flow rates.

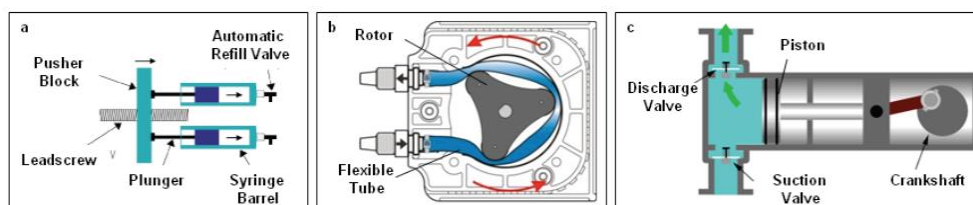


Figure 1.15: Mechanical pumps: (a) syringe pump; (b) peristaltic pump; (c) HPLC pump [2].

Non-mechanical pumps include those that function under the effect of electricity like the electro-hydrodynamic pump. Such pumps include electrodes to generate an electric field that accelerates charged molecules and thus form a flow [37].

The microreactor is connected to the other devices of the assembly via tubing, fittings, connectors and sleeves. These tubing can be made of polymer, glass, silicon or metal. In all cases, the tubing should withstand high pressures.

1.3.2.3 Light sources

Typical Hg lamps are also used with microfluidic systems for photochemical reactions. They are best suited when tubing reactors are coiled around them. When working with

microreactors, these lamps should be placed outside these reactors as their dimensions are larger than those of the reactors.

Lately, light emitting diodes (LEDs) are gaining a lot of interest in the field of continuous flow photochemistry. The LEDs can provide very narrow emission spectra (20 nm) rendering them suitable for a wide number of reactions. By using LEDs, side reactions are less likely to take place compared to other types of light sources that are broadband emitters. In most cases, the LEDs can also be matched with the maximum absorption wavelength of the chromophore thus increasing the photon flux efficiency and the reaction's yield. They require low power input and establish minimal heat energy loss so the system can be cooled down by a fan. They are also cost effective and are small enough to be placed on the microreactor [38, 39].

High Power LEDs are an effective replacement of mercury lamps in many power-demanding applications, they are precisely adjustable, stable power with rapid warm up time and present a long life (over 10,000 hours) so no lamp replacement is required for long time application such as continuous flow photochemistry. However, if the wavelength range of LEDs is constantly extended, the too low optical power (few $\mu\text{W}\cdot\text{cm}^{-2}$) of recently developed UV-B LEDs (315 – 280 nm) limits their use in photochemistry. Today, the use of LEDs in UV photochemistry is still limited to the range of near UV-A LEDs (365-400 nm) for which high power LEDs (up to $12\text{ W}\cdot\text{cm}^{-2}$) have recently been developed. [40-44].

1.3.2.4 Mixing systems

In continuous flow microreactors, reagents can be mixed before their introduction within the microreactor or simultaneously using a mixing system. The mixing system can be *via* T or V connections, micromixers... In a cylindrical tubing, based on the flow rate of the mixture, the mixing can be laminar or turbulent and that depending on the value of Reynold's

number R_e (Equation 1.8). Reynolds number varies with the velocity and the diameter of the tubing. Higher is the flow rate higher is the Reynold's number. In addition, lower is the diameter lower is the Reynolds number. If Reynold's number is below 2100 in a cylindrical channel, the flow will be laminar (Figure 1.16 (a)): the fluid flows in parallel layers, with no disruption between the layers [45, 46]. In contrary, the flow regime of a fluid will be chaotic in a turbulent flow when R_e is between 2040 and up to 4000 (Figure 1.16 (b)).

$$R_e = \frac{V \times d}{\mu} \quad \text{Equation 1.8}$$

R_e (Reynolds number); V (average velocity); d (hydraulic diameter of the channel); μ (viscosity).

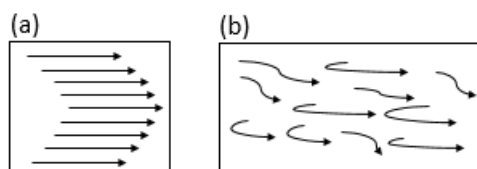


Figure 1.16: Types of flow: (a) laminar flow (b) turbulent flow.

In microreactors, the regime is usually laminar. Nevertheless, in mixers (such as T-junctions) chaotic perturbations can occur at the beginning of the mixing, just after the change of direction of the flow, even at low Reynolds number values. This results in mixing quality variations depending on the flow rate. Usually, better mixing is observed at higher flow rates.

The mixing within a microreactor can be passive or active. In the case of the multi-laminar flow, mixing can take place passively due to the passive diffusion of the two fluids that are flowing in parallel. This is due to the increase in the surface of contact between both fluids that improves the diffusion between the two phases [47].

In the case of active mixing, a force (ultrasonic, thermal, magnetic...) will be applied to improve the diffusion between the fluids [48]. However, active mixing requires the

fabrication of a more complex microreactor and requires high skills as it can induce turbulent flow [49].

1.3.2.5 Purification apparatus and analytical systems

One of the interesting options that are provided by the microfluidic technology is the ability to adjust online purification and monitoring systems. Tools that were integrated at the downstream of a microreactor are microextractor [50], a porous membrane that exclusively wets an organic solvent [51] a distillatory apparatus [52], a column containing a scavenger to remove residual byproducts [50] and another reactor for scaling up.

Rapid screening reactions can also be performed due to the online analytical systems that can be added like the automated measure of temperature and pressure, HPLC, IR, UV spectrometer...[53, 54]

1.3.2.6 Material and solvent constraints

In photochemical reactions, the solvent should be chosen to not quench the reaction and to be transparent to the desired wavelength (discussed before). When using microreactors, additional attention must be given to the solvent. The solvent should be able to dissolve all of the reagents to prevent any solid precipitation within the microfluidic system. Otherwise, clogging of the device and light scattering that might lead to side reactions will take place [5].

1.3.3 Types of Flow Systems used in Photochemistry

The falling film reactor was considered to be the first flow system that was used for photochemical reactions as it is composed of parallel channels that are engraved within the

metallic cylinder. However, the continuous flow reactors can be classified into two major groups: Chip and tubing devices.

1.3.3.1 Tubing devices

Tubing devices are composed of a UV transparent tubing of i.d. > 0.5 mm (PFA, FEP...) that is coiled around a light source (Figure 1.17). The reactor's volume can be easily adjusted by simply changing the length of the used tubing. However, this is the only factor that can be modified in these reactors compared to the chip devices which as listed before can be designed and engineered based on numerical estimations that tend to increase the yield of the reaction. However, Tubing systems also gain a lot of interest due to their simplicity: a tubing wrapped around a light source and a syringe pump are all that is needed to run the reaction. As a result, it is preferred to work with these systems using light sources that don't warm up like the LP Hg lamps or LEDs as temperature control is hindered in such reactors [22].

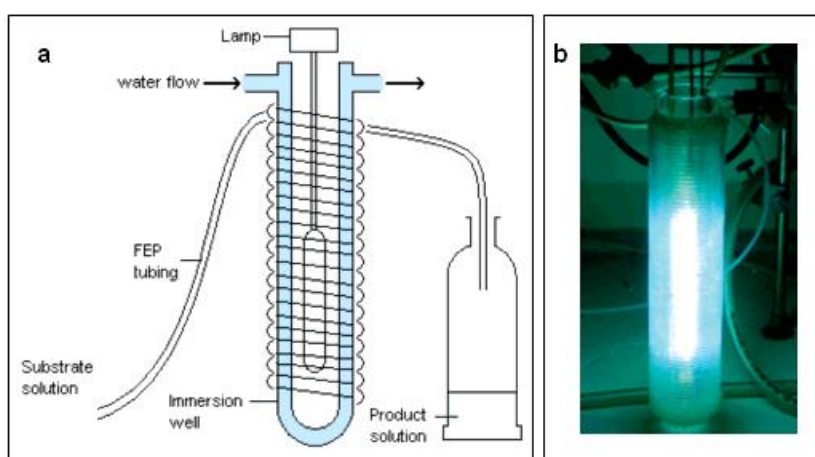
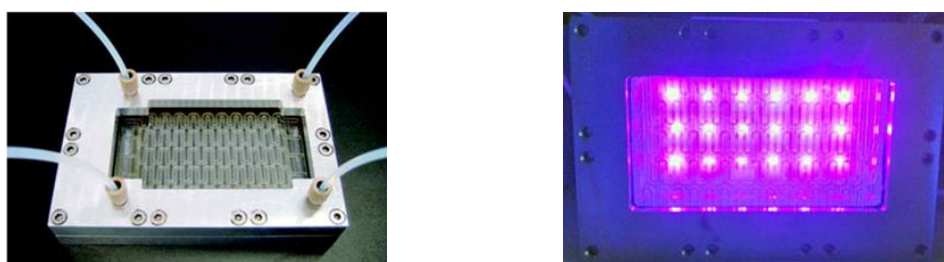


Figure 1.17: (a) Scheme of FEP flow reactor, (b) image of the system [2, 22]

1.3.3.2. Chip devices

Chip devices have microchannels that have a path length which is less than 1 mm (Figure 1.18). A syringe pump or an HPLC pump can be easily used for the control of the flow rate that can range between few microliters up to few mL per minute. They can be fabricated from a wide range of material like silicon, PDMS and glass. The ability to predesign and thus modulate the dimensions of the chip makes it possible to adjust to the reaction conditions. Temperature control can be established by adding a layer of channels to the chip allowing the flow of the cooling agent. Combining this microreactor to online analysis will provide a rapid way in reaction optimization and screening. The only drawback for such chips is to not being able to use fully the photons delivered by the light source. Since these chips cannot be bent around the light source, some of the source's radial irradiation will fail to reach the flat chip device. This in turn, makes it challenging to calculate the theoretical number of photons, photon flux, that reaches the system. However, the problem is relatively minimized when using the planar LEDs [22].

Figure 1.18: (a) Microfluidic glass reactor; (b) same reactor illuminated by UV LEDs



Corning® has designed an advanced flow reactor that is composed of multiple fluidic modules that can be added in series rendering to scale up. These chips are also adjusted with integrated energy and mass transfer layers. The Corning® Advanced-Flow™ G1 reactor was slightly upgraded to have the Corning® Advanced-Flow™ G1 photo reactor (Figure 1.19). It has additional tunable UV LEDs that can be adjusted to illuminate each chip from both

sides providing efficient light penetration. 365 nm and 405 nm LEDs are currently available for this reactor [55].

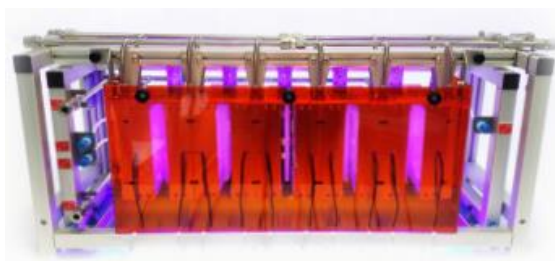


Figure 1.19: Corning® Advanced-Flow™ G1 photo reactor [55]

Tubing devices overpass the chip devices when it comes to the capturing of the emitted photons as they coil around the lamp giving no chance, in theory, for any photon to escape. This can have a great impact on the productivity within these reactors as the quantity of photons delivered to the reaction mixture significantly affects the course of the photochemical reaction. However, this advantage fades when using the planar LEDs that makes it impossible to wrap the tubing around them [22].

Jensen and coworkers fabricated two reactor prototypes. One is made up of Pyrex for photochemical reactions at 365 nm and another composed of quartz for shorter wavelengths. Both prototypes were composed of microchannels that are serpentine shaped as this is the best way to get the longest channel possible within a constrained space that has an outlet and an inlet on both extremities [56].

A glass microreactor with a serpentine shape but with two inlets was fabricated by De Mallo *et al.* [57]. This microreactor was used for liquid-gas reactions. The Mikroglas Dwell Device FOTURAN®60, which is used by our group, was also used by Fukuyama *et al.* This glass microreactor has an integrated cooling/heating system [58] .

So chip devices provide a wide range of optimizations that can't be given by the simple tubing systems like the advanced control of temperature and side reactions. However, in reactions like polymerization, it is much preferred to work in tubing systems rather than in

chips to prevent clogging. After all, it is more practical to dispose of a 100 € tubing than replacing a glass chip that costs ten times more.

1.3.4 Examples of Photochemical Reactions Performed in Continuous Flow

Several types of reactions were reported to be assessed using the microreactor technology like photocycloaddition, isomerization, cyclization, photocatalysis, polymerization...

Fukuyama *et al.* reported the [2 + 2] addition of vinyl acetates with various cyclohexenone derivatives using the dwell device. Yields were improved (71 % vs. 26 %) and reaction times were reduced by two (2 hours vs. 4 hours), compared to the same reaction run in batch [58] (Figure 1.20)

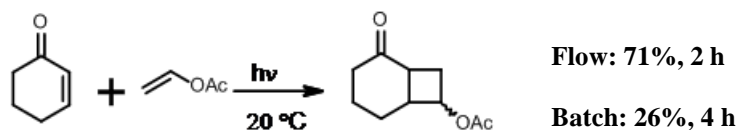


Figure 1.20: [2+2] Photocycloaddition of cyclohexenone and vinyl acetate.

Another [2 + 2] photocycloaddition was performed in a tubing by Conradi and Junkers. By optimizing the solvent and the power of the UV lamp, the yield of the cycloaddition of a 1:1 ratio of maleimide with octene was improved from 6 to 99 % after 10 minutes of irradiation (Figure 1.21). For batch conditions, excess of octene along with around 8-12 hours of irradiation were needed to get the same yields of those obtained in flow [59].

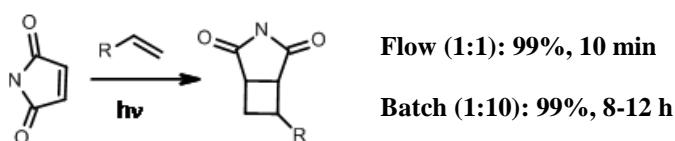


Figure 1.21: [2+2] Photocycloaddition of maleimide with an alkene

Jamison and co-workers used continuous flow microreactor for the photochemical rearrangement of nitrones using UVB lamp (Figure 1.22). The microreactor was composed of a tubing of i.d. 760 μm . The nitrones isomerized to the corresponding amides in 60-90% yields after 5-20 min of irradiation in the presence of trifluoroacetic acid [60].

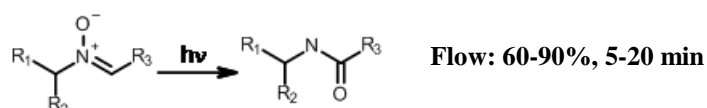


Figure 1.22: Photoisomerization of nitrones to amides.

An example of continuous-flow photocyclization was reported by Rueping and co-workers for the oxidative photocyclization of stilbene derivatives (Figure 1.23). The reaction was performed in FEP tubing (5 mL) that was irradiated by a high-pressure lamp. The oxidative cyclization of (*E*)-stilbene to phenanthrene gave 95% yield after 83 min of irradiation [61].

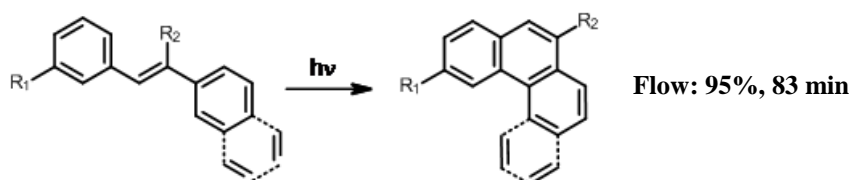


Figure 1.23: Photocyclization of stilbenes to phenanthrenes

Metal based photocatalysis in flow is also reported by several research groups. Maurya and coworkers reported the usage of Ruthenium catalyst for the generation of imidazoles from a vinyl azide and secondary amines (Figure 1.24). The reactor used was a tubing of i.d 760 μm coiled around an LED source. The flow results were more significant than those obtained in batch where 55% conversion was obtained after 12 h of irradiation. In flow the irradiation time was reduced to 44 min and the yield was improved to 65% [62].

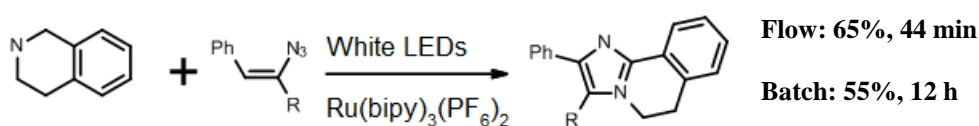


Figure 1.24: Formation of imidazoles from secondary amines and vinyl azides by photoredox catalysis

Recently, organic photocatalysis is also gaining a lot of interest. The activity of eosin Y in continuous flow was recently reported by Noël and co-workers. They used this organic catalyst for the aerobic oxidation of thiols to disulfides in a tubing (ID 760 μm , 950 μL) that was irradiated by white LEDs (Figure 1.25). Interestingly 87-99% yields were obtained in 20 mins of irradiation in flow compared to 16 hours in batch to get full conversion [63].

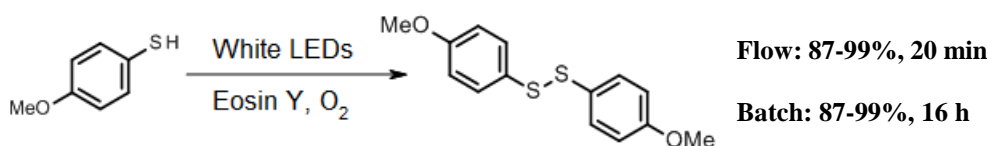


Figure 1.25: Oxidation of thiols to disulfides using Eosin Y.

Photopolymerization in flow was reported using a glass microreactor of an internal diameter of 1.5 mm. The polymerization of n-butyl acrylate was performed using UV irradiation and compared to batch and thermal polymerizations. Conversion up to 80 % was

obtained after only 38 s of irradiation in flow which was around five folds less than the batch conditions. Moreover, the D values were much less in flow than in batch (2.03 vs. 9.61) [64].

1.3.5 Advantages and Limitations

The continuous flow technology has proved to be an efficient technology that has exhibited a positive influence on a wide range of chemical reactions including photochemical reactions. This suggests that such technology can have a good impact on drug discovery and process development and that by decreasing the usage of reagents, energy, cost and time in the screening and optimization of reaction conditions that take place at the microscale level. Scaling up can be done later by connecting several microreactors or increasing reaction time. Automated and parallel microflow photochemical reactors are used in small-scale manufacturing plants for the innovative Heraeus Noblelight process of synthesis of anti-cancer precursors showing that this technology has a bright future in the drug industry [65].

Continuous flow reactors have also been reported to excel the batch reactors even in productivity by scaling up a batch reaction from sub-gram to over 500 g per day like the synthesis of the main medication against malaria artemisinin [66].

The geometry of the microreactors provides a large surface area to volume ratio thus improving heat and mass transfer that are direct contributors to the productivity, selectivity and residence time. Since small quantities of a reagent are inserted into the reactor at a time, handling hazardous compounds can be easily controlled in continuous flow especially that the system provides a good isolation from air and moisture and facilitates the work under inert conditions.

Rays of compact LEDs fit well to the dimensions of the microreactors and thus solve the problem of small photon flux that such reactors receive when illuminated by classical Hg

UV lamps. The prices of the UV LEDs are relatively high but will decrease along time which serves well the microreactor technology.

The microreactors' path lengths are less than 1 mm; thus, at a given time only a small quantity of the reaction mixture, even when concentrated, will be present to be fully and homogeneously irradiated. Working with high concentrations will not impact the homogeneity of the illumination due to the small path length (Beer Lambert's Law) and the productivity will not be altered by working at low concentrations in cases where side intramolecular reactions should be suppressed. The Irradiation time can be regulated by varying the flow rate with respect to the reactor's volume. This gives the possibility to work at very high flow rates and thus extremely small irradiation times which is not feasible using batch reactors. The latter can be explained by simply comparing two reactions of 10 s irradiation time, in flow the whole reaction mixture will be irradiated for 10 s whereas this is unlikely to take place in batch. Thus, environmentally friendly chemistry can be implemented using this technology that uses minimal quantities of solvents, reagents, byproducts and energy.

Like any other rising technology, the microreactor technology exhibits some drawbacks. The reagents should be soluble to prevent solid precipitation and thus clogging of the system. The cost and the complexity of the construction of such devices are also to be taken into consideration compared to the batch technology which has been used for centuries. However, the major drawback that limits its usage in mass production is the prolonged reaction times. This makes this technology useful in early stages of research for screening and optimization of conditions where only small quantities are sufficient.

In addition, designed microfluidic devices can be relatively expensive so they are used for specific reactions that require control over certain conditions. However, using tubing can

make the continuous flow chemistry simple and cost effective with all of the set up being commercially available.

With the wide range of advantages that it can provide when coupled with photochemistry for the synthetic chemistry, it is believed that it is a matter of time for synthetic chemists to adopt this green approach. The number of cited papers that focus on photochemical reactions in flow increased to 750 in 2015 showing that more and more research groups are using continuous flow [5].

CHAPTER TWO

CHEMICAL ACTINOMETRY

2.1 Introduction

The main aim of this work is to perform photochemical reactions, in the UV and visible ranges, in microfluidic systems and study the impact of the decrease in optical length, provided by these systems, on the reactions in total.

However, before discussing in details the different photochemical reactions assessed, it is important to characterize the Mikroglas ® Dwell Device microfluidic system that is widely used for photochemical reactions. Knowing the quantity of light that is delivered to the reaction mixture is important as the light intensity has a great impact on photochemical reactions.

So this brings us to *actinometry* which is the determination of the quantity of photons, photon flux Q , that is provided to the reaction system of *specific geometry* per unit of time[4]. This quantification of the photons received by the system can be done physically, using radiometers, or chemically using chemicals that, upon irradiation, undergo detectable changes that are proportional to the provided photon flux [67].

While chemical actinometry has been used since more than 70 years, physical actinometry is still considered a rapid and an easy actinometric method as it exhibits a continuous improvement of its accuracy due to the remarkable development of electronic equipment along with that of radiation detectors. However, the ability to get such actinometers of high accuracies is limited to a certain number of research labs due to their elevated prices. Moreover, their sensitivities decrease by the frequent exposure to the strong irradiations (decrease of 18% during one year) along with aging; not to mention the calibration of such apparatuses which should be ensured to get reliable measurements [67]. However, the biggest drawback of physical actinometry lies in the fact that they provide the

quantity of photons emitted by the light source Q_{emitted} and not those that reach the reaction mixture Q_{inside} . With phenomena like reflection at the reactor's surface (whether batch or flow), it is normal not to get full transmittance of light thus having a difference between the photons emitted and those that are involved in the photochemical reaction.

Due to all of these reasons mentioned above, along with the availability of a wide range of chemical actinometers, chemical actinometry is still widely used for determining the photon flux. Once choosing a suitable actinometer, this technique proves to give accurate and reproducible results without the need of recalibration. In addition, as these actinometers will be used to measure the photon flux inside the reactor, chemical actinometry will provide direct access to the ratio of the "active photons" that succeed to reach the reaction system after passing the reactor's surface.

2.1.1 Chemical Actinometers

Chemical actinometers are chemicals that, upon irradiation at a specific wavelength, exhibit chemical changes like decomposition, isomerization, reduction... Though they seem to act like other photosensitive chemicals, these actinometers have certain advantages that make them favored to be used for standard measurements of light energies. In 2004, the IUPAC [67] published the list of characteristics that good chemical actinometers exhibit:

- The photochemical reaction should be as simple as possible and can be easily monitored by spectroscopic techniques.
- The actinometer can be easily provided, commercially available and easily handled.
- The actinometer is well studied and described in the literature with given *quantum yield* values at the wavelengths used.

Though there is a direct relationship between the degree of the photochemical reaction and the photon flux received, like any other photochemical event, the *quantum yield* (ϕ) is an important factor for chemical actinometric measurements [4].

Note that when dealing with chemical actinometers, two factors should be taken into consideration.

2.1.1.1 Effect of refraction on the photon flux emitted by the light source

Consider that the light emitted has a photon flux Q_{emitted} . When propagating through the reactor, this beam of light will be subjected to two refractions: air – glass and glass – solvent. Assuming that the light beam is orthogonal to the surface of the reactor thus $i = r = 0$ and by applying Fresnel's Law the reflectance of light R is determined using the following Equation 2.1:

$$R = \left[\frac{n_1 \cos i - n_2 \cos r}{n_1 \cos i + n_2 \cos r} \right]^2 \text{ or } R = \left[\frac{n_1 - n_2}{n_1 + n_2} \right]^2 \quad \text{Equation 2.1}$$

Due to the law of conservation of energy, the transmittance T , which is the ratio of the light delivered to the system, is calculated using Equation 2.2 [68]:

$$T = 1 - R \quad \text{Equation 2.2}$$

So the photon flux determined by chemical actinometry, Q_{inside} is not the actual one delivered by the light source but rather the one received by the system. Additional calculation, indicated in Equation 2.3, should be done to get that emitted by the light source [67].

$$Q_{\text{emitted}} = \frac{Q_{\text{inside}}}{T} \quad \text{Equation 2.3}$$

2.1.1.2 Temperature

Most of the chemical actinometers don't show a strong dependence on the slight variations of the temperature [69]. However, a big change in the temperature might lead to a change in the density and thus in the concentration and eventually in the photochemical process. This can be easily excluded by working on the temperature range listed in literature for the used actinometer and by doing all of the reactions at a constant temperature [69].

2.1.2 Examples of Chemical Actinometers

A lot of chemical actinometers are extensively described in literature. The following part will include those that were mostly used.

2.1.2.1 Uranyl oxalate actinometer

UO_2^{2+} is used as a photosensitizer for the decomposition of the oxalate into CO , CO_2 and H_2O at a wavelength range 208-426 nm [70], [71]. The reaction is monitored by the titration of the remaining oxalate ions with potassium permanganate (Figure 2.1). Since the titration will lead to the loss of the reactant, this actinometer was then replaced by the ferrioxalate actinometer.

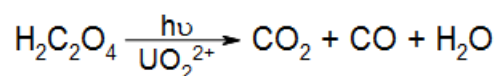


Figure 2.1: Uranyl oxalate actinometry reaction

2.1.2.2 Ferrioxalate actinometer

Ferrioxalate actinometer $\text{Fe}(\text{C}_2\text{O}_4)_3^{3-}$ is used in the UV and the Visible range up to 500 nm. Upon irradiation, the ferrioxalate will decompose giving rise to free ferrous ions (Figure 3.2). The reaction is monitored by measuring the quantity of the liberated Fe^{2+} ions after their complexation with phenanthroline. The formed colored tris-phenanthroline

complex of $\lambda_{\max} = 510 \text{ nm}$ is then detected by UV spectroscopy. Note that the complexation with phenanthroline is exclusive to the ferrous ions decomposed by irradiation [72] [73]



Figure 2.2: Ferrioxalate actinometry reaction

2.1.2.3 Reinecke's salt actinometer

The irradiation of an aqueous solution of Reinecke's salt or $\text{Cr}(\text{NH}_3)_2(\text{SCN})_4^-$ at a wavelength range 316-730 nm leads to the photo-substitution of one of the SCN groups by water. The reaction is monitored by the complexation of the liberated SCN^- with ferric nitrate to give a red-blood complex of $\lambda_{\max} = 450 \text{ nm}$ [74], [75]. This usage of this actinometer is restricted due to the possibility of the liberation of hydrogen cyanide.

2.1.2.4 Photochromic actinometers

The other type of actinometers, known as photochromic actinometers involves those having reversible transformation between two forms upon irradiation like Fulgide Aberchrome 540 and Azobenzene [4]. The advantage of this type of actinometers is that the photochemical change is reversible and thus the starting material can be easily regenerated.

The pale yellow flugicide 540 (A) undergoes photocyclization when irradiated with a wavelength in the UV range 310-370 nm or the visible range 435-545 nm to give rise to the red product (C) (Figure 2.3). This actinometer is not commercially available anymore so it should be prepared in the lab[76] [4].

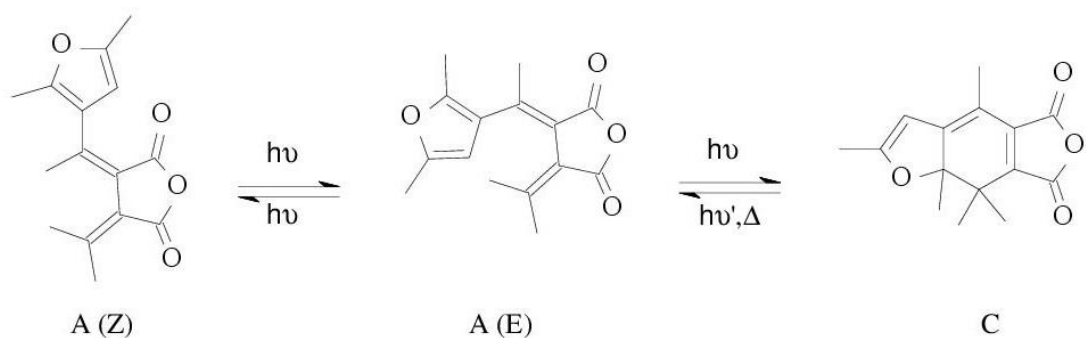


Figure 2.3: Fulgide aberchrome 540 actinometry reaction

Though all of the actinometers mentioned above are used and described a lot in literature, we have decided to use another actinometer for the chemical actinometry of our microfluidic system, which is also extensively described. Since our photoreactions in the UV region are usually done at $\lambda = 365$ nm, azobenzene is a good candidate as it absorbs at this wavelength, to undergo a reversible photoisomerization from the (*E*) to the (*Z*) form. This isomerization can be immediately detected using NMR spectroscopy of the actinometric solution without the need of complexation or titration or any other additional treatments. Moreover, azobenzene is commercially available and stable when placed in dark. Therefore, the following part will focus more on azobenzene as an actinometer and its photoisomerization processes.

2.1.3 Azobenzene

Aryl azo compounds were discovered in the mid-19th century. Known as azo dyes, they were used mostly in the dye industry as cheap coloring agents for textiles and ink [77]. Multiple modifications were done on these azo compounds with respect to the number of azo moieties, the nature of the aromatic ring (e.g. benzene, naphthalene) and the position and number of substituents in an attempt to have a wide range of cheap and easily prepared dyes [77]. The parent molecule of all of the azo dyes that has the simplest form is our chemical actinometer: azobenzene.

Azobenzene, $C_{12}H_{10}N_2$, is a diazene derivative that has two phenyl groups [77]. It is considered a simple photo-switchable molecule that exists in two different structural isomers, trans (*E*) and cis (*Z*) (Figure 2.4).

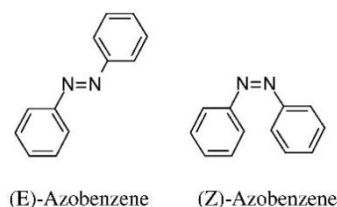


Figure 2.4: The trans (*E*) & cis (*Z*) isomers of azobenzene

2.1.3.1 Photochemistry of azobenzene

As the (*E*) conformation is more stable than the cis (*Z*) by 50 kJ/mol [78], the latter was first discovered in 1937 by Hartely when facing a problem in the reproducibility of the UV/Vis spectrum of the (*E*) form after being exposed to light. This led to the first report that demonstrates the cis-trans photoisomerization of azobenzene [79] (Figure 3.5).

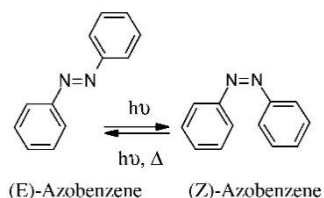


Figure 2.5: The isomerization reaction of azobenzene

Since both isomers have different physical properties and the interchange between both conformations is controlled as it is wavelength dependent, azobenzene derivatives are currently used in light triggered switches such as photo-switchable enzymatic cleavages for drug delivery systems [80] and in optical data storage memories [81]. The difference in the behavior of both isomers can be easily detected by UV/Vis and NMR spectroscopy. In both cases, the UV/Vis spectra exhibit major absorption bands that correspond to the $S_2 \leftarrow S_0$ and

$S_1 \leftarrow S_0$ transitions. $S_2 \leftarrow S_0$ is linked to the symmetry allowed ($\pi\text{-}\pi^*$) transition whereas the $S_1 \leftarrow S_0$ is associated with the symmetry forbidden ($n\text{-}\pi^*$) transition [82]. For the (*E*) isomer, The UV strong band, corresponding to the $S_2 \leftarrow S_0$ ($\pi\text{-}\pi^*$) transition, has a maximum absorption at $\lambda_{\text{max}} \approx 314$ nm whereas the visible weak band that corresponds to the $S_1 \leftarrow S_0$ ($n\text{-}\pi^*$) transition has a maximum absorption $\lambda_{\text{max}} \approx 440$ nm. On the other hand, the spectrum of (*Z*) isomer, though overlaps at certain regions with that of the (*E*) isomer, exhibits a stronger $n\pi^*$ band also near 430 nm but weaker $\pi\text{-}\pi^*$ bands at 280 nm and 250 nm [83]. Figure 2.6 shows the variation of the UV/Vis absorbance spectra of an azobenzene solution that was irradiated at 320 nm for variable times [84].

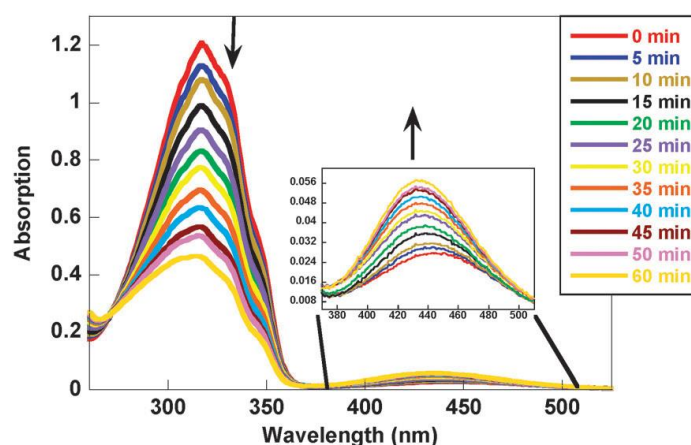


Fig. 2.6: The absorption spectrum of azobenzene upon irradiation with 320 nm light. [84]

Other than its stability by 50 kJ/mol, an amount of 200 kJ/mol of energy is required to induce the (*E*) to (*Z*) isomerization. This explains why the (*E*) isomer is the dominant form of azobenzene (> 99.99 %) in dark. This is also the case for all of the derivatives of azobenzene where the only way to obtain the cis form is by irradiation [83]. When both isomers absorb at a given wavelength, a photostationary state (PSS), which is an equilibrium between both isomers, is established. This state is very important for the kinetic studies related to chemical actinometry (section 2.1.4). The (*Z*) isomer can go back to the stable

form (*E*) by photoisomerization or by a first order thermal relaxation. That's why the temperature is an important factor for the actinometric study using azobenzene [83].

The degree of photoisomerization has usually been monitored by UV/Vis absorption spectroscopy. Lately, this method has been replaced by ¹H NMR spectroscopy as the latter easily provides quantitative and structural information in contrast to UV/Vis absorption spectroscopy that exhibits limitations in both aspects especially that the analysis can't be fully accomplished without the comparison with the spectra of known concentrations of both isomers [3].

2.1.3.2 Mechanism of photoisomerization of azobenzene

The mechanism of photoisomerization of azobenzene has been the subject of discussion for a long time. As the isomerization takes place within picosecond time scale, [85, 86] it is only recently, with the availability of spectroscopic techniques of adequate time resolutions, has it been possible to study this reaction in real time. That's why most of the mechanisms suggested in literature are mainly based on computational analysis [87].

Four mechanisms of the photoisomerization of azobenzene are postulated, where inversion and rotation are major mechanisms and concerted inversion and inversion-assisted rotation are sub divisions of the first two (Figure 2.7).

- a- Rotation: where the N=N π -bond is broken allowing a free rotation around the N-N bond. This will lead to the change in the dihedral angle C-N-N-C. The N-N-C bond remains constant at $\approx 120^\circ$.
- b- Inversion: One of the C-N=N bonds will increase to 180° so the N atom of the intermediate will hybridize from sp^2 to sp state. The dihedral angle C-N=N-C remains 0° .
- c- Concerted inversion: both C-N=N bonds will increase to 180° .

d- Inversion assisted rotation: both the dihedral angle C-N=N-C and the C-N=N angles change but with the change in the first is far more significant than the second is.

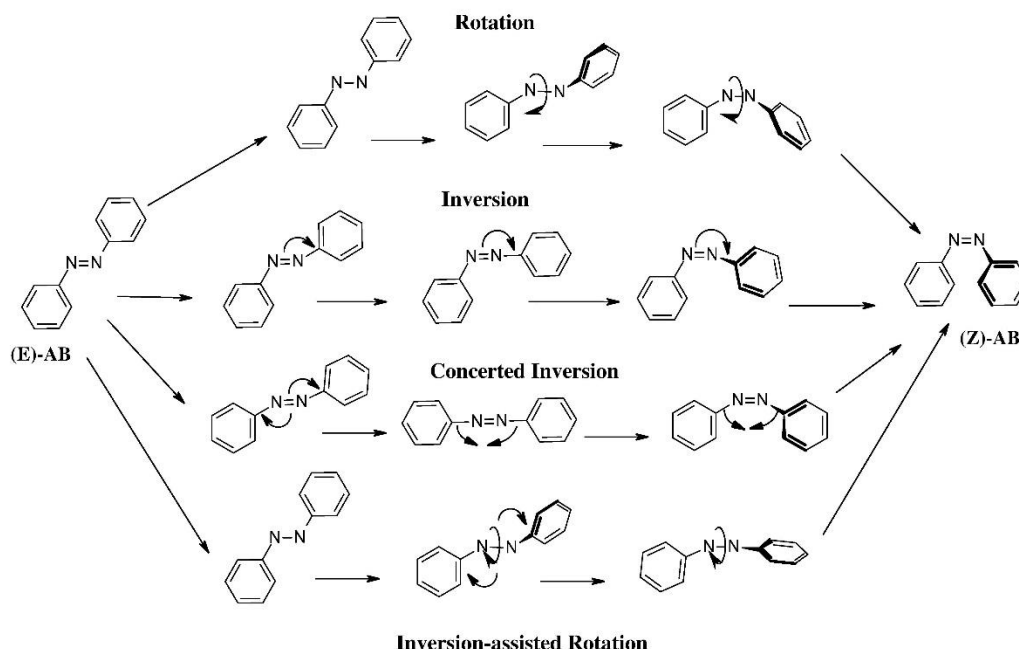


Figure 2.7: Mechanisms of azobenzene isomerization

The most accepted theory is that when excited to S_1 , photoisomerization takes place by inversion. However, this is not the same for the relaxation followed by the S_2 excitation. Some studies indicate that there will be a direct relaxation from the S_2 to the ground state by rotation [88]; [86], [85] while other theoretical calculations have shown that it's a stepwise relaxation from S_2 to S_1 followed by relaxation from S_1 to S_0 by inversion [89]. Newer studies even disagree with the inversion or rotation theories and consider additional mechanisms that have both inversion and rotation like concerted inversion and inversion-assisted rotation as more favorable and more likely to take place. [90, 91]

2.1.3.3 Mechanism of thermal isomerization of azobenzene

The thermal (*Z*) to (*E*) relaxation has been discussed widely since the first report of Hartley [79]. Two different pathways have been proposed: inversion, done by one of the nitrogen groups through a linear transition state [82, 92, 93] and rotation around the N–N bond [94]. The energy barrier for inversion is the energy change of the nonbonding orbital from sp² to sp hybridization whereas the energy barrier for rotation is the energy required to break the N=N π bond.

With the debate regarding the different mechanisms for the photoisomerization of azobenzene, one must note that the real advantage of azobenzene for actinometry is the facility in the kinetic and actinometric calculations. These two factors are far more important than the actual mechanism of isomerization for the practical applications.

2.1.3.4 Azobenzene as an actinometer

The early studies of the usage of azobenzene as an actinometer were focusing on the calculation of the quantum yields of the photoisomerization, in both senses, in different solvents and at different wavelengths. The results were used to verify the kinetic equations derived to determine the intensity of the irradiation emitted from the light source by comparing the value obtained to that provided by other actinometric methods.

Zimmerman *et al.* [95] studied the isomerization of azobenzene in isooctane at 25 °C over a wide range of wavelengths in the UV/visible range, light intensities and concentrations. They have shown that the composition at the photostationary state, and thus the quantum yield, depends highly on the wavelength regardless of the concentration of the azobenzene or the intensity of the light used. Moreover, they have derived a differential equation for the rate of the whole process taking into account the quantum yields of both photoreactions, the absorption coefficients of both isomers, the intensity of the irradiation and the composition at the PSS. They have also calculated the rate constant of the thermal

isomerization that was proved to follow a first order kinetics. Our group modified this equation to be able to use the ratio of both isomers, provided by ^1H NMR spectroscopy, without the need for UV spectroscopic measurements.

Another study done by Fischer in 1959 on Azobenzene confirmed Zimmerman's results regarding the importance of the wavelength of the used irradiation for the quantum yield values [69]. Moreover, he proved that the temperature is another important factor as the ratio of the Z isomer at the PSS increased remarkably from 40 % at -125°C to 80 % at -20°C . He also showed that the solvent is another factor that affects the PSS composition.

Gualitz group studied extensively the actinometric aspect of azobenzene under a wide range of conditions. In 1976, he made a method for the actinometric calculations (Equation 2.4) based on the UV spectroscopic measurements [96]

$$I_0 = \frac{-1}{Q(t_1 - t_2)} \left[\frac{F(E_1) + F(E_2)}{2} \ln \frac{E_2 - E_\infty}{E_1 - E_\infty} \right] \quad \text{Equation 2.4}$$

Where F is the photokinetic factor (Equation 2.5), Q is the pseudo quantum yield (Equation 2.6) and I_0 is the intensity of the emitted light.

$$F(E) = \frac{1 - 10^{-E}}{E} \quad \text{Equation 2.5}$$

$$Q = 1000 (\varphi_E \varepsilon_E + \varphi_Z \varepsilon_Z) \quad \text{Equation 2.6}$$

Using Equation 2.4, it was shown that at 313 nm, azobenzene can be used as an actinometer as its results were compatible to those obtained using ferrioxalate actinometry.

In 1981, the same group used azobenzene for the actinometric study over a wide range of wavelengths (254, 280, 365, 405, 436 nm) [97]. In 1985, he showed that Equation 2.4 is also applicable for concentrations of azobenzene up to 6.4×10^{-4} M and that by comparing the obtained values of I_0 to those obtained using dilute solutions of azobenzene [98].

The cis to trans photoisomerization was also proved by Siampiringue *et al.* [99] to be a good method for using azobenzene as a chemical actinometer.

2.1.4 Kinetic Studies of Azobenzene

The reversible photoisomerization of (*E*) azobenzene to form cis (*Z*) azobenzene is represented in the Figure 2.8; since the thermal isomerization is much slower than photoisomerization, the former will be neglected in the photokinetic calculations.

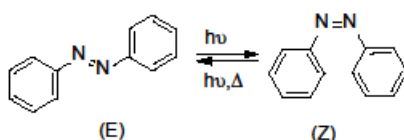


Figure 2.8: The Isomerization reaction of azobenzene

2.1.4.1 Thermal isomerization

As indicated by Zimmerman *et al.* [95] the thermal isomerization follows a typical first order kinetics (Equation 2.7). Z_0 is the fraction of the *Z* isomer right after irradiation, Z_t is the fraction of *Z* isomer after leaving the sample in dark for interval t of time and k' is the thermal rate constant.

$$\ln \frac{Z_t}{Z_0} = -k't \quad \text{Equation 2.7}$$

Thus plotting $\ln Z_t$ vs. time will give a linear curve whose slope is k' . Z_t can be expressed as in Equation 2.8:

$$Z_t = Z_0 e^{-k't} \quad \text{Equation 2.8}$$

2.1.4.2 Photoisomerization

The irradiation of a sample of (*E*) azobenzene will not go to completion but rather to a state of equilibrium, (PSS), that depends on the quantum yields of both photoisomerizations. In order to calculate the irradiance of a light source using azobenzene, the following differential equation is derived.

Given that z is the fraction of Z isomer, $(1-z)$ is the fraction of the E isomer, ΔA is the absorbance of the irradiated solution, ϵ_x is the extinction coefficient ($\text{mole}^{-1} \cdot \text{L} \cdot \text{cm}^{-1}$) of the isomer x , C_0 is the initial concentration ($\text{mol} \cdot \text{L}^{-1}$) and I_0 ($\text{ein} \cdot \text{s}^{-1}$) and I ($\text{ein} \cdot \text{s}^{-1}$) are the intensities of light emitted by the source and that transmitted by the irradiated solution respectively.

Beer lambert's law (Equation 2.9, Equation 2.10 and Equation 2.11):

$$\Delta A = \epsilon C l \quad \text{Equation 2.9}$$

$$\Delta A = \log \frac{I_0}{I} \quad \text{Equation 2.10}$$

$$\Delta I = I_0(1 - 10^{-\Delta A}) \quad \text{Equation 2.11}$$

So in this case, the absorbance of both the (E) and the (Z) fractions can be expressed as in Equation 2.12 and Equation 2.13 respectively:

$$\Delta A_E = \epsilon_E (1 - z) C_0 l \quad \text{Equation 2.12}$$

$$\Delta A_Z = \epsilon_Z z C_0 l \quad \text{Equation 2.13}$$

Using the approximation provided by Taylor's series, Equation 2.11 can be written in the following logarithmic form (Equation 2.14):

$$\Delta I = I_0(1 - 10^{-\Delta A}) = I_0 \ln 10 \Delta A \quad \text{Equation 2.14}$$

The overall rate of formation of the Z isomer is affected by three processes: the rate of photoisomerization (E) to (Z), the reverse photoisomerizations and the thermal isomerization that is neglected.

For photoisomerization reactions, the rate depends on the quantum yield of the photoisomerization (ϕ_x) and the intensity of light per unit volume (I^*). This is known as the photokinetic factor that is represented in Equation 2.15 [4].

$$\frac{d_{[\text{photoisomer}]}}{dt} = \phi I^* \text{ where } I^* = \frac{\Delta I}{V} \quad \text{Equation 2.15}$$

So the rate of formation of the Z isomer ($d[z]/dt$), excluding the thermal isomerization effect, can be written as in Equation 2.16

$$\frac{d[z]}{dt} = \frac{\varphi_E I_0 \ln 10 \varepsilon_E (1-z) C_0 l}{V} - \frac{\varphi_Z I_0 \ln 10 \varepsilon_Z z C_0 l}{V} \quad \text{Equation 2.16}$$

The term $\frac{I_0 l}{V}$ can be replaced by I_{photon} (ein.s.m^{-2}) and C_0 can be simplified from both sides of Equation 3.16 giving Equation 2.17

$$\frac{dz}{dt} = I_{\text{photon}} \ln 10 [\varphi_E \varepsilon_E (1-z) - \varphi_Z \varepsilon_Z z] \quad \text{Equation 2.17}$$

At PSS, $\frac{dz_{PSS}}{dt} = 0$ thus giving Equation 2.18 from Equation 2.17

$$I_{\text{photon}} \ln 10 [\varphi_E \varepsilon_E (1 - z_{PSS}) - \varphi_Z \varepsilon_Z z_{PSS}] = 0 \quad \text{Equation 2.18}$$

By rearrangement, φ_Z can be expressed as in Equation 2.19

$$\varphi_Z = \frac{\varphi_E \varepsilon_E (1 - z_{PSS})}{\varepsilon_Z z_{PSS}} \quad \text{Equation 2.19}$$

Substituting Equation 2.19 in Equation 2.18 will give Equation 2.20

$$\frac{dz}{dt} = I_{\text{photon}} \ln 10 \left[\varphi_E \varepsilon_E (1-z) - \frac{\varphi_E \varepsilon_E (1 - z_{PSS})}{\varepsilon_Z z_{PSS}} \varepsilon_Z z \right] \quad \text{Equation 2.20}$$

$$\frac{dz}{dt} = I_{\text{photon}} \ln 10 \frac{\varphi_E \varepsilon_E}{z_{PSS}} [z_{PSS}(1-z) - (1 - z_{PSS})z] \quad \text{Equation 2.20}$$

$$\frac{dz}{dt} = \frac{I_{\text{photon}} \ln 10 \varphi_E \varepsilon_E}{z_{PSS}} [z_{PSS} - z] \quad \text{Equation 2.20}$$

Or Equation 2.21 where $w = \frac{I_{\text{photon}} \ln 10 \varphi_E \varepsilon_E}{z_{PSS}}$

$$\frac{dz}{dt} = w [z_{PSS} - z] \quad \text{Equation 2.21}$$

Consider $y = z_{PSS} - z$, so Equation 2.21 can be written in the form of Equation 2.22

$$\frac{dy}{dt} = -w y \quad \text{Equation 2.22}$$

Integrating Equation 2.22, will finally give Equation 2.23

$$\ln y = -wt + \text{constant} \quad \text{Equation 2.23}$$

So plotting the graph of $\ln y$ vs. t will exhibit a linear relationship whose slope will be used to determine the value of I_0 .

Rearrangement of equation 2.19 will give Equation 2.24. In this case, by knowing the Z_{PSS} , ϕ_E and ε_E one can use them to find the product of $\phi_Z \varepsilon_Z$ without the need to know the exact values of these two constants that cannot be easily determined as the (E) isomer is the stable and the commercially available form.

$$\phi_Z \varepsilon_Z = \frac{\phi_E \varepsilon_E (1 - Z_{PSS})}{Z_{PSS}} \quad \text{Equation 2.24}$$

2.1.4.3 Rate law of the reversible isomerization of azobenzene

To determine the equilibrium constant K_{PSS} , the rate constant of the (E) to (Z) photoisomerization k_1 and the rate constant of (Z) to (E) photoisomerization k_{-1} , a kinetic model, described by [100], that is used for reversible reactions is applied. The relation between K_{PSS} , k_1 , k_{-1} is represented in equation 2.25.

$$K_{PSS} = \frac{[Z]_{PSS}}{[E]_{PSS}} = \frac{k_1}{k_{-1}} \quad \text{Equation 2.25}$$

The rate of formation of the Z isomer can be expressed as in Equation 2.26

$$\frac{d[Z]_t}{dt} = k_1[E]_t - k_{-1}[Z]_t \quad \text{Equation 2.26}$$

Where $[E]_t$ and $[Z]_t$ are the concentrations of the (E) and (Z) isomers at instant t . However, $[E]_t$ can be written as in Equation 2.27 where $[E]_0$ is the initial concentration of the (E) isomer.

$$[E]_t = [E]_0 - [Z]_t \quad \text{Equation 2.27}$$

The substitution of this value of $[E]_t$ in Equation 2.26 will give Equation 2.28

$$\frac{d[Z]_t}{dt} = -(k_1 + k_{-1})[Z]_t + k_1[E]_0 \quad \text{Equation 2.28}$$

At equilibrium $[Z]_t$ will be represented by $[Z]_{PSS}$, so Equation 2.27 can be modified to Equation 2.29 and the equilibrium constant K_{PSS} can be expressed by Equation 2.30

$$[Z]_{PSS} = [E]_0 - [E]_{PSS} \quad \text{Equation 2.29}$$

$$K_{PSS} = \frac{[Z]_{PSS}}{[E]_0 - [Z]_{PSS}} = \frac{k_1}{k_{-1}} \quad \text{Equation 2.30}$$

Rearrangement of Equation 2.30 will give Equation 2.31:

$$[E]_0 = \frac{k_{-1} + k_1}{k_1} [Z]_{PSS} \quad \text{Equation 2.31}$$

Substituting the value of $[E]_0$ of Equation 2.31 in Equation 2.28 will give Equation 2.32:

$$\frac{d[Z]_t}{dt} = -(k_1 + k_{-1})([Z]_{PSS} - [Z]_t) \quad \text{Equation 2.32}$$

$$\frac{d[Z]_t}{[Z]_{PSS} - [Z]_t} = -(k_1 + k_{-1}) dt \quad \text{Equation 2.32}$$

Note that this equation is the same as that of Equation 2.22 so that $w = k_1 + k_{-1}$.

The integration of Equation 2.32 will give a relation between $[Z]_t$ and t in the linear form Equation 2.33.

$$\ln \frac{[Z]_{PSS} - [Z]_t}{[Z]_{PSS} - [Z]_0} = -(k_1 + k_{-1}) t \quad \text{Equation 2.33}$$

Using Equations 2.29 and 2.30, numerical expressions between K_{PSS} and $[Z]_{PSS}$, Equation 2.34, and K_{PSS} with $[E]_{PSS}$, Equation 2.35, are established.

$$[Z]_{PSS} = \frac{K_{PSS}[E]_0}{K_{PSS} + 1} \quad \text{Equation 2.34}$$

$$[E]_{PSS} = \frac{[E]_0}{K_{PSS} + 1} \quad \text{Equation 2.35}$$

The nonlinear forms of the variation of $[Z]_t$ and $[E]_t$ that will be used to determine the overall rate law of the reversible photoisomerization of azobenzene are expressed in Equation 2.36 and Equation 2.37 respectively.

$$[Z]_t = \frac{K_{PSS}[E]_0}{K_{PSS} + 1} (1 - e^{-(k_1 + k_{-1})t}) = [Z]_{PSS} (1 - e^{-(k_1 + k_{-1})t}) \quad \text{Equation 2.36}$$

$$[E]_t = \frac{[E]_0}{K_{PSS} + 1} (1 + K_{PSS} e^{-(k_1 + k_{-1})t}) = [E]_{PSS} (1 + K_{PSS} e^{-(k_1 + k_{-1})t}) \quad \text{Equation 2.37}$$

2.2 Experimental Actinometric Measurements

The main idea of our work, in addition to characterizing our photoreactor, is to form a fixed protocol for the chemical actinometric studies, in microfluidic systems, using azobenzene. Several parameters were assessed:

- The concentration of irradiated azobenzene: diluted solutions of 6.4×10^{-4} M vs. relatively concentrated solutions of 0.01 M.
- The solvent used: isooctane, methanol and acetonitrile.
- The UV LEDs used of variable powers :70, 90 and 230 mW.cm^{-2}

The system used for the actinometric measurement is composed of the Mikroglas Dwell Device that is irradiated by two different UV LED systems.

- A lab assembled UV LEDs composed of 18 identical LEDs placed at equal distances to provide homogeneous illumination (HP LEDs A). The wavelength of the emitted irradiation is 365 nm. The average emitted photon flux of this UV LEDs assembly is around 90 mW.cm^{-2} . (Figure 2.9)
- UV LEDs (365 nm, irradiance up to 250 mW.cm^{-2}) Omnicure® AC475 model from Lumen Dynamics (Mississauga, Canada) (HP LEDs B). The power of these UV LEDs can be changed, thus 30 % power (irradiance 70 mW.cm^{-2}) and 100 % power (irradiance 230 mW.cm^{-2}) were assessed. (Figure 2.10). Note that in all of the cases the irradiance was measured at the surface of the reactor using a radiometer.



Figure 2.9: Set-up of the photoisomerization of azobenzene under flow conditions using HP LEDs A



Figure 2.10: Mikroglas Dwell device illuminated by HP LEDs B

A solution of Azobenzene in isooctane of concentration of 6.4×10^{-4} M was first prepared. Since this concentration is inconvenient for measurements by ^1H NMR, a more concentrated solution of Azobenzene (0.01M) was also assessed. The increase in the concentration of the azobenzene did not have a significant effect on our calculations (shown in the results section). As a result, we considered using the concentration of 0.01M of azobenzene for all of the following measurements.

The variable conditions performed are summarized in Table 2.1. The prepared solution of azobenzene was injected at various flow rates into the microfluidic system that was illuminated by the UV LEDs and kept at a constant temperature of 20°C using a cryostat. The flow rates were regulated by a Harvard Apparatus (Holliston, MA, USA) PHD ULTRA CP syringe pump equipped with an 8 mL stainless steel syringe. For every entry in Table 3.1, six measurements that correspond to different irradiation times were performed.

Table 2.1: Summary of the experiments done for the chemical actinometric assessment.

Entry	[Azobenzene]	Solvent	Irradiation system	Irradiance outside (mW.cm ⁻²)
A	6.4×10 ⁻⁴ M	Isooctane	HP LEDs A	90
B	0.01 M	Isooctane	HP LEDs A	90
C	0.01 M	Acetonitrile	HP LEDs A	90
D	0.01 M	Methanol	HP LEDs A	90
E	0.01 M	Isooctane	HP LEDs B	70 (30% power)
F	0.01 M	Isooctane	HP LEDs B	230 (100% power)

The composition of *Z* and *E* components of every irradiated solution was done by evaporating the solvent first using a rotary evaporator, then dissolving the residue in 500 μL of CDCl_3 to be injected in the NMR spectrometer. The degree of conversion was calculated using the ^1H spectrum by integrating the peaks that correspond to the *Z* and *E* isomers. NMR has shown to be a great and a quick method of analysis as the peaks that correspond to the different isomers were easily distinguished.

The composition at the PSS was determined by the irradiation of a sample for an extended time (around 2 h). Quantum yield values in each solvent were obtained from literature [4, 95].

As for the thermal isomerization, one PSS sample was placed in dark at room temperature and the variation in its composition was then monitored by ^1H NMR during the following 48 hours. This experiment was done to determine the value of k_{thermal} to verify the exclusion of this factor in the calculations mentioned in section 2.1.4.

2.2.1 Determination of the ϵ of azobenzene (*E*) and total transmittance *T* of the reactor

The ϵ values of the *E* isomer in isooctane, acetonitrile and methanol were determined by classical calibration curves having the absorbance vs. concentration. Using Beer-Lambert's law, the slope of each of the plotted straight lines corresponds to the absorption coefficient of azobenzene in the corresponding solvent (Table 2.2).

Table 2.2: Values of ϵ of azobenzene in different solvents

Solvent	ϵ ($M^{-1}.cm^{-1}$)
Isooctane	95
Methanol	312
Acetonitrile	276.9

By referring to Fresnel's law (Equation 2.1), $R_{air-Foturan} = \left[\frac{1-1.515}{1+1.515}\right]^2 = 0.042$ thus

$T_{air-Foturan} = 1 - R_{air-Foturan} = 0.958$. Similarly, $R_{Foturan-isooctane} = 0.0018$ and $T_{Foturan-isooctane} = 0.998$.

The total transmittance $T_{total} = T_{air-Foturan} \times T_{Foturan-isooctane} = 0.956$

Table 2.3 includes the total transmittance of light when working with the three solvents isooctane, acetonitrile and methanol.

Table 2.3: The total transmittance of light in the used solvents.

Solvent	$T_{air-Foturan}$	$T_{Foturan-solvent}$	T_{total}
Isooctane	0.958	0.998	0.956
Acetonitrile	0.958	0.996	0.955
Methanol	0.958	0.996	0.954

2.3 Results

The percentage of the *Z* isomer with the corresponding irradiation time are summarized in Table 2.4. The calculations will be explained based on entry A of Table 2.1 that corresponds to 6.4×10^{-4} M of Azobenzene in isooctane irradiated by HP LEDs A ($90 \text{ mW}.cm^{-2}$). Z_{PSS} was found to be equal to 20.8 and that by following the procedure listed in section 2.2. The results obtained were then used to plot the graph of $\ln(Z_{PSS}-Z_t)$ vs. time (Figure 2.11). The corresponding graph exhibits a linear relationship with a good correlation coefficient ($R^2 = 0.99$). The slope of the graph corresponds to the constant w , indicated in Equation 2.21, that will be used to determine the irradiance of the light (I_{photon}) inside the microreactor.

Table 2.4: The % of the Z isomer vs the irradiation time

Flow rate (ml/min)	Irradiation time (s)	% Z
0	0	0
4	17.25	4.4
3	23	8
2	35	11.6
1	69	18
0.5	138	20.5

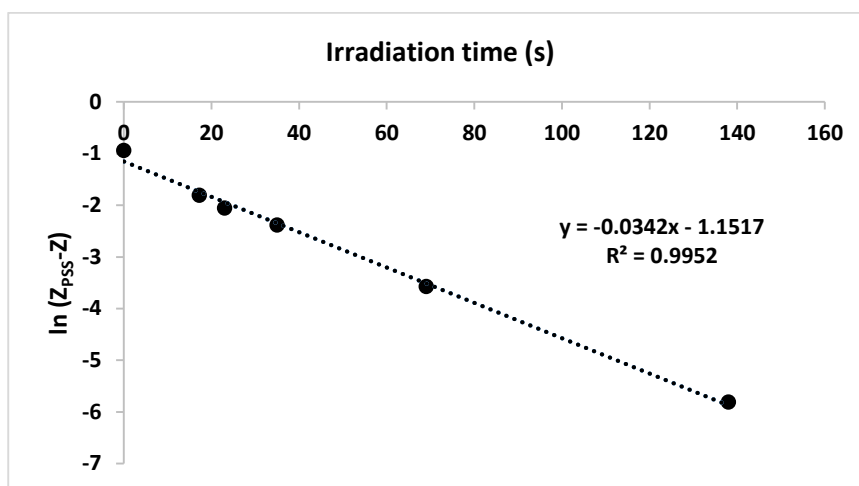


Figure 2.11: Graph of $\ln(Z_{pss}-Z_t)$ vs. time (s)

2.3.1 Calculation of Photon Flux emitted by the UV LEDs

The physical constants: refractive indices, quantum yields and absorption coefficients needed for the upcoming calculations are summarized in Table 2.5

Table 2.5: Physical constants used for calculations

Substance	Refractive index n	ϵ_E (L.mol ⁻¹ cm ⁻¹)	Φ_E	Φ_Z
air	1	--	--	--
Foturan glass ®	1.515	--	--	--
methanol	1.3284	312	0.15	0.35
acetonitrile	1.3441	277	0.15	--
isooctane	1.3914	95	0.12	0.48

With $w = \frac{I_{\text{photon}} \ln 10 \varphi_E \varepsilon_E}{Z_{PSS}}$ and $Z_{PSS} = 0.208$, $I_{\text{photon}} = 2.71 \times 10^{-3} \text{ ein.s}^{-1} \cdot \text{m}^{-2}$.

$$E_{\text{photon}} = N_A \frac{hc}{\lambda} = 6 \times 10^{23} \frac{6.64 \times 10^{-34} \times 3 \times 10^8}{365 \times 10^{-9}} = 327500 \text{ J.}$$

The photon flux Q_{inside} ($\text{W} \cdot \text{m}^{-2}$) is calculated by multiplying I_{photon} by the energy of 1 mole of photons. $Q_{\text{inside}} = 327500 \times 2.71 \times 10^{-3} = 887.4 \text{ W} \cdot \text{m}^{-2} = 88.7 \text{ mW} \cdot \text{cm}^{-2}$

By using Equation 2.3 and the value of total transmittance T from Table 2.3, $Q_{\text{emitted}} = \frac{Q_{\text{inside}}}{T}$, the irradiance outside the reactor should be $88.7 \div 0.9563 = 92.8 \text{ mW/cm}^2$.

2.3.2 The variation of Z and E Isomers with Time

Using the slope of the graph in Figure 2.11 that corresponds to $w = k_1 + k_{-1}$ and $Z_{PSS} = 0.208$, the following constants can be deduced.

$$K_{PSS} = \frac{0.208}{0.792} = 0.263, k_1 = 0.008 \text{ s}^{-1} \text{ and } k_{-1} = 0.030 \text{ s}^{-1}.$$

Using Equations 2.35 and 2.36, the graphs that represent the rate of formation of the Z isomer, the rate of disappearance of the E isomer, the photostationary state and the experimental values are represented in Figure 2.12.

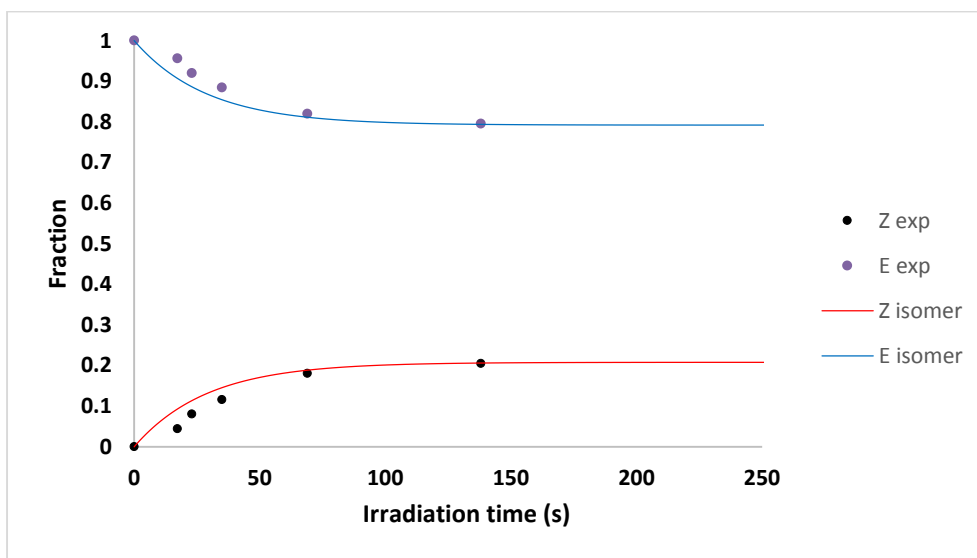


Figure 2.12: Rate Law

The same calculations were done for all of the other entries in Table 2.1 and are summarized in Table 2.6 (actinometry) and Table 2.7 (kinetics).

Table 2.6: Results of actinometric measurements.

Entry	Z _{PSS}	Equation	R ²	Q _{inside} (mW.cm ⁻²)	Q _{emitted} (mW.cm ⁻²)	Q _{radio} (mW.cm ⁻²)
A	0.208	y = -0.0342x - 1.1517	0.995	88.7	92.8	90
B	0.19	y = -0.0357x - 1.7066	0.992	84.6	88.5	90
C	0.315	y = -0.0742x - 1.0113	0.992	80.11	83.9	90
D	0.382	y = -0.0703x - 0.8482	0.996	81.6	85.5	90
E	0.203	y = -0.0255x - 0.7615	0.993	64.6	67.5	70
F	0.21	y = -0.0799x - 0.4417	0.992	209	218.9	230

Table 2.7: Results of kinetic measurements

Entry	K _{PSS}	k ₁ + k ₋₁ (s ⁻¹)	k ₁ (s ⁻¹)	k ₋₁ (s ⁻¹)
A	0.263	0.034	0.008	0.030
B	0.235	0.036	0.007	0.029
C	0.459	0.074	0.023	0.051
D	0.618	0.070	0.027	0.043
E	0.255	0.0255	0.006	0.020
F	0.266	0.080	0.017	0.063

2.3.3 Thermal Isomerization

The PSS sample of entry B was monitored. Table 2.8 summarizes the results obtained.

Table 2.8: Thermal isomerization of (Z) azobenzene to (E) azobenzene after PSS

Time (s)	Time (h)	% Z
0	0	20.8
64800	18	19.51
79200	22	19.15
93600	26	18.94
154800	43	17.92

By plotting $\ln Z$ vs. t (h.), the linear graph of correlation coefficient $R^2 = 0.9975$, is obtained (Figure 2.13). The slope of this straight line corresponds to $k_{\text{thermal}} = 0.0035 \text{ h}^{-1}$ or $\approx 1 \times 10^{-6} \text{ s}^{-1}$.

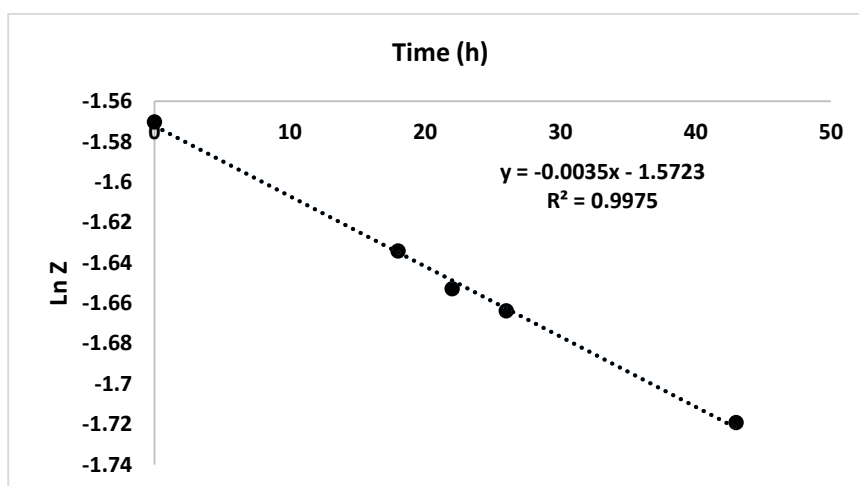


Figure 2.13: Kinetic graph of the thermal isomerization of azobenzene after PSS

2.4 Discussion

Table 2.6 includes all of the experimental data for the chemical actinometry of azobenzene of concentrations $6.4 \times 10^{-4} \text{ M}$ (entry A) and 0.01 M (entries B, C, D, E and F). UV LEDs A were used to irradiate entries A, B, C and D whereas entries E and F were

irradiated by UV LEDs B regulated to provide 30% and 100% power respectively. By comparing entries A and B, only a slight variation between the two experimental photon fluxes Q_{inside} are observed (88.7 vs. 84.6 $\text{mW}\cdot\text{cm}^{-2}$). This shows that the approximation taken when using Taylor Series is valid even when working at relatively concentrated solutions (entry B: 0.01 M). This provides an advantage of using the rapid ^1H NMR for monitoring the experiments rather than using UV spectrometry that was previously used for such experiments. When working in isooctane (entries A, B, E and F), the photostationary state has approximately the same amount of the Z isomer (0.208, 0.19, 0.203 and 0.21) which is in accordance with the literature. The study [95] stated that the factors that influence the composition at the photostationary state are the chosen solvent and irradiation wavelength regardless of the intensity of light.

When using the same light source and the same concentration of azobenzene (entries B, C and D), the obtained experimental photon flux Q_{inside} values are almost equal ($\approx 80\text{-}85 \text{ mW}\cdot\text{cm}^{-2}$). This highlights the advantages of the flow technology where even when working at small irradiation times (tens of seconds), the percentage of error is almost negligible due to the homogeneous illumination of the reaction mixture. In the same course, the data obtained is reproducible and the graphs exhibit good linear correlation coefficients ($R^2 = 0.99$) which are not easily achievable when working under batch conditions.

In all of the entries of Table 2.6, slight variations between the experimental photon flux delivered Q_{emitted} and that measured by the radiometer Q_{radio} were observed ($\approx 2\text{-}8\%$ difference). Using the radiometer when measuring the photon flux outside of the microreactor had some limitations as the microreactor's dimensions are smaller than those of the sensor; even when performed with extreme accuracy, there was a gap of few mm between the sensor and the reactor. This limitation by physical actinometry favors the usage of chemical actinometry in microfluidic systems especially that the latter gives the photon

flux inside the reactor. Moreover, the difference between the radiant power the reaction mixture receives Q_{inside} and that emitted by the lamp Q_{emitted} confirms the need for this kind of in situ measurement.

Referring to Table 2.7, the k_{-1} values of all entries were greater than those of k_1 which can be justified by the fact that the (*Z*) to (*E*) isomerization is more favored as the (*E*) isomer is more stable. Entries A, B, E and F, have similar K_{PSS} values since they are performed in the same solvent, isooctane, thus the photostationary state should have the same composition. The impact of the intensity of the light source is seen in the difference in the values of $k_1 + k_{-1}$, k_1 and k_{-1} between entries B, E and F (Table 2.9). By increasing the power of the light source, the system reaches the plateau more rapidly (entry B \approx 60 s vs. entry F \approx 25 s). This can lead to a limitation for this kind of assessment, since when working using elevated powers, a full kinetic assessment cannot be performed. For example in our case, the maximum flow rate that could be used was $14 \text{ ml}\cdot\text{min}^{-1}$ that corresponds to 5 s thus it was not possible to perform experiments with smaller irradiation times. Finally comparing the values of k_1 and k_{-1} of entry B to its k_{thermal} that is calculated from Figure 2.17 validates neglecting the thermal isomerization effect in the actinometric calculations ($k_1 0.0078 \text{ s}^{-1}$, $k_{-1} 0.0298 \text{ s}^{-1}$ vs. $k_{\text{thermal}} 1 \times 10^{-6} \text{ s}^{-1}$).

2.5 Conclusion

The photon flux received in the Mikrogilas Dwell Device photoreactor was measured by actinometry using azobenzene. Different solvents and irradiation powers were assessed showing that this method is convenient, accurate and rapid especially that a concentration of azobenzene suitable for the rapid ^1H NMR analysis was used. The difference between the in-situ photon flux and that provided by the light source necessities such actinometric measurements, as the photon flux is an important factor in photochemical reactions.

Moreover, these measurements aid well and support the process of switching from the batch to the flow microreactors due to the consistency of the results shown. The Dwell Device photoreactor was efficiently characterized by an actinometric method that is reproducible and provides accurate results. The amount of light reflected by the microreactor is in accordance with that provided by the manufacturers and by the theoretical calculations that were done using Fresnel's Law.

This work can be further extended by assessing the same protocol at different irradiation wavelengths including the visible region.

CHAPTER THREE

CYCLOADDITION

3.1 Introduction

One of the important aspects of organic chemistry is finding routes for the total synthesis of chemicals which are present in nature. As most of the natural organic material contain cycles, cycloaddition reactions continue to grab the attention of organic chemists [101].

Cycloaddition is a pericyclic reaction where concerted combination of two π -electron systems form a cyclic adduct having a reduction in the bond multiplicity with the formation of 2 new σ bonds replacing the π bonds. This form of addition enables the formation of C-C bond without the need of a nucleophile or electrophile [101].

3.1.1 Diels- Alder Addition

One of the famous cycloaddition reactions is the Diels–Alder reaction, also known as [4+2] cycloaddition. It takes place between a conjugated diene, with 4 π electrons, and a substituted alkene, which has 2 π electrons, to form a substituted six membered ring [102] (Figure 3.1). This work has led to awarding Otto Paul Hermann Diels and Kurt Alder the Nobel Prize in Chemistry in 1950. Since then, Diels-Alder addition has been widely used to prepare natural compounds like cortisone, prostaglandin, reserpine, taxol and tetracycline and Provitamin D₃ [103].

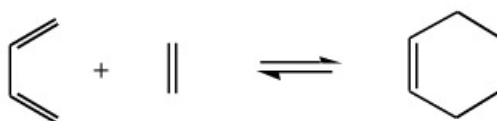


Figure 3.1: Diels Alder addition

The Diels-Alder reaction has provided extra flexibility for organic chemists with the ability to install different substitutions on different positions of the formed 6 membered ring with up to 4 new stereo centers on the resulting adduct. Moreover, it exhibits high regio and stereo selectivity and requires relatively mild conditions [102, 103] .

The formation of 4 membered ring adduct is also synthetically interesting. It is an important step in the synthesis of cyclobutane containing natural products like grandisol and caryophyllene [103] (Figure 3.2). Over 1600 natural products containing cyclobutane have been isolated from aquatic and terrestrial organisms. These compounds can have antiproliferative, antibiotic, cytotoxic and anti-inflammatory activities [103]. This form of rings can be formed by having [2+2] cycloaddition which is similar in concept to that of [4+2] cycloaddition.

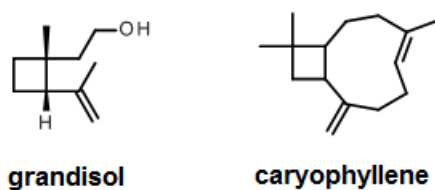


Figure 3.2: Examples of natural products prepared by cycloaddition

3.1.2 Frontier Molecular Orbital Theory

Although the Diels-Alder [4+2] cycloaddition takes place using thermal energy, a [2+2] cycloaddition is not favored under the same conditions. It was shown that [2+2] cycloaddition is induced photochemically and not thermally. This can be explained using Frontier Molecular Orbital (FMO) theory [104-107]

Usually, the number of molecular orbitals is equal to the total number of atomic orbitals that were present originally. As a result, bonding and anti-bonding molecular orbitals are found for each bond formed. For stable molecules, the electrons occupy the bonding orbitals [104-107].

For the dienophile (ethene) the π bonding and anti-bonding molecular orbitals are represented in the following FMO representation in Figure 3.3.

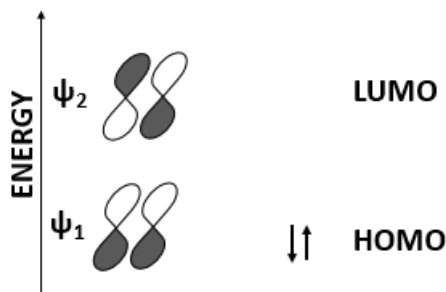


Figure 3.3: FMO representation of ethene

As for the diene, it has four electrons in the conjugated π system so can be represented as indicated in Figure 3.4 (a). According to Diel and Alders, cycloaddition results from the overlapping of the HOMO of the electron rich substrate (the diene) and the LUMO of the electron poor dienophile. The overlapping between these molecular orbitals is possible as they have the same orientation thus rendering [4+2] cycloaddition possible (Figure 3.4 (b)) [104-107]. As for the [2+2] cycloaddition, both ethenes will be having the same molecular orbitals as indicated in Figure 3.3. The interaction between their corresponding HOMO and LUMO will not lead to an overlap as there is phase mismatching. So the [2+2] cycloaddition is symmetry forbidden [104-107].

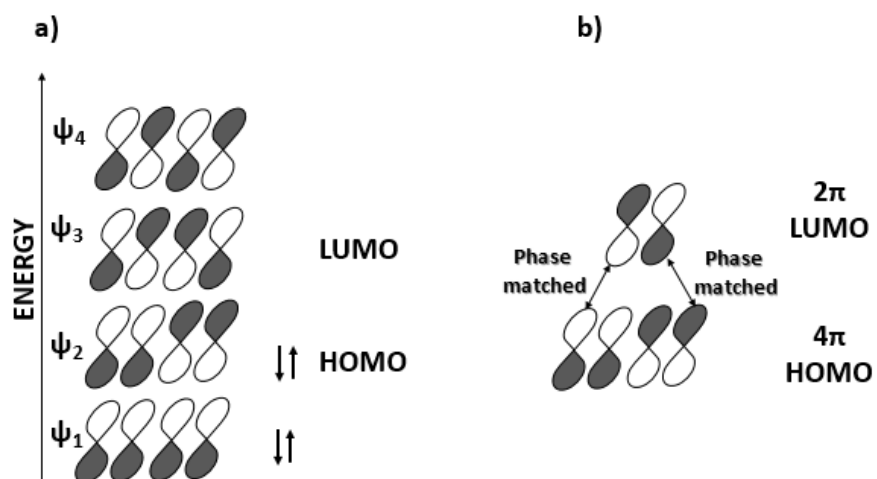


Figure 3.4: (a): FMO of diene, (b): Overlapping of orbitals in [4+2] cycloaddition

However, when the system is irradiated with enough energy to excite one of the electrons in the bonding orbitals to the upper anti-bonding orbital, the FMO represented in Figure 3.5 will be obtained. So, the overlapping of the LUMO and the new HOMO of the excited system needed for the cycloaddition will be successful due to phase matching and thus a reaction will take place [104-107].

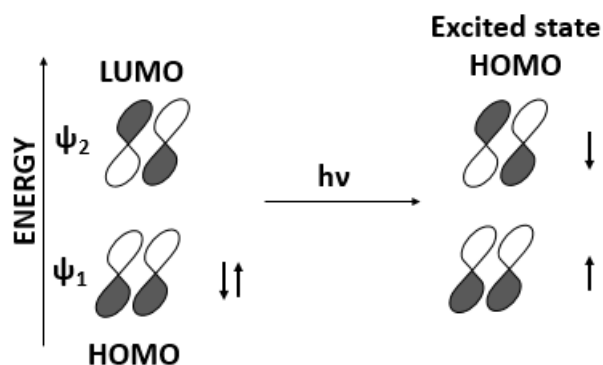


Figure 3.5: FMO of ethene following irradiation

3.2 Photocycloaddition

Photocycloaddition reactions were first discovered in the early 20th century [108]. They have grabbed more attention in the late 60s due to many reasons. Light is a traceless non-polluting agent so photochemical reactions are considered green reactions compared to thermal reactions. This fact becomes even more valid when the light used for the reaction is in the visible region. Visible light systems are more economic, commercially available and safer to be handled [109]. From the synthetic point of view, these reactions are also interesting as their outcome isn't the same as that of [4+2] cycloaddition. The intermediates produced upon photoexcitation makes it possible to have access to forming molecules of unique structures that can't be obtained using thermal pathways [109, 110]. Thus photoinduced cycloaddition can be considered complementary to the classical thermal addition. It is now included in the total synthesis of natural products [109, 110].

In addition, the corresponding intermediates form different regiochemical and stereochemical outcomes. stereoselective synthesis enables the formation of organic molecules with enhanced control over their 3D structure [110, 111]. Likewise, stereoselectivity provided by the photocycloaddition would limit the formation of mixture of stereoisomers. In addition to the loss of reagents and usage of wasteful separation procedures, there are cases where the presence of the both stereoisomers would lead to functional impairment of the active form along with various unwanted side effects. Having homochiral synthesis of molecules is a key goal in organic chemistry especially that a lot of chemicals having applications in medical sciences and agriculture are mainly produced as racemic mixtures [112].

3.2.1 [2+2] Cycloaddition using UV Irradiation

Most of the [2+2] photocycloaddition reactions absorb light in the harmful UV-B region [108]. However, as indicated in section 1.3.2.3, only very low power UV LEDs-B are currently available and thus can't be used in synthetic photochemistry. This makes sensitization the best way to perform [2+2] photocycloaddition reaction using high power UVA LEDs.

3.2.1.1 Sensitization

Sensitization, also known as indirect excitation energy transfer, is widely used in organic synthesis by using organic sensitizers such as benzophenone, eosin and pyrene [113]. As mentioned in the chapter 1, sensitization is the energy transfer from an excited molecule to another making the latter excited (Figure 3.6). This widens the range of irradiation wavelengths that can be used rather than being limited to those that excite the starting material only.



Figure 3.6: Sensitization (Z = sensitizer / M = substrate)

The sensitizer absorbs the light energy in preference to the substrate. In order to relax to the ground state, the sensitizer transfers this excess of energy to the substrate by collision leading to the change in the spin state of the latter and thus obtaining its excited state which is lower than that of the sensitizer [4].

4,4'-dimethoxybenzophenone (DMBP), the sensitizer used in this work, is type II photoinitiator since it's involved in a bimolecular reaction where its triplet excited state interacts with the substrate and activates it. It is a UV photoinitiator as it exhibits its 2 absorption bands within the UV region (Figure 3.7). The strong band in the region of 240-

300 nm corresponds to the $\pi \rightarrow \pi^*$ transition whereas the weak band in the region of 320-370 nm corresponds to the $n \rightarrow \pi^*$ transition [114].

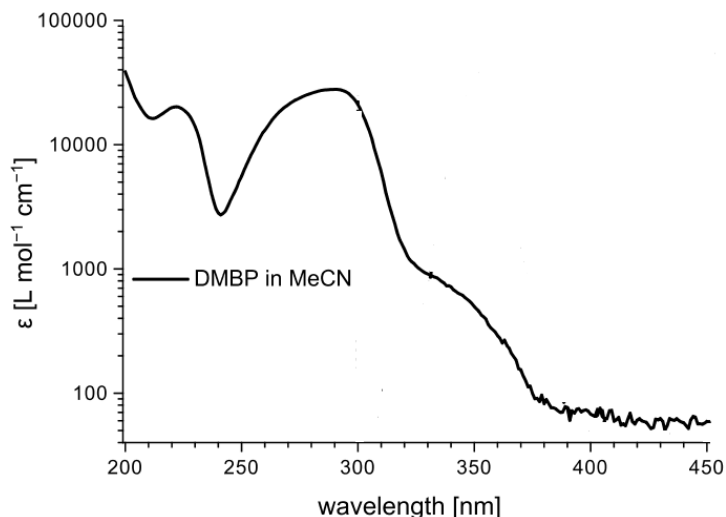


Figure 3.7: Absorption spectrum of DMBP in acetonitrile [114]

3.2.1.2 [2+2] photocycloaddition model experiment

In this work, benzophenone was used for the sensitization of the intramolecular [2+2] cycloaddition of 3-oxa-1,5-hexadienones using UV LEDs of $\lambda = 365$ nm in the Mikroglass® dwell device (Figure 3.8).

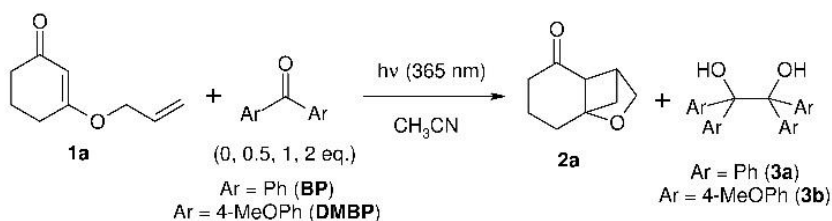


Figure 3.8: [2+2] intramolecular photocycloaddition of 3-oxa-1,5-hexadienones

This model reaction described before by Matlin [115-118] follows the Baldwin's rule of five so that the favored form will be the one having a five membered ring [119]. Having one of the two possible crossed or straight products depends on the length of the chain

(Figure 3.9). Straight form is obtained when 3 or more atoms are separating the two double bonds proving that the regioselectivity is influenced by the length of the chain. The starting material can be readily excited using an irradiation of $\lambda = 350$ nm. The cyclic moiety of the substrate prevents the twisting of the C=C thus promoting the progress of the reaction [115-117]. Note that the literature includes many reports that target such a reaction with various substituted 3-oxa-1,5-hexadienones[120-123].

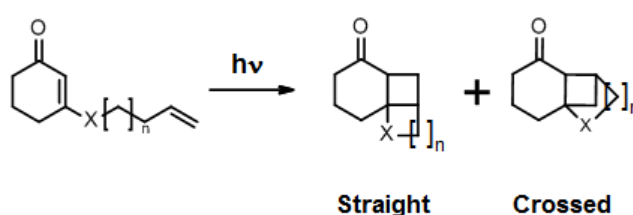


Figure 3.9: The straight and crossed [2+2] cycloadducts

The substrate absorbs the UV irradiation thus attaining the excited state. This will lead to the photoinduced electron transfer, provided by the solvent, thus obtaining the radical anion intermediate. This intermediate will then cyclize. Back electron transfer (BET) will take place in order to get the desired [2+2] cycloadduct with a yield of 58 % after 10 hours of irradiation [118] (Figure 3.10) when using **1a**.

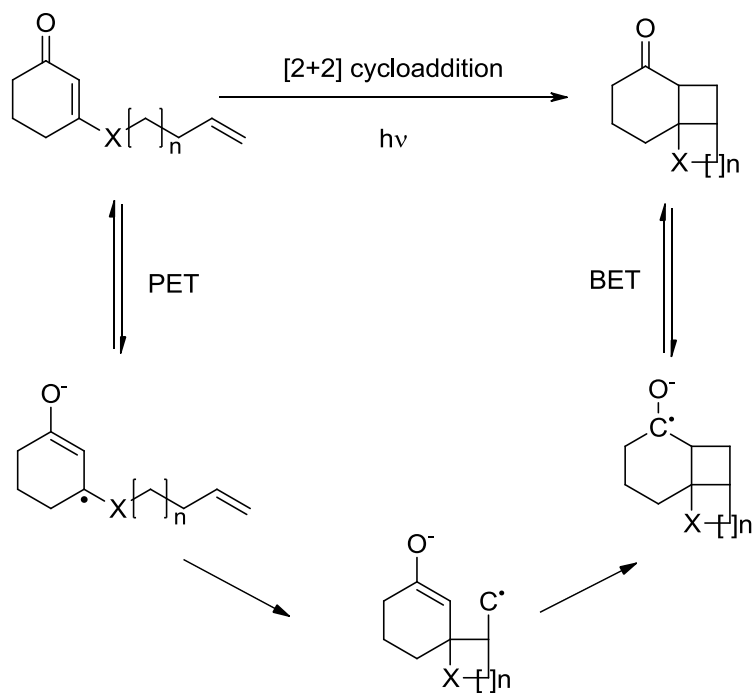


Figure 3.10: Proposed mechanism for the [2+2] photocycloaddition of 3-oxa-1,5-hexadienones

In this work, since the substrate doesn't absorb at $\lambda = 365$ nm, sensitization by benzophenone will be done. As described before, the benzophenone will absorb this light energy to reach its triplet excited state. For its relaxation, it will sensitize the substrate by transforming part of its extra energy to it. As a result, the substrate will be activated for cycloaddition. Note that the H abstraction of the benzophenone is competing with the excitation of the substrate for the quenching of benzophenone. That's why pinacolization also takes place to give the pinacol (**3**). After the excitation of the substrate, the cycloaddition mechanism will then occur in the same manner as that listed above.

3.2.2 Visible Light Photoredox Catalysis

The use of photoredox catalysts to absorb visible light and initiate chemical reactions has received an increased interest in recent years. Photoredox reactions can be performed under mild conditions at room temperature using the commercially available light bulbs. Since most of organic molecules don't absorb in the visible region, it is more likely to get

the desired reaction without having secondary side reactions. Note that a quantity of 1 mole % of catalyst loading is enough for the reaction to take place. In addition, the catalyst is regenerated during the course of the reaction so it can be collected and reused. [17, 18, 109].

Visible light for organic reactions has a lot of advantages. It would enhance the adoption of photochemistry by synthetic chemists especially that this enables the usage of household light bulbs. These bulbs are cheap, easy to obtain and definitely safer than any of the light sources which are found in synthetic labs like mercury lamps. In addition, expensive and specialized quartz glassware can be replaced by the traditional borosilicate glassware that are transparent to visible light. The idea of using visible light in organic chemistry is of great importance especially that this favors the shift toward greener synthetic processes that also minimizes the side effects of high energy irradiations like decomposition and secondary reactions [17, 19]

The usage of visible light in synthetic chemistry was supported by the photoredox properties of polypyridyl complexes of ruthenium and iridium. In general, these metal complexes are poor oxidants and reductants at the ground state [124, 125] However, they undergo single-electron transfer (SET) processes with organic substrates when photoexcited via their stable photoexcited states of prolonged lifetimes. This favors the involvement of these complexes in the bimolecular SET thus making them strong single electron reductants and oxidants. By photocatalysis, organic substrates that lack a chromophoric group can still undergo photochemical processes[19].

The usage of $\text{Ru}(\text{bpy})_3^{2+}$ in organic chemistry was limited although several organic reactions rely on single electron processes [126-129]. Photoinduced electron transfer processes were exclusive to organic photosensitizers that mainly absorb in the UV region.

The first reports that describe the usage of $\text{Ru}(\text{bpy})_3^{2+}$ as a photocatalyst in organic chemistry were done in 2008 by Yoon [130] and Mc Millan [131, 132] groups. They focused

on the [2 + 2] cycloaddition and α -alkylation of aldehydes. Later, $\text{Ru}(\text{bpy})_3^{2+}$ was used by Stephenson and co-workers for the dehalogenation of activated alkyl halides [133, 134].

3.2.2.1 Photochemistry of $\text{Ru}(\text{bpy})_3^{2+}$

$\text{Ru}(\text{bpy})_3^{2+}$ and other transition metal polypyridyl complexes exhibit broad and strong absorbance bands in the visible range. When $\text{Ru}(\text{bpy})_3^{2+}$ absorbs visible light, one of the metal's t_{2g} electrons is excited to the ligand's excited π^* orbital [124, 135]. This MLCT is then followed by an intersystem crossing to get the lowest MLCT triplet state from the singlet MLCT state. This triplet excited state of the complex is then involved in the single electron transfer process. As mentioned above, the lifetime of this state is long since the decay to the ground state of different multiplicity is spin forbidden Figure 3.11. [17]

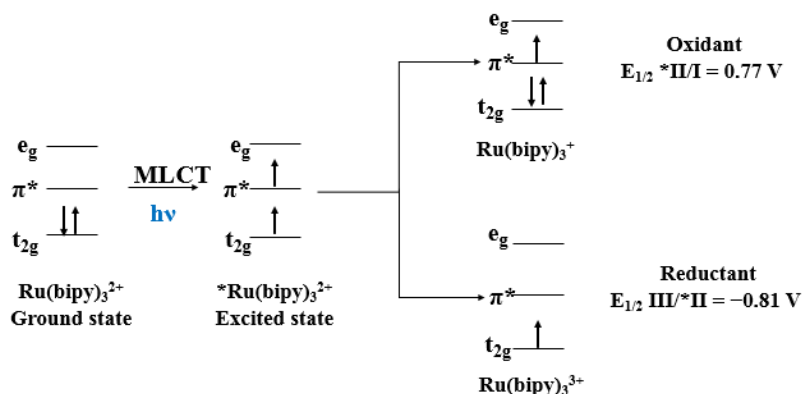


Figure 3.11: Simplified molecular orbital depiction of $\text{Ru}(\text{bpy})_3^{2+}$

In addition, the excited metal complex has stronger oxidizing and reducing potentials than the complex at the ground state. This was proven by determining the standard reduction potentials for both electrochemical half reactions including the excited complex (Figure 3.12).

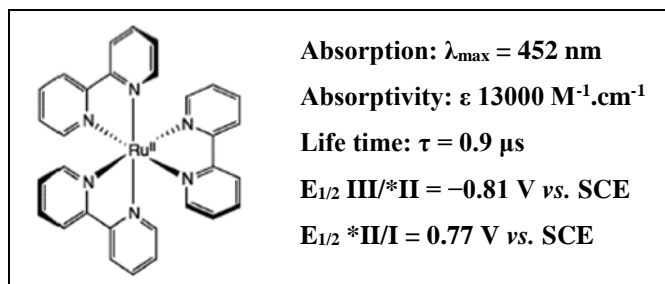


Figure 3.12: Structure and major properties of $\text{Ru}(\text{bpy})_3^{2+}$

The redox potential of the half reaction including the excited $^*\text{Ru}(\text{bpy})_3^{2+}$ is $E_{1/2} \text{ III}^*/\text{II} = -0.81 \text{ V}$ with respect to saturated calomel electrode (SCE) whereas that including $\text{Ru}(\text{bpy})_3^{2+}$ is $E_{1/2} \text{ III/II} = +1.29 \text{ V vs. SCE}$. This shows that the excited complex is stronger reductant than the ground state complex. Similarly $E_{1/2} \text{ *II/I} = +0.77 \text{ V vs. SCE}$ indicates that the complex is a stronger electron acceptor than the ground state complex ($E_{1/2} \text{ II/I} = -1.33 \text{ V vs. SCE}$) This implements the dual property of $^*\text{Ru}(\text{bpy})_3^{2+}$ as both a strong reductant and a strong oxidant [136, 137].

Oxidative quenching of $^*\text{Ru}(\text{bpy})_3^{2+}$ occurs if an electron acceptor A is present. This single electron transfer will lead to the formation of a radical anion of A and the oxidized form of the complex i.e. $\text{Ru}(\text{bpy})_3^{3+}$. To complete the cycle, a donor of electrons D can provide $\text{Ru}(\text{bpy})_3^{3+}$ with electrons to form a radical cation of D. The former is a strong oxidant ($E_{1/2} \text{ III/II} = +1.29 \text{ V vs. SCE}$) thus it will easily return to the Ru(II) ground-state species [17].

Conversely, a donor of electrons D provides the excited complex with an electron. This single electron transfer will lead to the reductive quenching of the complex to Ru(II) ground-state species along with the radical cation of the donor. This Ru intermediate complex ($E_{1/2} \text{ II/I} = -1.33 \text{ V vs. SCE}$) donates an electron to an acceptor thus closing the redox cycle. The common oxidative quenchers (A) are viologens, polyhalomethanes, dinitro- and dicyanobenzenes, and aryl diazonium salts whereas tertiary amines are the most common reductive quenchers [17].

Other than the donors and acceptors which are mentioned above, reductive or oxidative single transfer quenching of the excited complex can be done *via* organic substrates leading to a photochemical reaction. This phenomenon is of special interest as it is the pathway needed for our [2+2] cycloaddition by redox catalysis using visible light. Thus the most significant application for the photoredox properties of $\text{Ru}(\text{bpy})_3^{2+}$ is the single electron transfer processes involving organic substrates.

3.2.2.2 Intramolecular [2+2] photocycloaddition

The model reaction for monitoring the photocatalytic cycloaddition is the intramolecular [2+2] cycloaddition of a bisenone (**1e**). This reaction was previously described by Krische's group who used cobalt as a catalyst [138-141]. He proposed that the easily reducible bisenone will have a radical anion intermediate for the cycloaddition to take place *via* a single electron transfer process. This has made the Yoon group to question whether this radical anion can be formed when having a photoexcited $^*\text{Ru}(\text{bpy})_3^{2+}$. Their first publication in this area reported that efficient [2+2] intramolecular cycloaddition of the bisenone **1e** can be performed in the presence of LiBF_4 , and $i\text{-Pr}_2\text{NEt}$ photocatalyzed by visible light irradiated $\text{Ru}(\text{bpy})_3^{2+}$ [130].

The proposed mechanism is as follows (Figure 3.13). The photoexcitation of $\text{Ru}(\text{bpy})_3^{2+}$ will generate an excited state. $i\text{-Pr}_2\text{NEt}$ will act as the electron donor to $^*\text{Ru}(\text{bpy})_3^{2+}$ thus reductively quenching the latter into $\text{Ru}(\text{bpy})_3^+$ and forming amine radical cation $i\text{-Pr}_2\text{NEt}^+$. The formed reduced catalyst has $E_{\text{red}} = -1.2 \text{ V vs. SCE}$, thus it can't reduce **1e** that has reduction potential of -1.4 V vs. SCE . This is where LiBF_4 gets involved as a Lewis acid that activates the single electron transfer to the enone and stabilizes the formed enone radical anion that will then undergo the [2+2] cycloaddition. The primary product of

cycloaddition is a ketyl radical that loses an electron to get the neutral cycloadduct. This can be achieved via the radical cation $i\text{-Pr}_2\text{NEt}^{+\bullet}$ that easily gets this extra electron [19, 130].

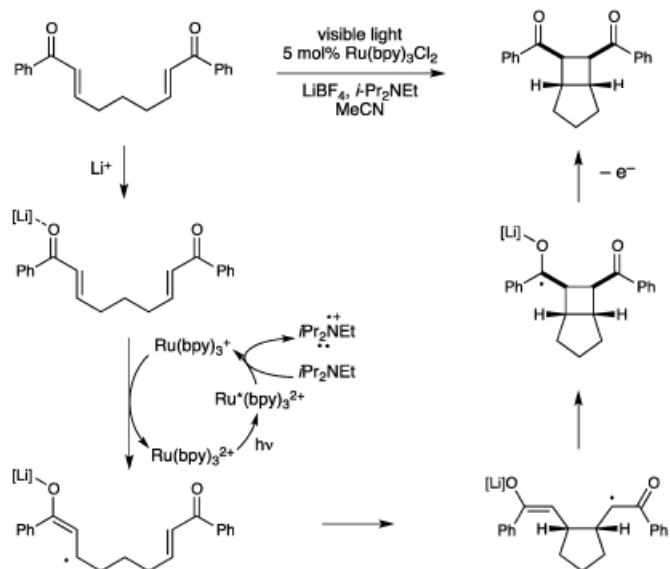


Figure 3.13: Mechanism of intramolecular [2+2] cycloaddition of a bisenone (1e) [109]

A wide range of visible light sources can be used for this type of cycloadditions. In addition, sunlight can also initiate such reactions with comparable yields of conversion with respect to irradiation time.[19].

Yoon reported a significant difference in yields and stereoselectivity between the photocycloaddition and the former electrochemical cycloaddition described by Krische's group [138-141]. Using photoredox catalysis high yields with excellent diastereoselectivity were obtained compared to moderate yields and poor diastereoselectivity for the cycloaddition of the same substrates in acetonitrile and in the presence of Lewis acid but using electrochemical conditions [138-141]. This difference was explained as in photocycloaddition there is an *in situ* formation of the strong oxidant amine radical cation. This shortens the lifetime of the reactive ketyl radical by producing both the neutral

cycloadduct and regenerating $i\text{-Pr}_2\text{NEt}$ thus limiting the possibility of having secondary reactions [19].

From the suggested mechanism described above, it's shown that this reaction depends mainly on three important components [19]:

- $\text{Ru}(\text{bpy})_3^{2+}$ that absorbs the visible photon energy and sensitizes the electron transfer process.
- $i\text{-Pr}_2\text{NEt}$ the reductive quencher that provides the substrate with an electron to form a radical anion intermediate.
- LiBF_4 the Lewis acid that activates the enone for its reduction and stabilizes the formed radical anion.

The important feature about these three components is that the alteration in their quantities or nature would lead to remarkable changes in the mechanism and thus obtaining a totally new product.

3.2.2.3 Photoinduced reductive cyclization

When the Lewis acid is replaced by a Brønsted acid, reductive coupling product is obtained instead of the [2 + 2] cycloadducts (Figure 3.14) [19, 142]. This can be attributed to the difference in the reactive intermediates present in both systems. When a Brønsted acid is present, the bisenone will be protonated forming oxocarbenium ion. $\text{Ru}(\text{bpy})_3^{2+}$ will be transformed into its photoexcited state ($^*\text{Ru}(\text{bpy})_3^{2+}$) when irradiated with visible light. Reductive quenching of this excited intermediate by $i\text{-Pr}_2\text{NEt}$ will give an amine radical cation and the reduced form of the catalyst $\text{Ru}(\text{bpy})_3^+$ complex that will donate a single electron to the oxocarbenium ion to form a neutral radical intermediate (Figure 3.15). Note that this intermediate differ in nature than that of the [2+2] cycloaddition intermediate which is a radical anion. The neutral radical intermediate will undergo cyclization to form a keto

radical that will receive a hydrogen atom from the amine radical cation forming the reductive cyclization product [19, 142].

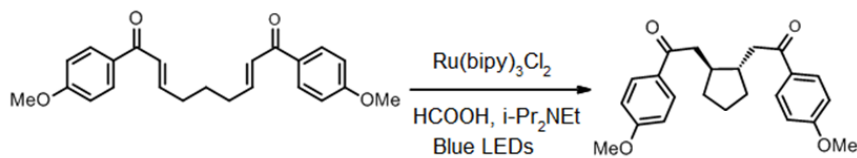


Figure 3.14: Reductive cyclization of a bisenone (1f) using a Brønsted acid [142]

This differences in the mechanisms and the intermediates of both reactions lead to remarkable outcomes. First cycloaddition is a net neutral redox process whereas reductive cyclization is a net 2 electron reductive reaction. Cycloaddition is stereo selective forming adduct with the bonds at the ring junction to be cis. For reductive cyclization, the β,β bond with the cycle are majorly trans [19].

Even for the reactivity, [2+2] cycloaddition was shown to take place only when having at least one aryl group in the bisenone to stabilize the radical anion intermediate formed. Aliphatic enone failed to undergo [2+2] cycloaddition. In contrary, no such problems are faced during reductive cyclization showing that an addition of a Brønsted acid to the reaction mixture a remarkable change in reactivity is attained [19].

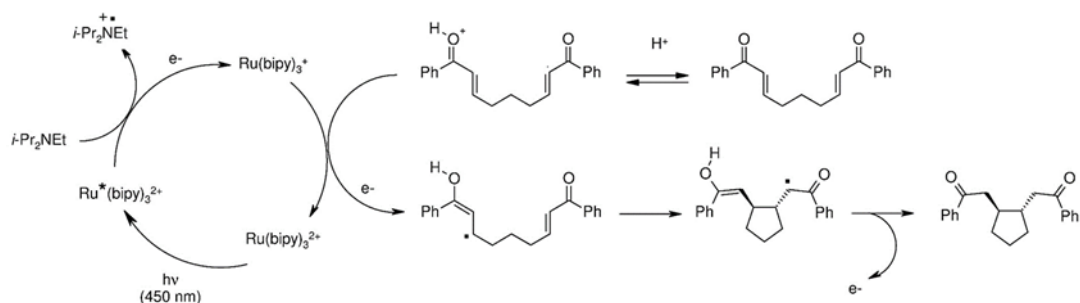


Figure 3.15: Mechanism of reductive cyclization of bisenone [142]

In this work, the effect of the usage of flow microreactor instead of the classical batch reactor for this reaction is assessed. Yields, selectivity and kinetics are taken into consideration. Moreover, both reductive cycling and [2+2] cycloaddition reactions of bisenone (**1f**) in the visible region using $\text{Ru}(\text{bpy})_3^{2+}$ will be studied.

3.3 Results and Discussion

3.3.1 Synthesis of starting material

The 3-oxa-1,5-hexadienones (**1a-1d**) used in the intramolecular [2+2] cycloaddition via sensitization under UV irradiation are prepared following the general procedure listed in the literature [117] and represented in the Figure 3.16. Cyclohexadiones and allyl alcohols are refluxed for 16 h in toluene in the presence of a catalytic amount of *p*-toluenesulfonic acid. Yields varying between 75 and 93% were obtained.

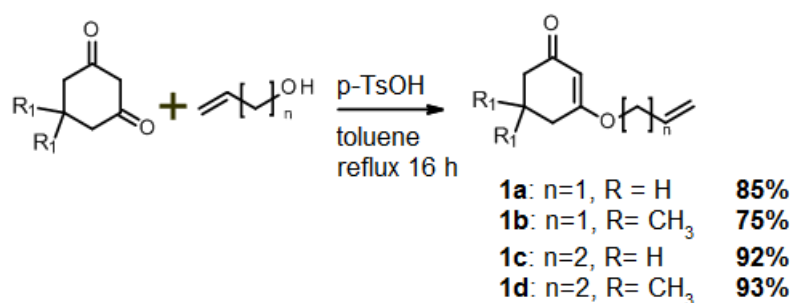


Figure 3.16: Preparation of 1a-1d

1,9-bis-(4-methoxy-phenyl)-nona-2,7-diene-1,9-dione (**1f**) used in the intramolecular [2+2] cycloaddition that is photocatalyzed by $\text{Ru}(\text{bpy})_3\text{Cl}_2$ using blue LEDs is prepared *via* a 2 step reaction. The first step is preparing 1-(4-methoxy-phenyl)-2-(triphenyl- λ -phosphoranylidene) ethanone (**1g**) by mixing 4-methoxyphenacyl bromide with triphenylphosphine over night (Figure 3.17) [143]. Using Wittig reaction, glutaraldehyde and **1g** provide **1f** with 95% yield (Figure 3.18) [140].

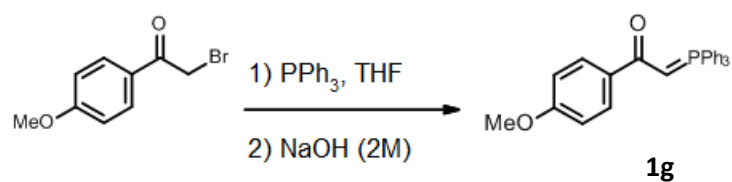


Figure 3.17: Preparation of **1g**

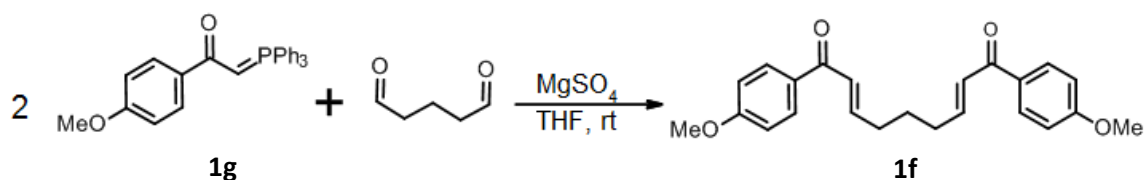


Figure 3.18: Preparation of **1f**

3.3.2 [2+2] cycloaddition via sensitization under UV irradiation in flow

The 3-oxa-1,5-hexadienones (**1a-1d**) and the sensitizer are dissolved in acetonitrile and injected within the Mikroglas® Dwell Device that is illuminated by UV LEDs 365 nm as indicated in the Figure 3.19



Figure 3.19: Mikroglas® Dwell Device illuminated by HP LEDs A 365 nm

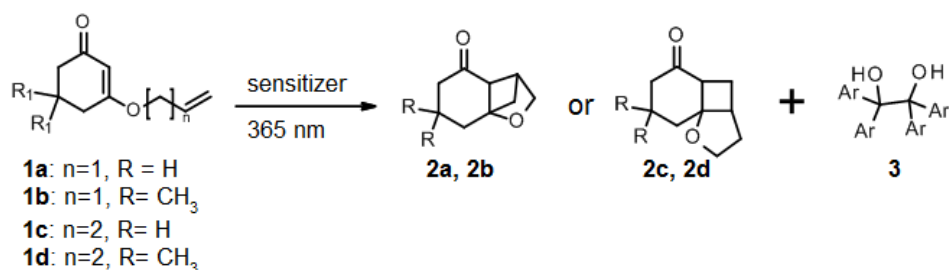


Figure 3.20: Intramolecular [2+2] cycloaddition of 3-oxa-1,5-hexadienones using UV irradiation

The various reactions covered by this study are summarized in Figure 3.20. The direct intramolecular [2+2] photocycloaddition protocol reported by Tamura and co-workers [115, 116] and later by Matlin group [117] for the formation of **2a** was first evaluated with hexane as the solvent under degassed conditions and gave a moderate yield of 47% after 10 h at 350 (± 40) nm in a Pyrex tube located at the center of a Rayonet® irradiation chamber (model RPR 208). This result is in accordance with the original procedure described by Matlin [117]. As expected, no “straight product” or ring opening side product was observed. Replacing hexane by dry acetonitrile increased the yield from 47% to 58% for the same irradiation time and concentration. The reaction was found to follow a first order rate law ($k = 2.46 \times 10^{-5} \text{ s}^{-1}$) from kinetic measurements done by GC-MS and confirmed by ¹H NMR. We then compared the speed rate of this batch experiment with the one of a microflow photochemical reaction realized in a FEP tubing (800 μm i.d., length = 10 m) enrolled in the Rayonet chamber and located at 2 cm from the 8 fluorescent tubes (350 ± 40 nm, 20 W). This set-up, is similar in principle to a set-up recently described by Oelgemöller group [40, 114]. For the reaction done in acetonitrile, the flow rate was set at 8 $\mu\text{L}\cdot\text{min}^{-1}$ which corresponds to a residence time of 10 h 30 min, the measured yield was 69%. Kinetic measurement ($k = 2.97 \times 10^{-5} \text{ s}^{-1}$) by varying the flow rate confirmed 20% of acceleration from batch to flow. Preliminary attempts to switch the batch reaction with **1a** from Rayonet UV lamps (350 ± 40 nm) to a monochromatic high power (350 $\text{mW}\cdot\text{cm}^{-2}$) UV LED source (365 ± 15 nm,

Hamamatsu LCL1) resulted in only 1% conversion after 10 h. This change in reactivity is explained by the too low absorbance of **1a** at 365 nm ($\epsilon_{365} = 30 \text{ mol.L}^{-1}.\text{cm}^{-1}$) compared to its higher absorbance ($440 < \epsilon_{350-310} < 2250 \text{ mol.L}^{-1}.\text{cm}^{-1}$) in the polychromatic range of Rayonet® lamps

We next turned our attention toward a sensitized intramolecular [2+2] photocycloaddition protocol for the formation of **2a** using benzophenone (BP) or (DMBP) as photosensitizers. Indeed, both known photosensitizers absorb readily at 365 nm ($\epsilon_{365}(\text{BP}) = 69 \text{ mol.L}^{-1}.\text{cm}^{-1}$ and $\epsilon_{365}(\text{DMBP}) = 135 \text{ mol.L}^{-1}.\text{cm}^{-1}$).

The results of the screening experiments performed in the Mikrogas ® Dwell Device are summarized in Table 3.1. Note that the UV LEDs used in this case are the lab assembled 18 HP LEDs (365 nm, HP LEDs A) whose irradiance was shown to be $90 \text{ mW}.\text{cm}^{-2}$ (Chapter 2).

Table 3.1: Screening of conditions for the photosensitized reaction of 1a in a Dwell device microreactor irradiated with HP UV-LEDs A (365 nm). (a): in batch using LEDs $350 \text{ mW}.\text{cm}^{-2}$

Entry	Time (min.)	Sens. (eq.)	Zn(OTf) ₂ eq.	2a Conv. (%)	3 Conv. (%)
1	230	-	-	0	-
2	40	BP (0.5)	-	13	50
3	60	BP (0.5)	-	14	69
4	230	BP (0.5)	-	15	98
5	230	DMBP (0.5)	-	32	69
6	1150	DMBP (0.5)	-	43	80
7	230	DMBP (1.0)	-	60	60
8	383	DMBP (1.0)	-	80	73
9	230	DMBP (2.0)	-	86	66
10^a	230	DMBP (2.0)	-	74	n.d.
11	230	DMBP (1.0)	0.1	55	< 2
12	230	DMBP (2.0)	0.01	66	< 4

Similar to batch, the energy of the supplied wavelength (365 nm) failed to activate the cycloaddition of the substrate (entry 1). Adding the sensitizer benzophenone (0.5 eq) however led to the formation of the cycloadduct (entries 2-4). Irradiation in flow for 230 minutes gave 15 % conversion to the desired product and to the formation of the pinacol product of the sensitizer. Since DMBP absorbs better than BP at 365 nm by a factor of 2, its presence as a sensitizer led to doubling the conversion to 32 % after the same irradiation time as for BP sensitized reaction (entry 4 vs. entry 5). Increasing the quantity of DMBP to 1 eq also enhanced the cycloaddition reaction to give 60 % conversion after 230 minutes (entry 7) and 80% after only 385 minutes of irradiation (entry 8). We decided then to increase the quantity of DMBP till saturation that corresponds to 2 eq (0.074 M) in dry acetonitrile (entry 9). This was possible in the flow system whose path length is 500 μm rendering it possible to use high concentrations of the sensitizer without affecting light transmission along this short distance. The reaction was remarkably speeded up as around 86 % of the cycloadduct was obtained after only 230 minutes of irradiation which is by far the best result obtained. Using the same composition as in entry 9, a reaction in batch (entry 10) was performed but using UV LEDs which are four times stronger than those used in flow (350 $\text{mW} \cdot \text{cm}^{-2}$ vs. 90 $\text{mW} \cdot \text{cm}^{-2}$). Despite using these stronger LEDs, the system was less efficient as it gave only 74 % conversion compared to 86 % conversion in flow. This can be explained as the batch system has a path length of around 1 cm. The saturated solution limits the transmission of light throughout the reaction mixture leaving a portion unilluminated.

When working in batch, the extended residence and thus illumination of the sensitizer and its pinacol (**3**) leads to having additional products that we could not identify (entry 10). This is not the case when working in flow as there is a continuous extraction of the pinacol from the illuminated reactor limiting such side reactions.

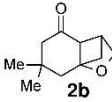
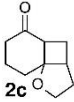
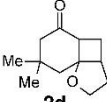
Limiting the secondary pinacolization reaction can have a positive effect on the [2+2] cycloaddition. The DMBP absorbs the UV irradiation to form a triplet excited state[114]. Following this excitation, the DMBP can even sensitize our substrate and trigger the [2+2] cycloaddition or combine with another DMBP molecule and form the pinacol (**3**). Interestingly, the addition of Zn(OTf)₂ metal salt, showed a complete inhibition of the pinacolisation side reaction and slightly altered the rate of [2+2] cycloaddition through non-elucidated pathways (entries 11-12). The additive turned out to be active at a low catalyst loading, as 1 mol% of zinc salt was enough to inhibit the pinacolisation. We suppose that Zn(OTf)₂ acts as a selective catalytic quencher. In any case the energy transfer from DMBP* to 3-(alkenyloxy)cyclohex-2-enone appears less affected than the H abstraction involved along the pinacolisation formation.

After optimizing the best conditions for having improved yields for the [2+2] cycloaddition (entry 1, Table 3.2) in flow, we decided to extend the scope of the method to various substrates by focusing on the chain length in order to compare rates of formation of “crossed” products and “straight” products under strictly identical sensitized conditions (Table 3.2). In addition, UV LEDs of the same wavelength (365 nm) but with irradiance of 230 mW cm⁻² (HP LEDs B) were also used in this section to demonstrate the impact of the increase in the irradiance of light on the reaction kinetics. Batch reactions in round bottom flask (path length =2 cm) and a cuvette (path length = 1 cm) were used to assess the reactivity with respect to the reactor’s dimensions.

The rates of formation of adducts strongly depend on their corresponding structures. This is verified by comparing the results of entries 1, 5, 9 and 13. The crossed products require much more time to be formed as 86% of **2a** (entry 1) and 70% of **2b** (entry 5) were formed after 230 minutes of irradiation. In contrast, both **2c** and **2d** rates’ of formation are increased by more than 10 folds as 19 minutes of irradiation were enough to give 94% (entry

9) and 93% (entry 13) of these straight adducts respectively. This is in accordance with the results reported where 46% of **2a** was formed after 19 h of irradiation and 82% of **2c** after 8 hours of irradiation [118]. In the case of the straight cycloadduct formation, the groups involved are in close proximity rendering it easier for cyclization to take place compared to the crossed cycloadduct whose corresponding groups are relatively distant (steric effect).

Table 3.2: Scope of photosensitized intramolecular [2+2] cycloaddition reaction. Batch reactions are performed in a round bottom flask and is irradiated from one side. Reactions performed in the cuvette (l=1cm) were also irradiated from one side.

Entry	Reactor	Product	Time (min)	% Conv.
1	Dwell Device HP-Led A		230	86
2	Dwell Device HP-Led B		115	96
3	Batch HP-Led B		224	46
4	Cuvette HP-Led B		224	95
5	Dwell Device HP-Led A		230	87
6	Dwell Device HP-Led B		50	94
7	Batch HP-Led B		158	47
8	Cuvette HP-Led B		158	93
9	Dwell Device HP-Led A		19	94
10	Dwell Device HP-Led B		10	93
11	Batch HP-Led B		41	42
12	Cuvette HP-Led B		41	89
13	Dwell Device HP-Led A		19	93
14	Dwell Device HP-Led B		2.5	91
15	Batch HP-Led B		15	49
16	Cuvette HP-Led B		15	96

The reaction was significantly speeded up by using UV LEDs B of higher irradiance. Crossed products **2a** and **2b** were formed in higher conversions (96% & 94%) after only 115 minutes and 50 minutes thus decreasing the irradiation time by a minimum of 2.5 folds (entries 1-2, entries 5-6). Similarly around 90% of straight adducts **2c** and **2d** were obtained after 10 and 2.5 minutes respectively. This highlights the impact of light power on the rates of photochemical reactions. It also provides an easy way to speed up the experiment by simply increasing the power of the light supplied. It is not the case when working with thermal-based experiments as the increase in temperature might lead to the decomposition of the desired products.

Batch experiments for each substrate were performed using the same conditions with the light source UV LEDs B. The results follow the same trend as those obtained in flow regarding the rates of formations of crossed and straight cycloadduct (entries 3- 4; 7- 8; 11- 12). The reactions were remarkably slower in batch than in flow especially when using the round bottom flask (entries 3, 7, 11) where the speed of the reaction is decreased by around 4 to 12 folds. The impact of switching from flow to batch was less significant when using the cuvette as the rates were decreased by around 2 to 6 folds. The cuvette's path length that is half that of the round bottom flask explains why the rates were doubled when using the former. This emphasizes the importance of the reactors' dimensions on its performance especially when an external component such as light should be efficiently integrated within the reaction mixture.

The responses of the assessed substrates (**1a-1d**) to the change in the reactors dimensions or the power of the UV source were neither homogeneous nor correlated. This can be due to the differences among the substrates' time needed for sensitization and their corresponding excited states' lifetimes.

3.3.3 Kinetics of [2+2] Cycloaddition using Sensitization

Similar to classical sensitization, the [2+2] cycloaddition reactions proceed as indicated in Equations 3.1, 3.2 and 3.3:



The DMBP (B) absorbs light energy to form a singlet excited state ${}^1B^*$ that relaxes rapidly to its triplet excited state ${}^3B^*$ via intersystem crossing (Equation 3.1). The triplet DMBP is quenched by transferring the excess of energy to the substrate (S) leading to the sensitization of the latter (S^*). The excited substrate will then undergo the [2+2] cyclization to form the product C (Equation 3.2). Excited DMBP can also extract a proton from the surrounding to form the pinacol (P) (Equation 3.3).

Intramolecular cyclizations follow first order kinetics. The pinacolization however should be second order. Since cyclization is negatively affected by the increase in pinacolization, we postulated the following simple differential equation for the [2+2] photocycloaddition (Equation 3.4).

$$\frac{d[C]}{dt} = k_1[S]_t - k_2[B]_t^2 \quad \text{Equation 3.4}$$

So for the substrate (S), the following equations can be used (Equations 3.5-5.8).

$$-\frac{d[S]}{dt} = k_1[S] \quad \text{Equation 3.5}$$

$$[S]_t = [S]_0 \times e^{-k_1 t} \quad \text{Equation 3.6}$$

$$\ln \frac{[S]_t}{[S]_0} = -k_1 t \quad \text{Equation 3.7}$$

$$[S]_t = [S]_0 - [C]_t \quad \text{Equation 3.9}$$

$$\ln([S]_0 - [C]_t) = -k_1 t \quad \text{Equation 3.10}$$

As for the pinacolization reaction, Equations 3.11 and 3.12 can be used.

$$-\frac{d[B]}{dt} = k_2[B]^2 \quad \text{Equation 3.11}$$

$$\frac{1}{[B]_t} = \frac{1}{[B]_0} + k_2 t \quad \text{Equation 3.12}$$

However, since the degree of pinacolization is very small, both plots of $\ln[B]$ vs. t and $1/[B]$ vs. t are almost linear. So to confirm the second order nature of pinacolization we decided to study the kinetics of pinacolization reactions in flow for 2 solutions of DMBP (0.074 M and 0.037M) without the addition of any substrate (Figure 3.21).

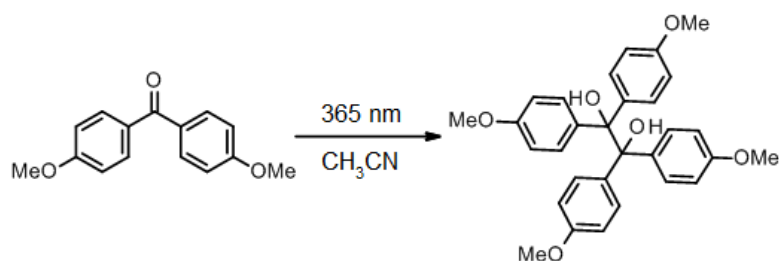


Figure 3.21: Pinacolization reaction of DMBP

3.3.3.1 Determination of reaction order of pinacolization

For $[B_0] = 0.074$ M, Table 3.3 includes the variation of pinacolization with the irradiation time. The plot of $1/([B]_0 - [P])$ vs. t (Figure 3.22) gives a linear graph with a slope that corresponds to the rate constant $k = 0.0198 \text{ M}^{-1} \text{ min}^{-1}$. Thus the apparent rate is $1.084 \times 10^{-4} \text{ M} \cdot \text{min}^{-1}$.

Table 3.3: Results of pinacolization reaction in flow for $[B]_0 = 0.074 \text{ M}$

Flow rate ($\mu\text{l}/\text{min}$)	T irradiation (min)	% Pinacol
200	6	1.3
150	7.5	1.7
100	11.5	2.4
75	15	2.8
30	38	5
20	57	8
10	115	14.8

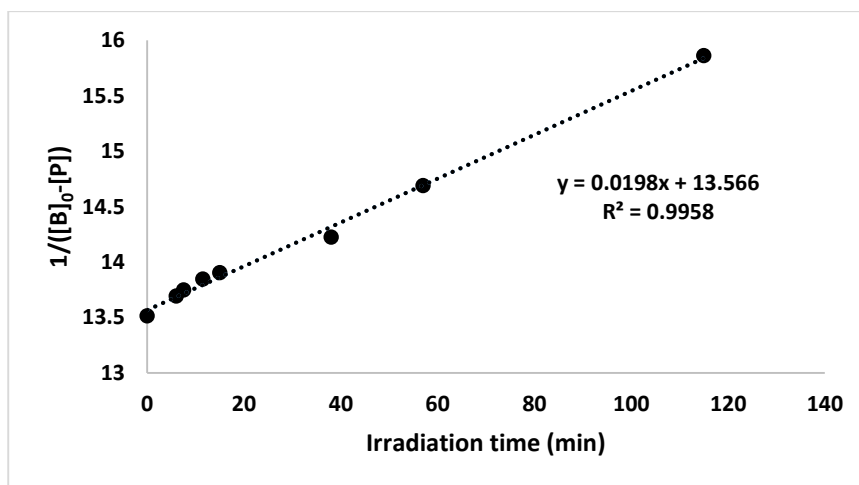


Figure 3.22: Graph of $1/[B]_0 - [P]$ vs. t where $[B]_0 = 0.074 \text{ M}$

Similarly working with $[\text{DMBP}] = 0.037 \text{ M}$ (Table 3.4) gave a linear correlation between $1/([B]_0 - [P])$ vs. t with $k = 0.0204 \text{ M}^{-1} \text{ min}^{-1}$ (Figure 3.23) and the apparent rate' is $2.793 \times 10^{-5} \text{ M} \cdot \text{min}^{-1}$.

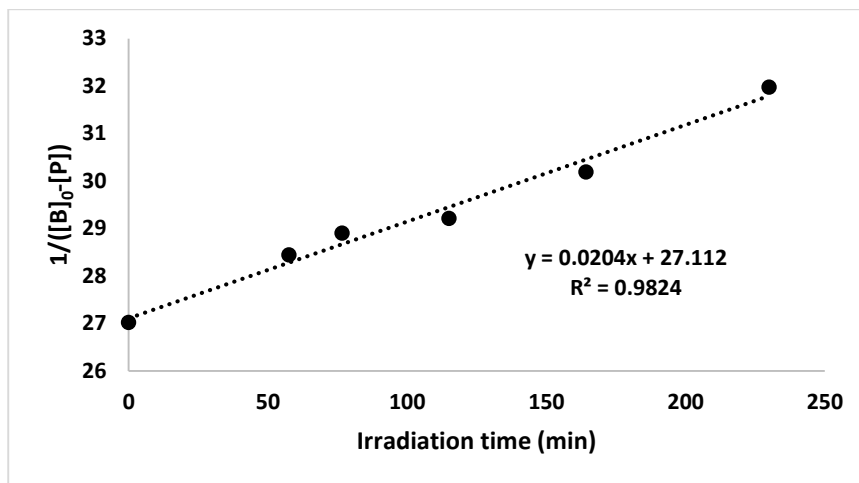


Figure 3.23: Graph of $1/[B]_0-[P]$ vs. t where $[B]_0 = 0.037$ M.

Table 3.4: Results of pinacolization reaction in flow for $[B]_0 = 0.037$ M

Flow rate ($\mu\text{l}/\text{min}$)	Irradiation time (min)	% Pinacol
20	57.5	5
15	77	6.5
10	115	7.5
7	164	10.5
5	230	15.5

For the reaction to be second order, Equation 3.13 should be applicable

$$\frac{\text{rate}}{\text{rate}'} = \frac{k B_0^2}{k B_0'^2} = \frac{0.074^2}{0.037^2} = 4 \quad \text{Equation 3.13}$$

Substituting the obtained apparent values of rate and rate' gives a ratio of 3.88 (Equation 3.14) which can be rounded to 4. So we confirm that the pinacolization follows second order kinetics.

$$\frac{\text{rate}}{\text{rate}'} = \frac{1.084 \times 10^{-4}}{2.793 \times 10^{-5}} = 3.88 \approx 4 \quad \text{Equation 3.14}$$

3.3.3.2 Determination of reaction order of [2+2] cycloaddition

We then used the most reactive substrate **1d** and performed reactions in flow. In order to confirm our hypothesis indicated in Equation 3.4, the concentration of the substrate was varied to check the impact of this variation on the rate of the reaction

Case 1: $[B]_0 = 0.074 \text{ M}$, $[S]_0 = 0.037 \text{ M}$.

Using HP LEDs B and varying the flow rate using the syringe pump, results summarized in Table 3.5 were obtained.

Table 3.5: Results of sensitized [2+2] cycloaddition in flow where $[S]_0 = 0.037 \text{ M}$

Flow($\mu\text{l min}^{-1}$)	Time (min)	% [2+2] cycloadduct	% Pinacol
2500	0.46	44	1
1500	0.77	65	1.4
920	1.25	72	2.6
460	2.5	91	5.4
230	5	98.8	9.9

Using equations 3.10 and 3.12 where $[S]_0 = 0.037 \text{ M}$ and $[B]_0 = 0.074 \text{ M}$, the following graphs of $\ln([S]_0 - [C]_t)$ vs. t (Figure 3.24) and $1/[B]$ vs. t (Figure 3.25) are obtained. Strictly linear correlations were obtained with the slopes that correspond to $k_1 = 0.8584 \text{ min}^{-1}$ and $k_2 = 0.6562 \text{ M}^{-1} \text{ min}^{-1}$ respectively.

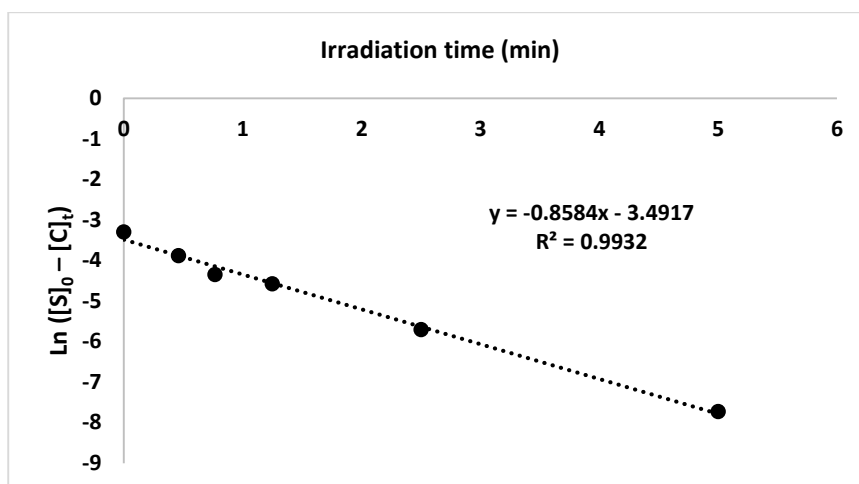


Figure 3.24: Plot of $\text{Ln} ([S]_0 - [C]_t)$ vs. t (min) with $[S]_0 = 0.037$ M and $[B]_0 = 0.074$ M

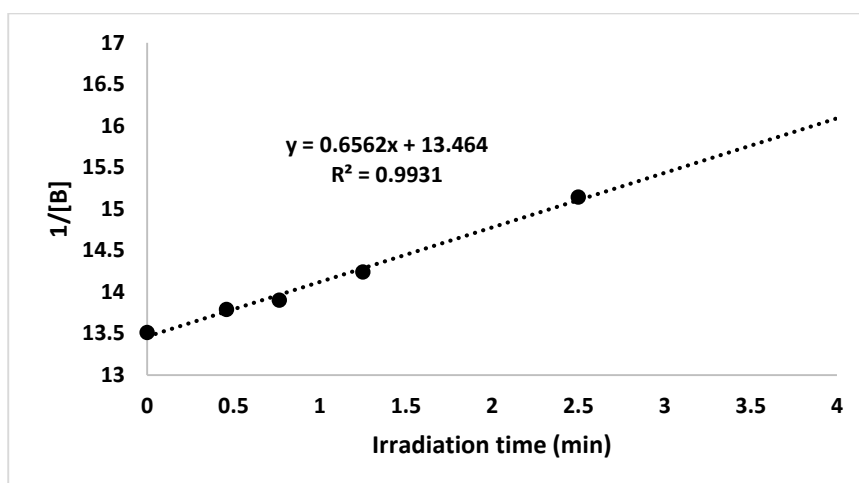


Figure 3.25: Plot of $1/[B]_t$ vs. t (min) with $[S]_0 = 0.037$ M and $[B]_0 = 0.074$ M

Case 2: $[B]_0 = 0.074$ M, $[S]_0 = 0.01$ M.

Table 3.6 includes the results for the [2+2] cycloaddition and pinacolization taking place in flow when $[B]_0 = 0.074$ M, $[S]_0 = 0.01$ M. The kinetic graphs have strong correlations with $R^2 = 0.995$ for Figure 3.26 and 0.994 for Figure 3.27. In this case, $k_1 = 1.0225 \text{ min}^{-1}$ and $k_2 = 0.2468 \text{ M}^{-1} \text{ min}^{-1}$.

Table 3.6: Results of sensitized [2+2] cycloaddition in flow where $[S]_0 = 0.01\text{ M}$

Flow ($\mu\text{l min}^{-1}$)	Time (min)	% [2+2] cycloadduct	% Pinacol
1500	0.8	67	0.8
1200	0.95	72	1
920	1.25	80	1.2
690	1.7	85	1.8
460	2.5	93	2.4
230	5	99.5	4.2

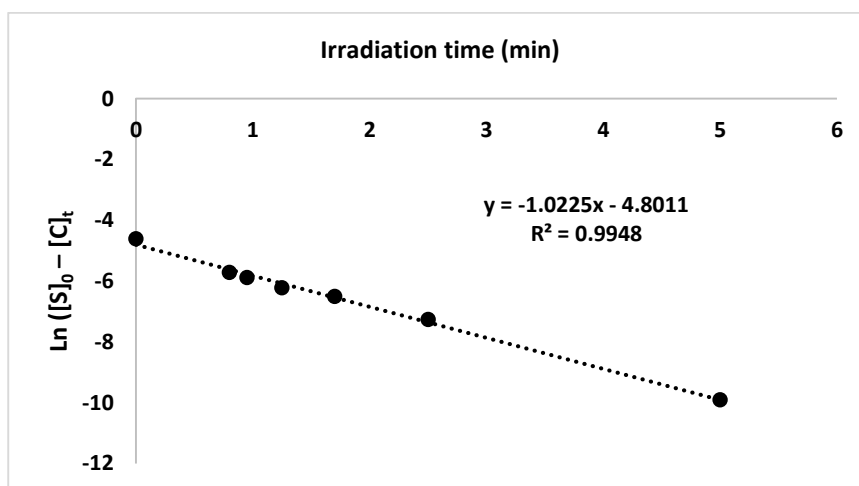


Figure 3.26: Plot of $\text{Ln} ([S]_0 - [C]_t)$ vs. t (min) with $[S]_0 = 0.01\text{ M}$ and $[B]_0 = 0.074\text{ M}$

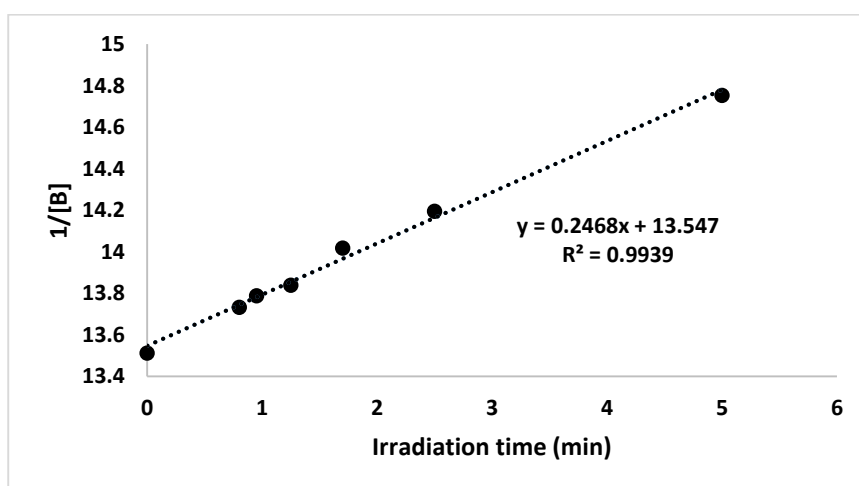


Figure 3.27: Plot of $1/[B]_t$ vs. t (min) with $[S]_0 = 0.01\text{ M}$ and $[B]_0 = 0.074\text{ M}$

Case 3: $[B]_0 = 0.074 \text{ M}$, $[S]_0 = 0.02 \text{ M}$.

The results summarized in Table 3.7 fit to the first order kinetics for the variation of $[S]$ with respect to time with $k_1 = 0.6303 \text{ min}^{-1}$ (Figure 5.28). As for the pinacolization reaction (Figure 5.29), second order kinetics fit perfectly with the experimental results with $k_2 = 0.1765 \text{ M}^{-1} \text{ min}^{-1}$. In both cases high correlation coefficient were obtained (0.998 and 0.999 respectively).

Table 3.7: Results of sensitized [2+2] cycloaddition in flow where $[S]_0 = 0.02 \text{ M}$

Flow ($\mu\text{l min}^{-1}$)	time (min)	% [2+2] cycloadduct	% Pinacol
1500	0.77	30	0.3
920	1.25	55	0.7
460	2.5	79	1.5
230	5	96.5	3
115	10	99.8	5.7

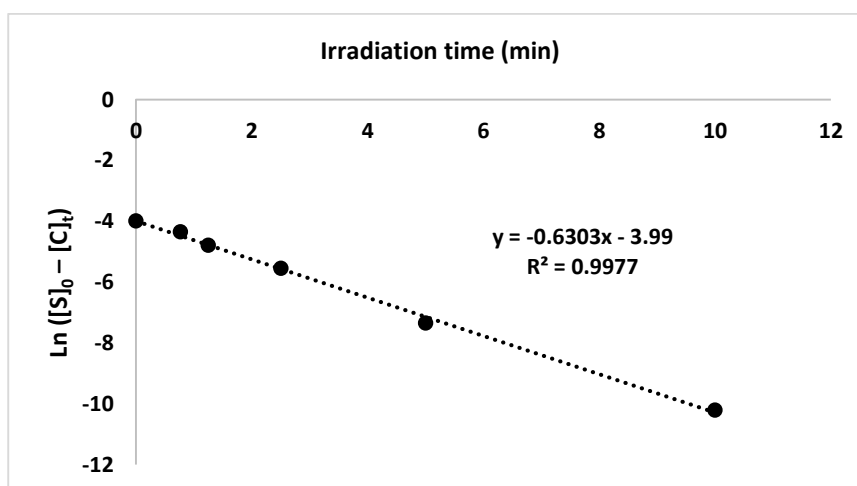


Figure 3.28: Plot of $\text{Ln} ([S]_0 - [C]_t)$ vs. t (min) with $[S]_0 = 0.02 \text{ M}$ and $[B]_0 = 0.074 \text{ M}$

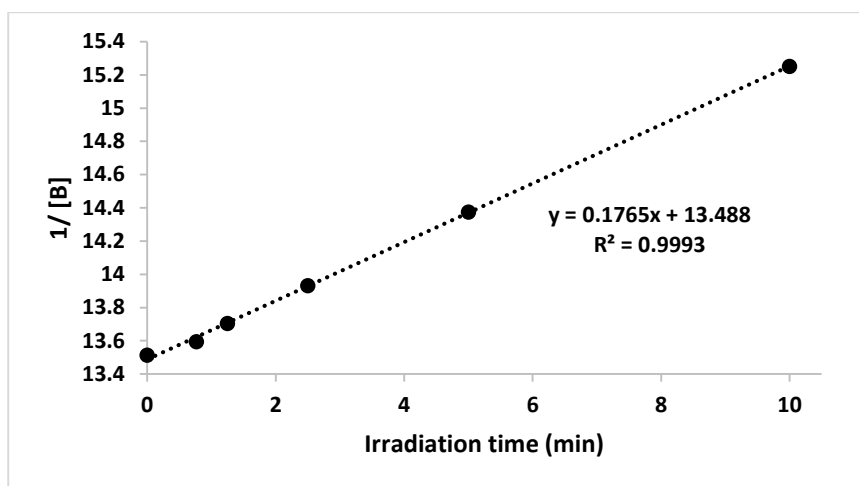


Figure 3.29: Plot of $1/[B]_t$ vs. t (min) with $[S]_0 = 0.02$ M and $[B]_0 = 0.074$ M

Case 4: $[B]_0 = 0.074$ M, $[S]_0 = 0.08$ M.

Concentrated solutions of the substrate with benzophenone were also injected within the Mikroglas Dwell Device at different flow rates while being irradiated using HP LEDs B (Table 3.8). Similar to the previous cases, substituting the values of $[S]_0$ and $[B]_0$ in equations 3.10 and 3.12 and plotting the corresponding graphs (Figures 3.30 and 3.31) gave straight lines whose slopes correspond to $k_1 = 0.7173 \text{ min}^{-1}$ and $k_2 = 1.0044 \text{ M}^{-1} \text{ min}^{-1}$.

Table 3.8: Results of sensitized [2+2] cycloaddition in flow where $[S]_0 = 0.08$ M

Flow ($\mu\text{l min}^{-1}$)	Time (min)	% [2+2] cycloadduct	% Pinacol
920	1.25	68	2.6
690	1.7	75	3.6
460	2.5	85	7
230	5	97	13
175	6.5	99	15.8

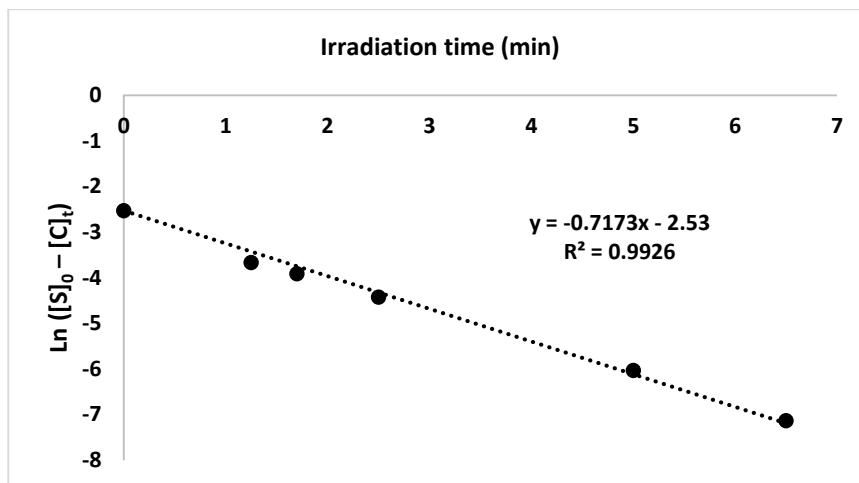


Figure 3.30: Plot of $\ln ([S]_0 - [C]_t)$ vs. t (min) with $[S]_0 = 0.08$ M and $[B]_0 = 0.074$ M

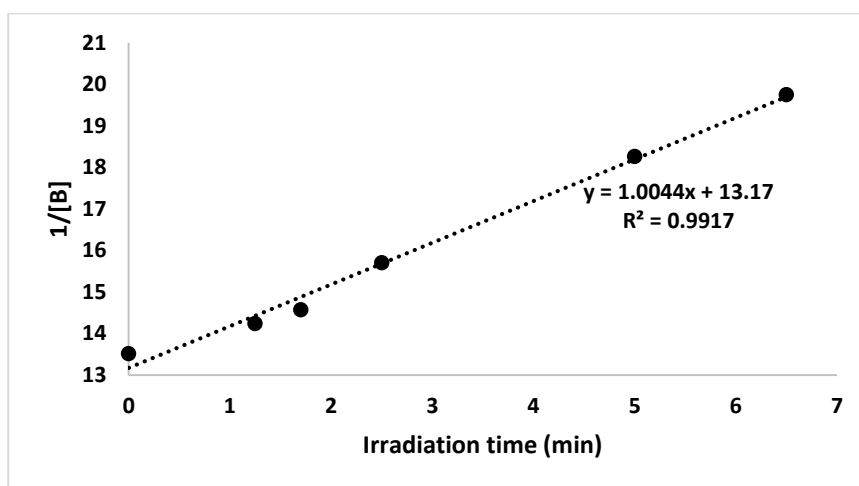


Figure 3.31: Plot of $1/[B]_t$ vs. t (min) with $[S]_0 = 0.08$ M and $[B]_0 = 0.074$ M

The results of the 4 cases are summarized in Table 3.9. Note that the rate of the reaction is calculated based on the postulation included in Equation 3.4.

Table 3.9: Summary of the kinetic results for the variation of [S]₀. (a): the ratio of the concentration of the substrate in entry 1 to another entry (x) , (b): obtained using Equation 3.4 , (c): the ratio of the rate in entry 1 to that of the other entries (x)

Entry	[S] ₀	[B] ₀	[S] _{0 (1)} / [S] _{0 (x)} ^a	[B] _{0 (1)} / [B] _{0 (x)}	Rate [C] ^b	rate ₁ /rate _x ^c
1	0.037	0.074	1	1	0.02817	1
2	0.02	0.074	1.85	1	0.01164	2.16
3	0.01	0.074	3.7	1	0.00888	3.17
4	0.08	0.074	0.46	1	0.05188	0.54

In entry 2 of Table 3.9, the ratio of [S]_{0 (1)} / [S]_{0 (x)} is 1.85 which is close in value to that of the ratio of rate ₁/rate _x (2.16). These ratios also give almost equal values in entries 3 and 4 (3.7 & 3.17; 0.46 & 0.54). Note that if the second part of Equation 3.4 ($-k_2[B]_t^2$) is excluded, these values will be further deviated as the ratio of rate ₁/rate _x will significantly change. This proves that the rate of formation of the cycloadduct also depends on pinacolization as indicated in Equation 3.4.

However, Changing the concentration of DMBP also altered the value of k_1 for a given [S]₀. This shows that the kinetics of such sensitized systems are more complicated and need advanced calculations.

We assumed that the increase in the rate of [2+2] cycloaddition should lead to a decrease in the rate of pinacolization as more DMBP would be involved in sensitizing the substrates rather than coupling with another DMBP. This turned out to be untrue as it is clear that the k_2 values of pinacolization of [DMBP] in the absence of the substrate are significantly smaller than those when the substrate is present ($k_2 = 0.0198 \text{ M}^{-1} \text{ min}^{-1}$, Figure 3.22 vs. $1.0 \text{ M}^{-1} \text{ min}^{-1}$, Figure 3.31). It appears that the increase in the concentration of **1d** leads to the increase in pinacolization. Since we have shown that the substrate doesn't absorb at 365 nm, the only remaining possibility is that the cycloadduct formed (**2d**) absorbs at this wavelength and acts as a sensitizer to DMBP.

3.3.3.3 Kinetic studies of the other substrates

After confirming the suggested kinetic orders for the [2+2] cycloaddition and pinacolization reactions, kinetics measurements in flow were done on 0.074 M of DMBP and 0.037 M of substrates **1a**, **1b**, **1c** and **1d**. The results are summarized in Table 3.10.

Table 3.10: Summary of the kinetic results for photosensitized intramolecular [2+2] cycloaddition of substrates 1a-1d in flow

Entry	Substrate	k_1 (min ⁻¹)	R ²	k_2 (M ⁻¹ min ⁻¹)	R ²
1	1a	0.0445	0.993	0.1919	0.98
2	1b	0.0656	0.994	0.4959	0.987
3	1c	0.2567	0.981	0.597	0.991
4	1d	0.8584	0.993	0.6562	0.993

Similar to the previous kinetic curves of the other photochemical reactions performed in flow, the plotted kinetic curves exhibit strong linear correlations. The correlation coefficients of both pinacolization and [2+2] cycloaddition of all of the substrates are in the range of 0.99. **1a** is the least reactive with $k_1 = 0.0445 \text{ min}^{-1}$ (entry 1). The reactivity is enhanced by 1.5 folds with the substituted dimethyl **1b** with $k_1 = 0.0656 \text{ min}^{-1}$ (entry 2). Similarly an increase in the rate of the reaction is also observed between the unbranched **2c** (entry 3) and the branched **2d** (entry 4) straight cycloadducts but to a higher extent (3 folds). The remarkable increase in reactivity between crossed and straight products is clearly demonstrated as the rate increased by around 6 folds (**1a** vs. **1c**) and 13 folds for the dimethylated substrates (**1b** vs. **1d**).

Regarding pinacolization, its rate also increases with the increase in the rate of [2+2] cycloaddition in all of the entries supporting our suggestion that the cycloadducts absorb at this wavelength and thus sensitize DMBP.

3.3.4 Limitations of the Sensitized Reaction

The main reason for not being able to support or exclude the hypothesis that the formed cycloadduct absorbs 365nm radiation and sensitizes DMBP is the difficulty in purifying the formed products. Flash chromatography is not efficient as the adducts are unstable on silica. Trying various eluents with different compositions, prewashing the column with a base and using reversed phase and alumina columns were not useful for the purification of the products **2a-2d** by chromatography.

3.3.5 Visible Light Induced Intramolecular [2+2] Cycloaddition using $Ru(bpy)_3Cl_2$

Using visible light the intra molecular [2+2] photocycloaddition of the bisenone **1f** using $Ru(bpy)_3Cl_2$ as a photoredox catalyst was performed in flow using blue LEDs (Figure 3.32, Figure 3.33). Table 3.11 includes the first group of experiment performed using white LEDs. Note that all of the yields indicated below are NMR yields.

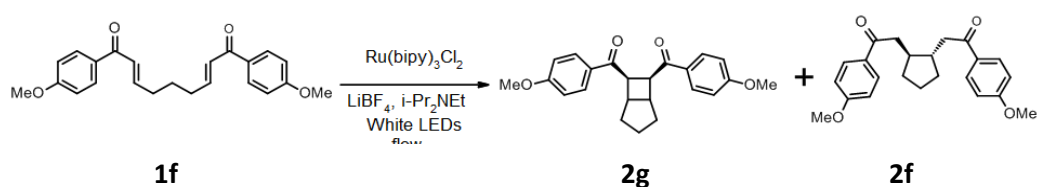


Figure 3.32: Visible light induced intramolecular cycloaddition of bisenone in flow using $Ru(bpy)_3Cl_2$



Figure 3.33: Set up for the photocycloaddition in flow using $Ru(bpy)_3Cl_2$ and blue LEDs

Entries 1, 2 and 3 are control experiments (Table 3.11). In the three cases, no reaction took place thus showing the importance of the photocatalyst, the electron donor and the Lewis acid for the cycloaddition reaction. Following the conditions used by Yoon group [130], with 5 mol % catalyst, 2 eq of *i*-Pr₂NEt and 2 eq of LiBF₄, 1 hour of irradiation in flow was enough to obtain full conversion of the starting material (Entry 4) compared to 5 hours in batch (Entry 5) thus increasing the rate by 5 folds by switching into flow. However, the [2+2] cycloadduct was not the only product obtained and not even the major one as another product (*product 2*) was found and in major quantities (entry 4, 24% **2g** vs. 75% **2f**). Similar ratio of [2+2] cycloadduct/ *product 2* was also obtained in batch (entry 5).

In order to identify *product 2*, we tried the conditions listed by the same author that favor reductive cycloaddition and give a reductive adduct. Such a protocol uses Brønsted acid (HCOOH) instead of Lewis acid [142]. So in entries 6 and 7, 2.5 mol % of Ru(bpy)₃Cl₂, 10 eq. of *i*-Pr₂NEt and 5 eq of HCOOH were used in flow and batch conditions respectively. This reaction is more rapid than the [2+2] cycloaddition as it is quantitative after 45 minutes of irradiation using white LEDs (entry 6) compared to 1 hour for the full disappearance of the starting material under [2+2] cycloaddition conditions (entry 4) in flow. Similarly, reductive cyclization performed in batch was also more rapid than the [2+2] cycloaddition (entry 5 vs. entry 7). The ¹H NMR of the reductive cycloadduct obtained **2f** using the conditions of entry 6 fits to *product 2* obtained using the [2+2] cycloaddition conditions of entries 4 and 5.

Table 3.11: Screening of conditions for the intramolecular [2+2] cycloaddition reaction of 1f in a Mikroglas ® Dwell device irradiated with white LEDs and catalyzed by Ru(bpy)₃Cl₂. (a) performed in batch, (b) using 5 equ of HCOOH.

Entry	Time (h)	Catalyst (mole %)	i-Pr ₂ Net (eq)	LiBF ₄ (eq)	% 2g	% 2f	% 1f
1	1	5	0	0	0	0	100
2	1	0	0	2	0	0	100
3	1	5	2	0	7	0	93
4	1	5	2	2	24	75	1
5 ^a	5	5	2	2	23	70	7
6 ^{a,b}	3	2.5	10	0	0	95	5
7 ^b	0.75	2.5	10	0	0	100	0

After identifying the second product obtained, the second step was trying to optimize the conditions to get the [2+2] cycloadduct as the major/ only product (Table 3.12). Replacing the white LEDs by blue LEDs (entry 1) had no impact on the rate of the reaction as the rate of disappearance of the starting material was almost the same (Table 3.11 entry 4 vs. Table 3.12 entry 1). However, the ratio of **2g**/**2f** increased from 0.32 in entry 4 using white LEDs (Table 3.11) to 0.7 using the blue LEDs in Table 3.12 entry 1. This was not the case when using LEDs of different wavelength (entries 2, 3, 4, Table 3.12). With green irradiation, the reaction was much slower where 32% of the starting material remained unreacted (entry 2). Similar results were obtained when using UV LEDs (entry 4) and no reaction was observed using the red LEDs (entry 3). This can be due to the fact that the maximum absorbance of the photocatalyst Ru(bpy)₃Cl₂ is in the blue region. Eventually, its catalytic activity is at its peak when supplied with blue irradiation and decreases with varying the irradiation wavelength.

Table 3.12: Intramolecular [2+2] cycloaddition reaction of **1f in a Mikroglas® Dwell device irradiated for 1 hour with different visible LEDs using Ru(bpy)₃Cl₂ (5 mol %), i-Pr₂NEt (2 eq) and LiBF₄ (2 eq)**

Entry	LEDs	% 2g	% 2f	% 1f
1	blue	40	57	3
2	green	23	46	32
3	red	0	0	100
4	UV	20	53	27

After choosing the blue LEDs as the optimum irradiation for the conversion and the ratio of **1g/1f**, we decided to modify the other conditions of the reaction (Table 3.13)

Replacing LiBF₄ by Zn(OTf)₂ was enough to cease cycloaddition. No reaction was achieved in entry 1 (Table 3.13) proving the important role that the Lithium ion plays in the mechanism of cycloaddition. This is in accordance to what is listed by Yoon where no reaction took place when replacing LiBF₄ by Bu₄NBF₄ or NaBF₄. Using LiPF₆ gave only the reductive adduct (entry 2) whereas LiOTf gave both the [2+2] cycloadduct and the reductive adduct but with less proportion of [2+2] cycloadduct compared to using LiBF₄ (Table 3.13 entry 3: 0.23 vs. Table 3.12 entry 1: 0.7). LiPF₆ is extremely sensitive to humidity and LiOTf has a lower dissociation constant than LiBF₄. This shows that the properties of the Lewis acid also plays an important role in the selectivity of the reaction. Moreover, Ru(bpy)₃(BF₄)₂ is more soluble in acetonitrile [130, 144]. This explains why LiBF₄ is the most suitable Lewis acid for such a reaction [145]. Changing the quantity of both i-Pr₂NEt and LiBF₄ gave no remarkable impact on the selectivity towards the [2+2] cycloaddition (Table 3.13, entries 4 and 5). Decreasing the quantity of the catalyst into 0.7 mol % (entry 6) and 0.1 mol % (entry 7) remarkably decreased the rate of the reaction with 40% and 76% of unreacted starting material respectively. However, this change in catalyst loading improved the selectivity towards the [2+2] cycloaddition without hindering the reductive cyclization.

We then assessed the impact of the photocatalyst used by replacing Ru(bpy)₃Cl₂ with other photocatalysts. eosin Y is described as a photoredox catalyst [146, 147]. Its activity, however, was less than that of Ru(bpy)₃Cl₂ as 40% of the **1f** was unreacted after 2 hours of green irradiation. Moreover, it only provided the reductive adduct **2f** (entry 8). Similarly, using 1 equ of thioxanthone provided 82% of **2f** after 2 hours of white LEDs irradiation in flow (entry 9).

The reaction time was decreased using flow confirming the importance of light on the kinetics of such a photochemical reaction. However, we were not capable of reproducing the results obtained by Yoon as it seems that [2+2] cycloaddition and reductive cyclization are competitive reactions.

Table 3.13: Screening of conditions for the intramolecular [2+2] cycloaddition reaction of 1f in a Mikroglas® Dwell device irradiated with visible LEDs and catalyzed by Ru(bpy)₃Cl₂. (a) with 2 eq of Zn(OTf)₂, (b) with 2 eq of LiPF₆, (c) with 2 eq of LiOTf, (d) with 2 eq of Eosin Y, (e) with 2 eq of thioxanthone

Entry	Time (h)	LEDs	Catalyst (mol %)	i-Pr ₂ NEt (eq)	LiBF ₄ (eq)	% 2g	%2f	%1f
1 ^a	1	blue	5	2	2	0	0	100
2 ^b	1	blue	5	2	2	0	98	2
3 ^c	1	blue	5	2	2	18	77	5
4	1	blue	5	5	5	31	65	4
5	1	blue	5	10	5	24	70	6
6	1	blue	0.7	2	2	32	28	40
7	1	blue	0.1	2	2	23	10	67
8 ^d	2	green	0	2	0	0	60	40
9 ^e	2	white	0	2	0	0	82	18

Once we were capable of identifying the reductive adduct, a kinetics study was performed for the reaction in flow using the conditions of entry 4 (Table 3.11). The irradiation time was varied by changing the flow rate by a syringe pump. The ¹H NMR yields

of the three components: Bisenone **1f**, [2+2] cycloadduct **2g** and reductive adduct **2f** for each irradiation time are represented in Table 3.14.

The quantity of **1f** decreased with the increase in the irradiation time until full disappearance after around 1 h of irradiation with white LEDs. On the other hand, both the [2+2] cycloadduct **2g** and the reductive adduct **2f** increased until reaching an equilibrium of a ratio of 1:3 respectively (entries 6, 7). This made us postulate that a parallel (competitive) reaction is taking place as the starting material is converting simultaneously to form both products.

Table 3.14: Summary of the photoredox induced cyclization of bisenone in flow using white LEDs

Entry	Flow rate (μl/min)	Time (min)	2g (%)	2f (%)	1f (%)
1	200	6	6	40.5	53.5
2	150	8	7	45	48
3	100	11.5	9	55	34
4	60	19	20	61.5	18.5
5	30	38	24	74	2
6	20	57.5	22.5	77	0.5
7	10	115	23	77	0

3.3.5.1 Kinetics of parallel reactions

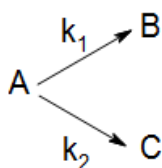


Figure 3.34: Representation of parallel reactions

Consider that both reactions $A \rightarrow B$ and $A \rightarrow C$ follow first order kinetics as both are intramolecular reactions (Figure 3.34) where A is **1f**, B is **2g** and C is **2f**. Thus the variation

of A, B and C with respect to irradiation time can be represented in Equations 3.15, 3.3.16 and 3.3.17 respectively.

$$\frac{-dA}{dt} = (k_1 + k_2)[A] \quad \text{Equation 3.15}$$

$$\frac{dB}{dt} = k_1[A] \quad \text{Equation 3.16}$$

$$\frac{dC}{dt} = k_2[A] \quad \text{Equation 3.17}$$

The integrated forms for the equations above are Equations 3.18, 3.19 and 3.20.

$$A = A_0 e^{-(k_1+k_2)t} \quad \text{Equation 3.18}$$

$$B = \frac{k_1}{k_1 + k_2} A_0 (1 - e^{-(k_1+k_2)t}) \quad \text{Equation 3.19}$$

$$C = \frac{k_2}{k_1 + k_2} A_0 (1 - e^{-(k_1+k_2)t}) \quad \text{Equation 3.20}$$

In such a condition, Equation 3.21 is true.

$$\frac{B}{C} = \frac{k_1}{k_2} \quad \text{Equation 3.21}$$

In order to determine k_1 and k_2 , $\ln A$ vs. t is plotted. The slope of the formed straight line corresponds to the addition of both rate constants. The ratio of B/C is then used to determine the ratio of the rate constants. Such two values will be then used to calculate k_1 and k_2 .

By referring to Equation 3.15 the variation of the logarithm of the bisenone **1f** with respect to time gave the following graph (Figure 3.35). The plot exhibits a strictly linear relationship between the logarithm of the bisenone and the irradiation time with $R^2 = 0.9957$.

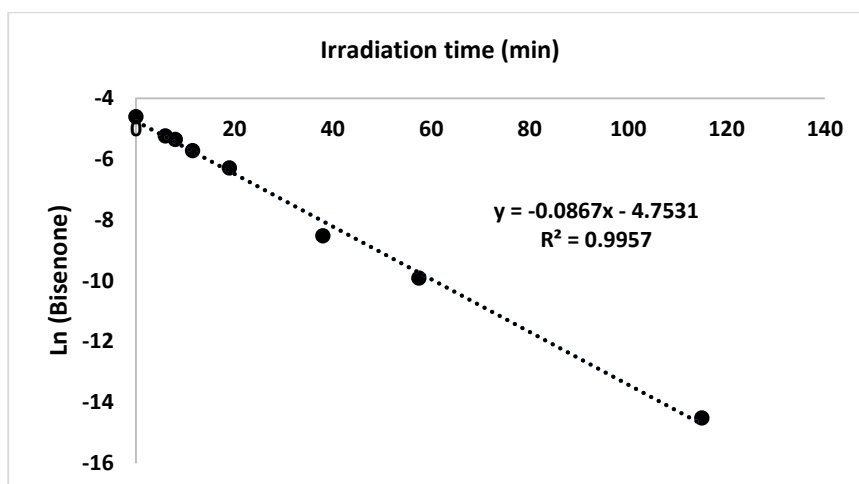


Figure 3.35: Variation of Ln[Bisenone] with respect to irradiation time (min)

The slope of the graph above provides the first equation to find k_1 and k_2 as $k_1+k_2 = 0.0867 \text{ min}^{-1}$. The ratio $\frac{[2+2]\text{cycloadduct}}{\text{reductive adduct}}$ at t_∞ corresponds to 0.295 thus providing the second equation needed to determine k_1 and k_2 .

Solving the system of 2 equations for the 2 unknowns gave $k_1 = 0.0198 \text{ min}^{-1}$ and $k_2 = 0.0669 \text{ min}^{-1}$. Substituting these values in equations 3.18, 3.19 and 3.20 with A corresponding to the bisenone, B to the [2+2] cycloadduct, C to the reductive adduct and $A_0 = 0.01 \text{ M}$, the following graph is obtained (Figure 3.36).

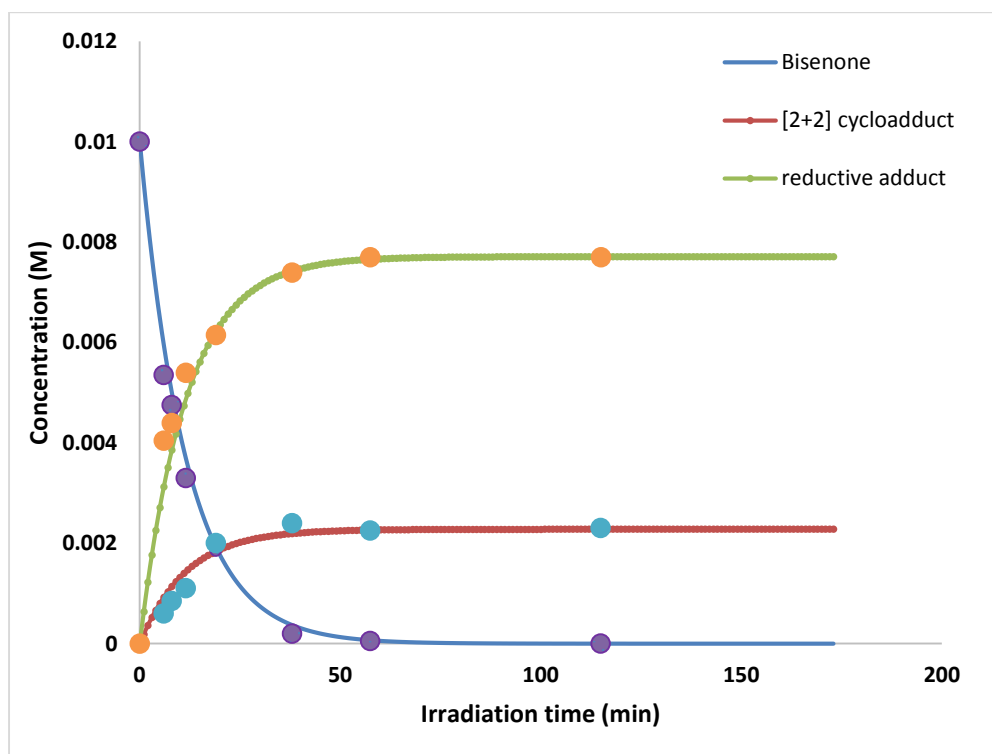


Figure 3.36: Variation of Bisenone (blue), [2+2] cycloadduct (red) and reductive adduct (green) vs. irradiation time (min) in a competitive reaction.

The results summarized in Table 3.14, Figure 3.35 and Figure 3.36 confirm our postulation that the reductive and [2+2] cycloaddition are two competitive reaction when using the photoredox catalysis by $\text{Ru}(\text{bpy})_3\text{Cl}_2$. When observing the mechanisms of both reaction listed in literature, the reductive cyclization is formed *via* enol radical intermediate whereas the [2+2] cycloaddition is formed following a radical anion intermediate. If those suggested mechanisms are true, it means that in our case there is a source of proton that initiates the reductive cyclization. This is less likely to be the case as we used our best efforts to make sure to work under extremely dry conditions especially when our results were not compatible to those obtained in literature. Even adding MgSO_4 to the reaction mixture to remove moisture failed to provide the desired [2+2] cycloaddition as the major product. Another hypothesis is that the intensity of the LEDs used in our case is strong so that the [2+2] cycloadduct is then converting into the reductive adduct. This hypothesis can be

excluded since in Figure 3.36, it is clear that the composition of the mixture remained constant even after 1 extra hour of irradiation confirming that both reactions are parallel. Moreover, we also tested the reaction using a blue fluorescent lamp (23 W) and both products were also found. Trying to decrease the intensity of light by putting the flow system at a distance from the light source also failed to favor the [2+2] cycloaddition reaction. One last hypothesis that could be true and we haven't tested yet is the impact of the substitution on the phenyl group. *p*-methoxy substitutions tend to make the substrate more reactive compared to the unsubstituted phenyl substrates so it might be the reason behind the observed limited selectivity. This hypothesis is less likely to be true as **1f** is listed in literature to perform [2+2] cycloaddition reaction without having any side reactions. Note that photochemical reactions are known to be extremely sensitive to impurities that might be a limitation to its reproducibility.

3.4 Conclusion

This chapter focuses on the intramolecular [2+2] photocycloaddition reaction performed in the UV and the visible region in flow. We chose the intramolecular [2+2] photocycloaddition of 3-(alkenyloxy)cyclohex-2-enones as a model reaction in the UV region. This reaction is described in literature to be efficient at 254 nm. We decided to perform this reaction in flow using the LED technology which is more efficient than classical fluorescent lamps. However, LEDs with wavelengths as low as 254 nm are still rare along with the rising safety alerts when working with high energy wavelengths. Adding a sensitizer that absorbs at 365 nm was the best solution for such a complication. Though benzophenone does not absorb strongly at this wavelength, it succeeded to sensitize the substrate to undergo cycloaddition at rates which are even more enhanced than classical 254 nm conditions. Applying this approach in flow with 90 mW.cm⁻² UV LEDs significantly accelerated the

reaction to give 86% conversion after 230 minutes of irradiation. Additional Increase in the power of the light source enhanced the rate even more with having around 94 % conversion after only 2 hours. Batch results were by far less rapid with 46% conversion after the same time of irradiation. This highlights the importance of the reactors dimensions on the rate of the reaction. We then did a kinetic study and proved that intramolecular [2+2] cycloaddition follows first order kinetics whereas pinacolization, the side reaction performed by the sensitizer, follows second order kinetics. However, the kinetics should be further developed as the quantity of DMBP altered significantly the rate of cycloaddition as the latter depends greatly on the sensitization by DMBP. In contrary to our assumption, the acceleration of the cycloaddition reaction led to an increase in the rate of pinacolization reaction. A full study for such a result couldn't be performed as we couldn't purify the cycloadducts due to their limited stability. This problem can be overcome by grafting the benzophenone on SBA-15 (Figure 3.37) or Merrifield to have a solid powder that activates the reaction and can be easily removed by filtration. However, this approach is only limited to batch reactors as flow reactors are not suitable for such conditions. In this section, we successfully used sensitization as a good substitute of using high energy irradiation systems. Its combination with the advantages of flow conditions rendered the usage of concentrated solution of the sensitizer thus accelerating significantly this reaction.

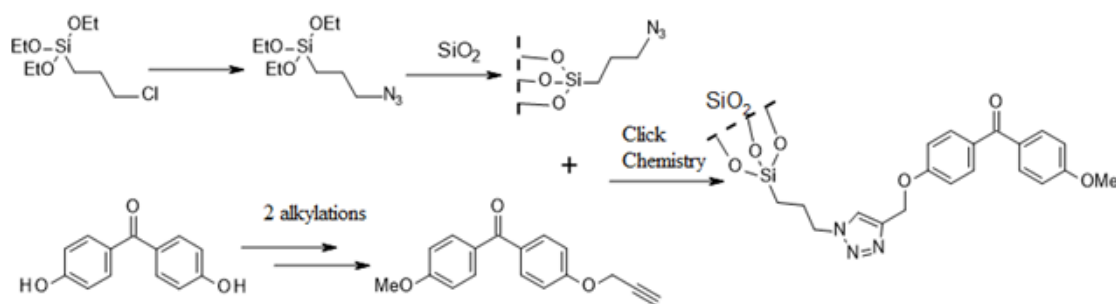


Figure 3.37: Method of preparation of SBA 15 grafted with benzophenone by click chemistry

For the visible region, Ru(bpy)₃Cl₂ was used as a photoredox catalyst for the [2+2] intramolecular cycloaddition of a bisenone **1f** in flow. Though the rate of the reaction was increased by 4 folds, we couldn't get the [2+2] cycloadduct as the major product. The reaction was shown to be guided by two parallel reactions, the major reductive cyclization and the minor [2+2] cycloaddition. Varying the light's intensity, wavelength and the composition of the reaction mixture couldn't improve the rate of the reaction in concern. Since having both products is widely listed in literature but with different catalytic systems, we consider that this reaction might be extremely sensitive to impurities that limits its reproducibility.

CHAPTER FOUR

PHOTO-INDUCED ATRP USING EOSIN Y

4.1 Introduction

A polymerization reaction is considered “living” when the polymer chains are initiated simultaneously and no unwanted side reactions like termination take place [148]. The formed polymer chains are active for successive polymerizations as long as they are supplied with the monomer. In theory, living polymers have a polydispersity index (\bar{D}) of 1.0 as all of the polymers are initiated and undergo the propagation step at the same time and with the same rate. However, such polymers do not exist; there is a continuous progress in the field where a \bar{D} as small as 1.05 is reported [149, 150]. The term living/controlled polymerization corresponds to the polymerization processes whose side reactions are negligible compared to the propagation step and where molecular weight distributions are narrow.

A living polymerization has the following features [151]:

- The kinetics of the reaction are first order with respect to the monomer.
- The % of conversion is directly proportional to the monomer to initiator ratio (known by the degree of polymerization (DP))
- Narrow dispersed polymers are obtained
- The formed polymers continue to be reactivated for further polymerization.

Depending on the nature of the active species, living polymerizations can be classified as ionic and radical polymerizations.

4.2 Ionic Polymerization

4.2.1 Anionic Polymerization

Living anionic polymerization, is the oldest living polymerization method that was discovered by M. Szwarc in 1956 [152]. It takes place when the active intermediate that initiates the polymerization is negatively charged. Typical initiators include sodium in liquid ammonia, Grignard reagents and triphenylmethyl sodium $[(C_6H_5)_3C-Na]$. However, the most commonly used initiator is the alkyllithium reagents like butyl lithium that decomposes into the positively charged lithium ion Li^+ and a negatively charged carbanion. This carbanion will attack a carbon of the $C=C$ of the monomer. This will lead to the movement of the π electrons and settlement on a carbon other than those involved in the $C=C$ thus forming a carbanion which is the initiator of the anionic polymerization (Figure 4.1). Note that monomers having electron withdrawing groups like nitrile ($-CN$) or chloride ($-Cl$), favor this form of polymerization as these groups contribute to the stability of the carbanion formed throughout the polymerization. These monomer include acrylonitrile $[CH_2=C(CN)]$, vinyl chloride $[CH_2=C(Cl)]$, methyl methacrylate $[CH_2=C(CH_3)COOCH_3]$ [153] This form of polymerization yields narrow dispersed polymers (< 1.1). The technique is main method adapted by industry for the production of thermoplastic elastomers [154].

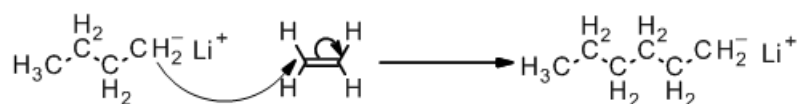


Figure 4.1: Initiation of Anionic Polymerization

4.1.2 Cationic Polymerization

The first report of cationic polymerization was in 1984 by T. Higashimura and coworkers [155]. The active species involved in the initiation step is electron deficient. In general, π electrons of the C=C bond of the monomer attacks this electron deficient species forming the cationic intermediate; this is initiation (Figure 4.2). In the propagation step, the formed cationic active species (carbocation) will then react with another monomer producing another carbocation but with additional monomer unit. The same process is repeated several times along with the increase in the polymer's chain size. The polymerization is terminated when the carbocation reacts with an anion or loses a proton H^+ . Aqueous Aluminum chloride or borontrifluoride are commonly used in cationic polymerizations. They react effectively with monomers having electron donating groups like methyl propylene and phenyl styrene [156].

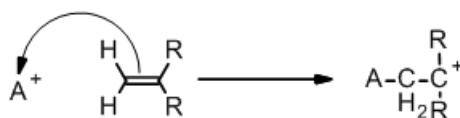


Figure 4.2: Initiation of Cationic Polymerization: A^+ is the active species like aqueous aluminum chloride

4.3 Radical Polymerization

Ionic polymerizations, though powerful, can be used for limited types of monomers under specific reaction conditions; working using protic solvents or polar functional groups leads to side reactions. These limitations for this technique favored the development of radical polymerization which involves the formation of a radical initiator [157].

Controlled/living radical polymerization (CRP) led to a phenomenal boost in the classical polymer science by enabling the synthesis of polymers of definite molar masses,

low distributions, diverse composition and various architectures [158]. It has provided the possibility to incorporate a wide variety of functional groups into polymers that acquired new properties rendering their usage in novel applications like nanotechnology, biomedicine, energy and defense. CRP counts for 40-45% of the total synthetic polymers produced [159]. This is due to the high reactivity of the radical, the compatibility with a wide range of monomers with polar functional groups and polar solvents including water [160].

The formation of the radical initiator in CRP can be induced thermally or photochemically. The formed radical will form a bond with one of the carbon atoms of the monomer's C=C thus transferring one of the π electrons to a carbon other than the carbon atoms initially involved with the double bond. The formed radical having the initiator and a monomer unit is the active radical intermediate.

The active chain ends of the polymers formed by radical polymerization can undergo termination by binding to each other or by disproportionation. This establishes a difficulty in controlling the molecular masses of the formed polymers that can end up to be polydisperse. Such undesired terminations can be eliminated by transforming these active species, temporarily, into dormant inactive species. Having a dynamic equilibrium between active/dormant species ensures that only a small quantity of the polymer is active at a very short period of time, thus limiting the possibility of having undesired termination processes [150, 161].

CRPs that have been widely used include nitroxide-mediated radical polymerization (NMP) [162, 163], atom-transfer radical polymerization (ATRP) [150, 161, 164, 165], and reversible addition-fragmentation chain transfer radical polymerization (RAFT) [166-168]

4.3.1 Nitroxide Mediated CRP

In 1980, nitroxides, stable free radicals, were used to control the free radical polymerization [169]. Such polymerizations involve the interaction between transient radicals and persistent (stable) radicals. Dormant adducts result from the combination of the stable and the reactive transient radicals. In the dormant state, neither of the two radical species can interact with other radicals. However, the dissociation of this adduct can be controlled leading to the liberation of both radical species. The transient radical will then combine to one of the monomers forming the radical active intermediate. This is followed by successive addition of the monomer to the end of the polymer chain that ends up to be a growing transient radical. When the concentration of the stable radical is high, it will react with the transient radical thus deactivating any further addition. This capping will lead to the transfer of the polymer into the dormant phase so the concentration of the transient radical will decrease making it less likely to undergo termination. In this case, living free radical polymerization was established [162].

This form of controlled polymerization involves nitroxides as initiators without the need of a catalyst. The most commonly used are those which are 2,2,6,6-tetramethylpiperidiny-1-oxyl (TEMPO) based [162, 163]. This initiator will decompose thermally at the C-O bond into two radicals (Figure 4.3). The nitroxide radical is more stable making it the persistent radical. The other transient and highly reactive vinylic radical that is released will react with monomers like styrenes, acrylamides and methacrylates and contribute to the propagation process. An alternation of dissociation and capping will take place between the stable nitroxide radical and the transient radical at the polymer's end resulting in the control of this free radical polymerization. As a result, molecular weights of low dispersity are obtained [162, 163]. Other than monomers, this technique was also reported to be efficient for co-polymerization to form block copolymers[170]

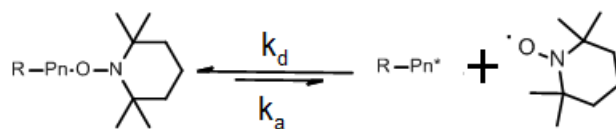


Figure 4.3: Nitroxide Mediated CRP

4.3.2 Reversible Addition-Fragmentation Transfer Polymerization (RAFT)/ Macromolecular Design via the Interchange of Xanthates (MADIX)

E. Rizzardo and G. Moad introduced RAFT in 1988 [166]. During the same period, Zard's group developed MADIX [171]. Both RAFT and MADIX follow the same mechanism. However, MADIX solely refers to the use of xanthates, whereas RAFT covers thiocarbonyl thio compounds in general (Figure 4.4)[172]

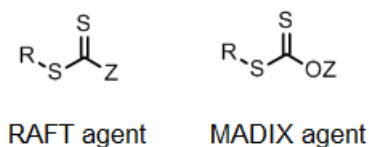


Figure 4.4: RAFT and MADIX agents

During the reaction, a radical initiator (like AIBN) will decompose to form a radical that will attack a monomer including carboxylic acids, amides and tertiary amines to form a radical propagating species. The RAFT/MADIX agent will add to this species to form a RAFT/MADIX radical adduct. This adduct will dissociate into a new active radical and a dormant polymer- thiocarbonyl thio species. If the liberated active species is $R\bullet$, it will start a new polymer chain. However if it is the polymer chain $Pn\bullet$, the latter will continue growing. The homogeneous growth of the polymers is provided by the rapid transfer of the RAFT/MADIX agent between the different dormant and active radical species (Figure 4.5) [168, 172, 173].

The RAFT/MADIX agent (X) should be chosen in a way that the exchange reaction is much faster than the propagation reaction. The best conditions having the optimum initiator and RAFT/MADIX agent favors the formation of polymers of well-controlled masses and dispersity [166-168, 173]

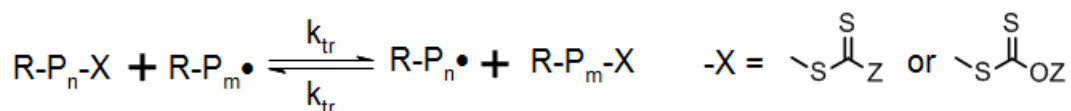


Figure 4.5: RAFT/MADIX Polymerization

4.3.3 Atom Transfer Radical Polymerization (ATRP)

ATRP, the topic of our work, is one of the most developing areas in polymer chemistry with more than 11 000 papers published between 1995 and 2011 [150]. It proceeds by a mechanism similar to that of nitroxide mediated CRP involving transient and active radicals. It was first described by 2 independent groups in 1995 [164, 165] showing an elevated level of control of molecular weights that exhibit very narrow distributions. Usually, ATRP requires the presence of a transition metal ligand complex that undergoes oxidation followed by the extraction of a single electron from an alkyl halide initiator (dormant species) forming a highly reactive organic radical (transient species). This will lead to the propagation of this radical with the unsaturated monomer present. The control of the length of the polymer chain is established when the polymer transient radical abstract the halide back from the metal leading to the formation of a dormant polymer [161] .

The general mechanism of ATRP is represented in Figure 4.6. Note that this mechanism is the same regardless of the method of activation [150, 161, 174].

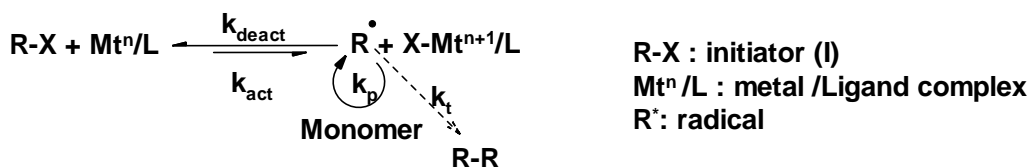


Figure 4.6: Mechanism of ATRP

Alkyl halides are used as the initiators or dormant species and the control is achieved by metal catalyzed activation/deactivation cycle. The transition metal/Ligand of low oxidation state (activator) interacts with the alkyl halide to generate the alkyl radical by homolytic cleavage and the oxidized transition metal/Ligand (deactivator). This process takes place with a rate constant k_{act} which is by far less than that of the deactivation process k_{deact} . The small quantities of the active radical succeed to attack the unsaturated polymer and undergo chain propagation in the same manner as that of classical radical polymerization with rate constant k_p . This takes place before the high oxidation state metal complex deactivates the alkyl radical to reform the dormant alkyl halide and the activator. Though negligible, termination by coupling or disproportionation also occurs with rate constant k_t . When termination or other side reactions take place, the quantities of the metal/ligand increase leading to shifting towards the deactivation process. Repeating the activation/ deactivation cycles for all dormant species allows the uniform growth of all polymer chains. This autoregulation system ensures the living nature of ATRP.

The key reaction which is the reason behind giving ATRP its name is the atom (halogen) transfer that is responsible for the homogeneous growth of the polymer chains. This is obtained by the fast initiation and the rapid deactivation process. As a result, ATRP provides linear relationship between the degree of conversion and the mass of the polymer obtained.

4.4 Characterization of Polymers

4.4.1 Degree of Conversion

The first important factor that polymer chemists focus on is determining the amount of the monomers that have actually undergone ATRP. Having high % of conversion within small reaction times continues to be of great interest due to the energy and time saving that it provides. The degree of conversion can be determined gravimetrically or by ^1H NMR spectroscopy. A detailed explanation of this part is found in the experimental section.

4.4.2 Kinetics

The plot of $\ln([M]_0/[M])$ vs. time will give a linear curve whose slope is k_p . If the curve is not linear, this indicates the occurrence of termination so that the value of $[R^*]$ is changing with time. Having a linear plot shows that the polymerization performed is well controlled.

[161]

4.4.3 Molecular Weight

Another important factor for polymers is the molecular weight. For a controlled polymerization, M_n of the formed polymers should increase linearly with the increase in the degree of conversion. $M_{n,th} = M_{monomer} \times \text{conversion} \times DP$ [161].

This factor is linked to many physical properties like transition temperatures of the different stages (liquid, wax, rubber & solid) and mechanical properties like strength, viscosity, viscoelasticity [175] There are various types of molecular weight averages that can be calculated for polymers. In this work, we shall focus on the types of averages that can give an indication about the dispersity of the polymer. They are the number-average molecular weight M_n and mass average molecular weight M_w .

4.4.3.1 Number average molecular weight M_n

Number average molecular weight (M_n) follows the conventional definition of average value. It is the ratio of the total weight of the polymer to the number of polymer molecules. These possible molecular masses of the polymers are designated by M_i . N_i is the number of the polymer molecules whose masses are M_i . So the total mass of the polymers will be $N_i \times M_i$. Thus the number average molecular mass M_n is as indicated in Equation 4.1 [176-178]

$$\overline{M}_n = \frac{\sum_{i=1}^{\infty} N_i M_i}{\sum_{i=1}^{\infty} N_i} = \frac{\text{Total weight}}{\text{Number of Polymers}} \quad \text{Equation 4.1}$$

4.4.3.2 Weight average molecular weight M_w

Weight Average Molecular Weight depends on the mass or the size of the polymers along with their number (Equation 4.2). In this case, the number of molecules N_i which is found in the previous equation is replaced by weight $w_i = N_i \times M_i$ [176-178].

$$\overline{M}_w = \frac{\sum_{i=1}^{\infty} N_i M_i^2}{\sum_{i=1}^{\infty} N_i M_i} \quad \text{Equation 4.2}$$

M_w , is highly affected by the large molecules that contribute greatly to its value due to the square function in its formula. So the M_w is sensitive to changes in the number of large molecules more than that of small molecules. In contrary, low mass polymers contribute greatly to M_n because for small molecules, a certain mass includes a large number of molecules.

4.4.3.3 Polydispersity index (\overline{D})

Another important challenge the polymer chemists continue to work on is having polymers that include molecules of masses of similar and ideally identical values. This can be represented by the weight distribution plot. The more broad the plot is, the more disperse

is the polymer and vice versa. For cases like ATRP where in theory all of the molecules start propagation at the same time in the same rate, the distribution is too steep that the values of the average molecular weights M_n and M_w are almost identical.

Scientists utilize the “polydispersity index” as a method of determining the homogeneity of the fabricated polymers. It measures the width of the weight distribution by dividing the weight average molecular weight over the number average molecular weight (Equation 4.3). The minimum value of this index is 1 where $M_n = M_w$ (ideal case). In ATRP values of \mathcal{D} as small as 1.05 were obtained confirming the control aspect of this polymerization [149, 150].

$$\mathcal{D} = \frac{M_w}{M_n} \quad \text{Equation 4.3}$$

Note that M_n , M_w and \mathcal{D} can be determined using Gel Permeation Chromatography (GPC) [179]. This method requires a calibration by standard polymers of known molecular weights. The retention time of the polymer will be compared to that of the standards in order to determine the M_n , M_w and \mathcal{D} . 2D NMR is also used to determine M_w [180] and ^1H NMR for M_n [177].

Calculating the mass of the polymer based on its diffusion (D) is due to the Stokes–Einstein equation for spherical particles of radius R_H (Equation 4.4)[181]

$$D = \frac{kT}{6\pi\eta R_H} \quad \text{Equation 4.4}$$

Where k is the Boltzmann constant, T is the absolute temperature, and η is the solvent viscosity. On the basis of Equation 4.4, for monodispersed polymers, D can be correlated to molar mass M (Equation 4.5) [180].

$$D = AM^\alpha \quad \text{Equation 4.5}$$

Where A and α are constants that correlates to different polymers. The logarithm of Equation 4.5 will give a linearized form (Equation 4.6).

$$\log D = \alpha \log M + \log A$$

Equation 4.6

Running different standards of known M_w on DOSY NMR will provide their corresponding diffusion constants D . These values will be used to plot a calibration curve $\log D$ vs. $\log M_w$ that the reference for the determination of the M_w of the polymers by DOSY NMR.

4.4.4 Tacticity

For polymers, various configurations can contribute greatly to the physical properties of the polymer [182]. Vinyl monomers with different substitutions will give rise to various possible arrangements of atoms i.e. structures. There are three possible arrangements (positional isomers) of propene monomers, like Methyl Methacrylate (MMA) upon polymerization (Figure 4.7).

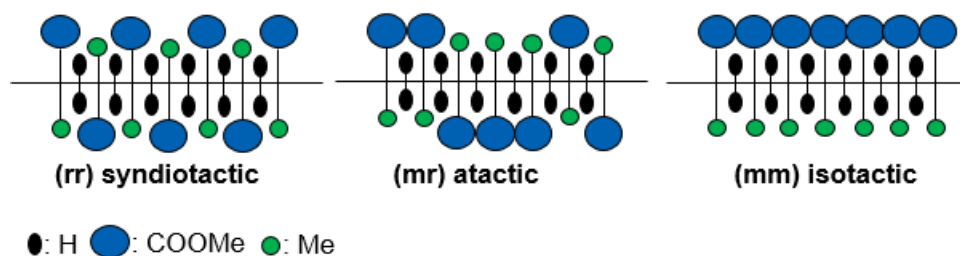


Figure 4.7: The three possible arrangements in PMMA

The polymer is said to be isotactic (mm) when all of the methyl groups are on the same side (in front or behind) with respect to the backbone. If the methyl groups alternate regularly along the chain, then the polymer is said to be syndiotactic (rr). Finally, irregular arrangement of the orientation of the methyl groups gives atactic polymers (mr). The tacticity of the polymer has significant effect on its physical properties like the glass transition temperature [183, 184].

For example the melting point of isotactic polypropylene is 160-170 °C. This temperature drops by around 30°C for syndiotactic polypropylene. However atactic polypropylene's melting point drops till below 0 °C. In addition, there is a remarkable difference in the mechanical nature of these different isomers. Isotactic polypropylene is hard with great resistance to stress whereas atactic polypropylene is soft and rubbery. This can have a great impact of the industrial usage of these different stereoisomers of the same polymer [182, 185]

The tacticity of a polymer can be easily determined using the comparison of the ^1H NMR of a synthesized polymer to those of standards of the same polymer but with the three different configurations (Figure 4.8). In addition, a lot of research focused on the tacticity of polymers like PMMA and the spectra of these configurations are described in literature [186, 187].

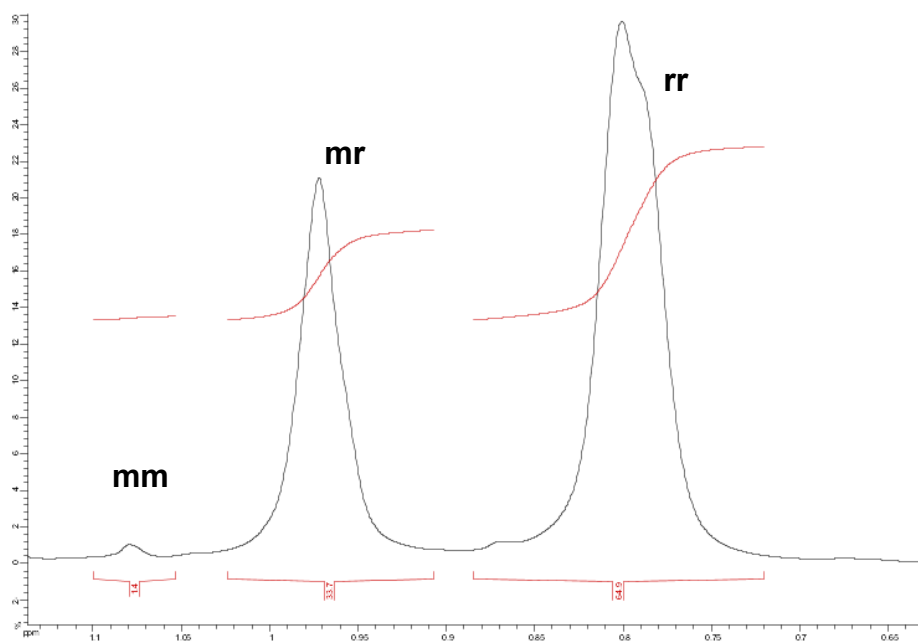


Figure 4.8: Determination of the three triads by ^1H NMR, peak at 1.02 ppm corresponds to mm configuration, at 0.97 ppm to mr and at 0.8 ppm to rr configuration of PMMA.

4.5 Components of ATRP

ATRP is a multicomponent system composed of a monomer, alkyl halogen initiator and a transition metal catalyst with a ligand. Depending on the method of induction, the temperature or the characteristics of the light source should also be taken into consideration.

4.5.1 Monomers

Similar to any free radical polymerization, ATRP acts on unsaturated monomers like styrenes, (meth) acrylates, (meth) acrylamides, and acrylonitrile (Figure 4.9). These monomers have substituents that stabilize the formed radical. Note that these monomers don't behave in the same aspect in ATRP and each has its own equilibrium constants k_{act} and k_{deact} constants [151][161].

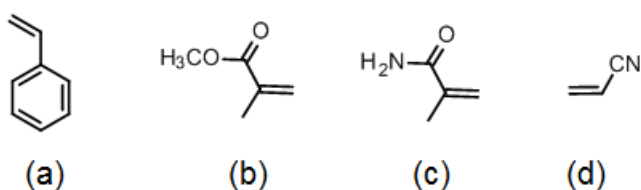


Figure 4.9: Structures of common ATRP initiators. (a): styrene, (b): Methyl methacrylate, (c): Methyl acrylamide, (d): acrylonitrile.

4.5.2 Initiators

In ATRP, the initiator has an important role in determining the mass of the polymer to be formed. If the initiation step is fast along with negligible termination, theoretically, the number of the polymer chains will be equal to that of the added initiator. As a result, the theoretical molecular weight and the degree of polymerization are inversely proportional to the concentration of the initiator. Alkyl halides are mainly used in ATRP as initiators for the halide group to migrate between the metal complex and the growing chain during the

activation and deactivation processes. Alkyl halides with activating groups like carbonyl, aryl and allyl are good candidates since the activation rate depends on the initiator's structure. Figure 4.10 shows the activities of various alkyl halides used as initiators. For having narrow polydispersity, k_{act} of the initiator should be more than the rate of propagation [150, 151, 161, 188, 189].

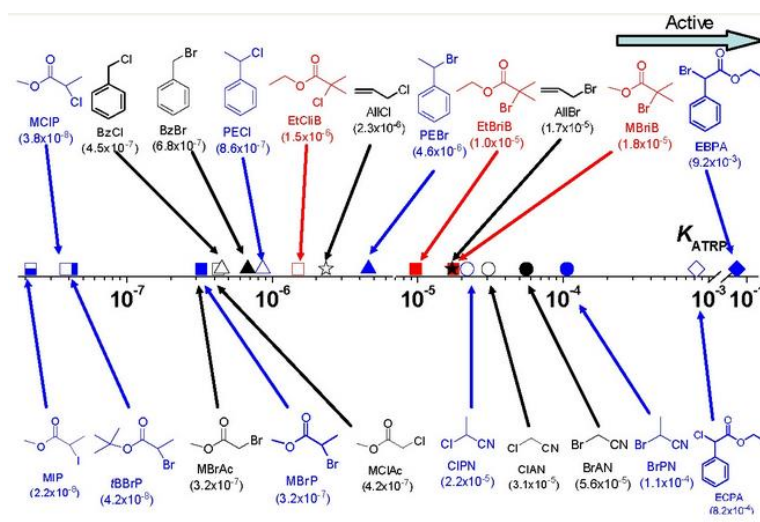


Figure 4.10: Activities of various alkyl halide initiators used in ATRP [150]

4.5.3 Catalysts

The most important feature in ATRP is the catalyst as it regulates the position of the equilibrium between the dormant and the active radical states. An efficient catalyst should meet the following points [150, 161, 190]:

- Initiation should be much more rapid than propagation so that the polymerization of all of the chains start at the same time.
- The equilibrium between the dormant and the active radical species should be strongly shifted toward the dormant side. This is to prevent the presence of elevated levels of the active radical thus leading to termination.

- The process by which the halogen is transferred to the active radical to deactivate it should be rapid enough to ensure the homogeneity of the growth rate of polymers.
- Any side reactions like oxidation, reduction or H abstraction of the radical should be limited.

So the metal component of the catalyst should have the following points:

- The transition metal should have two oxidation states with a difference of 1 electron.
- The metal should have an affinity towards halogens.
- The ligand and the metal should exhibit strong interactions.
- The halogen should be able to fit within the coordination sphere surrounding the metal.

The choice of the organic component of the catalyst, the ligands is of great importance.

The role of the ligand is to solubilize the metal catalyst in the reaction mixture in addition to its involvement in regulating the redox potential of the catalyst [161, 191].

4.6 Limitations of ATRP

Monomers with ionic or carboxylic acid groups are not favored in ATRP as they react with the catalyst thus altering the equilibrium [192]. However, the main limitation in ATRP is the usage of the metal catalyst/ligand complex that is hard to be removed. Such catalytic systems, if not removed, induce aging of the polymer along with the significant toxicological problem. There are several methods for the removal of the catalyst like passing over alumina or immobilizing the catalyst. The latter can show limitation in the control of the polymerization process [193].

4.7 Photoinduced ATRP

CRP can be externally switchable/regulated [194, 195]. There are various stimuli for CRP like heat [161], applied voltage [196, 197], mechanical force [198, 199] and light [200, 201]. The photochemical stimulus has been widely used for radical polymerization for the synthesis of coatings, resins, adhesives, microelectronics and for photolithography [160, 202-205]. However, most of the commonly used photopolymerizations are neither photo-switchable nor “living” [195]. The pioneering work done by Otsu and coworkers was the first successful attempt of photoinduced CRP. Using dithiocarbonate, the group was capable of forming polymers whose molar masses increase linearly with the monomer conversion [201].

Photoinduced CRP enables to work under mild thermal conditions to generate the initiating radical, activate the catalyst and to reinitiate polymer chains over several cycles.

In the recent years, efficient strategies of photocontrolled living radical polymerizations were reported. These strategies resemble the well-known thermal CRP methods like NMP, RAFT and ATRP. Though these methods are relatively new, the field of photoinduced CRP is growing and developing rapidly [160, 195, 206, 207]. The section below summarizes the different methods reported on the photo-induced ATRP.

The mechanism of photo-induced ATRP is the same as that described above in section 4.3.3. The most common catalysts for photo-induced ATRP are Cu(I)/L and X-Cu(II)/L complexes that act as activators and deactivators respectively [160].

However, there are additional photo-induced ATRP techniques that are not used in the conventional thermal ATRP like those that start with the transition metal of the higher oxidation state, X-Cu(II)/L , in order to control the oxidation of the activator [208, 209]. The disadvantage of such techniques is the use of high catalyst loading to maintain the controlled aspect of ATRP. Regenerating the activator during ATRP by an in situ reduction

of the deactivator can decrease the catalyst loading into 100 ppm [206, 209, 210]. The reduction of the deactivator is feasible by adding organic reducing agents, introducing an external radical initiator, applying a cathodic current or via irradiation with light [211-214].

Photoinduced ATRP can be classified based on the primary photochemical process: photoinitiated and photoredox ATRP. The former involves the homolytic cleavage of a photoinitiator whereas the latter sponsors an electron transfer reaction that either generates the activator or establishes the ATRP equilibrium [195].

In photoinitiated ATRP, photoinitiators undergo in situ photo-cleavage using UV/Vis irradiation that generates free radicals. These radicals reduce the deactivator Cu(II)/L to Cu(I)/L. Photoinitiators like benzophenone (BP), and (2,4,6-trimethylbenzoyl) diphenylphosphine oxide (TMDPO) were used for UV initiated ATRP of MMA. Without the need of an alkyl halide initiator, the UV photolysis of BP and TMDPO formed radicals that played a dual role as initiators for polymerization and reducing agents for the deactivator Cu(II)/PMDETA [215, 216].

Eosin Y, erythrosin B and Irgacure 819 were also reported to be used as visible light photoinitiators. However, the experimental average molecular masses M_n for Eosin Y and Erythrosin B sensitized ATRP were much higher than the theoretical values distributions ranging between 1.28–1.6. Polymers with molecular weights that are compatible with the expected values and with narrow dispersities ($\bar{D} \approx 1.11$ –1.18) were obtained by the Irgacure 819 system [217-219].

4.7.1 ATRP by Photoredox Catalysis

4.7.1.1 Copper mediated

In photoredox mediated ATRP, the single electron transfer reaction is the key process. Following excitation by irradiation, the excited photocatalyst can undergo oxidative or

reductive quenching that results in the SET to the alkyl halide thus generating the alkyl radical. The alkyl radical will add to a monomer and propagation takes place. The exact mechanism of photoredox ATRP and the regeneration of the photocatalyst at its initial state depends on the catalytic system. The advantage of this process is that the photocatalyst is the only reagent that should absorb light. The initiator or the polymer don't need to be incorporated by a photochromic group. Efficient photocatalyst should have a long lived excited state to ensure efficient SET like Ir(ppy)₃, $\tau = 1900$ ns, and Ru(bipy)₃²⁺, $\tau = 900$ ns [21]. The control of ATRP is established by efficient reversible activation/deactivation processes that involve the alkyl and halide radicals without the need of adding additional radical sources. The system is light switchable: in the absence of light, the alkyl and halide radicals combine to form the dormant species. The re-exposure to light leads to the regeneration of the radicals (active species)

Matyjaszewski and co-workers reported visible/sunlight mediated ATRP using Cu(II)Br₂/L; following absorption of irradiation, the LMCT in the photoexcited state of Cu(II)Br₂/L will lead to its reduction to the corresponding Cu(I)Br/L. In that study TPMA and tris((4-methoxy-3,5-dimethylpyridin-2-yl)amine) (TPMA*) were utilized as ligands [220].

Later, the aliphatic tertiary amine tris[2-(dimethylamino)-ethyl]amine (Me₆TREN) was used as a ligand for Cu-mediated photo-ATRP by Haddleton and co-workers [221]. Monomer conversion of (>95%) was obtained, affording poly(acrylates) with dispersities as low as 1.05 and over 99% end-group fidelity.

Poly and Lalevée and co-workers reported a copper-based catalyst, bis(1,10-phenanthroline)-copper(I) (Cu(phen)₂⁺), that performed photoredox ATRP using a household blue LED [222]. Using ethyl α -bromophenylacetate (EBPA) as the initiator and

a low catalyst loading (80 ppm), good control over the polymerization of MMA in dimethylformamide (DMF) was observed.

The proposed mechanism involved the oxidative quenching of $\text{Cu(I)}^*/\text{L}$ following excitation resulting in the formation of Cu(II)-Br/L and a propagating radical. To regenerate the Cu(I) /L , triethylamine (TEA) was added to accelerate the reduction of Cu(II)/L as it acts as an electron donor.

4.7.1.2 Other metals mediated

The development in the photoredox catalysis in organic chemistry inspired the usage of multiple photocatalyst/ligand systems for photoredox ATRP. Few examples of some of the metal based catalysts are listed below.

$\text{Ru(bpy)}_3\text{Cl}_2$ was assessed for the photopolymerization of various methacrylates. Though the catalyst succeeded in performing radical polymerization, the D values were relatively large (≈ 2) and irradiation using blue LEDs for 20 h gave a polymerization of 76% [223].

In 2012, Fors and Hawker reported the first example of using (*fac*- $[\text{Ir(ppy)}_3]$) to conduct photo-CRP of methacrylates [16]. The proposed mechanism was similar to that of Cu(I) /L that involves the oxidative quenching of photoexcited Ir(III)^* . The latter reduces R-Br initiator to produce an alkyl radical, thereby initiating polymerization. The formed highly oxidizing Ir(IV) complex reacts with the propagating radical to regenerate Ir(III) . Irradiation On/off experiments proved the livingness of the polymerization of MMA as the reaction ceased and restarted in response to the absence and presence of light. Moreover, a formed PMMA polymer was successfully used as a macroinitiator for the polymerization of benzyl methacrylate (BnMA) monomer.

Iron has also been studied as a catalyst in ATRP. The last article published by Matyjaszewski and co-workers reported Fe-based photoredox ATRP of methacrylic monomers without the presence of additional ligands. The masses of the formed polymers were in accordance with the theoretical values and the dispersity index of polymer was as low as 1.15 [224]

Digold bis(diphenylphosphino)methane dichloride ($[\text{Au}_2(\mu\text{-dppm})_2]\text{Cl}_2$) was able to catalyze photo-CRP of various (meth)acrylates but with poor control that is attributed to the inefficient deactivation of propagating radicals by $\text{Au}_2(\text{III})$ complexes [225].

4.7.1.3 Metal-Free Photoredox Catalysis

The metal free radical polymerizations are already known and used since decades like the usage of BP in photoinitiated ATRP [216]. However, stoichiometric quantities are needed of such photoinitiators to produce the polymers. Though efficient, organometallic photoredox catalysts exhibit elevated prices and toxicity profiles that limit their usage on the larger scale. Metal free catalysts like fluorescein and xanthene dyes have been successfully applied to photoredox reactions like radical substitutions at α -amino and β -carbonyl moieties [146]. Similar relatively environmentally benign organic photocatalysts are now being employed in CRP after their huge success in organic synthesis as they outperformed organometallic and inorganic catalysts in some cases [226-228].

Hawker, Fors, and co-workers reported the first example of “metal-free ATRP” that was catalyzed by an organic photocatalyst using 380 nm irradiation at room temperature [229]. A commercially available 10-methylphenothiazine (Me-PTH) was first tested; broad dispersity was observed due to catalyst decomposition. A nitrogen substituent was added to the phenothiazine ring to stabilize PTH. The high reduction potential of PTH, which surpassed that of $\text{Ir}(\text{ppy})_3$ led to the formation of highly controlled polymers with

well-defined masses. The system is suitable for various functional groups as the polymerization of N,N-dimethylaminoethyl acrylamide (DMAEMA) using 0.1 mol % PTH provided polymers of narrower dispersity compared to the system with 0.005 mol % Ir(ppy)₃ ($\bar{M}_w = 1.11$ vs 3.69).

Similarly, Miyake and Theriot reported another example of metal-free photo-CRP of MMA involving perylene as a photoredox catalyst [230]

Fluorescein (FL) was used as the organic photocatalyst for the ATRP of MMA under blue light irradiation. Following ten hours of irradiation in batch, 90 % conversion and PMMA of \bar{M}_w 1.5 were obtained [231].

4.8 Continuous -Flow Photopolymerization

Photo-induced ATRP is difficult to scale as a larger reaction requires stronger irradiation systems to maintain the same reaction conditions. Moreover, working with bigger systems will face a difficulty in having uniform irradiation [232]. Similar to any photochemical reaction, light intensity has a critical importance and was shown to have significant impact on molecular weight and \bar{M}_w [195]. This urges the need for a new system for different reaction scales to ensure homogeneous and sufficient irradiation. To address this challenge, researchers have utilized continuous-flow technology for photo-CRP

One of the first ATRP attempts in flow did a comparison between the thermal and photopolymerization of butyl acrylate in continuous flow [233]. The latter was performed under UV using 2,2-dimethoxy-2 phenylacetophenone as photoinitiator. The photopolymerization surpassed the thermal polymerization as 38 s were enough to have 81% conversion with a \bar{M}_w of 2.03 compared to thermal polymerization that gave after 120 s, 86% conversion with a broad polymer of \bar{M}_w 3.59.

The photopolymerization of MA using copper as a photoredox catalyst was performed in continuous flow by Junkers and co-workers [234]. They compared the performance of a PFA milliscale tubular reactor with a glass-chip microreactor. Much faster conversions (90 % 20 min) along with controlled polymerizations were achieved. Poly MA was then used as a macroinitiator for polymerization of Butyl acrylate (nBA) in flow to give a copolymer of $\bar{D} = 1.16$.

Later, continuous flow was used for the cobalt mediated polymerization of vinyl acetate (VAc) under UV irradiation by Detrembleur, Junkers, and co-workers [235]. In comparison to batch conditions, a faster polymerization was achieved in the flow. However, the polymerization lost its controlled nature after 53% conversion.

Recently, Hawker, Poelma, and coworkers reported the continuous-flow synthesis of poly(MMA) using their Ir catalyzed photoredox CRP irradiated by 380 nm irradiation. First-order kinetics were observed under both batch and flow conditions. Compared with batch, the rate increased by at least by 50% giving 42% of polymerization and 1.21 \bar{D} after 220 minutes [236].

4.9 Eosin Y

The section below provides some of the properties and the applications of eosin Y, which is used in this work, as a photoredox catalyst.

Eosin Y is the 2',4',5',7'-tetrabromo derivative of fluorescein (Figure 4.11). This classic dye is known for a long time and has been used in cell staining [237], lip sticks [238], as pH indicator [239] and an indicator for the analytical determination of halides [240].

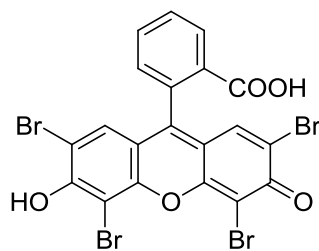


Figure 4.11: Structure of Eosin Y

Visible light irradiation excites the eosin Y to its singlet excited state. The excited eosin Y undergoes rapid intersystem crossing to the lowest triplet state. This state has a relatively long life span of 24 μs [241, 242] rendering it suitable for photoredox catalysis. Eosin Y exhibits maximum absorption at 539 nm with a molar extinction coefficient $\epsilon = 60\,803\text{ M}^{-1}\text{ cm}^{-1}$ [147]. In our case the, since the green LEDs used emit at 530 nm, we found that the molar extinction coefficient $\epsilon_{530} = 54052\text{ M}^{-1}\text{ cm}^{-1}$ (Figure 4.12) which is in accordance with literature values.

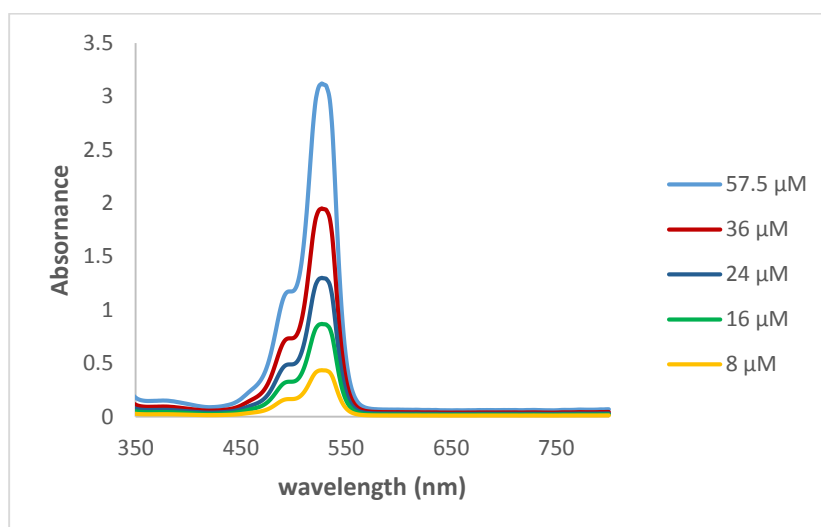


Figure 4.12: Absorption spectra of Eosin Y at different concentrations

The excited eosin Y is more oxidizing or reducing than the ground state eosin Y. The estimated excited state oxidation and reduction potentials along with the measured redox potential values of the ground state [243, 244] are given in Figure 4.13.

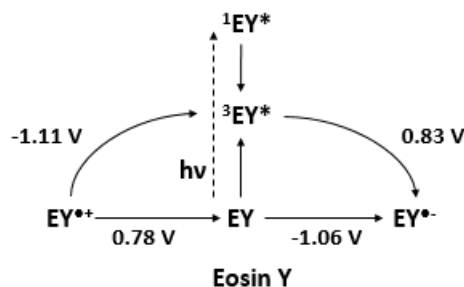


Figure 4.13: The redox potentials of Eosin Y in the ground and excited states

Eosin Y has been extensively used in organic synthesis for reactions like reduction [127], oxidation [147][245] and generation of aryl radicals [246]. It has also been used as a visible light photoredox catalyst in flow for the oxidation of thiols [63], α -trifluoromethylation of ketones [247], reductive dehalogenation of α -bromoacetophenone [248] and in dual catalysis with imidazolidinone for the enantioselective α -alkylation of aldehydes [247]. In all of these cases eosin Y has shown to be an effective photoredox catalyst that in some cases outperforms even the metal based catalysts [63].

4.10 Plan of Work

The aim of this part is to utilize a metal free catalyst (eosin Y) that absorbs in the green region as a photocatalyst for the polymerization of MMA. Such a photocatalyst can be easily removed by washing with water, less toxic than classical metal based catalysts and more cost effective (13 euros /g eosin Y, vs. 1160 euros /g iridium catalyst, Sigma Aldrich ®). Not to mention the usage of visible light instead of UV irradiation where the former is cheaper and easier to apply. We intend to accelerate the polymerization reaction that usually takes around 10 hours to get high % of conversion by switching to the continuous flow technology that provides higher photon flux to the reaction mixture and thus increases the rate of the reaction.

We shall characterize the polymers formed by such a system and determine whether such an assembly succeeds to support the well-controlled feature of ATRP or not.

4.11 Results and Discussion

4.11.1 Batch vs. flow

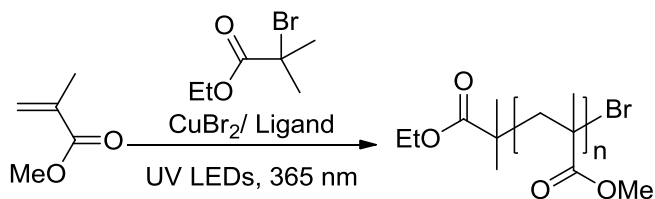


Figure 4.14: Cu II/Ligand mediated ATRP of MMA

The first part of this work was to determine the impact of switching from batch to flow on the rate of metal catalyzed ATRP (Figure 4.14). The polymerization of MMA with CuBr₂/Ligand was performed using UV, white and green LEDs at room temperature. In a typical procedure, the reaction mixture containing the monomer (methyl methacrylate, MMA), copper bromide (CuBr₂), ligand (N,N,N',N'',N'''-pentamethyldiethylenetriamine, PMDETA or Tris(2-pyridylmethyl)amine TPMA) and the initiator (ethyl 2-bromoisobutyrate, EBiB) were dissolved in a DMF–methanol (1 : 0.5, v/v) mixture under an argon atmosphere at a ratio of [MMA] : [EBiB] : [CuBr₂] : [PMDETA] (100 : 1 : 0.1 : 0.3). For batch conditions, the reaction vial was irradiated for 5 h and the obtained polymer was immediately isolated and then analyzed. As for the flow conditions, the reaction mixture after being degassed is transferred into a syringe that will pump the reaction mixture into the FEP tubing reactor (i.d. 800 μm) that is illuminated by a LED system. A sample of the collected solution is used for ¹H NMR and the formed polymer was then precipitated, dried and analyzed. Table 4.1 includes the results of the Cu catalyzed photopolymerization under different conditions. In the first experiment (entry 1) white LEDs were used. In entry 2 eosin

Y (0.1 eq) was also added in order to irradiate by green LEDs as eosin Y has its λ max at 539 nm. Starting from entry 4, UV LEDs of 365 nm were used. The impact of the ligand on polymerization was studied in entries 4-7 by changing the Ligand (PMDETA vs TPMA) and its quantity (0.3 eq vs. 1 eq). In entry 8 the irradiance of the light source was decreased to 90 mW.cm⁻² instead of 230 mW.cm⁻² that was used in all of the other UV reactions (entries 3-7).

In entries 1 and 2 where the LEDs used are white and green respectively, no polymerization was achieved. However when irradiating by UV LEDs, this procedure resulted in poly(methyl methacrylate) (PMMA) with a narrow dispersity (1.47) that was determined by gel permeation chromatography (entry 3). The monomer conversion after 5 h was 60%. This shows that the Cu(II)/PMDETA complex doesn't absorb in the visible region, or the absorption is not enough to initiate the catalytic cycle for the polymerization. A study, however, reported forming PMMA following the same conditions but with SKYWHITE fluorescent lamp [249]. The emission spectra of this lamp includes strong emissions in the UV region that we assume to be the active portion of the lamp's emission [248]. This explains the reason behind the difference between this work and their work. The white LEDs emit only in the visible region and the green LEDs emit at $\lambda \approx 530$ nm so they don't possess the energy needed for the activation of the Cu(II)/Ligand complex.

Table 4.1: Cu-catalyzed ATRP in batch and flow conditions. a: white LEDs, b: Green LEDs, c: UV LEDs 200 mW.cm⁻², d: UV LEDs 85 mW.cm⁻², e: [MMA]: [EBiB] : [CuBr₂] : [Ligand]:[Eosin Y], f: determined by ¹H NMR, g: Determined by GPC

Entry	Ligand	Composition ^e	Case	% Conv ^f	Time	Đ ^g
1 ^a	PMDETA	100:1:0.1:0.3	batch	---	5 hrs.	
2 ^b	PMDETA	100:1:0.1:0.3:0.1	batch	----	5 hrs.	
3 ^c	PMDETA	100:1:0.1:0.3	batch	60	5 hrs.	1.47
4 ^c	PMDETA	100:1:0.1:0.3	flow	46	45 min	1.33
5 ^c	PMDETA	100:1:0.1:1	flow	56	45 min	1.3
6 ^c	TPMA	100:1:0.1:0.3	flow	60	45 min	1.28
7 ^c	TPMA	100:1:0.1:1	flow	64	45 min	1.21
8 ^d	TPMA	100:1:0.1:1	flow	25	45 min	1.55

For the flow conditions, the reaction mixture was transferred into a syringe and was injected inside the FEP tubing reactor (800 μm, 2.24 mL) at a flow rate 50 μL.min⁻¹ that corresponds to 45 min of irradiation with UV LEDs. Using the same conditions as Entry 3 but switching to continuous flow (entry 4) was enough to attain 46% conversion and a better Đ value (1.33) though the irradiation time is decreased by around 6.5 folds. Increasing the ratio of the added ligand PMDETA from 0.3 to 1 resulted in higher monomer conversion and higher M_n (56%) and a slightly improved dispersity (entry 5). This is in accordance with literature as the primary role of the ligand is to solubilize the transition metal salts. Increasing the quantity of the ligand will therefore increase the availability of the catalyst and thus improve the ATRP process [161]. Replacing the ligand PMDETA by TPMA had also a positive impact on the degree of polymerization and the dispersity of the formed polymer (entry 6, Đ = 1.28). This is because TPMA is considered to be one of the best ligands for the Cu catalyst as the formed complex displays high values of K_{ATRP} and k_{deact} [161]. The impact of light intensity on photoinduced ATRP was assessed by decreasing the irradiance of the UV LEDs from 230 mW.cm⁻² (entry 7) to 90 mW.cm⁻² (entry 8). Such a change in the irradiance was enough to decrease the % of conversion from 64 % to only 25% showing the

importance of the intensity of light on the course of photochemical reactions like photoinduced ATRP.

From these experiments we conclude that photoinduced ATRP using Cu(II)/Ligand under UV irradiation was significantly improved, in terms of kinetics and PDI, by replacing the batch setting by a flow microreactor. Under flow conditions, changing irradiation intensity and the ligand's type and loading can also have a significant impact on the polymerization process in a way which is similar to that usually obtained when using batch.

4.11.2 Metal vs. metal free ATRP under visible light irradiation

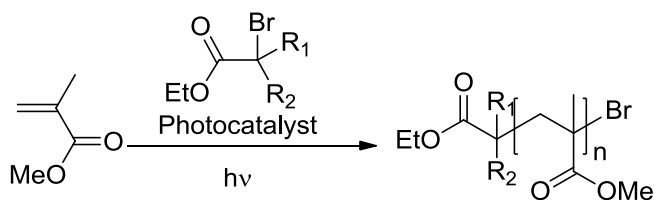


Figure 4.15: ATRP of MMA using: a: Ru(bpy)₃Cl₂ and blue LEDs, b: Eosin Y and green LEDs in both batch and flow conditions

Using the same general protocol listed in 4.11.1, visible light induced polymerization using Ru(bpy)₃Cl₂ that has its peak of absorption in the blue region was performed (Table 4.2) (Figure 4.15). Following the same composition as that indicated by Zhang and co-workers [223] and using our blue LEDs gave 85% of conversion after 20 hours of irradiation. The polymer formed had a relatively broad dispersity ($\bar{D} = 1.96$) but in accordance with the results by the group where after 20 hours of irradiation, 76% of monomer conversion gave a PMMA of $\bar{D} = 2$ [248]. Changing from the batch to the flow conditions and injecting the sample in the FEP tubing reactor (800 μm , 2.24 mL) at a flow rate of 9.5 $\mu\text{L}\cdot\text{min}^{-1}$ that corresponds to 430 min of irradiation gave the same % of conversion but with a better polydispersity ($\bar{D} = 1.63$, entry 2 Table 4.2). This again proves the positive impact of the flow technology on the kinetics and the properties of the polymers formed. Our previous

encounter with eosin Y as a photoredox catalyst that is used in [2+2] photocycloaddition made us try it, as a photocatalyst and not a sensitizer under the same conditions as those of Ru(bpy)₃Cl₂ by adding the electron donor i-Pr₂NEt that is important for completing the photoredox cycle of the catalyst (described in section 4.11.6) (Figure 4.15)

Table 4.2: Visible light induced ATRP in batch and flow conditions. a: blue LEDs, b: Green LEDs, c: initiator is EBPA instead of EBiB, d: [MMA]: [EBiB] : [photocatalyst] : [i-Pr₂NEt], e: determined by ¹H NMR, f: Determined by GPC

Entry	Catalyst	Composition ^d	Case	Conv. ^e	Time (min)	Đ ^f
1^a	Ru(bpy) ₃ Cl ₂	200:1:0.02:10	batch	84	1200	1.96
2^a	Ru(bpy) ₃ Cl ₂	200:1:0.02:10	flow	86	430	1.63
3^b	Eosin Y	200:1:0.02:10	batch	54	360	1.64
4^b	Eosin Y	200:1:0.02:10	flow	70	216	1.58
5^b	Eosin Y	200:0:0.02:10	flow	3	216	--
6^b	Eosin Y	200:1:0:10	flow	0	216	--
7^c	Eosin Y	200:1:0.02:10	flow	0	216	--
8^b	Eosin Y	200:1:0.02:0	flow	0	216	--
9^b	Eosin Y	200:1:0.1:10	flow	43	216	1.86
10^b	Eosin Y	200:1:0.006:10	flow	50	216	1.85
11^{b,c}	Eosin Y	200:1:0.02:10	flow	91	180	1.42

Interestingly, eosin Y was capable of performing photo-induced polymerization at a relatively smaller time and with better polydispersity (Table 4.2 Entry 3) compared to the metal catalyst Ru(bpy)₃Cl₂ (Entry 1). Working under flow (Table 4.2 entry 4) made it possible to accelerate ATRP reaction rate (3.6 h, 70%) as well as improving the control of the polymerization (Đ = 1.58).

It was important to show that all of the factors that are usually involved in a photo-induced polymerization are a necessity for the eosin Y mediated polymerization. Using flow and working under inert conditions, several control experiments were carried out with removing an essential component one-by-one, and the results are shown in Table 4.2 (entries

5, 6, 7 and 8). The polymerization without light, initiator EBiB, *i*-Pr₂NEt, or eosin Y was completely absent, which confirms that each of these components is required for successful polymerization. The control test results support that the polymerization by eosin Y proceeds through the photocatalytic initiation mechanism that is proposed in section 4.1.1.6

The second step was to determine the impact of the loading of eosin Y on the polymerization. When having 0.01 mol % of eosin Y with respect to the monomer, the % of conversion was 70 % (Entry 4). Increasing the loading by 5 folds in Entry 9 led to the decrease in both the kinetics and the control over the polymerization (43%, \bar{D} = 1.86). Similar impact was also observed when decreasing the quantity of the catalyst loading by 3 folds (Entry 10). As explained in Chapter 1 for a given chromophore having a specific extinction coefficient at a specific wavelength, the higher the concentration of this chromophore, the smaller will be the depth of the light's propagation. In the case of eosin Y, we have demonstrated that its molar extinction coefficient is $54052 \text{ M}^{-1} \cdot \text{cm}^{-1}$ at $\lambda = 530 \text{ nm}$. For entry 4, the concentration of eosin Y is around 0.5 mM thus, by applying Beer Lambert's Law, the light is still capable of propagating through the whole microreactor with 99.3 % of the light is absorbed along the 800 μm . This is not the case when having 2.5 mM of eosin Y as in entry 10. After only 148 μm , 99% of the light will already be absorbed by the mixture leaving only 1 % of light to the remaining part. As a consequence, only a part of the reaction mixture will be irradiated leading to the decrease in % of conversion. When the catalyst loading is too small as in Entry 10, though the light can pass easily throughout the path length, the quantity of the catalyst is not enough to activate all of the initiators thus leading to the decrease in the % of conversion. The results of entries 4, 9 and 10 indicate that a small, but sufficient, quantity of the catalyst is needed to initiate polymerization.

One of the parameters that have a great influence on the kinetics of the ATRP is the choice of the initiator. By referring to [157] we decided to assess an initiator that has a higher

k_{act} than EBiB. So we replaced EBiB by EBPA in Entry 11. After only 3 hours of irradiation the rate of polymerization increased remarkably to get more than 90% conversion and the polydispersity of the polymer decreased to 1.42. The choice of initiator has a great impact on the degree of polymerization and the properties of the polymer since these two parameters depend on the stability of the formed radical out of this initiator. Both EBiB and EBPA form stable radicals, however, the stability of the EBPA radical is enforced by the presence of the phenyl group. As a result, the corresponding k_{act} will be higher leading to the increase in the degree of polymerization. In the same course having more active initiators will also lead to more controlled polymerization that impacts both the M_n and the polydispersity of the formed polymer.

4.11.3 Kinetic study

We decided then to investigate the kinetics and the development of M_n as function of monomer conversion of the Eosin Y induced ATRP of MMA in flow when having EBiB or EBPA as an initiator (Figure 4.16).

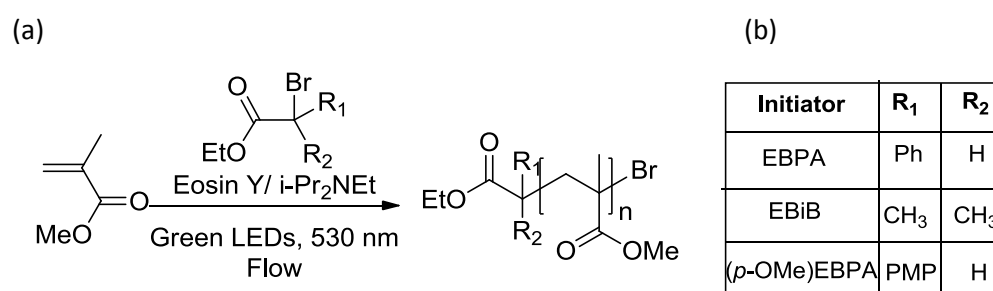


Figure 4.16: a: Eosin Y mediated ATRP of MMA using different initiators; b: composition of the different initiators used.

4.11.3.1 EBPA

For ATRP initiated by EBPA, there exist a strictly linear relationship between $\ln([M_0]/[M])$ and the irradiation time indicating that the polymerization is 1st-order with respect to the monomer concentration (Figure 4.17); the concentration of active radicals remains constant throughout the polymerization. The linear semi-logarithmic plots also suggests that the concentration of the propagating radicals is almost constant throughout the polymerization. Molecular weights follow the theoretical values after about 20% conversion suggesting complete initiation (Table 4.3, Figure 4.18). Values of \bar{D} (1.36-1.49) can indicate relatively slow deactivation caused by either low deactivator concentration or low values of deactivation rate constants.

The advantage of working under flow conditions is displayed by comparing the results in flow to that in batch in entry 7. Other than the rate of the reaction that is diminished by around 6 folds (entry 4 vs. entry 7), the polymer formed is of higher polydispersity ($\bar{D} = 1.64$). Homogeneous and effective illumination proves to be an important parameter that impacts both the kinetics and the quality of polymers synthesized. A recent study working using a similar organocatalyst, fluorescein in batch using blue LEDs also reported similar limitations of the catalytic system in terms of the activation of the initiator, rate of ATRP and dispersity of the formed polymers [231]. In their case there was a big gap between the theoretical and experimental GPC values that started to decrease gradually after 50% conversion, \bar{D} ranged between 1.39-1.66 and 56% of polymerization was obtained after 9 hours of irradiation using blue LEDs. This shows that flow technology can be a good solution to some of the limitations observed by organocatalysis in batch.

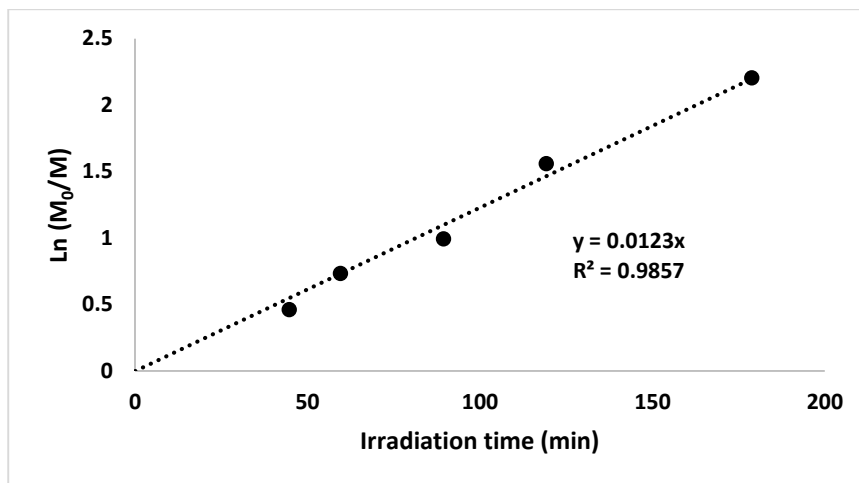


Figure 4.17: A plot of $\ln([M]_0/[M]_t)$ versus irradiation time for polymerization using EBPA as an initiator. Conversions were determined by ^1H NMR analysis

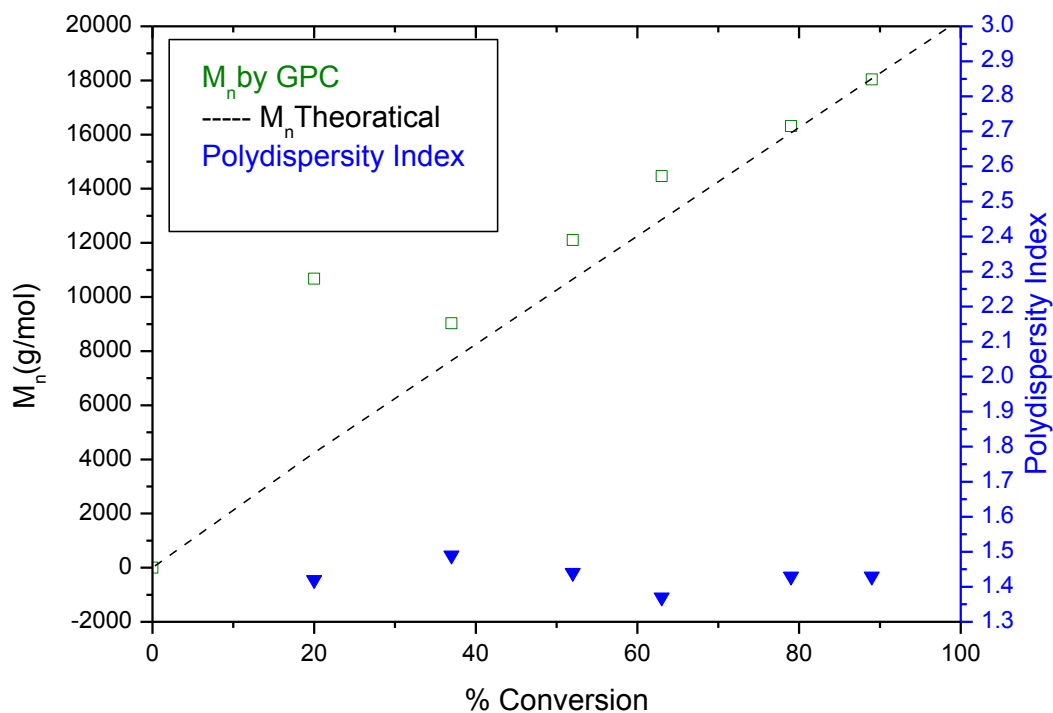


Figure 4.18: M_n (green) & \bar{D} (blue) of PMMA as a function of monomer conversion using EBPA as an initiator. M_n & \bar{D} values were determined by GPC relative to PMMA standards. Conversions were determined by ^1H NMR analysis. Dashed line represents $M_{n,\text{theoretical}} = M_{\text{monomer}} \times \text{conversion} \times \text{DP}$.

Table 4.3: Eosin Y catalyzed ATRP of MMA using EBPA as an initiator in flow. a: performed in batch, b: determined by ¹H NMR, c: $M_n \text{ theo} = [\text{MMA}]/[\text{EBPA}] \times \text{conv} \times M_{\text{MMA}} + M_{\text{EBPA}}$, d: determined by GPC

Entry	Time (min)	% Conv ^b	$M_n \text{ theo}$ ^c	M_n by GPC	\bar{D} ^d
1	36	20	4250	10680	1.42
2	45	37	7650	9030	1.49
3	60	52	10650	12100	1.44
4	90	63	12860	14470	1.37
5	120	79	16060	16320	1.43
6	180	89	18060	18040	1.43
7 ^a	360	54	11080	24280	1.64

4.11.3.2 EBiB

Similar results were obtained for EBiB. The kinetic diagram (Figure 4.19) shows that its rate is 2.5 times less than the rate of EBPA. Interestingly, the M_n values of the formed polymers differ from the theoretical values by a factor of 2.5 (Table 4.4) proving that the efficiency of initiation has a great impact on the control over the polymerization. In the same course, the \bar{D} values are also augmented and range between 1.4-1.6. However, the kinetic curve and the variation of M_n vs. % conversion (Figure 4.20) are both linear. For batch conditions, changing the initiator from EBPA to EBiB had no impact neither on the % of conversion nor on the M_n values. Approximately the same values were obtained in both cases (54% vs. 56 %, 24280 vs. 24260).

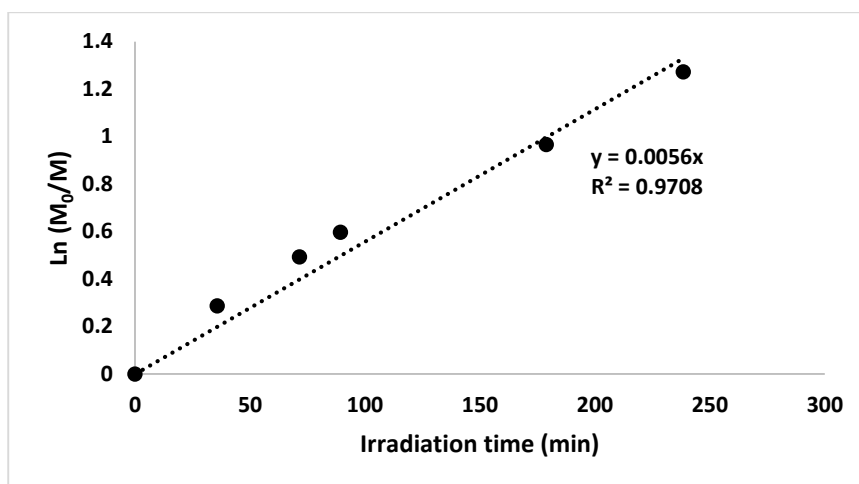


Figure 4.19: A plot of $\ln([M]_0/[M]_t)$ versus irradiation time for polymerization using EBiB as an initiator. Conversions were determined by ^1H NMR analysis

Table 4.4: Eosin Y catalyzed ATRP of MMA using EBiB as an initiator in flow. a: performed in batch, b: determined by ^1H NMR, c: $M_n \text{ theo} = [\text{MMA}]/[\text{EBiB}] \times \text{conv} \times M_{\text{MMA}} + M_{\text{EBiB}}$, d: determined by GPC

Entry	Time (min)	% Conv. ^b	$M_n \text{ theo}$ ^c	$M_n \text{ by GPC}$	\bar{D} ^d
1	36	25	5200	13110	1.42
2	72	39	8000	18250	1.41
3	90	45	9210	19380	1.60
4	180	58	11810	20670	1.51
5	240	68	13810	24870	1.58
6 ^a	360	56	11400	24260	2.09

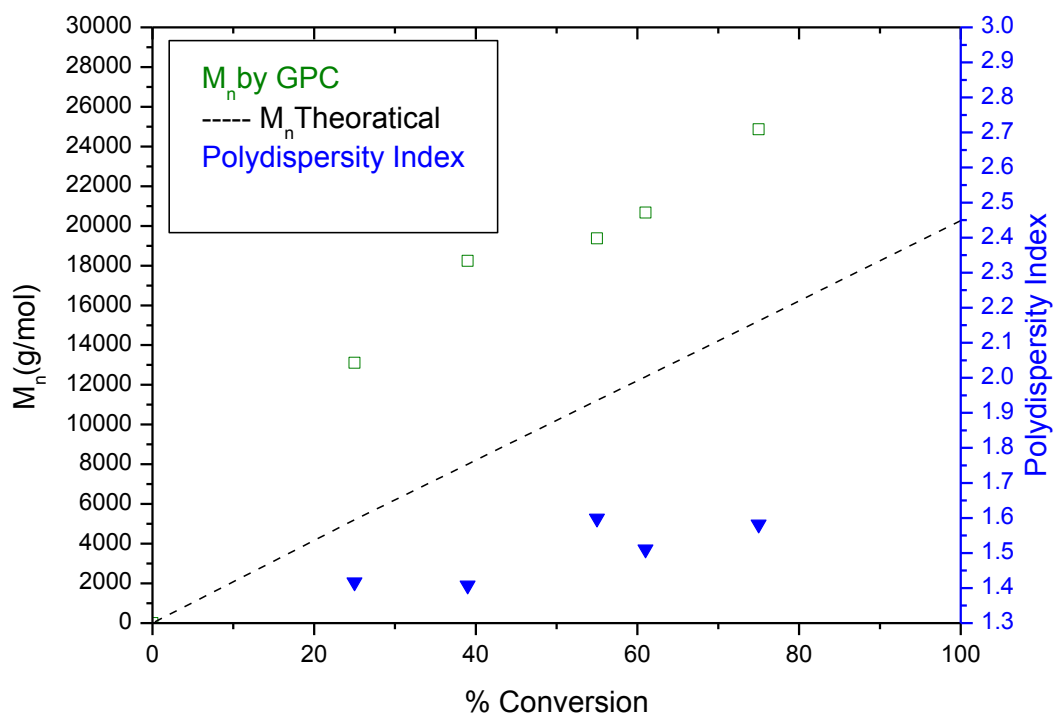


Figure 4.20: M_n (green) & \bar{D} (blue) of PMMA as a function of monomer conversion using EBiB as an initiator. M_n & \bar{D} values were determined by GPC relative to PMMA standards. Conversions were determined by ^1H NMR analysis. Dashed line represents $M_{n,\text{theoretical}} = M_{\text{monomer}} \times \text{conversion} \times \text{DP}$.

4.11.3.3 (*p*-OMe)-EBPA

Since the choice of the initiator, as exhibited above, has a great impact on the polymerization process, we decided to test a modified EBPA that has a methoxy group at the para position of the phenyl group. By theory, the corresponding radical will be more stable than that of EBPA since electron donating groups, like methoxy, at the para position tend to stabilize a radical site [250]

The initiator in concern was synthesized by referring to the procedure listed in literature[251]. Its NMR spectra were in accordance to those listed before. We then used it for ATRP catalyzed by eosin Y. Surprisingly, this modification to EBPA didn't improve its activity but rather weakened it. The rate of polymerization was reduced by a factor of 1.2

(Figure 4.21), along with the increase in the gap between the M_n determined by GPC and the theoretical value (Table 4.5). It seems that in the case of (*p*-OMe)-EBPA, the impact on k_{deact} was more significant than on k_{act} . Moreover, the \bar{D} values were less using this initiator supporting our hypothesis regarding the increase in the value of k_{deact} . (Figure 4.22). Similarly, no remarkable improvement in the batch results of this initiator were recorded.

Table 4.5: Eosin Y catalyzed ATRP of MMA using (*p*-OMe)-EBPA as an initiator in flow. a: performed in batch, b: determined by ^1H NMR, c: $M_n \text{ theo} = [\text{MMA}]/[(p\text{-OMe})\text{-EBPA}] \times \text{conv} \times M_{\text{MMA}} + M_{(p\text{OMe})\text{EBPA}}$, d: determined by GPC

Entry	Time (min)	% Conv. ^b	$M_n \text{ theo}$ ^c	M_n by GPC	\bar{D} ^d
1	36	25	5280	7360	1.39
2	45	33	6880	10940	1.51
3	60	45	9280	13200	1.37
4	90	60	12290	13270	1.47
5	120	70	14290	19500	1.46
6 ^a	360	50	10290	21750	1.79

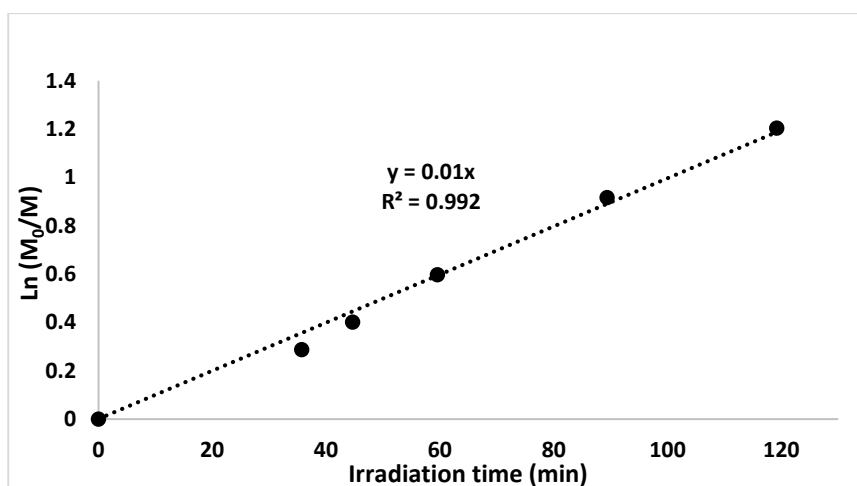


Figure 4.21: A plot of $\ln([M]_0/[M]_t)$ versus irradiation time for polymerization using (*p*-OMe)-EBPA as an initiator. Conversions were determined by ^1H NMR analysis

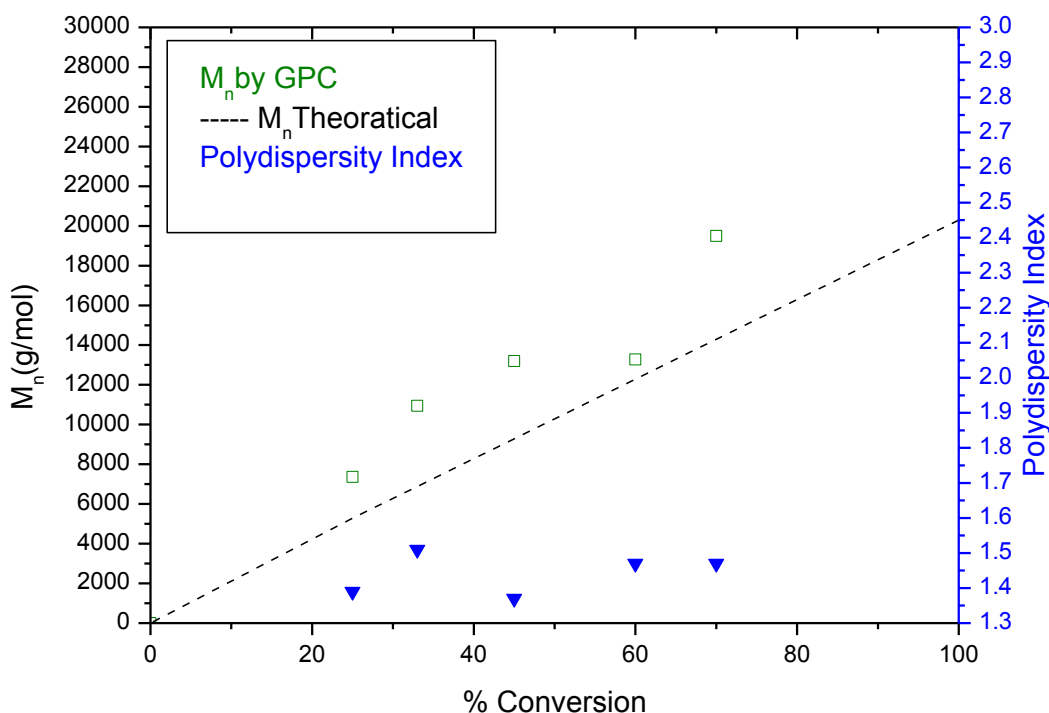


Figure 4.22: M_n (green) & D (blue) of PMMA as a function of monomer conversion using (*p*-OMe)-EBPA as an initiator. M_n & D values were determined by GPC relative to PMMA standards.

Conversions were determined by ^1H NMR analysis. Dashed line represents $M_{n,\text{theoretical}} = M_{\text{monomer}} \times \text{conversion} \times \text{DP}$.

4.11.4 Controlled “on–off” light switching regulation of polymerization

To confirm the necessity of light and the efficiency of eosin Y photocatalyst for the activation and deactivation processes involved in ATRP, polymerization of MMA initiated by EBPA was performed. The green LEDs were turned on and off intermittently during the reaction that was performed in flow (light off at 0-1, 2-3, 4-5, and 6-7 h in Figure 4.23). The reaction mixture was first kept in dark for 1 hour, no polymerization was observed. Later the mixture was injected into the flow reactor irradiated by the green LEDs at a flow rate of $30 \mu\text{L}\cdot\text{min}^{-1}$ that corresponds to 1 hour of irradiation giving a 42% yield. A sample was removed for precipitation and the rest was kept in dark for 1 hour. ^1H NMR analysis indicated no

increase in the % yield following this LEDs off period. Still in flow, the same protocol was repeated giving a 64 % yield after the second 1 hour irradiation. And finally the third round gave 75% yield. No change in the % of conversion or M_n values was observed in any of the LEDs off sessions.

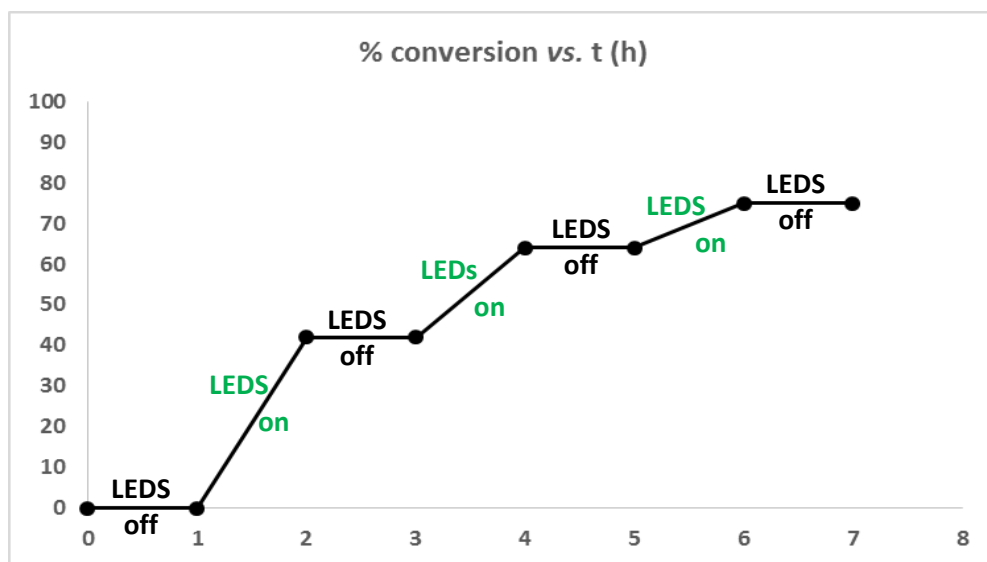


Figure 4.23: Plot of monomer conversion versus time using EBPA as an initiator demonstrating the effect of green light on the control over polymerization propagation through repeated “on-off” cycling of irradiation and light source removal

Table 4.6 shows the yield of PMMA and \bar{D} as a function of time. M_n gradually increased from 9360 to 13820 and the \bar{D} decreased with the increase in the yield (1.78-1.41). The gradual increase of the yield with the irradiation time clearly indicates that the polymerization is driven by light. The polymerization was ceased when the light was turned off and it only increased in response to the irradiation. This indicates that the control over the formation and termination of active species can be performed by using a simple on-off operation of light. The yield increased steadily within each irradiation and the linear relationship between $\ln ([M]_0/[M])$ and time of light exposure suggests a constant propagation radical concentration during the whole polymerization process (Figure 4.24).

Table 4.6: Effect of visible light irradiation on the yield and \bar{D} value of Eosin Y mediated ATRP of MMA with EBPA as initiator. a: after 1 hour darkness, b: determined by ^1H NMR, c: M_n theo= $[\text{MMA}]/[\text{EBPA}] \times \text{conv} \times M_{\text{MMA}} + M_{(\text{EBPA})}$, d: determined by GPC

Entry	Time (h)	Conv ^b	M_n theo ^c	M_n by GPC	\bar{D} ^d
1	0	0	273	n.d	n.d
2 ^a	1	0	273	n.d	n.d
3	2	0.42	8680	9360	1.78
4 ^a	3	0.42	8680	n.d	n.d
5	4	0.63	12890	10460	1.56
6 ^a	5	0.63	12890	n.d	n.d
7	6	0.75	15290	13820	1.41
8 ^a	7	0.75	15290	n.d	n.d

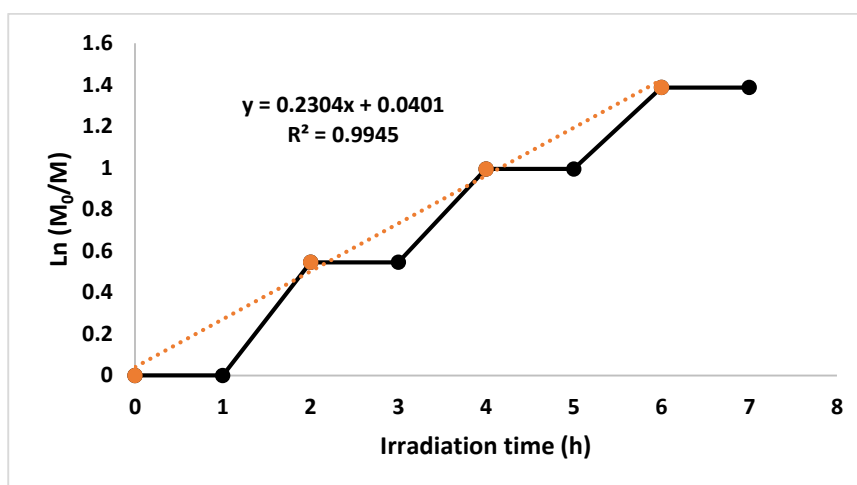


Figure 4.24: $\text{Ln}([\text{M}]_0/[\text{M}])$ as a function of exposure time during an “on-off” irradiation cycles.

Visible light irradiation can have a good control over the ATRP that is catalyzed by eosin Y as demonstrated by the periodic on-off irradiation process. The polymerization is initiated by the irradiation and terminated when this irradiation is off so the process is strictly driven by irradiation stimulus. During the LEDs off periods, the polymerization is paused by having dormant alkyl bromides that are protected from any side radical reaction leading to a

stagnant conversion and molecular weight; however, these formed polymers are available for reactivation upon re-exposure to light.

Note that in our case the \bar{D} decreased and followed the normal trend of ATRP which was not observed when using $\text{Ru}(\text{bpy})_3\text{Cl}_2$ where the \bar{D} values increased due to the presence of short chain polymers from the previous irradiation session. Using eosin Y/flow assembly ensured that there is no accumulation of any short chain polymers as the illumination is efficient enough to activate all of the present polymers and increase the degree of polymerization in a coherent aspect.

4.11.5 Macroinitiator

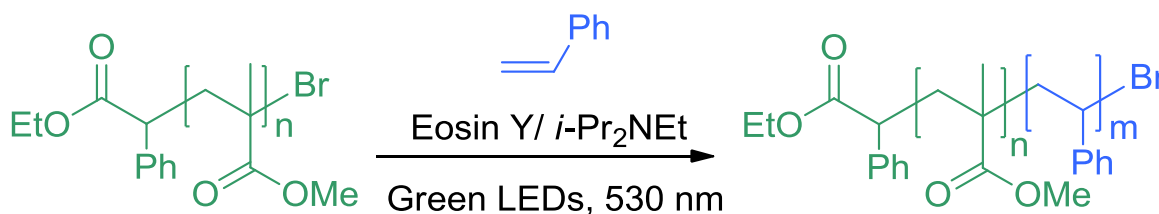


Figure 4.25: Eosin Y mediated ATRP of styrene using PMMA as a macroinitiator

Since the best conditions were given by EBPA, The “livingness” of the eosin Y photoinduced ATRP and the termination of the formed polymers by active bromide ion is demonstrated by the copolymerization of styrene with a PMMA–Br macroinitiator (Figure 4.25). First, the PMMA–Br macroinitiator was synthesized by photoinduced ATRP in flow to get PMMA–Br ($M_n=13110$, $\bar{D} = 1.42$). The formed polymer was then precipitated, and dried then added to the reaction mixture ([styrene]: [PMMA–Br]: [Eosin Y]: [*i*-Pr₂NEt] ratio of 200: 1: 0.02: 10) that was injected in the flow system irradiated by the green LEDs to have a residence time of 240 min. The reaction yielded PMMA–PS with M_n 14860 and \bar{D} 1.41.

The GPC traces of the macroinitiator and the product are displayed in Figure 4.26. The clear shift of M_n to higher molecular weight indicates an effective copolymerization by re-

initiation. ^1H NMR of the formed polymer demonstrates clearly the presence of both PMMA and PS (polystyrene) (Figure 4.27) showing that there was a 9.5 % immersion of styrene. By doing the calculation, the mass of PS added will be around 2000 which is in accordance with the increase in the mass of the macroinitiator from 13110 to 14860. The polymerization done by eosin Y proves to have sufficient alkyl bromine chain ends and high propagation efficiency.

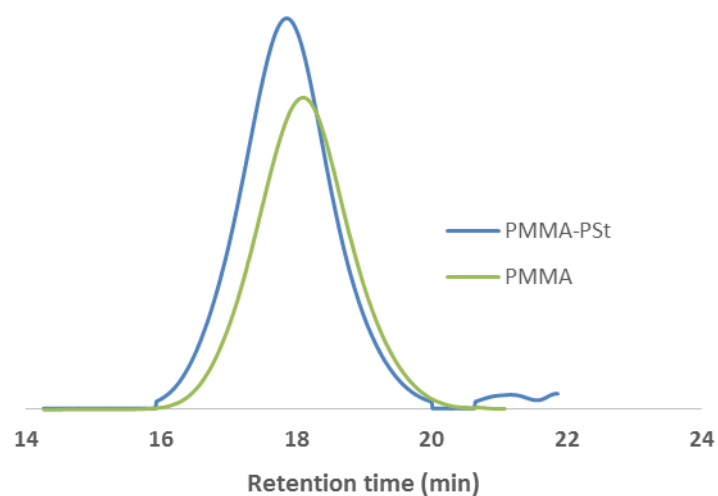


Figure 4.26: GPC trace of PMMA-Br (green) and PMMA-PS (blue) showing molecular weight shift after styrene addition to PMMA-Br that is catalyzed by eosin Y in continuous flow

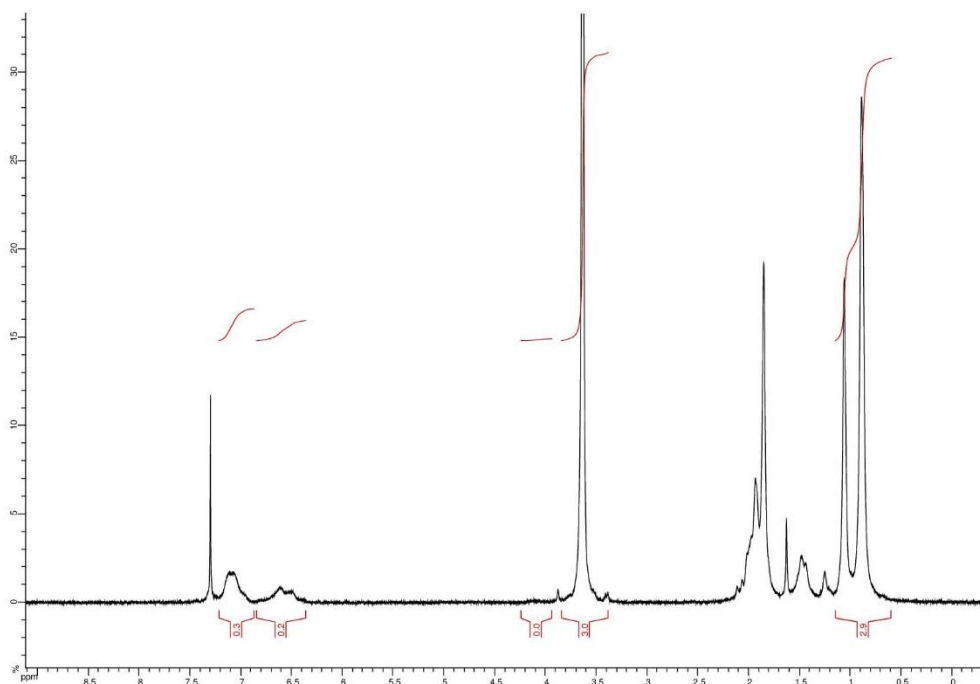


Figure 4.27: ^1H NMR trace of PMMA-PS showing the presence of the PS ^1H peaks (7.2-6.5 ppm) and those of PMMA after styrene addition to PMMA-Br that is catalyzed by eosin Y in continuous flow.

4.11.6 Mechanism

The suggested mechanism of the eosin Y photoinduced electron transfer (PET)-ATRP is represented in Figure 4.28. Upon irradiation with green LEDs, eosin Y absorbs the irradiation and affords its excited state EY^* . $i\text{-Pr}_2\text{NEt}$ the electron donor, reductively quenches EY^* by a single electron transfer to form a radical anion $\text{EY}^{\bullet-}$ and an amine radical cation $i\text{-Pr}_2\text{N}^+\text{Et}$. The latter will then recapture an electron when oxidizing the bromide ion Br^- into bromine radical Br^\bullet . The radical anion $\text{EY}^{\bullet-}$ having the optimum redox potential ($\text{EY}/\text{EY}^{\bullet-} = -1.06\text{ V}$) would transfer an electron to the alkyl bromide that can be the initiator ($\text{R}^\bullet/\text{RX} = -0.37\text{ V}$) or the polymer chains formed subsequently. This will generate a radical (alkyl or propagating) that can attack the monomer that induces propagation along with the regeneration of the ground state EY is then used for subsequent cycles.

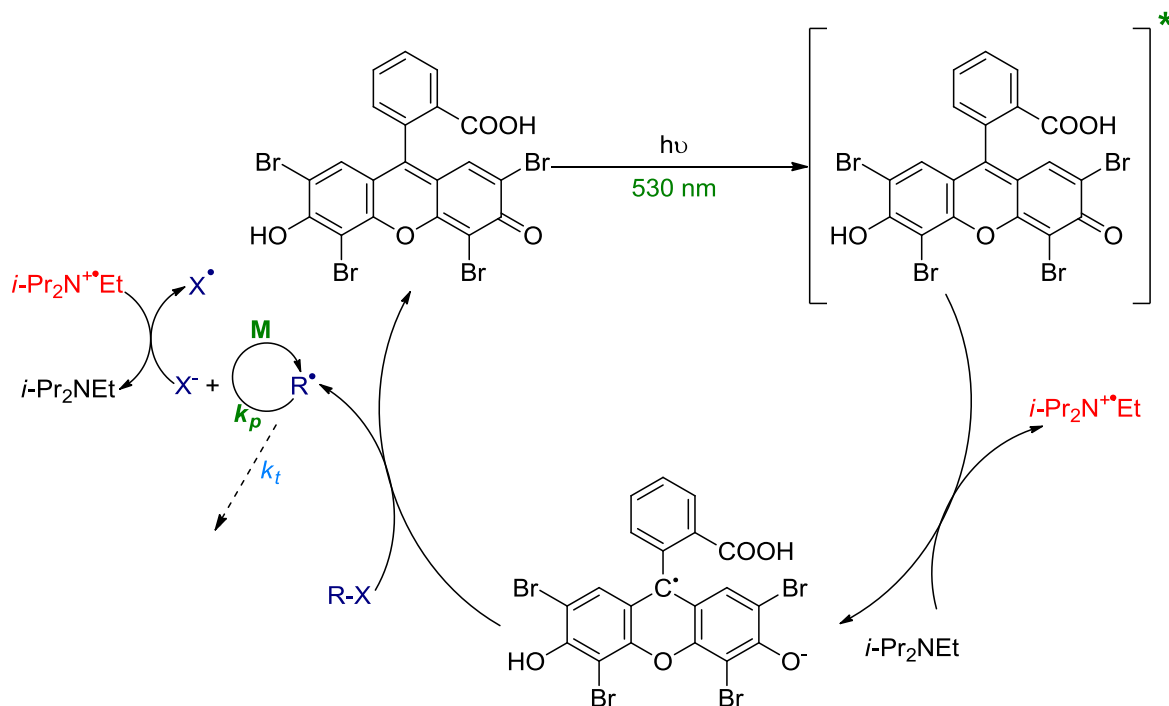


Figure 4.28: Proposed mechanism of ATRP using Eosin Y

The bromine radical $\text{Br} \cdot$ that is formed by the electron transfer to the radical cation $i\text{-Pr}_2\text{N}^+\text{Et}$ will be used for the deactivation of propagation. The bromide ion Br^- is regenerated following the addition of monomer to alkyl bromides, formation of terminated species and reduction of the dormant polymer. This suggested mechanism shows that Eosin Y has a well-established activation deactivation processes that result in the control of the molecular weights and polydispersities of the formed polymers.

4.11.7 Determination of M_w by Diffusion Ordered Spectroscopy (DOSY)

Similar to GPC, 2D-NMR is reported to be used for the determination of the weight average molecular mass M_w of the polymer. By referring to the protocol listed in reference [252] We run DOSY NMR for PMMA standards of known M_w at 20 °C in CDCl_3 instead of benzene- d^6 . Each standard gave a value of diffusion coefficient (D) in $\text{m}^2 \cdot \text{s}^{-1}$ whose logarithmic value was plotted as function of the logarithmic value of the corresponding M_w .

The calibration curve represented in Figure 4.29 was obtained. The plot has an excellent linearity between $\log D$ vs $\log M_w$ with $R^2 = 0.999$ showing the efficiency of the used protocol for such an assessment.

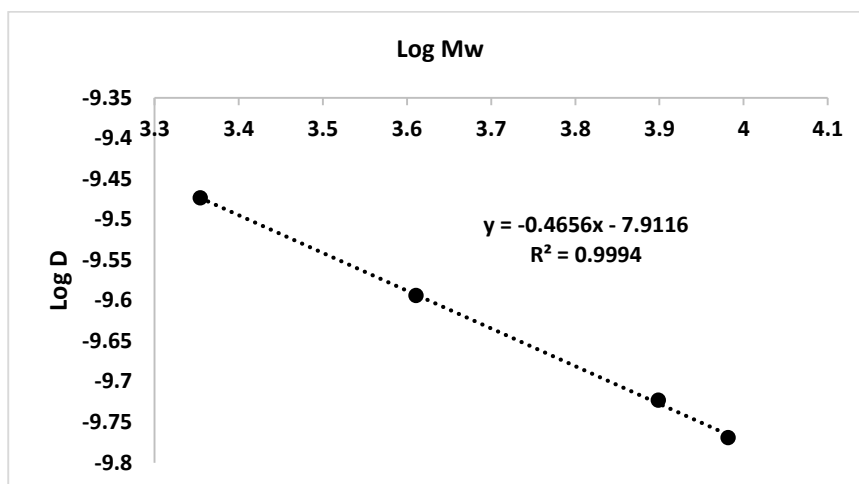


Figure 4.29: PMMA calibration curve in $CDCl_3$ used for M_w prediction

Later, seven samples of PMMA polymers chosen randomly whose M_w values were determined by GPC were analyzed by DOSY to determine their diffusion coefficients using the same protocol of that of the standards ($CDCl_3$, $20^\circ C$). Knowing the value of (D) and by using the equation of the calibration curve $\log D = -0.4656 \log M_w - 7.9116$, the M_w values of synthesized PMMA were calculated. Table 4.7 includes the M_w values of the tested polymers using GPC and DOSY NMR. Interestingly, the two methods almost gave the same M_w values in all of the entries. The % of difference between both values varies between 0.08 % in entry 1 to a maximum value of only 5.5 % in entry 7. This shows that DOSY NMR can be a good analytical method for the characterization of polymers. NMR spectroscopy can provide the full characterization of the polymer: % conversion, tacticity and M_n by 1H NMR and M_w by DOSY NMR rendering it complementary to GPC.

Table 4.7: M_w measurements of PMMA synthesized in flow by DOSY NMR and GPC. a: Equation of the PMMA standard calibration curve is $y = -0.4656 \log M_w - 7.9116$ ($R^2 = 0.9994$). M_w (DOSY) was calculated from the calibration curve using the experimental values of D . b: Calculated from M_w (GPC) and M_w (DOSY).

<i>Entry</i>	<i>D by DOSY NMR ($m^2 \cdot s^{-1}$)</i>	<i>M_w by DOSY NMR ^a</i>	<i>M_w by GPC</i>	<i>% diff ^b</i>
1	1.10E-10	24917	24897	-0.08
2	1.20E-10	20744	20265	-2.36
3	1.25E-10	19098	19153	0.29
4	1.26E-10	18709	18039	-3.7
5	1.28E-10	18024	17977	-0.26
6	1.30E-10	17550	17288	-1.52
7	1.96E-10	7190	6814	-5.5

The only limitation in NMR spectroscopy is the calculation of M_n using the end group analysis. This technique is based on integrating a peak that corresponds to the polymer and another that corresponds to the initiator. For polymers with high M_n values, the initiator peaks will be too small hindering their accurate integration. This limitation can be partially overcome by running the sample for number of scans of 1024 or more. As a result, it is not recommended to use ^1H NMR for polymers whose masses exceed 25 000 [177].

4.11.8 Tacticity

To investigate the impact of polymerization in flow on the tacticity of the formed polymer, we used ^1H NMR to calculate the % of the three triads mm, mr and rr. Table 4.8 includes the tacticity of the polymers initiated by EBPA in flow at various flow rates (entries 1-6) and in batch (entry 7). The mm triad ranges between 2.79 and 3.33%, mr triad 31.45 and 33.67 % and the rr triad between 65.76 and 63%. Considering that the % of error given by NMR is around 3 %, it can be deduced that regardless of the % of conversion or whether the reaction is performed in batch or flow the % of each of the triads is almost the same. Replacing EBPA by EBiB (entries 8-9) or (*p*-OMe)-EBPA (entries 10-11) also had no

impact on the tacticity of the formed polymers as it is clear that there is no remarkable difference between any of the given data. This is in accordance with the reason behind tacticity that does not depend on the initiator type but rather develops during the formation of the polymer. In most of the radical polymerization cases, atactic (mr) are the most abundant form. However, metal or metal/ligand catalytic systems tend to produce a mixture of the triads [183] . Similarly, eosin Y follows the same trend as the metal based catalytic systems and provides the three triads with the highest proportion going to syndiotactic (rr) which is the most stereo-chemically favored.

Table 4.8: Tacticity of PMMA formed by Eosin Y catalysis in flow. a: in batch, b: by ¹H NMR analysis

Entry	Initiator	Time (min)	%Conv ^b	mm ^b	mr ^b	rr ^b
1	EBPA	36	20	3.2	33	63.8
2	EBPA	45	37	2.91	33.19	63.9
3	EBPA	60	52	3.1	32.2	64.7
4	EBPA	90	63	3.33	33.67	63
5	EBPA	120	79	2.76	33.14	64.1
6	EBPA	180	89	2.84	32.96	64.2
7^a	EBPA	360	54	2.79	31.45	65.76
8	EBiB	240	68	2.58	31.96	65.46
9^a	EBiB	360	56	2.98	30.95	66.07
10	(<i>p</i> -OMe)-EBPA	120	70	2.94	33.82	63.24
11^a	(<i>p</i> -OMe)-EBPA	360	50	3.04	31.61	65.35

4.12 Conclusion

Since the last decade, there is a great interest in the development of the photo-induced controlled radical polymerizations like ATRP. Copper/Ligand catalytic systems prove to be the best by providing narrow dispersed polymers with a linear relationship between the % of conversion and the molecular mass M_n of the formed polymer. This provides the possibility to predict and thus pre-adjust the ratio of monomer/ initiator to get polymers of the desired masses. Moreover, a significant advantage of working using light is that the polymerization

is strictly controlled by presence/absence of irradiation. Upon irradiation the reaction takes place with first order kinetics. The absence of light is enough to cease the polymerization as the active species will change into dormant species that are reactivated upon light exposure. This is not the case with thermal polymerization whose drawback is the inability to control the termination of radical chain reaction. Metal based catalytic systems were also assessed in flow for polymerization which proved to be efficient as the rate of the reaction was automatically enhanced from 20 hours to 1-2 hours due to the higher photon flux received by the reaction mixture within the confined microreactor. However, one of the disadvantages of the metal based catalysis is the toxicity and the elevated prices of the catalysts used. This has made some researchers focus on developing polymerization using organic photocatalysts like PTH and most recently Fluorescein. Fluorescein in batch had limitations regarding the activation of the initiator, thus forming polymers whose masses are much bigger than expected along with high \bar{M}_w values. Using Fluorescein in batch needed around 12 hours of blue irradiation to get 90% conversion of MMA. Our work focused on using the derivative of Fluorescein, eosin Y as a photoinitiator for ATRP of MMA irradiated by green LEDs using three different initiators EBPA, EBiB and (*p*-OMe)-EBPA. Interestingly by using EBPA as an initiator, 3 hours of irradiation in flow were enough to have 89% conversion. The variation in the flow rate and thus in the irradiation times gave a series of polymers of low polydispersity (< 1.5) whose masses are close to the theoretical values. A linear relationship was obtained between the % of conversion and the molecular mass M_n showing that eosin Y catalytic system sponsors a well-controlled ATRP. We believe that working under flow conditions is the main reason behind this control of polymerization by eosin Y, which was not observed by working with fluorescein in batch. The strong illumination provided to the reaction mixture favors a rapid activation of the initiator thus having polymers with masses close to the theoretical values. EBiB and (*p*-OMe)-EBPA also proved

to be good initiators but to a less extent compared to EBPA regarding both the rate and the dispersity of the polymers. This also displays the importance of the choice of the initiator for the polymerization process especially for organic catalysts that usually, but not always, have limitations compared to metal based catalysts. By using eosin Y, the formed polymers are proved to be terminated by Br and thus can be used for further polymerizations as macroinitiators. Light is an important factor for the described catalytic system as the activation and deactivation of the process depended greatly on the presence/absence of light. In the same course, changing the light intensity also had an impact on the yield of polymerization. The described system however, has no impact on the tacticity of the formed polymers as both batch and flow, metal based and metal free polymers gave the same proportion of the three triads mm, mr and rr with the dominance of the latter which is a major feature in metal based radical polymerizations. DOSY NMR was proved to be an efficient technique for the determination of M_w of polymers making NMR spectroscopy favored for the full characterization of polymers (% conversion, M_n , M_w , tacticity) whose masses don't exceed 25 000.

In conclusion, this work has combined the advantages of the continuous flow and the metal free catalysis to provide well defined polymers of controlled masses and narrow dispersity within short irradiation times by visible light and by using safe, easily removed and cheap resources with solvent and time saving analytical techniques.

CHAPTER FIVE

C-C AND C-O BOND FORMATION VIA PHOTOREDOX CATALYSIS

5.1 Introduction

Radical chemistry is an important pillar in organic synthesis. There is a continuous development in this field in an attempt to have various systems that produce radicals [159, 253-255]. The common pathways involve the generation of the radical by stimulus like heat, light or a redox reaction.

Among the various reactions that are currently in use, the formation of a C-C bond is one of particular importance as it serves well toward developing new complex chemicals. Such a transformation is facilitated by using organometallic reagents (R-M) [256]. As a result, these reagents are widely used in synthetic chemistry. Organometallic compounds like organomagnesium (Grignard reagent) and organolithium are used but to a certain limit due to their high sensitivity to air and moisture. The result of extensive research toward more practical organometallic was cuprates, organozincs, silicates, aluminates, organoborons, and stannanes [257, 258].

Organoboron compounds are the most popular among all. Their advantages lie in the variety of the methods of preparation of the organoboron compounds [258], their relatively low toxicity compared to other organometallic compounds [259], their ultimate degradation into the environmentally friendly boric acid and the ease in the removal of the boron side product by aqueous extraction [260-262]. In addition, most of these compounds are highly stable [263], commercially available and have high tolerance to a wide range of functional groups [264, 265]. Boronic acids are linked to the therapeutic and biological activities of natural products [258, 266]. However their main feature is their usage as synthetic agents for

the formation of C-C and C-N bonds. They appear in transition metal catalyzed reactions, like Suzuki-Miyaura reactions [267, 268]. However organoboranes like alkyl and alkynyl boranes are unstable under atmospheric conditions as the vacant orbital of the boron can easily be attacked by oxygen or water [263, 269]. One solution for this drawback, which is the topic of this section is trifluoroborate salts.

5.1.1 Synthesis of the Starting Trifluoroborates

These crystalline compounds that first emerged in 1960 by Chambers are very stable to air and water but highly reactive in a variety of reactions [258, 259]. They are commercially available or can be easily prepared by mixing the corresponding boronic acid with KHF_2 solution. They can also be prepared starting from the corresponding alkyl halide *via* a 2 step reaction (Figure 5.1) [260, 261]. The high affinity of boron towards fluorides favors the formation of trifluoroborates. They exhibit exceptional stability towards air, moisture and nucleophiles. Despite their stability, they are very reactive in a wide range of reactions [258, 263]. They also have shown to exhibit stronger medicinal and biological activity compared to boronic acids due to the fluorine hydrogen bonds within their active site [270]. The drawback of trifluoroborates lies in their instability to silica gel and their insolubility in nonpolar solvents. However, they can be easily purified by crystallization [258].

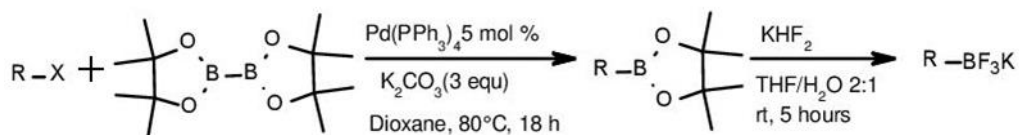


Figure 5.1: Synthesis of the potassium trifluoroborates

5.1.2 Generation of carbon-centered radicals from organoboron derivatives via oxidation

Radicals from trifluoroborates can be generated using oxidants like Mn(III) and Cu(II) or by photoredox catalysis. The list below includes the major reports that demonstrated the *in situ* generation of the radical from trifluoroborates, followed by the involvement of such radicals in cross coupling, addition to alkenes and addition to other radicals.

In 2010 Fensterbank and co-workers reported the first generation of radicals out of alkyl, aryl and alkenyl trifluoroborates using Cu(II) as an oxidant [271]. They first optimized the conditions using the benzyl trifluoroborate. In order to determine whether the oxidation of the trifluoroborate took place, TEMPO was added so that the formed adduct could be used to monitor the reaction. The best conditions were obtained when using Cu(OAc)₂ (1.2 eq.) in DMSO at 120° C giving 88% of conversion (Figure 5.2). Good yield for the radical generation was also obtained by adding CuCl₂ in diethyl ether [271].

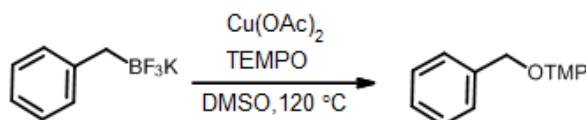


Figure 5.2: Generation of radicals from trifluoroborates using oxidants [41]

Similarly Molander *et al* used alkyl and alkoxy trifluoroborates for the direct alkylation of hetero aryls [272]. The reaction is based on the generation of alkyl radical from borate via an oxidant (Mn (III), Mn (VII), Ce (II), Fe (II) salts). The formed radical will then attack the heteroaryl (Lepidine) forming a radical anion intermediate that undergoes oxidation to give the heteroalkyl adduct. The optimum conditions were when using 2.5 eq of Mn(OAc)₃, TFA (1 eq), and aqueous ethanol mixed for 18 hours at 50 ° C (Figure 5.3). The proposed mechanism involved the homolytic cleavage of the carbon-boron that is facilitated by Mn(III) [272].

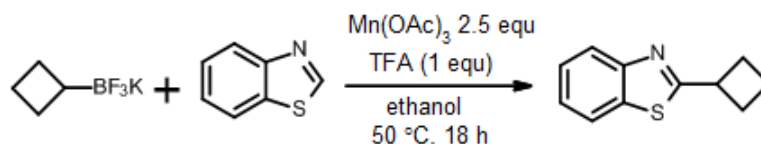


Figure 5.3: Alkylation of heteroaryls following radical formation using oxidants.

The group of Chenter performed a Heck reaction between vinyl arenes and trifluoroborates using $\text{Cu}(\text{OTf})_2/\text{Ligand}$ (20 mol %) as a catalyst and MnO_2 as an oxidant [273]. The reaction required heating for 24 h at 105 °C (Figure 5.4). The methodology was further extended to alkyl trifluoroborates. The proposed mechanism involved the *trans*-metalation of the trifluoroborate with Cu (II) followed by the cleavage of the C-Cu (II) bond thus generating the alkyl radical.

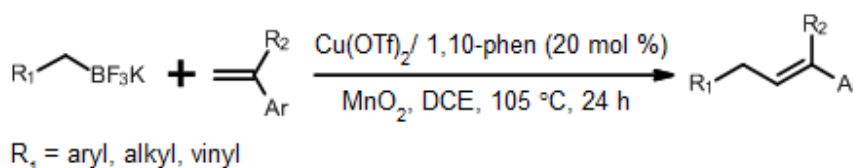


Figure 5.4: Heck reaction using oxidants and $\text{Cu}(\text{OTf})_2$

It was shown that organic radicals can be generated from organoborates upon oxidation, but require an excess amount of oxidant or co-oxidant [273].

5.1.3 Generation of carbon-centered radicals from organoboron derivatives via visible light photoredox catalysis

Conventional systems using oxidants include the usage of toxic or explosive material or high energy irradiation along with the production of undesirable waste products [255, 274]. Such unfavorable conditions triggered the search for safer, more efficient and eco-

compatible pathways with selective outcomes [275, 276]. In this course, redox reactions are gaining special attention as several research groups use such processes for asymmetric transformations that were successfully applied to natural products' synthesis [133, 277, 278]. As mentioned in chapter 3, in this strategy light irradiation is a powerful tool to generate single electron transfer by using low catalyst loading and under mild conditions [18]

Pioneer work concerning the generation of carbon centered radicals by photoredox catalysis was done by Akita *et al.* who reported the generation of the alkyl radical from trifluoroborates by using blue LEDs. In their study two photoredox catalysts, Ru(bpy)₃Cl₂ and Ir/Ligand were used [279]. They first optimized conditions for the radical generation (catalyst loading, catalyst type, ligand type) by using benzyl trifluoroborate. Similar to Fensterbank [271], they utilized TEMPO as radical trapping agent. Various Ir/Ligand (2 mol %) were used. [Ir(dF(CF₃)ppy)₂(bpy)] PF₆ gave the best results with 99% after 8 hours of blue LED irradiation (Figure 5.5).

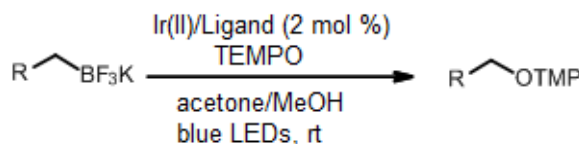


Figure 5.5: C-O bond formation via photoredox catalysis

Similar to Ru(bpy)₃Cl₂, Ir polypyridine complexes also undergo SET when exposed to light irradiation leading to the generation of carbon-centered radicals. Iridium catalysts exhibit advantages over Ru catalyst as they have the ability to support heteroleptic ligands without the loss of photocatalytic efficacy. They are also much stronger oxidants [280]. Another advantage is the relatively long lifetime of the excited state of some of the Ir catalyst/ligand complexes (2.3 μs vs. 0.9 μs for Ru catalyst) thus promoting the chemical

transformations [17]. The commercially available iridium catalysts Ir(III)/L₁ (Figure 5. 6) is used in this work.

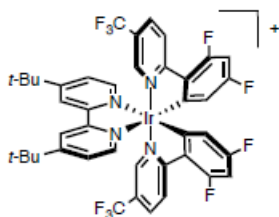


Figure 5.6: Structure of Ir(dF(CF₃)ppy)₂(dtbbpy)⁺

Following irradiation, the singlet excited state ¹Ir(III)^{*}/L₁ relaxes to its corresponding triplet excited state ³Ir(III)^{*}/L₁. The latter can undergo SET to/from other organic molecules thus serving as a single electron oxidant or reductant. Usually the photoredox catalyst is then regenerated to its initial ground state following the SET.

Ir(III)/L₁ can serve as a single electron reductant following its reductive quenching by an electron donor ($E^0(\text{M}/\text{M}^-) = -1.37 \text{ V vs. SCE, in MeCN}$). This species is a stronger reductant than the corresponding photoexcited catalyst ($E^0(\text{M}^+/\text{M}^*) = -0.89 \text{ V vs. SCE in MeCN}$). Under the opposite conditions, that is oxidative quenching, the formed oxidized species M⁺ is a strong single electron oxidant ($E^0(\text{M}^+/\text{M}) = 1.69 \text{ V vs. SCE in MeCN}$). Based on the given redox potentials of the different species that are summarized in Table 5.1, it is clear that the Ir catalyst can act as single oxidants or reductants and that based on the nature of organic substances present (electron donors/acceptor) that promotes one pathway over the other. The generation of carbon radicals from organoborates by Ir photoredox catalysis takes place *via* the reductive quenching pathway [11, 47, 48, 51, 53, 54, 60].

Table 5.1: Redox potentials of the possible transitions of Ir(III)/ L₁

M ^{ox} /M ^{red}	E _{red} (V) / SCE
M/ M [•]	-1.37
M ⁺ / M	1.69
M ⁺ / M [*]	-0.89
M [*] / M [•]	1.21

The reaction mechanism of C-O bond formation involves the irradiation of the Ir catalyst that will be photoexcited to generate Ir (III)*. SET from the organoborate to this excited Ir(III)* will lead to reductive quenching the catalyst forming Ir (II). Carbon central radicals will be generated from the organoborate and trapped by TEMPO to form the C-O coupling product. The ground state Ir (III) will be regenerated by TEMPO that will act also as a sacrificial receptor [279] (Figure 5.7).

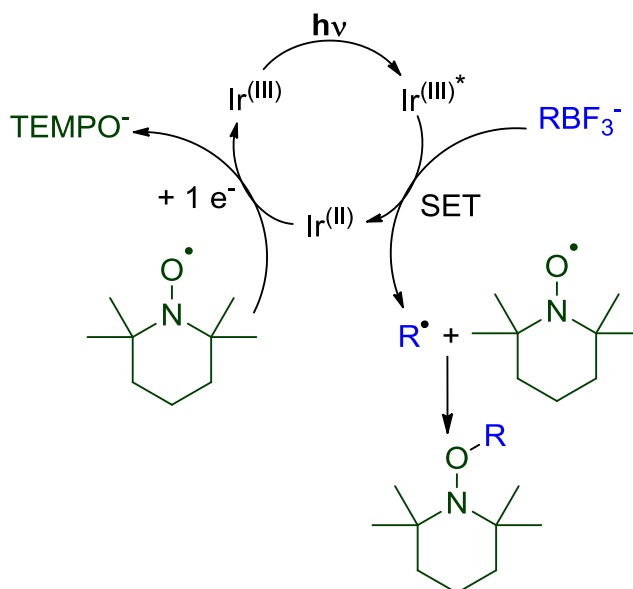


Figure 5.7: Mechanism of C-O bond formation via photoredox catalysis

They then assessed the activity of the formed radical by adding it to a deactivated alkene with an electron withdrawing group (Figure 5.8). Interestingly, the addition of the benzyl trifluoroborate to butyl vinyl ketone gave 81 % after 8 hours [279].

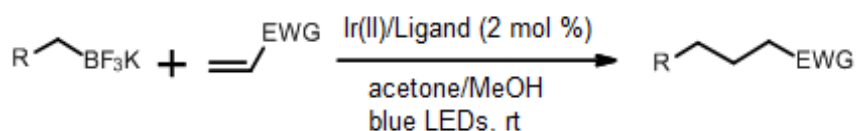


Figure 5.8: C-C bond formation via photoredox catalysis

The same mechanism for the generation of the carbon central radical of the C-O formation is applicable for that of the C-C formation. However, the formed carbon radical will add to the electron deficient alkene forming a radical intermediate. The latter will be then reduced by SET from the reductively quenched Ir(II) to regenerate Ir(III). Protonation by the solvent methanol leads to the formation of the C-C coupling adduct [279] (Figure 5.9).

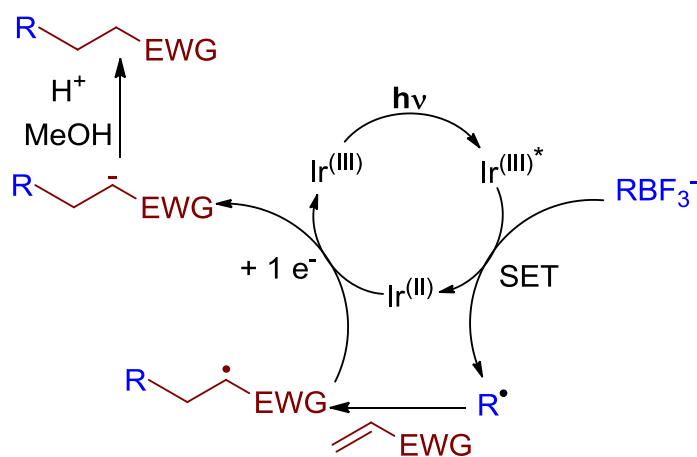


Figure 5.9: Mechanism of C-C bond formation via photoredox catalysis

The success in adding the radicals generated by photoredox catalysis to alkenes made the same group test the efficiency of the alkoxy trifluoroborates in performing the same

reaction. Indeed 2 mol % of the Ir catalyst was enough to provide quantitative addition of the benzyl alkoxy radical generated from its trifluoroborate to the cyclopenten-1-one after 24 h of blue irradiation [281] (Figure 5.10).

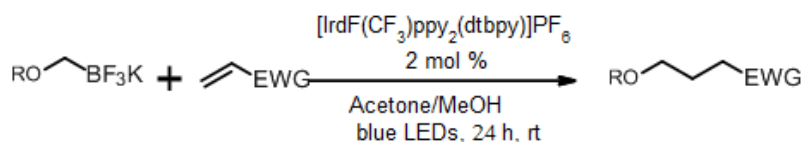


Figure 5.10: Alkoxy trifluoroborates for C-C bond formation via photoredox catalysis

Being able to form various primary amino alkyl structures is of great interest as such reagents are present in many biologically active compounds [282, 283]. The Akita group managed to use the photoredox ability of the Ir (II) /Ligand catalyst to generate amino alkyl radicals from the easily prepared amino alkyl trifluoroborates [266]. These radicals are then added to alkenes with electron withdrawing groups. The reaction was very rapid with the formation of 92 % of the adduct of a Boc protected amino methyl trifluoroborate and methyl acrylate after only 1 hour of irradiation (Figure 5.11). The reaction was proved to be efficient with various alkenes [266].



Figure 5.11: C-C bond formation using amino alkyl trifluoroborates via photoredox catalysis

The first report that describes the thio alkylation of olefins was published in 2015 (Figure 5.12). The reaction was also assessed in sun light giving a remarkable 75% conversion after 8 hours of exposure to sun light. [284].

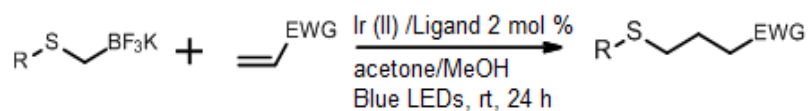


Figure 5.12: C-C bond formation using thio alkyl trifluoroborates via photoredox catalysis

Chen *et al.* demonstrated a new pathway for the formation of C(sp³)-C(sp²) bond using trifluoroborates and photoredox catalysis [285]. Using the classical cross coupling conditions, the addition of alkyl radical to vinyl carboxylic acid requires *trans*-metalation followed by strong heating or strong oxidant addition for decarboxylation. This limits the usage of this functional group in such reactions [286, 287]. The group was capable of forming this cross coupling reaction after the generation of the radical from the trifluoroborate using Ru(bpy)₃(PF₆)₂ as a photocatalyst (Figure 5.13). The reaction took place at room temperature using blue LEDs and 1.5 eq. of oxidant. The reaction gave the corresponding cross coupling product with elevated yields after 15 hours of irradiation [285].

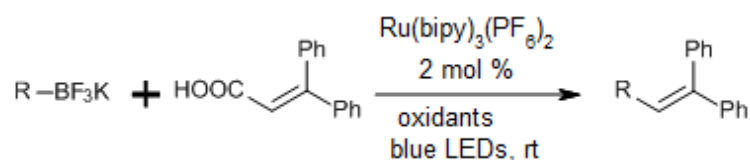


Figure 5.13: Addition of alkyl radical to vinyl carboxylic acid via photoredox catalysis

Photoredox catalysts were also used in combination with the Ni catalyst for cross coupling reactions with alkyl halides and benzyl trifluoroborate as cross coupling partners. Molander and coworkers coupled photoredox cross with coupling via single electron *trans*-metalation instead of the traditional cross coupling having two electron *trans*-metalation that requires high temperature and basic conditions [288] (Figure 5.14). The combination of alkyl halide to [Ni]⁰/Ligand (3 mol %) has led to the oxidation of the latter to Ni(II)/L. Irradiated by a fluorescent lamp, the excited iridium catalyst Ir*(III)/L (2 mol %) will extract a single

electron from the benzyl trifluoroborate leading to the generation of the benzyl radical and the reduced Ir (II)/L. The benzyl radical will then be captured by the Ni(II)/L to form an intermediate that will undergo a reductive elimination to generate the desired cross coupling product. The reaction is compatible with a wide range of benzyl trifluoroborates and benzyl halides giving yields up to 91%. By using this dual catalysis, the catalyst loading and the reaction time could be reduced compared to traditional methodologies [288].

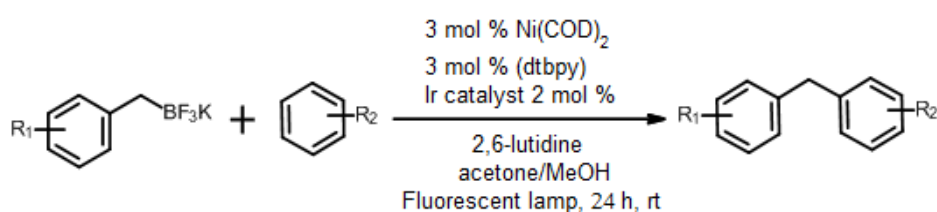


Figure 5.14: Dual catalysis for cross coupling

This dual catalysis approach was also tested by the same group using secondary alkyl trifluoroborates as coupling agents with benzyl halides [289]. The cross coupling of cyclic alkyl trifluoroborates with 4-bromobenzoate gave 92% conversion after 24 h of irradiation at room temperature with 2.5 mol % of Ir (II) /L catalyst and 5 mol % of Ni catalyst (Figure 5.15). This was a great accomplishment as Ni catalyzed cross coupling reactions for secondary alkyl borates required very high temperatures and catalyst loading and achieved less results[290, 291].

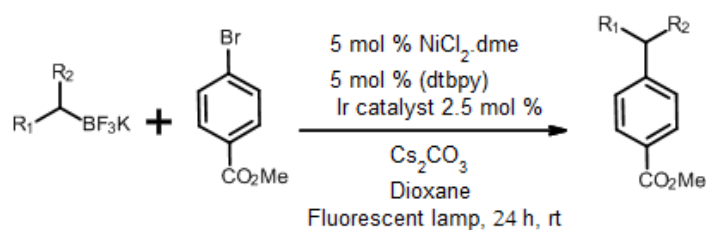


Figure 5.15: Dual catalysis for cross coupling using secondary alkyl trifluoroborates

The synthesis of benzylic ethers by the cross coupling of alkoxy trifluoroborates with benzyl bromides was also reported by Molander group using the same dual catalysis concept [292]. They achieved good yields 43-95% by using 2 mol % of Ir catalyst, 3 mol% of Ni catalyst at room temperature with a fluorescent lamp as a light source [292] (Figure 5.16). Such a cross coupling requires working at 100 °C with strong basic conditions when using the classical Ni catalyzed coupling [293].

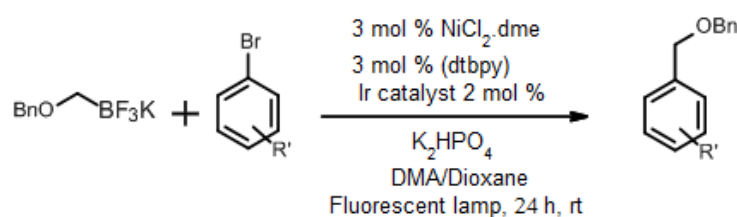


Figure 5.16: Dual catalysis for the synthesis of benzylic ethers by cross coupling

5.2 Objective

The combination of photoredox catalysis with stable trifluoroborates is of great significance for synthetic chemistry. It opens up the possibility to synthesize molecules that require harsh conditions under classical conditions.

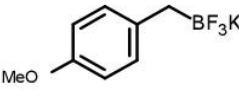
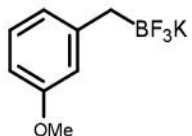
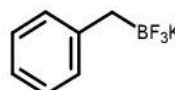
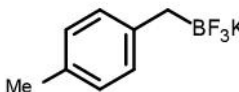
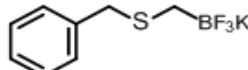
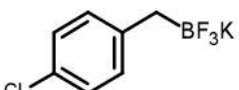
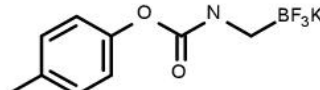
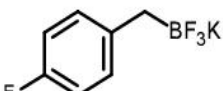
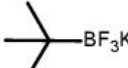
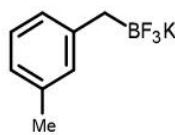
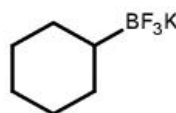
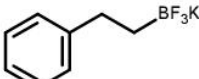
In our quest to demonstrate the potential of the continuous flow technology, we decided to study the generation of the alkyl radicals by photoredox catalysis in order to improve the overall process. The C-O and the C-C bond formations were tested in continuous flow under UV irradiation as the Iridium catalyst absorbs much better at this wavelength (Figure 5.18). We also investigated the impact of the substitution on the benzyl group of the trifluoroborate on the reaction rate by plotting the Hammett equation.

5.3 Results and Discussion

5.3.1 Preparation of Trifluoroborates

The various trifluoroborates (**1h-1t**) were prepared following the procedure indicated by Vedejs and coworkers [260, 261]. The yields ranged between 95 % for **1 h** and 43 % for **1n** (Table 5.2).

Table 5.2: Yields of the preparation of the trifluoroborate salts (**1h-1t**)

Organoborate	Symbol	% yield	Organoborate	Symbol	% yield
	1 h	95		1 o	75
	1 i	68		1 p	65
	1 j	76		1 q	92
	1 k	81		1 r	51
	1 l	74		1 s	64
	1 m	89		1 t	73
	1 n	43			

5.3.2 C-O bond formation from potassium trifluoroborates in batch and in flow

5.3.2.1 Optimization of the metal photocatalyzed C-O bond formation

5.3.2.1.1 Influence of the metal catalyst

Different photo-catalysts were tested for the generation of the radical. Ru(bpy)₃Cl₂, and Ir(III)/ L₁ were used with blue LEDs in batch and in the Mikroglas ® Dwell Device (Figure 5.17). The *p*-methoxybenzyltrifluoroborate salt was our model substrate since it was reported to be the most active trifluoroborate for the C-O bond formation with TEMPO. The results are summarized in Table 5.3. Note that the NMR yield was determined with 1,3,5-trimethoxybenzene as internal standard.

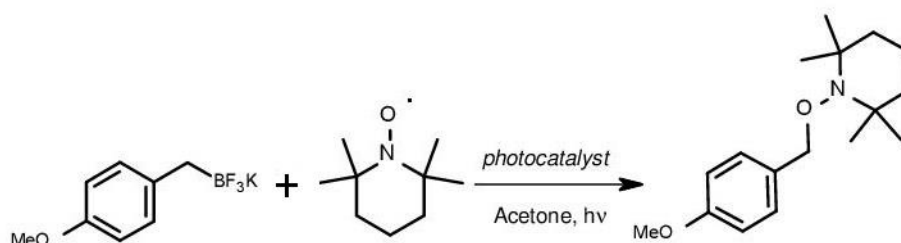


Figure 5.17: C-O bond formation in flow via photoredox catalysis

The first 2 entries of Table 5.3 are the results obtained by Yasu and coworkers [279]. Poor conversion in batch after prolonged irradiation under blue LEDs was obtained with Ru(bpy)₃Cl₂ after (entry 1). Using flow device, the reaction time was decreased to 7 hours to obtain 95% of conversion (entry 3), displaying the advantage of working using microfluidic systems for photochemical reactions. The reaction was quantitative using Ir(III) after 18 h of Blue irradiation under batch condition (entry 2).

Table 5.3: Results of C-O bond formation in flow via metal based photoredox catalysis

Entry	Condition	Photocatalyst	mole %	LEDs	Time	% conv ^a
1 ^a	batch	Ru(bpy) ₃ Cl ₂	2	blue	21 h	12
2 ^a	batch	Ir(III)/ L ₁	2	blue	18	99
3	flow	Ru(bpy) ₃ Cl ₂	2	blue	7 h	> 95
4	batch	Ir(III)/ L ₁	2	UV	15 min	> 98
5	flow	Ir(III)/ L ₁	1	UV	2.5 min	98
6	batch	Ir(III)/ L ₁	1	UV	2.5 min	30
7	flow	----	----	UV	2.5 min	< 5
8	flow	Ru(bpy) ₃ Cl ₂	1	UV	2.5 min	6
9	batch	Ir(III)/ L ₁	1	blue	2.5 min	3
10	flow	Ir(III)/ L ₁	1	blue	2.5 min	22
11	flow	Ir(III)/ L ₁	1	violet	2.5 min	13
12	batch	Ir(III)/ L ₁	1	violet	2.5 min	2

5.3.2.1.2 Influence of the wavelength of irradiation

Interestingly, irradiating this system with UV LEDs was enough to get the reaction into completion after only 15 minutes (entry 4, Table 5.3). This was justified when performing the UV/Vis absorbance spectrum of Ir(III). The latter exhibits its maximum absorption in the UV region and absorbs slightly in the visible region (Figure 5.18). Using Ru(bpy)₃Cl₂ as catalyst under UV irradiation gave only 6% of conversion (entry 8). This is in accordance with the fact that Ru(bpy)₃Cl₂ exhibits its maximum absorption at 450 nm thus its activity is less significant when working at 365 nm. This highlights the importance of the choice of the optimum wavelength of irradiation to get higher yields in photochemical reactions. The reaction time was further diminished into only 2.5 min by combining continuous flow with UV LEDs (365 nm) although only half of the catalyst loading was used (1 mol %, entry 5). Using the same catalyst loading and irradiation time, the reaction gave 30% conversion when performed in batch (entry 6). Almost no reaction was observed in absence of the photocatalyst (entry 7 vs. entry 5).

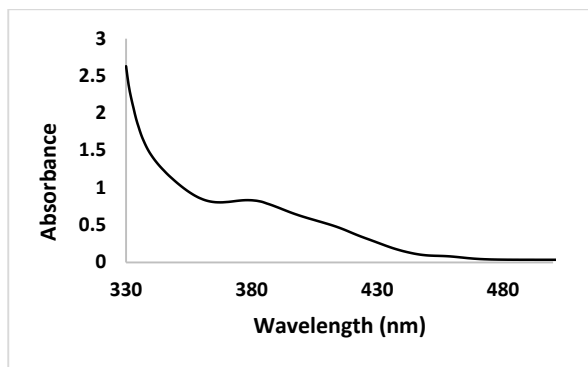


Figure 5.18: Absorption spectrum of $[\text{Ir}(\text{dF}(\text{CF}_3)\text{ppy})_2(\text{dtbbpy})](\text{PF}_6)$

The catalytic system was then assessed using violet LEDs in both batch and flow systems (entries 11, 12; Table 5.3). Only 13% of conversion was obtained after 2.5 min of violet irradiation. The switch into batch decreased the conversion to 2% (entry 12 *vs.* entry 11). Irradiation with blue LEDs exhibits better conversion than using the violet LEDs (entry 10: 22% *vs.* entry 11: 13%). This result is not in agreement with the absorption spectrum of the used catalyst where the absorption at 450 nm (blue region) is much less than that at the violet region (410 nm). Such a difference can be attributed to the difference in the power of the blue and the violet LEDs. The rate of the reaction, considering that it exhibits first order kinetics with respect to the trifluoroborates, increased by the same factor ≈ 10 folds when changing from batch system to flow system regardless of the wavelength of the used irradiation. Knowing that the batch reactions were carried out in flasks of same dimensions, this enforces the impact of the path length on the kinetics of photochemical reactions. Though the catalyst loading has a great impact on the kinetics of the reaction (entry 4 *vs.* entry 6), working using the flow system under UV with 1 mol % of catalyst loading provided the best optimized conditions of the reaction that balance between the reduction of time and that of cost.

5.3.2.1.3 Metal free photocatalyzed C-O bond formation

In order to develop a greener and more sustainable version, the organocatalyst eosin Y was tested using green LEDs under batch and flow conditions (entries 1-5, Table 5.4).

Table 5.4: Results of C-O bond formation in flow catalyzed by eosin Y in flow using green LEDS

Entry	Condition	mole %	Time (h)	% conv
1	batch	1	7	10
2	flow	1	7	70
3	flow	5	3	68
4	flow	10	3	84
5	batch	10	3	8

This catalyst proved to be efficient for the reaction of the trifluoroborate salts with TEMPO. Considering that this is a metal free catalytic system, it is a remarkable result. The reaction time decreased remarkably by increasing gradually the catalyst into 1, 5 and 10 mol % (entries 2, 3 and 4 respectively). Thus, 7 hours of irradiation in flow gave 70% conversion (entry 2), increasing the catalyst loading to 5 mol % (entry 3) was enough to decrease the irradiation time by around 2.3 folds to obtained the same level of conversion. Doubling the catalyst loading (entry 4) lead to 84% after 3 hours of irradiation. For flow device, their small path length makes it possible to work at high catalyst loading with homogeneously illumination which is hindered when working in batch conditions. Ended, with 10% of catalyst, 84 % of conversion was obtained in flow but only 8 % in batch (entries 1 and 5). However, it's important to note that when working with eosin Y which exhibits very high absorptivity at 530 nm, an increase of the catalyst loading has had a negative impact on the kinetics of the reaction.

Considering a first order with respect to the trifluoroborates: the rate of the reaction under flow condition was increased by 3.5 folds when increasing the catalyst loading from 1 to 10 mol %. On the other hand, the rate of the reaction was only increased by around 1.8

folds in batch condition (entries 1 and 5). Moreover, with a 1 mol % of catalyst loading, the rate increased by around 10 folds from batch to flow (entries 1 and 2). However, it was only increased by only 2 folds when working at 10 mol % catalyst loading. This shows that even in flow, the transmittance of light through the small path length can be seriously attenuated by increasing the loading of the photocatalyst that absorbs highly at the given wavelength. Knowing that ϵ eosin Y = 54052 M⁻¹. cm⁻¹ at λ = 530 nm, for the case of 1 mol % loading, full absorbance of light is attained after 2600 μ m which is by far more than the path length of the used microfluidic system which is 500 μ m (Beer Lambert's Law). In contrary, the 10 mol% of eosin Y will lead to the full absorbance of light after only 260 μ m which is around half the path length thus leading to the decrease in the elevation of the rate of the reaction when switching from batch to flow as a portion of the reaction mixture which is loaded into the system is not irradiated. Using eosin Y, the best condition will be 5 mol % (entry 3) whose full absorbance will be after a distance of 516 μ m which is slightly greater than the actual path length. In this case, all of the reaction mixture will be illuminated and the quantity of the catalyst is relatively big enough to increase the rate of the reaction. This shows that metal free photoredox generation of carbon centered radicals is a promising field that can be further developed.

5.3.2.2 Scope of the metal photocatalyzed reaction in flow by UV irradiation

With the optimum conditions in hand we screened the scope of the reaction with TEMPO in the Mikroglass Dwell Device under the UV irradiation by 365 nm LEDs catalyzed by 1 mol % of Ir(III)/L₁ Different benzyltrifluoroborates (with electron donating and electron withdrawing substitutions), allyltrifluoroborates, secondary, tertiary and cyclic trifluoroborates (**1h-1u**) were tested (Figure 5.19). Table 5.5 summarizes the results obtained for the reaction

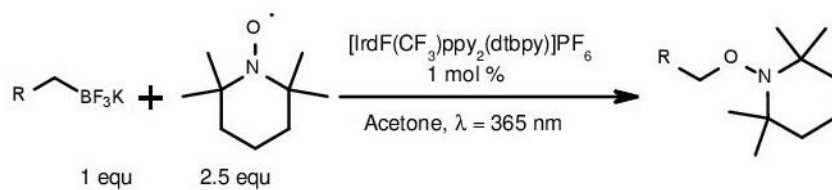
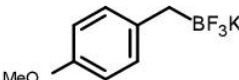
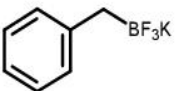
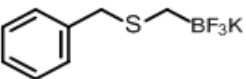
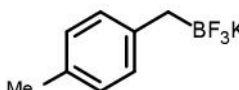
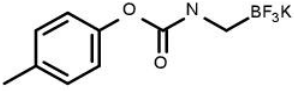
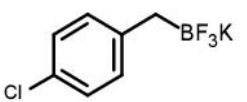
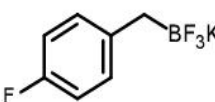
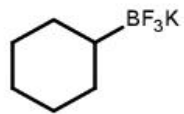
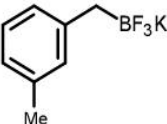
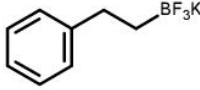
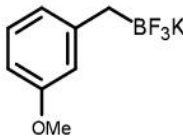


Figure 5.19: C-O bond formation of various trifluoroborates in flow using Ir(III)/ L₁ at $\lambda = 365 \text{ nm}$.

Table 5.5: Results of the C-O bond formation of various trifluoroborates in flow using Ir(III)/ L₁ at $\lambda = 365 \text{ nm}$.

Entry	Organoborate	T (min)	% yield	Entry	Organoborate	T (min)	% yield
1		2.5	98	8		40	75
2		45	89	9		60	28
3		20	99	10		60	35
4		80	38	11		360	40
5		80	90	12		360	25
6		40	98	13		360	trace
7		90	67				

First, *para* and *meta*-substituted benzyl trifluoroborates were assessed (Table 5.5, entries 1-7). Unsubstituted benzyl trifluoroborate gave 89% of conversion after 45 minutes under UV irradiation, this is a significant reduction of the reaction time since this reaction required 18 hours to go to completion under blue irradiation with higher catalyst loading (2 mol %) under batch conditions [279]. Reduced reaction time was obtained for benzyl trifluoroborates with electron donating group at the *para* position. Thus, quantitative yield was obtained in 2.5 minutes with *p*-methoxy-substituted boronate (entry 1) whereas 20 minutes were necessary for the *p*-methyl derivative (entry 3). As the stability of the formed radical increases with the increase in the strength of the electron donation [159, 253, 294], In the same way, electron withdrawing groups at the *para* position had a negative impact, on a different level, on the stability of the formed radical thus leading to an increase of the reaction time compared to the unsubstituted benzyl trifluoroborate [159, 253, 294]. For instance, the *p*-fluoro benzyl trifluoroborate needed around twice the time than the unsubstituted benzyl trifluoroborate to get the same level of conversion (entry 5) and the *p*-chloro benzyl trifluoroborate gave only 35% yield after 75 minutes of irradiation (entry 4).

The effect of substituent at the *meta* position (entries 6 and 7) was then investigated. For *m*-methyl-benzyl trifluoroborate (entry 6), the reaction time was in the same range than the non-substituted one (entry 2) but much slower than *p*-methyl trifluoroborate (20 min 99.5% vs 40 min 98 %, entry 3). The same effect was observed for the methoxy group; at the *para* position, OCH₃ had a strong stabilizing effect so the reaction was complete after couple of minutes. In contrary, OCH₃ had a destabilizing effect at the *meta* position as only 67% of conversion was achieved after 90 minutes of irradiation which is significantly less than the unsubstituted benzyl trifluoroborate. These results are discussed in the next section as a more detailed study on the kinetics of the different substituted benzyl trifluoroborates (section 5.3.3) was later performed.

The impact of the stabilization of the radical formed due to resonance was also observed when allyl trifluoroborate reacted with TEMPO to give 75% yield after only 40 minutes (entry 8). Moreover, with heteroatomic benzylic trifluoroborates (entries 9,10) the rate of the reaction was slower, the product were generated with 28 % and 35 % yield respectively along with unreacted starting material. The reaction is also compatible with tertiary alkyl trifluoroborate (entry 11). The newly developed flow process gave 40% of conversion after only 6 hours of irradiation compared to 47 % after 72 hours in batch under blue irradiation. Secondary alkyl trifluoroborate yielded 25 % of product after 6 hours. This result represents a significant improvement compared to the blue batch process since only traces of product was observed after 24 hours (entry 12) For primary alkyl trifluoroborate (entry 13) only trace of adduct was obtained. This can be explained as the redox potential of Ir (III)* /Ir (II) is 1.21 V vs. SCE compared to 1.81V vs. SCE for the trifluoroborate of entry 13 This makes the electron transfer, which is the reduction of the excited Ir III*, less likely to happen as the couple have a less oxidizing potential than the trifluoroborate. In contrast, the benzyl trifluoroborate (entry 2) has a redox potential of 1.05V vs. SCE thus can easily reduce the excited Ir (III)* into Ir (II) and liberate its corresponding radical.

5.3.3 Hammett correlation for the C-O bond formation from substituted benzylic trifluoroborates

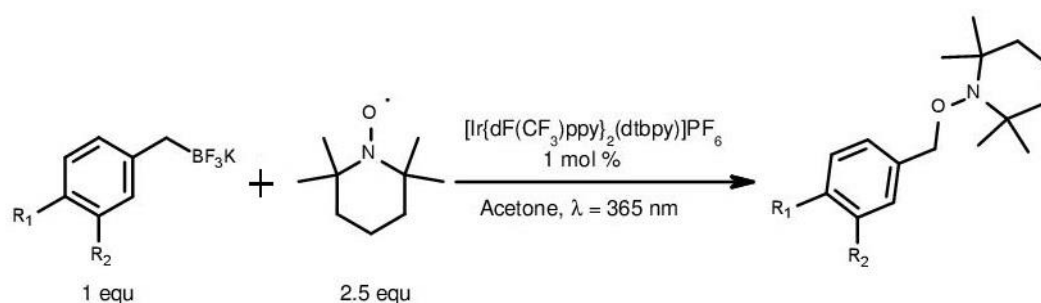


Figure 5.20: Benzyl trifluoroborates of different substitutions for C-O bond formation in flow via photoredox catalysis

After observing a remarkable impact of the type and the position of the substituents on the benzyl trifluoroborate for the coupling with TEMPO, we decided to verify whether there is a correlation between the rates of the radical addition with TEMPO and the different substituents on these benzyl trifluoroborates. This brought us to determine the Hammett equation (Figure 5.20).

The Hammett equation is a plot that relates the different reaction rates to their corresponding *meta* and *para* substituents. Every substitution has a substituent constant (σ) that indicates theoretically the impact of this substitution on the reaction rate with respect to the unsubstituted form whose σ is zero. The substituent constant σ can be considered as a quantitative description of electronic effects. It is defined as the subtraction of the pKa of benzoic acid in water from the pKa of the substituted benzoic acid: $\sigma = pK_{aX\text{-benzoic acid}} - pK_{aH\text{-benzoic acid}}$. The rate constant of the reaction in concern is determined for every substituted form. The Hammett equation is then determined by plotting $\log(k_x/k_H)$ vs. σ . The linear correlation between the obtained data shows whether the impact of the substitution on the reaction is the same or opposite to that of the ionization of benzoic acid; the reaction which was used by Hammett as a reference. Moreover, it can also predict the behavior of other substituted benzyl forms that were not covered. Knowing the σ value of a specific substituent is then enough to determine the corresponding rate constant by simply referring to the Hammett plot.

In our case, to determine the Hammett plot, the kinetic curves for the reaction of TEMPO with benzyl trifluoroborates of different substituents at the *meta* and the *para* positions and that of no substituents ($R_1=R_2=H$) are plotted. These curves were then used to extrapolate the rate constants k_x .

For a given benzyl trifluoroborate a series of five reactions of different irradiation times were performed in flow using UV irradiation. The percentage of conversion was

determined by ^1H NMR with an internal standard. Note that for every reaction, 1 mol % of Ir(III)/ L_1 , 2.5 eq of TEMPO and 1 eq of standard are added with respect to the trifluoroborate (50 μmol) that are dissolved in acetone. The time of irradiation was regulated by adjusting the flow rate of the syringe pump and the flow system used is the Mikroglass Dwell Device (i.d = 500 μm). Table 5.6 includes the different benzylic trifluoroborates that were used in this study.

Table 5.6: The substituted benzyl trifluoroborates used in this study

Entry	R ₁	R ₂
1	H	H
2	OMe	H
3	Cl	H
4	F	H
5	Me	H
6	H	OMe
7	H	Me

The rate law of the reaction can be written as follows (Equation 5.1):

$$V_{(t)} = k \times [\text{RBF}_3\text{K}]_t^a \times [\text{TEMPO}]_t^b \quad \text{Equation 5.1}$$

So we formulate a hypothesis that the reactions follows a first order kinetics with respect to the trifluoroborate. Thus we can deduce the following equations (Equations 5.2-5.6):

$$-\frac{d[\text{RBF}_3\text{K}]}{dt} = k[\text{RBF}_3\text{K}] \quad \text{Equation 5.2}$$

$$[\text{RBF}_3\text{K}]_t = [\text{RBF}_3\text{K}]_0 \times e^{-kt} \quad \text{Equation 5.3}$$

$$\ln \frac{[\text{RBF}_3\text{K}]_t}{[\text{RBF}_3\text{K}]_0} = -kt \quad \text{Equation 5.4}$$

$$[RBF_3K]_t = [RBF_3K]_0 - [x] \quad \text{Equation 5.5}$$

$$\ln(1 - x) = -kt \quad \text{Equation 5.6}$$

Where $[x]$ is the concentration of the formed adduct and x is its fraction. So a linear plot will be obtained for the variation of the logarithmic of the fraction $1-x$ with respect to irradiation time t .

5.3.2.1 Benzyl trifluoroborate

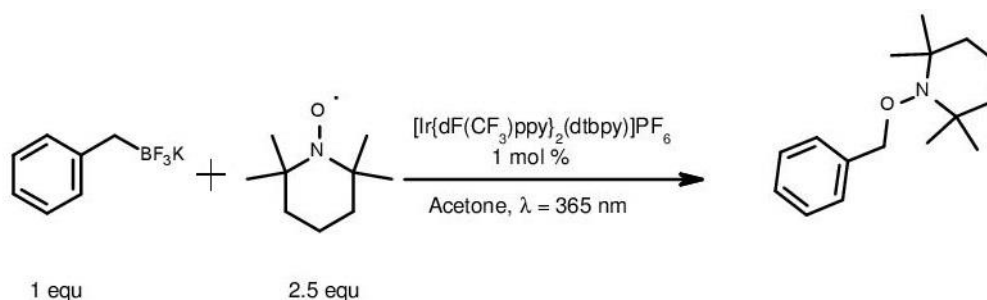


Figure 5.21: Reaction of benzyl trifluoroborate with TEMPO in flow via Ir(III)/ L₁ catalysis in UV

The results of the reaction of benzyl trifluoroborate with an excess of TEMPO catalyzed by Ir(III)/ L₁ (1 mol %) under UV are summarized in the Table 5.7 (Figure 5.21):

Table 5.7: Results of the flow reaction of benzyl trifluoroborate with TEMPO

Flow rate ($\mu\text{L}\cdot\text{min}^{-1}$)	Irradiation time (min)	% Conv
460	2.5	8
288	4	16
192	6	22
115	10	37
25	46	89

$$-\frac{d[\text{C}_6\text{H}_5\text{CH}_2\text{BF}_3\text{K}]}{dt} = k_H[\text{C}_6\text{H}_5\text{CH}_2\text{BF}_3\text{K}]$$

$$[\text{C}_6\text{H}_5\text{CH}_2\text{BF}_3\text{K}]_t = [\text{C}_6\text{H}_5\text{CH}_2\text{BF}_3\text{K}]_0 \times e^{-k_H t}$$

$$\ln \frac{[\text{C}_6\text{H}_5\text{CH}_2\text{BF}_3\text{K}]_t}{[\text{C}_6\text{H}_5\text{CH}_2\text{BF}_3\text{K}]_0} = -k_H t$$

$$[\text{C}_6\text{H}_5\text{CH}_2\text{BF}_3\text{K}]_t = [\text{C}_6\text{H}_5\text{CH}_2\text{BF}_3\text{K}]_0 - [x]_H$$

$$\ln(1 - x_H) = -k_H t \quad \text{Equation 5.7}$$

The plot of $\ln(x_H)$ vs. t (Equation 5.7) gave a strictly straight line with a correlation coefficient of 0.999 (Figure 5.22). This shows that the reaction follows a first order kinetics with respect to the trifluoroborate and thus verifies the assumed hypothesis. The rate constant k_H in this case will be the slope of the plot which is $0.0477 \cdot \text{min}^{-1}$. This value of the constant rate k_H will be considered as the reference value for the Hammett equation.

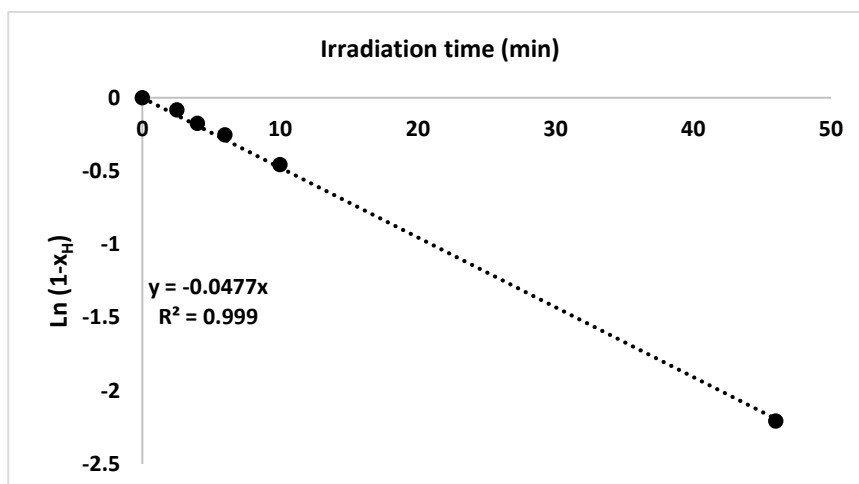


Figure 5.22: Kinetic plot of the flow reaction of benzyl trifluoroborate with TEMPO

5.3.2.2 *p*-methoxybenzyl trifluoroborate

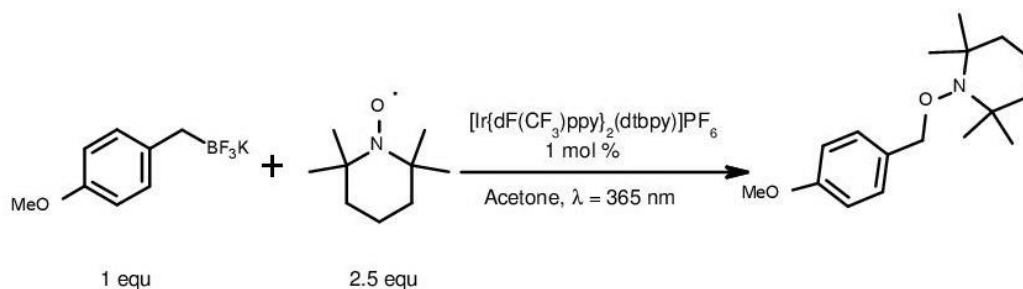


Figure 5.23: Reaction of *p*-methoxybenzyl trifluoroborate with TEMPO in flow via Ir(III)/ L_1 catalysis in UV

The variation of the % of conversion in response to the irradiation time of the reaction in Figure 5.23 is summarized in the Table 5.8.

Table 5.8: Results of the flow reaction of *p*-methoxybenzyl trifluoroborate with TEMPO

Flow rate ($\mu\text{L}\cdot\text{min}^{-1}$)	Irradiation time (min)	% Conv
460	2.5	98
575	2	94
767	1.50	87
1150	1	76
1725	0.67	58
2300	0.5	43

$$-\frac{d[\text{p-OCH}_3\text{C}_6\text{H}_4\text{CH}_2\text{BF}_3\text{K}]}{dt} = k_{p\text{-OCH}_3}[\text{p-OCH}_3\text{C}_6\text{H}_4\text{CH}_2\text{BF}_3\text{K}]$$

$$[\text{p-OCH}_3\text{C}_6\text{H}_4\text{CH}_2\text{BF}_3\text{K}]_t = [\text{p-OCH}_3\text{C}_6\text{H}_4\text{CH}_2\text{BF}_3\text{K}]_0 \times e^{-k_{p\text{-OCH}_3}t}$$

$$\ln \frac{[\text{p-OCH}_3\text{C}_6\text{H}_4\text{CH}_2\text{BF}_3\text{K}]_t}{[\text{p-OCH}_3\text{C}_6\text{H}_4\text{CH}_2\text{BF}_3\text{K}]_0} = -k_{p\text{-OCH}_3}t$$

$$[\text{p-OCH}_3\text{C}_6\text{H}_4\text{CH}_2\text{BF}_3\text{K}]_t = [\text{p-OCH}_3\text{C}_6\text{H}_4\text{CH}_2\text{BF}_3\text{K}]_0 - [x]_{p\text{-OCH}_3}$$

$$\ln(1 - x_{p\text{-OCH}_3}) = -k_{p\text{-OCH}_3}t \quad \text{Equation 5.8}$$

The plot of $\ln(1 - x_{p\text{-OCH}_3})$ (Equation 5.8) is represented in Figure 5.24. The *p*-methoxy substituent had a significant impact on the rate of the reaction compared to the unsubstituted benzyl trifluoroborate. The kinetic curve fits perfectly with the first order kinetics with a slope of $k_{p\text{-OCH}_3} = 1.3434 \text{ min}^{-1}$ and a correlation coefficient of 0.993.

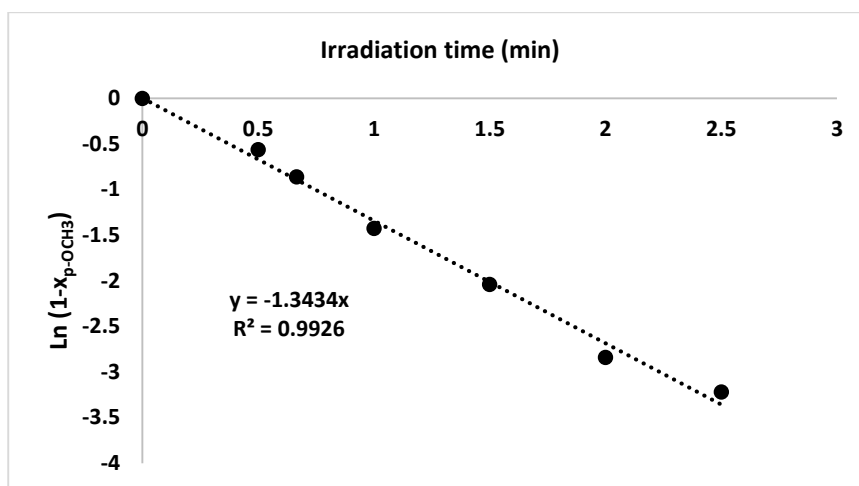


Figure 5.24: Kinetic plot of the flow reaction of *p*-methoxybenzyl trifluoroborate with TEMPO

5.3.2.3 *p*-methylbenzyl trifluoroborate

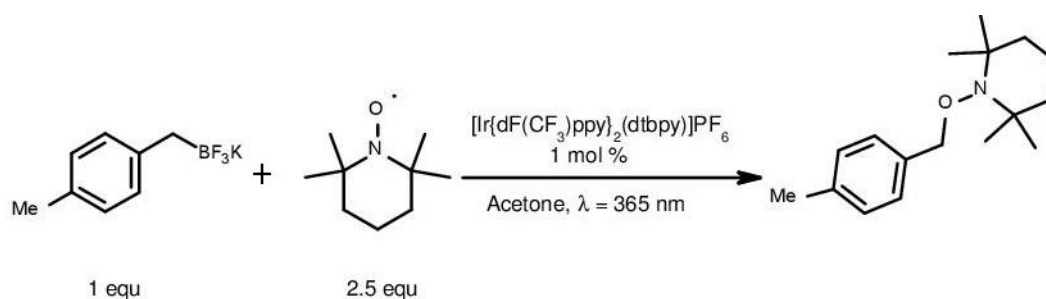


Figure 5.25: Reaction of *p*-methylbenzyl trifluoroborate with TEMPO in flow via Ir(III)/ *L*₁ catalysis in

UV

The *p*-methylbenzyl trifluoroborate's C-O bond formation with TEMPO (Figure 5.25) took only 20 minutes to have almost full conversion. The whole set of data gathered are summarized in the Table 5.9. Its linear kinetic curve of Equation 5.9 gives a rate constant of $k_{p\text{-CH}_3} = 0.2626 \text{ min}^{-1}$ with a high correlation coefficient R^2 of 0.998 (Figure 5.26).

Table 5.9: Results of the flow reaction of *p*-methylbenzyl trifluoroborate with TEMPO

Flow rate ($\mu\text{L}\cdot\text{min}^{-1}$)	Irradiation time (min)	% Conv
460	2.5	52
230	5	75
115	10	91
575	2	446
57.5	20	99.5

$$-\frac{d[\text{p-CH}_3\text{C}_6\text{H}_4\text{CH}_2\text{BF}_3\text{K}]}{dt} = k_{\text{p-CH}_3} [\text{p-CH}_3\text{C}_6\text{H}_4\text{CH}_2\text{BF}_3\text{K}]$$

$$[\text{p-CH}_3\text{C}_6\text{H}_4\text{CH}_2\text{BF}_3\text{K}]_t = [\text{p-CH}_3\text{C}_6\text{H}_4\text{CH}_2\text{BF}_3\text{K}]_0 \times e^{-k_{\text{p-CH}_3}t}$$

$$\ln \frac{[\text{p-CH}_3\text{C}_6\text{H}_4\text{CH}_2\text{BF}_3\text{K}]_t}{[\text{p-CH}_3\text{C}_6\text{H}_4\text{CH}_2\text{BF}_3\text{K}]_0} = -k_{\text{p-CH}_3}t$$

$$[\text{p-CH}_3\text{C}_6\text{H}_4\text{CH}_2\text{BF}_3\text{K}]_t = [\text{p-CH}_3\text{C}_6\text{H}_4\text{CH}_2\text{BF}_3\text{K}]_0 - [x]_{\text{p-CH}_3}$$

$$\ln(1 - x_{\text{p-CH}_3}) = -k_{\text{p-CH}_3}t$$

Equation 5.9

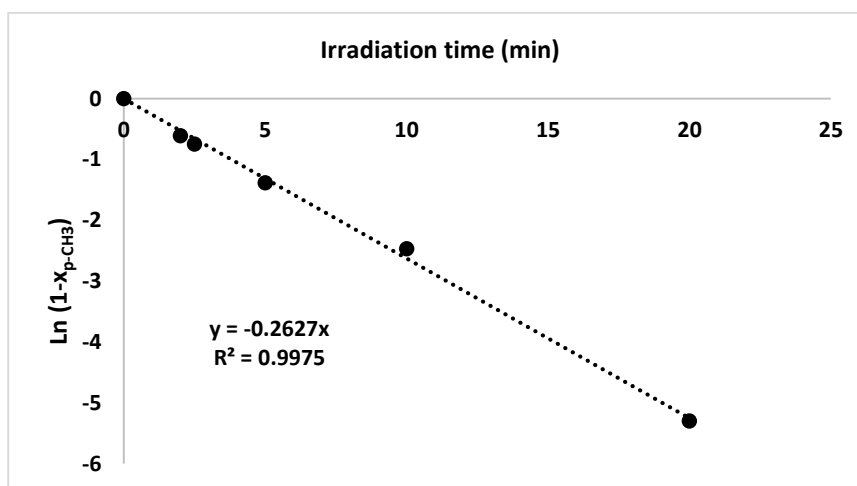


Figure 5.26: Kinetic plot of the flow reaction of *p*-methylbenzyl trifluoroborate with TEMPO

5.3.2.4 *p*-chlorobenzyl trifluoroborate

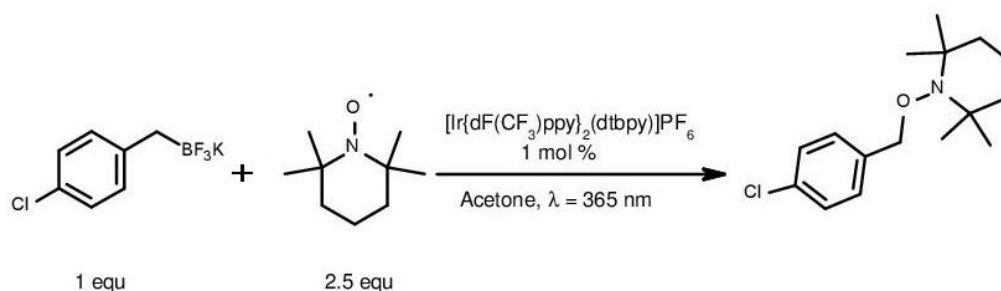


Figure 5.27: Reaction of *p*-chlorobenzyl trifluoroborate with TEMPO in flow via Ir(III)/ *L*₁ catalysis in

UV

$$-\frac{d[\text{p-ClC}_6\text{H}_4\text{CH}_2\text{BF}_3\text{K}]}{dt} = k_{p\text{-Cl}}[\text{p-ClC}_6\text{H}_4\text{CH}_2\text{BF}_3\text{K}]$$

$$[\text{p-ClC}_6\text{H}_4\text{CH}_2\text{BF}_3\text{K}]_t = [\text{p-ClC}_6\text{H}_4\text{CH}_2\text{BF}_3\text{K}]_0 \times e^{-k_{p\text{-Cl}}t}$$

$$\ln \frac{[\text{p-ClC}_6\text{H}_4\text{CH}_2\text{BF}_3\text{K}]_t}{[\text{p-ClC}_6\text{H}_4\text{CH}_2\text{BF}_3\text{K}]_0} = -k_{p\text{-Cl}}t$$

$$[\text{p-ClC}_6\text{H}_4\text{CH}_2\text{BF}_3\text{K}]_t = [\text{p-ClC}_6\text{H}_4\text{CH}_2\text{BF}_3\text{K}]_0 - [x]_{p\text{-Cl}}$$

$$\ln(1 - x_{p\text{-Cl}}) = -k_{p\text{-Cl}}t \quad \text{Equation 5.10}$$

The presence of the chloro substituent at the para position remarkably decreased the reaction rate (Table 5.10) of the reaction represented in Figure 5.27. This is displayed by the slight inclination of its kinetic curve of equation 5.10 with $k_{p\text{-Cl}} = 0.0059 \text{ min}^{-1}$ as a slope (Figure 5.28). However there still exist a good correlation coefficient among the data collected ($R^2=0.988$).

Table 5.10: Results of the flow reaction of *p*-chlorobenzyl trifluoroborate with TEMPO

Flow rate ($\mu\text{L}\cdot\text{min}^{-1}$)	Irradiation time (min)	% Conv
57.5	20	12
115	10	7.5
46	25	15
23	50	27
15	77	35

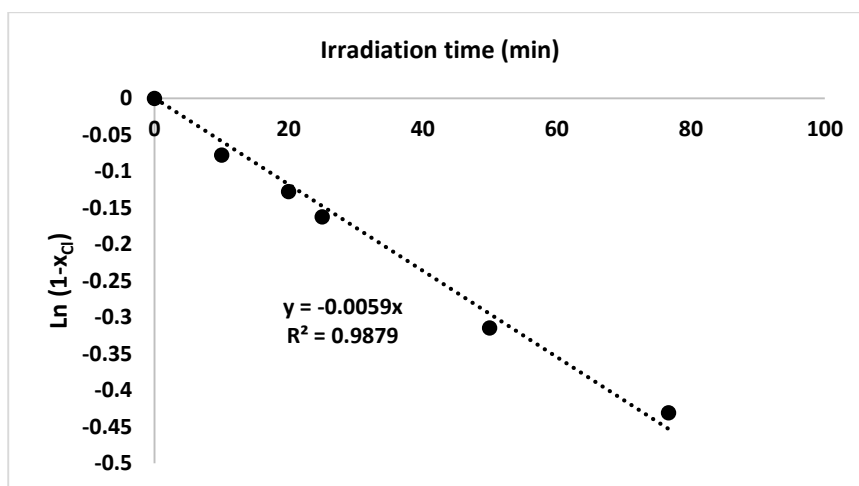


Figure 5.28: Kinetic plot of the flow reaction of *p*-chlorobenzyl trifluoroborate with TEMPO

5.3.2.5 *p*-Fluorobenzyl trifluoroborate

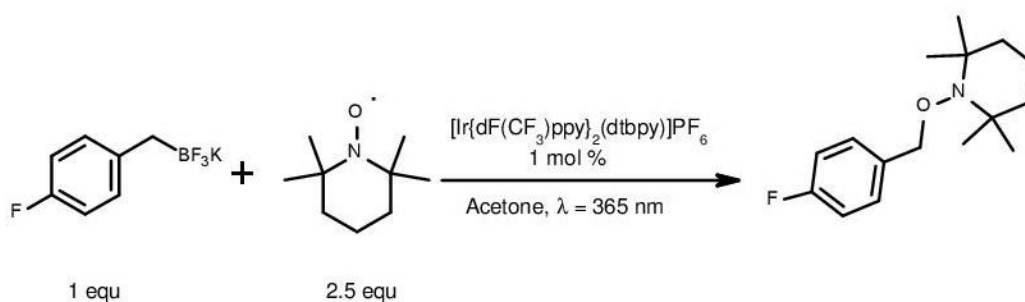


Figure 5.29: Reaction of *p*-fluorobenzyl trifluoroborate with TEMPO in flow via Ir(III)/ *L*₁ catalysis in

UV

90 % conversion of the fluorobenzyl trifluoroborate into its corresponding TEMPO adduct was obtained after 80 minutes of UV irradiation in flow (Table 5.11, Figure 5.29). This is by far much faster than with the chloro substitution. From the linear graph of correlation coefficient of 0.989, we can deduce that the rate constant k_{p-F} of the fluorobenzyl substituent is 0.0284 min^{-1} (Figure 5.30, Equation 5.11).

Table 5.11: Results of the flow reaction of *p*-fluorobenzyl trifluoroborate with TEMPO

Flow rate ($\mu\text{L}\cdot\text{min}^{-1}$)	Irradiation time (min)	% Conv
152	15	26
114	20	33
57	40	68
38	60	82
28.5	80	90
60	38	67

$$-\frac{d[\text{p} - \text{FC}_6\text{H}_4\text{CH}_2\text{BF}_3\text{K}]}{dt} = k_{\text{p-F}}[\text{p} - \text{FC}_6\text{H}_4\text{CH}_2\text{BF}_3\text{K}]$$

$$[\text{p} - \text{FC}_6\text{H}_4\text{CH}_2\text{BF}_3\text{K}]_t = [\text{p} - \text{FC}_6\text{H}_4\text{CH}_2\text{BF}_3\text{K}]_0 \times e^{-k_{\text{p-F}}t}$$

$$\ln \frac{[\text{p} - \text{FC}_6\text{H}_4\text{CH}_2\text{BF}_3\text{K}]_t}{[\text{p} - \text{FC}_6\text{H}_4\text{CH}_2\text{BF}_3\text{K}]_0} = -k_{\text{p-F}}t$$

$$[\text{p} - \text{FC}_6\text{H}_4\text{CH}_2\text{BF}_3\text{K}]_t = [\text{p} - \text{FC}_6\text{H}_4\text{CH}_2\text{BF}_3\text{K}]_0 - [x]_{\text{p-F}}$$

$$\ln(1 - x_{\text{p-F}}) = -k_{\text{p-F}}t$$

Equation 5.11

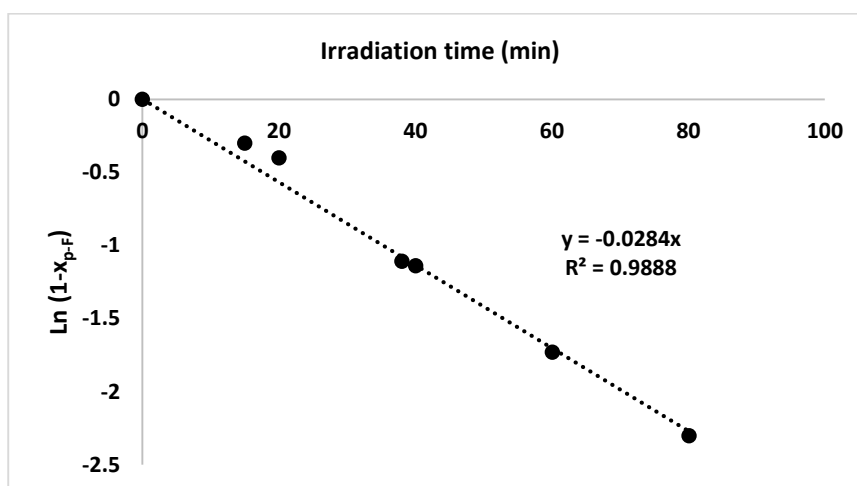


Figure 5.30: Kinetic plot of the flow reaction of *p*-fluoro benzyl trifluoroborate with TEMPO

5.3.2.6 *m*-methylbenzyl trifluoroborate

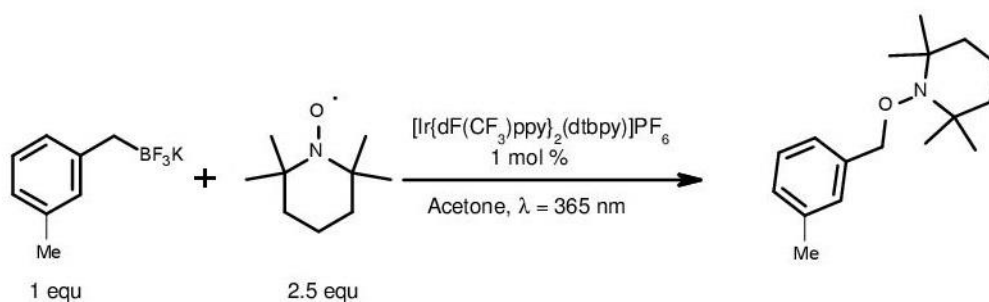


Figure 5.31: Reaction of *m*-methylbenzyl trifluoroborate with TEMPO in flow via Ir(III)/ L₁ catalysis in UV

The effect of the *meta* position substitution on the rate of the reaction was assessed using *m*-methylbenzyl trifluoroborate as a substrate (Figure 5.31). The % of conversion with respect to the irradiation time was affected by this substitution (Table 5.12).

Table 5.12: Results of the flow reaction of *m*-methylbenzyl trifluoroborate with TEMPO

Flow rate ($\mu\text{L}\cdot\text{min}^{-1}$)	Irradiation time (min)	% Conv
575	2	14
115	10	54
57.5	20	87
288	4	24
28.75	40	98
76.5	15	72

$$-\frac{d[m - \text{CH}_3\text{C}_6\text{H}_4\text{CH}_2\text{BF}_3\text{K}]}{dt} = k_{m-\text{CH}_3}[m - \text{CH}_3\text{C}_6\text{H}_4\text{CH}_2\text{BF}_3\text{K}]$$

$$[m - \text{CH}_3\text{C}_6\text{H}_4\text{CH}_2\text{BF}_3\text{K}]_t = [m - \text{CH}_3\text{C}_6\text{H}_4\text{CH}_2\text{BF}_3\text{K}]_0 \times e^{-k_{m-\text{CH}_3}t}$$

$$\ln \frac{[m - \text{CH}_3\text{C}_6\text{H}_4\text{CH}_2\text{BF}_3\text{K}]_t}{[m - \text{CH}_3\text{C}_6\text{H}_4\text{CH}_2\text{BF}_3\text{K}]_0} = -k_{m-\text{CH}_3}t$$

$$[m - \text{CH}_3\text{C}_6\text{H}_4\text{CH}_2\text{BF}_3\text{K}]_t = [m - \text{CH}_3\text{C}_6\text{H}_4\text{CH}_2\text{BF}_3\text{K}]_0 - [x]_{m-\text{CH}_3}$$

$$\ln(1 - x_{m-\text{CH}_3}) = -k_{m-\text{CH}_3}t \quad \text{Equation 5.12}$$

Indeed the plot of the logarithm of $(1-x_{m-CH_3})$ vs. the irradiation time (Equation 5.12, Figure 5.32) gave a straight line of correlation coefficient of 0.992 and a slope 0.0962 min^{-1} that corresponds to the value of the rate constant of this reaction.

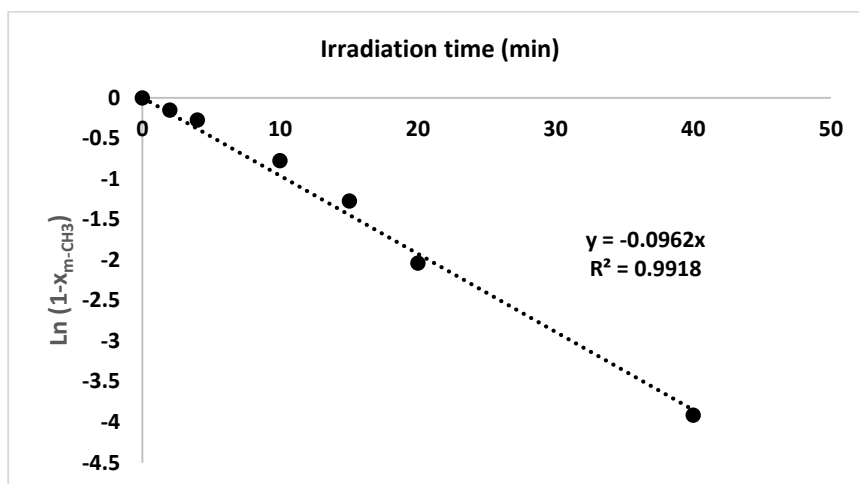


Figure 5.32: Kinetic plot of the flow reaction of *m*-methylbenzyl trifluoroborate with TEMPO

5.3.2.7 *m*-methoxybenzyl trifluoroborate

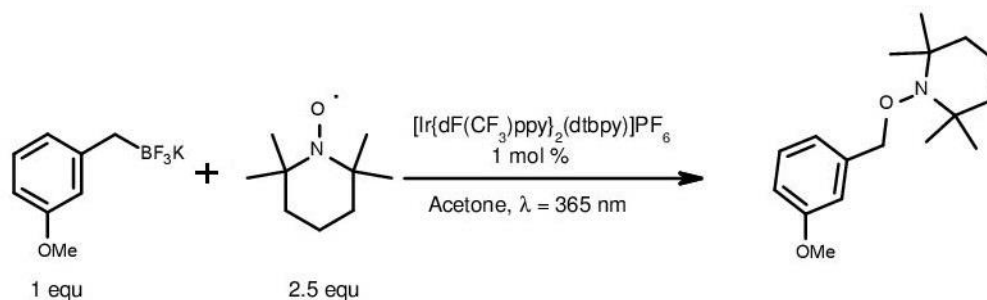


Figure 5.33: Reaction of *m*-methoxybenzyl trifluoroborate with TEMPO in flow via Ir(III)/ L_1 catalysis in UV

The variation of the formation of the C-O bond of TEMPO with the benzyl trifluoroborate having methoxy substitution at the *meta* position with respect to the irradiation time (Figure 5.33) is summarized in the Table 5.13. Similar to the previous cases where the reaction follows a first order kinetics (Equation 5.13), the plot of $\ln(1-x)$ vs. t gave

a straight line of high correlation coefficient ($R^2 = 0.984$). The rate constant of this reaction extrapolated from the given graph is 0.0833 min^{-1} (Figure 5.34).

Table 5.13: Results of the flow reaction of *m*-methoxybenzyl trifluoroborate with TEMPO

Flow rate ($\mu\text{L}\cdot\text{min}^{-1}$)	Irradiation time (min)	% Conv
76.6	15	18
57.5	20	30
28.75	40	38
12.78	90	67

$$-\frac{d[(m - OCH_3C_6H_4CH_2BF_3K)]}{dt} = k_{m-OCH_3}[m - OCH_3C_6H_4CH_2BF_3K]$$

$$[m - OCH_3C_6H_4CH_2BF_3K]_t = [m - OCH_3C_6H_4CH_2BF_3K]_0 \times e^{-k_{m-OCH_3}t}$$

$$\ln \frac{[m - OCH_3C_6H_4CH_2BF_3K]_t}{[m - OCH_3C_6H_4CH_2BF_3K]_0} = -k_{m-OCH_3}t$$

$$[m - OCH_3C_6H_4CH_2BF_3K]_t = [m - OCH_3C_6H_4CH_2BF_3K]_0 - [x]_{m-OCH_3}$$

$$\ln(1 - x_{m-OCH_3}) = -k_{m-OCH_3}t \quad \text{Equation 5.13}$$

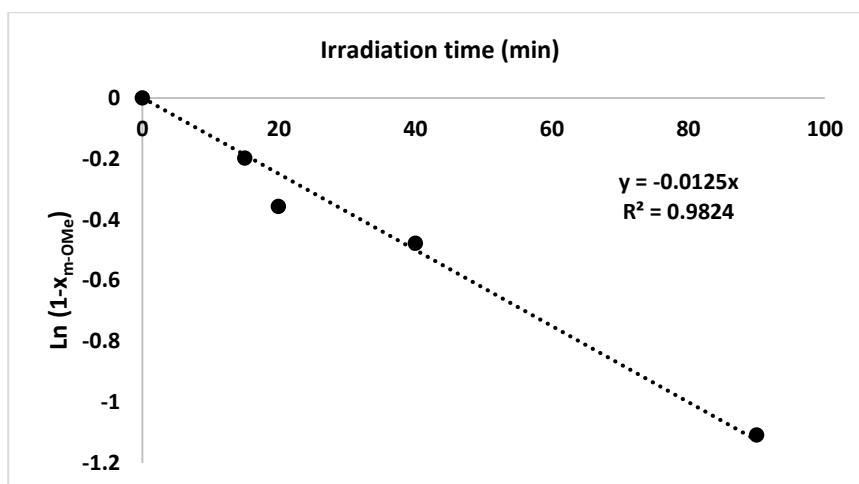


Figure 5.34: Kinetic plot of the flow reaction of *m*-methoxybenzyl trifluoroborate with TEMPO

5.3.2.8 Hammett plot

For each of the substituted benzyl trifluoroborate, the rate constant k_x of its reaction with TEMPO displayed in this work along with the sigma and sigma⁺ values given by literature are summarized in the Table 5.14.[294]

Table 5.14: Summary of the rate constants, σ and σ^+ values [294] of each of the tested substituted benzyl trifluoroborates.

Entry	R ₁	R ₂	k _(x) (min ⁻¹)	σ	σ^+	log(k _x /k _H)
1	H	H	0.0477	0	0	0
2	OMe	H	1.3434	-0.268	-0.778	1.4496
3	Me	H	0.2627	-0.17	-0.311	0.7409
4	Cl	H	0.0059	0.227	0.114	-0.9077
5	F	H	0.0284	0.062	-0.073	-0.2252
6	H	Me	0.0962	-0.069	-0.066	0.3047
7	H	OMe	0.0125	0.115	0.047	-0.5816

The impact of the substitution, whether type (-OCH₃, -CH₃, Cl and F) or position (*para* and *meta*) was significant on the rate of the reaction with TEMPO using Ir(III)/ L₁ and UV LEDs in continuous flow. Note that in all of the cases there was a strong linear correlation between the variations of the logarithm of the substrate with respect to irradiation times confirming the first order nature of the kinetics with respect to the substrate. The obtained constant k (k = 0.0477 min⁻¹) obtained for benzyl trifluoroborate (entry 1) is considered the reference for the Hammett experiment. The *para*-methoxy substitution gave the biggest implement in the kinetics of the reaction with a k value of 1.3434 min⁻¹ (entry 2). This shows that electron donating substitutions at the *para* position have a positive impact on the kinetics. In the same course but to a less extent the methyl substitution at the *para* position

also increased the rate of the reaction (Entry 3). On the other hand, electron withdrawing substituents like F (Entry 4) and Cl (Entry 5) had a negative impact on the kinetics of the reaction as their corresponding rate constants, 0.0059 min^{-1} and 0.0284 min^{-1} , are less than that of the reference rate constant 0.0477 min^{-1} . As for the *meta* substitution, the methyl group kept its positive effect on the kinetics of the reaction (Entry 6) whereas the methoxy group switched from supporting to diminishing the rate of the reaction (Entry 7).

To explain this variation we should note that the more stable the radical formed is, the more favored the reaction will be. Whenever a substitution is added into a position, two factors determine whether it will have a stabilizing or destabilizing effect: resonance and inductive effects [159, 253, 294].

For our system, in order for the radical to be formed, an electron should be released out of the benzyl trifluoroborate. The electron withdrawing groups like Cl and F tend to decrease the electronic density of the bond making it less likely to undergo oxidation thus exhibiting a destabilizing effect. In contrary, the methyl group has an electron donating inductive effect which is much significant at the *para* position than the *meta* position. The methyl group thus has a stabilizing effect regardless of its position [159, 253, 294].

At the *para* position, the methoxy group has a strong resonance effect due to the oxygen's lone pair that contributes with the resonance structures. This renders the methoxy group to have a stabilizing effect as the radical to be formed will be stabilized by resonance that the methoxy group participates in. In contrary, at the *meta* position the methoxy group loses this resonance effect to the electron withdrawing inductive effect of the electronegative oxygen (as in Cl and F) leading to a destabilizing effect [159, 253, 294].

To determine the correlation between the impact of the substituents of a benzyl group on the kinetics of the reaction, two parameters: Hammett σ and Brown-Okamoto σ^+ are mainly used.

So we decided to plot and compare both correlations ($\log(k_x/k_H)$ vs σ and vs σ^+). By referring to the Figure 5.35, it is clear that the correlation with respect to σ constant is almost linear with $R^2 = 0.9816$ in contrast to that with the σ^+ constant that has a correlation coefficient of 0.7816. The value of the sensitivity constant ρ corresponds to the slope of the obtained straight line which is -4.7241. The negative sign of the sensitivity constant indicates that during the mechanism of the rate determining step, a loss of charge is observed. This is in accordance with the proposed mechanism as the generation of the radical out of the trifluoroborate, which is most likely to be the rate determining step, takes place as a result of the loss of 1 electron that is given to the Ir(III)*/L₁ catalyst for its reductive quenching to Ir(II)/L₁. Although there are studies support that σ^+ provides better correlations for radical experiments [295], this topic is still controversial as Pryor *et al.* emphasized that ‘there is no reason to assume that correlations for radical reactions are accurately measured by the σ^+ scale’[296]. The experiments that favor σ^+ were based on the extraction of the H from toluene. This shows that when it comes to radical reactions, the optimum correlation coefficients are case dependent and no general rule can be established especially with the absence of σ^+ scale that can be generalized to fit all of the radical reactions [297].

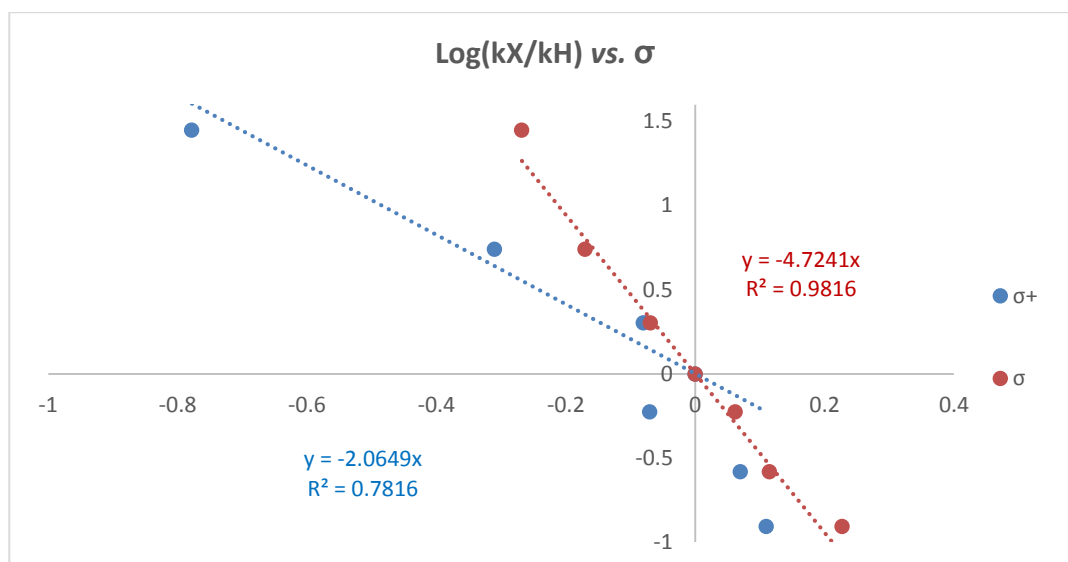


Figure 5.35: Hammett plot using σ (red) and σ^+ (blue) values

5.3.4 C-C bond formation from potassium trifluoroborates under UV in flow

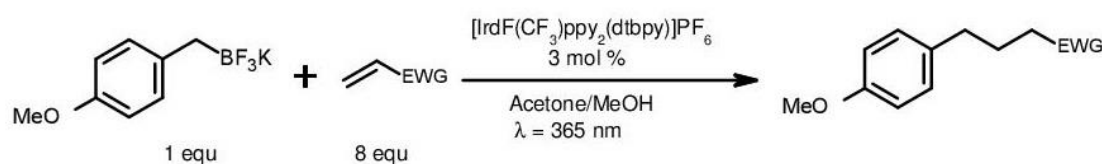


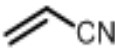
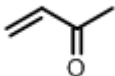
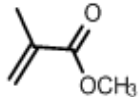
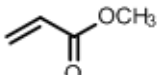
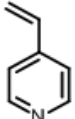
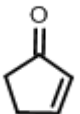
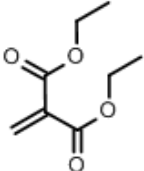
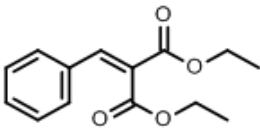
Figure 5.36: C-C bond formation in flow via photoredox catalysis in UV

We demonstrated that the photoredox catalyst Ir(III)/ L_1 is capable of generating radicals from trifluoroborates in flow under UV irradiation within tens of minutes. So the second step was to extend the range of applications for such a system by add this radical to an excess (8 eq) of an alkene bearing an EWG that would favor such an addition. The excess of the Michael acceptor was important as working with 1 eq led to the formation of a homocoupling product.

We selected *p*-methoxy trifluoroborate as it exhibited full formation of the corresponding radical after only 2.5 minutes. We then assessed its addition to various alkenes using 3 mol % of Ir(III) / L_1 in acetone/ MeOH 3:1 (Figure 5.36). The flow system used was

the Mikglass Dwell device that was irradiated by UV LEDs 365 nm of irradiance 230 mW.cm⁻¹. Table 5.15 summarizes the results obtained.

Table 5.15: Results of the C-C bond formation in flow using Ir(III)*/L₁ as a photocatalyst at 365 nm wavelength

Entry	Alkene	Time	% yield
1		15 min	94
2		30 min	90
3		30 min	57
4		30 min	43
5		3 h	48
6		3 h	40
7		3h	0
8		3h	trace
9		3h	0

The addition of the *p*-methoxy benzyl trifluoroborate to acrylonitrile catalyzed by Ir(III)/ L₁ in flow gave 94 % after only 15 minutes (entry 1). This result is by far more enhanced than the batch condition that gave 85 % after 10 hours [279]. The addition to butyl vinyl ketone was also efficient to give 90 % conversion after 30 minutes (entry 2). Methyl methacrylate (entry 3) and methyl acrylate (entry 4) gave 57% and 43 % conversion respectively after 30 minutes of irradiation in flow.

The addition of the trifluoroborate to 4-vinyl pyridine needed around 3 hours to give around 48% of the coupled product (entry 5), slightly more than the cyclic alkene, 2-cyclohexen-1-one that gave 40 % conversion for the same irradiation time (entry 6). In contrary the radical formed from the benzyl trifluoroborate was incapable of coupling with the cyclopenten-1-one (entry 7). Though having a strong electron withdrawing group moiety, 1, 3-diethyl ester-2-methylene-propanedioic acid only gave trace of the coupling product after 3 hours (entry 8). This can be due to steric hindrance as both molecules have relatively large substituents. In the same course the more substituted propanedioic acid of entry 9 also didn't successfully add to the *p*-methoxy trifluoroborate radical.

5.4 Conclusion

Research on trifluoroborates is gaining a lot of attention thanks to their high reactivity and stability, eco-compatibility and tolerance to wide range of functional groups. There are many reports in literature that use trifluoroborates as coupling partners for metal catalyzed cross-coupling reactions. In addition, these species are a good source of radical as they can undergo oxidation in the presence of oxidants. However, in most of the cases harsh basic and thermal conditions are needed. To overcome these limitations, an elegant methodology was developed to generate radical from trifluoroborates salt by Photoredox catalysts to allowing the formation of C-O and C-C bond Reaction times however were relatively

long (10-24 h) and the conditions were not compatible with primary and secondary alkyl trifluoroborates. To improve this methodology we decided to perform the reaction in flow under the UV conditions instead of using blue LEDs since Ir(III) / L₁ absorbs much more at 365 nm than 450 nm. Indeed the combination of UV irradiation and flow decreased dramatically the reaction times and radical was generated from secondary trifluoroborates salts. The variation of the rate of the reactions for different substituted benzyl trifluoroborates was shown to be in linear correlation ($R^2 = 0.981$) with the σ values given for the Hammett correlation plot. This gives the possibility to predict the kinetics of a wide range of benzyl substituents by simply knowing their corresponding σ values that are reported in literature. A metal free version was also developed with eosin y as catalyst in flow, this new methodology was shown to be more efficient than the reported metal based catalyzed reaction in batch. This confirms the remarkable potential of flow chemistry for UV photocatalyzed process.

CHAPTER SIX

CONCLUSION

The work presented herein was concerned with the exploration of various photochemical reactions using the microflow technology.

Chapter 1 introduced briefly both concepts of photochemistry and microflow technology. It emphasized the factors rendering miniaturization a key point in improving the productivity and selectivity of photochemical reactions. The chapter was concluded with several examples listed in literature of photochemical reactions performed in flow.

Chapter 2 focused on developing a rapid chemical actinometric technique that measures the quantity of light that reaches the reaction mixture in a microfluidic system. Azobenzene was used as the chemical actinometer. Numerical equations were developed to work with concentrated solutions of azobenzene to get a rapid and simple analysis using ^1H NMR spectroscopy. These numerical equations were proved to be efficient and gave irradiance values that are close to the expected when working using different solvents and LEDs powers. This protocol can be further developed to cover wider range of wavelengths as this work was only checked on 365nm.

Chapter 3 described the intramolecular [2+2] cycloaddition in both visible and UV light using microflow technology. When working under UV, sensitization was needed to work using UV-B irradiation instead of the high energy UV-A irradiation for the chosen [2+2] intramolecular cycloaddition of 3-oxa-1,5-hexadienones. Sensitization was enough for the reaction to take place. Using the flow technology and HP UV LEDs, the cycloaddition of the slowest substrate assessed **1a** was quantitative after around 2 hours of irradiation compared to 57% after 10 hours of irradiation when performed in batch using UV-A source. Kinetic assessments confirmed the first order nature of this intramolecular reaction and the

second order nature of the pinacolization of the sensitizer. The only limitation of the provided protocol was the inability to purify the formed cycloadduct from the sensitizer used. One of the solutions for this problem is using Merrifield or SBA 15 that are grafted with the sensitizer for the reaction to be performed, in batch, using UV-B irradiation.

Working using Ru(bpy)₃Cl₂ in blue for the intramolecular [2+2] cycloaddition of bisenone **1f** was also assessed in flow. The irradiation time was decreased by 4 folds compared to batch conditions. However, another competitive reaction, reductive cyclization, was also taking place regardless of the reactor used. Kinetic studies confirmed that intramolecular [2+2] cycloaddition and reductive cyclization are competitive (parallel) reactions.

Chapter 4 covered controlled polymerization of methyl methacrylate in flow using different catalysts including the metal free eosin Y. Interestingly, eosin Y was shown to be an efficient photoredox catalyst when working using green LEDs as it provided 90% yield after only 3 hours of irradiation in a tubing fluidic device. The polymers formed had good polydispersity indices (≈ 1.5), with their M_n values in accordance to the theoretical values. Changing from the batch to the flow conditions remarkably improved the reactivity and the quality of the formed polymers as in batch 24 hours of irradiation was needed to get polymers of broad dispersity (PDI= 1.8). Eosin Y mediated ATRP was shown to be controlled by light exposure. The polymers formed were also used as macroinitiators proving their livingness. Eosin y can be easily removed by water, is metal free and cost effective as it is available for public use (13 € for 1 g).

Chapter 5 included the assessment of iridium catalyzed generation of carbon radicals from trifluoroborates via UV-B irradiation in flow as the iridium catalyst absorbs strongly in the UV region. The aim was to improve the reaction which is previously described in batch using blue LEDs.

Indeed the generation of carbon radical from various alkyl, allyl, heterobenzyl and benzyl trifluoroborates was significantly more efficient in flow under UV compared to the previously reported conditions. The formed radicals were trapped with an excess of TEMPO thus forming a new C-O bond. For instance, 2 mol % of the catalyst and 18 hours of blue irradiation were needed to get 98% of benzyl-TEMPO adduct. Using only 1 mol % of the catalyst and UV LEDs gave the same conversion after only 2 hours. For more reactive substrates like the *p*-methoxybenzyl trifluoroborate, the reaction is quantitative after only 2.5 min.

A linear Hammett plot

was obtained following the kinetic study of various substituted benzyltrifluoroborates. This has proved that there is a strong correlation between the impact of the substituents of a benzyl group on the kinetics of the generation of the carbon radical via photoredox catalysis.

The reactivity of the generated radicals was also tested by the addition of *p*-methoxybenzyl trifluoroborate to various Michael acceptors to form new C-C bond. Adding the *p*-methoxybenzyl trifluoroborate to acrylonitrile gave 94% conversion after only 15 min of irradiation compared to 80% after 10 hours of irradiation using batch reactor irradiated by blue LEDs. However, in our case we had to increase the catalyst loading to 3 mol %.

Generating carbon radicals from trifluoroborates can be also further extended by working using the metal free eosin Y catalyst that has shown to be a good candidate for such reactions.

So this work has confirmed the impact of miniaturization on the reactivity of photochemical reactions. With slight modifications to the conditions, the reactions can be

even further improved. This shows that microflow technology is a promising field toward greener chemical processes.

CHAPTER SEVEN

EXPERIMENTAL PART

Chemicals

The catalysts $\text{Ru}(\text{bpy})_3\text{Cl}_2 \cdot 6\text{H}_2\text{O}$, $\text{Pd}(\text{PPh})_3$ and $[\text{Ir}(\text{dF}(\text{CF}_3)\text{ppy})_2(\text{dtbbpy})](\text{PF}_6)$ were purchased from Strem Chemicals Inc., Copper (II) bromide (CuBr_2) from Sigma-Aldrich® and $\text{Na}_2\text{Eosin Y}$ was purchased from Alfa Aesar. All other chemicals and solvents were purchased from Sigma-Aldrich® except for the benzyl chlorides/ bromides, used in the synthesis of the trifluoroborates, which were purchased from Alfa Aesar. Anhydrous N,N-Diisopropylethylamine ($i\text{-Pr}_2\text{NEt}$) was further distilled over KOH and stored in dark under argon before usage. Methyl methacrylate, used in polymerization, and the alkenes bearing electron-withdrawing groups, which were used to form a C-C bond with trifluoroborates, were passed over alumina to remove stabilizers immediately prior to use. All other reagents were used as received.

Anhydrous isooctane, acetonitrile, N, N- dimethylformamide (DMF), tetrahydrofuran (THF), dioxane and $\geq 99\%$ (GC) toluene and dichloromethane were used as received. CHROMASOLV® Plus acetone and methanol were stored with active molecular sieves (3 Å) for 24 hours before usage.

Flow Systems

1- Mikroglas Dwell Device® microreactor made of Foturan glass of dimensions (1.15 m \times 2000 μm \times 500 μm). The 1.15 m long channel of this dwell device offers extended reaction time. Moreover, the reactor includes a channel for the flow of heat exchange fluid thus providing temperature control. The Foturan glass is resistant to aggressive liquids (strong acids, bases) allowing the usage of a

wide range of solvents in addition to its transparency up to 300 nm making it favorable for UV/Vis photochemical reactions (Figure 7.1). In this study, this reactor was used in the chemical actinometry, [2+2] cycloaddition and the boronic acid salts' radical activity.

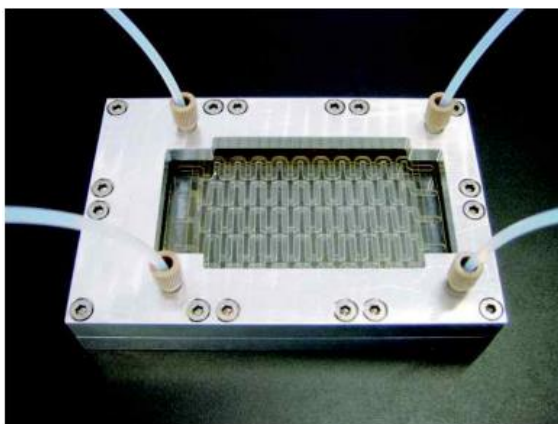


Figure 7.1: Mikroglas Dwell Device ®

2- Lab designed microreactor composed of FEP tubing (i.d. 800 μm) fitted on a metallic grid. Since polymerization can lead to the clogging of the microreactor, it was decided to use this type of disposable, cheap flow reactor for photoinduced ATRP instead of using the Mikroglas Dwell device (100 € vs 3500 €). Two of these reactors were prepared to fit the UV and the Visible LED systems present in the lab (Figure 7.2).



Figure 7.2: Tubular microfluidic systems

Syringe pump

The different flow rates of the reactions performed were regulated using a Harvard Apparatus (Holliston, MA, USA) PHD ULTRA CP syringe pump.

LED Systems

- 1- Blue ($\lambda = 450$ nm) & green ($\lambda = 530$ nm) high power spots (50 W electrical power, 4500 lumen, $0.02 \text{ W}\cdot\text{cm}^{-2}$) LED from Bridgelux (Livermore, CA, USA) were used in Photoinduced ATRP.
- 2- UV LEDs A: Lab designed UV LEDs assembly that is composed of 18 HP LEDs ($\lambda = 365$ nm) of total irradiance of $90 \text{ mW}\cdot\text{cm}^{-2}$. The panel's dimensions were designed to fit well to those of the dwell device. The LEDs are placed at equal distances in order to provide homogeneous illumination. This system was first used for chemical actinometry. It was then replaced by the following stronger LED systems for the other type of reactions (Figure 7.3).
- 3- UV LEDs B: Omnicure® AC475 of $\lambda = 365$ nm and irradiance up to $250 \text{ mW}\cdot\text{cm}^{-2}$ was used in boronic acid salts' radical activity and the [2+2] cycloaddition as its dimensions fit well to those of the Mikrogas Dwell Device.
- 4- UV LEDs C: Omnicure® AC7300 of $\lambda = 365$ nm and irradiance up to $3 \text{ W}\cdot\text{cm}^{-2}$ purchased from Lumen Dynamics (Mississauga, Canada) was used in chemical actinometry and photoinduced ATRP.



Figure 7.3: Lab designed HP UV LEDs A

Analytical Methods

Proton and carbon magnetic resonance spectra (^1H NMR and ^{13}C NMR) were recorded on a Bruker AVANCE 300 spectrometer (^1H 300 MHz and ^{13}C 75 MHz) using tetramethylsilane (TMS) as the internal standard. Chemical shifts, δ , are given in ppm and coupling constants, J , in Hz. ^1H NMR data are reported as follows: chemical shift, multiplicity (s = singlet, d = doublet, t = triplet, dd = doublet of doublets, dt = doublet of triplets, td = triplet of doublets, m = multiplet, brs = broad singlet), coupling constants and integration.

Size exclusion chromatography analyses were performed at 25 °C on a Waters system equipped with a guard column, a 600 mm PLgel 5 mm Mixed C column (Polymer Laboratories), and a Waters 410 refractometric detector. THF was used as an eluent at a flow rate of 1 mL.min⁻¹. All molecular weights (M_n , M_w) and molecular weight distributions (dispersities, M_w/M_n , PDI) were determined by calibration to known, standard poly (methyl methacrylate) samples purchased from Polymer Laboratories.

GC-MS spectra were recorded using a Thermo Finnigan POLARIS-Q TRACE GC Ultra gas chromatographer/mass spectrometer. UV spectra were recorded using a Varian Cary 100 UV-visible spectrophotometer.

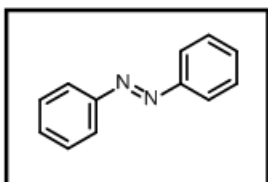
Thin-layer chromatography was performed on Merck TLC plate with 60 F₂₅₄. The purification of the obtained products was performed by flash chromatography using PuriFlash® 215 equipped with a UV 190 - 840 nm - and puriFlash® ELSD – detectors purchased from Interchim. Pre-packed flash chromatography Silica HP (30 μm) columns were used.

Chemical Actinometry

General procedure of photoisomerization of Azobenzene

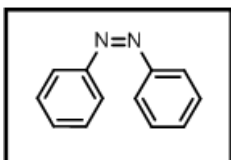
A solution of (E) azobenzene of concentration 6.4×10^{-4} M in isooctane was injected into the Mikrogilas Dwell Device, irradiated by UV LEDs A, at various flow rates. The flow rates were chosen depending on the desired irradiation times ranging between 9 s and 140 s. The solvent of irradiated samples is evaporated followed by dissolving the residue in 500 μ l of CDCl_3 to be injected in the NMR spectrometer. The degree of conversion was calculated using the ^1H spectrum by integrating the peaks that correspond to the Z and E isomers. The results obtained were then used to determine the photon flux inside the microreactor (discussed in Chapter 3). A more concentrated solution (0.01 M) in isooctane, acetonitrile and methanol were also assessed. The chemical actinometry of azobenzene in isooctane (0.01 M) was then performed using UV LEDs B at 30 % and 100 % power.

Azobenzene (E)



^1H NMR (300 MHz, CDCl_3): δ 7.93-7.87 (multiplet, 4H), δ 7.54-7.42 ppm (multiplet, 6H). ^{13}C NMR (75 MHz, CDCl_3): δ 152.25, 130.96, 129.02, 122.86 ppm.

Azobenzene (Z)



^1H NMR (300 MHz, CDCl_3): δ 7.22-7.17 (multiplet, 4H), δ 7.14-7.07 (multiplet, 2H), δ 6.82-6.78 ppm (multiplet, 4H). ^{13}C NMR (75 MHz, CDCl_3): δ 153.99, 129.36, 127.78, 120.32 ppm.

Calculation of the Degree of Conversion

The fraction of the formed Z isomer was determined using Equation 6.1 where I_Z and I_E are the integrals of the peaks that correspond to the Z and E isomers respectively.

$$\% Z = \frac{\Sigma I_Z}{\Sigma I_Z + \Sigma I_E} \quad \text{Equation 7.1}$$

Determination of the Absorption Coefficient “ ϵ ” of Azobenzene (E)

In isooctane:

Table 7.1 and Figure 7.4 correspond to the variation of the absorbance A as function of the concentration of azobenzene in isooctane. The linear plot with R^2 of 0.999 has a slope of 95 $\text{L}\cdot\text{mol}^{-1}\cdot\text{cm}^{-1}$ is then the absorption coefficient ϵ azobenzene (E) in isooctane.

Table 7.1: Variation of Absorbance of (E) Azobenzene in Isooctane as Function of Concentration

[E] mol.L ⁻¹	A
0.00E+00	0
1.10E-03	0.089
1.65E-03	0.14
2.47E-03	0.224
3.70E-03	0.338
5.55E-03	0.528
8.33E-03	0.803
1.25E-02	1.189

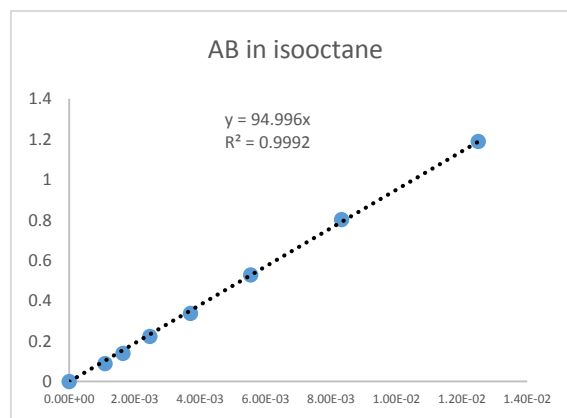


Figure 7.4: Plot of Absorbance vs. Concentration of Azobenzene (E) in Isooctane

In Acetonitrile:

Similarly, by observing Table 7.2 and Figure 7.5, the absorption coefficient of azobenzene (E) in acetonitrile is $276.9 \text{ L}\cdot\text{mol}^{-1}\text{cm}^{-1}$.

Table 7.2: Variation of Absorbance of (E) Azobenzene in Acetonitrile as Function of Concentration

[E] mol.L ⁻¹	A
0.00E+00	0
2.60E-04	0.075
3.91E-04	0.105
7.81E-04	0.215
1.56E-03	0.436
3.13E-03	0.864

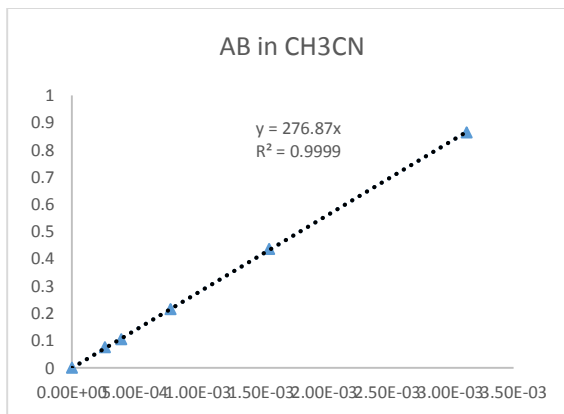


Figure 7.5: Plot of Absorbance vs. Concentration of Azobenzene (E) in Acetonitrile

In Methanol:

The absorption coefficient of azobenzene (E) in methanol is $312 \text{ L}\cdot\text{mol}^{-1}\text{cm}^{-1}$ in reference to the results of Table 7.3 and Figure 7.6

Table 7.3: Variation of Absorbance of (E) Azobenzene in Methanol as Function of concentration

[E] mol.L ⁻¹	A
0.00E+00	0.000
3.90E-04	0.123
7.81E-04	0.232
1.56E-03	0.456
3.13E-03	0.995

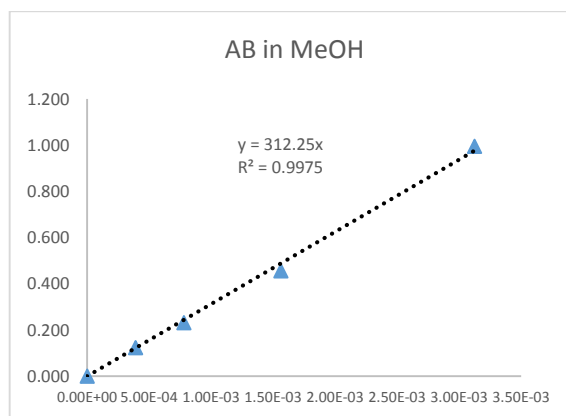
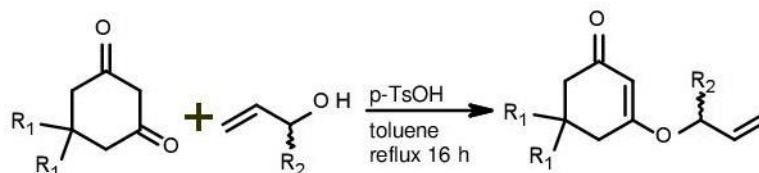


Figure 7.6: Plot of Absorbance vs. Concentration of Azobenzene (E) in Methanol

Intramolecular [2+2] photocycloaddition

Photosensitized under UV irradiation

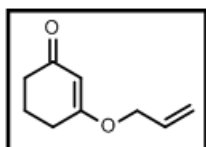
General procedure for the synthesis of 3-oxa-2-cyclohexen-1-ones:



Cyclohexane-1,3-dione (27 mmol) was dissolved in 25 mL of toluene along with allyl/homoallyl alcohol (2.3 equ.) and a catalytic amount of p-toluenesulfonic acid (5-10 mg). The reaction mixture was heated at reflux for 16 h using a Dean-Stark trap to remove the water. The crude reaction mixture was transferred to a separatory funnel and washed with NaHCO₃, water, and brine. The organic layer was dried over MgSO₄, and the solvent was concentrated *in vacuo*. Purification was done by flash chromatography (EtOAc/petroleum ether=1:4).

3-(2-Propenyloxy)-2-cyclohexen-1-one (1a)

According to the general procedure, 3 g (27 mmol) of cyclohexane-1,3-dione with 4 ml (59 mmol, 2.2 equ.) of allyl alcohol and 7 mg of p-TsOH in 25 ml of toluene afford 3-(2-Propenyloxy)-2-cyclohexen-1-one as a colorless oil (yield = 85%) after purification by flash chromatography ((EtOAc/petroleum ether=1:4)

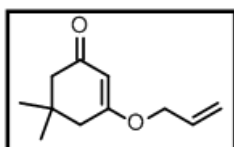


¹H NMR (300 MHz, CDCl₃): δ 5.94 (tdd, *J* = 5.6, 10.5, 17.2 Hz, 1H), 5.35 (multiplet, 3H), 4.35 (td, *J* = 1.6, 5.6 Hz, 2H), 2.41 (t, *J* = 6.25 Hz, 2H), 2.33 (dd, *J* = 6.0, 7.3 Hz, 2H), 1.96 (quint, *J* = 6.5 Hz, 2H) ppm. ¹³C NMR

(75MHz, CDCl₃): δ 199.6, 177.5, 131.3, 118.8, 103.0, 77.3, 69.0, 36.6, 28.9, 21.1 ppm. UV (nm): 240. MS (EI): *m/z* = 152.0(40).

5,5-dimethyl-3-(2-Propenyloxy)-2-cyclohexen-1-one (1b)

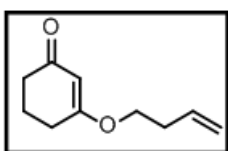
According to the general procedure, 3.75 g (26.8 mmol) of 5,5-dimethylcyclohexane-1,3-dione with 4.3 ml (63.3 mmol, 2.3 equ.) of allyl alcohol and 7 mg of p-TsOH in 25 ml of toluene afford 5,5-dimethyl-3-(2-Propenyloxy)-2-cyclohexen-1-one as a yellow oil (yield = 75%) after purification by flash chromatography ((EtOAc/petroleum ether=1:4)



$^1\text{H NMR}$ (300 MHz, CDCl_3): δ 5.93 (tdd, $J = 5.5, 10.5, 17.3$ Hz, 1H), 5.32 (multiplet, 3H), 4.35 (td, $J = 1.6, 5.5$ Hz, 2H), 2.27 (s, 2H), 2.18 (s, 2H), 1.04 (s, 6H) ppm. $^{13}\text{C NMR}$ (75MHz, CDCl_3): δ 199.6, 176.0, 131.4, 118.9, 102.0, 69.2, 50.7, 42.8, 35.54, 28.3 ppm. MS (EI): $m/z = 180.1(35)$.

3-(2-butenyloxy)-2-cyclohexen-1-one (1c)

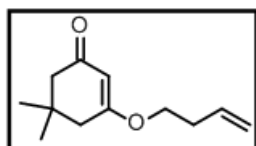
According to the general procedure, 4.5 g (27 mmol) of cyclohexane-1,3-dione with 5.4 ml (63 mmol, 2.3 equ.) of 3-butenyl alcohol and 7 mg of p-TsOH in 25 ml of toluene afford 3-(2-butenyloxy)-2-cyclohexen-1-one as a yellow oil (yield = 92%) after purification by flash chromatography ((EtOAc/petroleum ether=1:4).



$^1\text{H NMR}$ (300 MHz, CDCl_3): δ 5.84-5.66 (m, 1H), 5.29 (s, 1H), 5.13-4.99 (m, 2H), 3.82 (t, $J = 6.6$ Hz, 2H), 2.42 (q, $J = 6.6$ Hz, 2H), 2.34 (t, 6.2 Hz, 2H), 2.27 (t, 6.2 Hz, 2H), 1.91 (m, 2H) ppm. $^{13}\text{C NMR}$ (75MHz, CDCl_3): δ 199.8, 177.9, 133.6, 117.5, 102.8, 36.8, 32.9, 32.4, 29.0, 21.3 ppm. MS (EI): $m/z = 180.1(35)$.

5,5-dimethyl-3-(2-butenyloxy)-2-cyclohexen-1-one (1d)

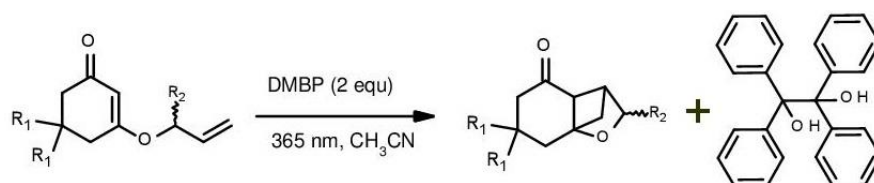
According to the general procedure, 5.27 g (27 mmol) of cyclohexane-1,3-dione with 5.4 ml (63 mmol, 2.3 equ.) of 3-butenyl alcohol and 7 mg of p-TsOH in 25 ml of toluene afford 3-(2-butenyloxy)-2-cyclohexen-1-one as a



yellow oil (yield = 93%) after purification by flash chromatography(EtOAc/petroleum ether=1:4).

^1H NMR (300 MHz, CDCl_3): δ 5.85-5.68 (m, 1H), 5.31 (s, 1H), 5.15-5.03 (m, 2H), 3.83 (t, $J= 6.7$ Hz, 2H), 2.49-2.39 (qt, $J = 6.7, 1.5$ Hz, 2H), 2.23 (s, 2H), 2.16 (s, 2H), 1.04 (s, 6H) ppm. ^{13}C NMR (75MHz, CDCl_3): δ 199.5, 176.1, 133.6, 117.5, 101.6, 67.6, 50.7, 42.9, 32.8, 32.4, 28.3 ppm. MS (EI): $m/z = 180.1(35)$.

General procedure for the [2+2] cycloaddition under flow conditions.



A solution of 3-(2-ketenyl)oxy-2-cyclohexen-1-one (0.55 mmol) and 4,4'-dimethoxybenzophenone (2 equ, 1.1 mmol) in acetonitrile (15 mL) was degassed by purging with argon for 15 minutes. The solution was then transferred into a syringe that was connected to the Mikroglas Dwell Device that was irradiated with the UV LEDs C (irradiance $250 \text{ mW}\cdot\text{cm}^{-2}$, 100% power). Six data having different irradiation times were done. In each case, for a given irradiation time that is regulated by varying the flow rate, 2 mL of the reaction mixture was collected. The solvent was then removed under reduced pressure and the crude was analyzed by ^1H NMR to determine the % of conversion. The results were later used to plot the kinetic curve and identify the rate order of the reaction.

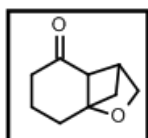
General procedure for the [2+2] cycloaddition under batch conditions.

After performing the reactions in flow and determining the percentage of conversion along time, batch conditions were performed and that by placing the 2 mL of acetonitrile having the 3-(2-ketenyl)oxy-2-cyclohexen-1-one (0.074 mmol) and the 4,4-

dimethoxybenzophenone (1.4 mmol, 2 equ) in a Pyrex tube. The reaction mixture was degassed and placed at the same distance as that of the flow system to UV LEDs B with stirring. The irradiation time was chosen relative to the time needed, in flow, to get 98% of conversion. Similarly, the solvent was removed under low pressure and the crude was analyzed by ^1H NMR to determine the % of conversion and compare it to that of the flow conditions.

10-oxatricyclo[5.2.1.0^{1,6}]decan-5-one (2a).

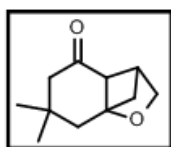
According to the general procedure, 11.25 mg (0.074 mmol) of 3-(2-Propenyloxy)-2-cyclohexen-1-one and 35.8 mg of 4,4-dimethoxybenzophenone (0.148 mmol, 2 equ.) dissolved in 2 ml of acetonitrile and injected within the Dwell Device at a flow rate of 10 μl . Min-1 that corresponds to 1h 55 min of irradiation gave 95% (NMR yield) of 10-oxatricyclo[5.2.1.0^{1,6}]decan-5-one (3a)



^1H NMR (300 MHz, CDCl_3): δ 3.86 (d, $J = 5.9$ Hz, 1H), 3.63 (d, $J = 6.0$ Hz, 1H), 3.15 (t, $J = 2.9$ Hz, 1H), 2.48 (broad s, 1H), 2-1.6 (m, 6H), 1.82 (dd, $J = 2.8, 7.5$ Hz, 1H), 1.61 (dd, $J = 1.6, 7.5$ Hz, 1H) ppm. ^{13}C NMR (75MHz, CDCl_3): δ 199.7, 177.4, 131.4, 118.9, 103.1, 69.1, 36.7, 29.0, 21.2 ppm. MS (EI): $m/z = 152.1(5)$.

3,3-dimethyl-9-oxatricyclo[5.2.1.0^{1,6}]decan-5-one (2b).

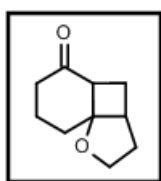
According to the general procedure, 13.5 mg (0.074 mmol) of 5,5dimethyl-3-(2-Propenyloxy)-2-cyclohexen-1-one and 35.8 mg of 4,4-dimethoxybenzophenone (0.148 mmol, 2 equ.) dissolved in 2 ml of acetonitrile and injected within the Dwell Device at a flow rate of 7 μl . Min-1 that corresponds to 2h 38 min of irradiation gave 98% (NMR yield) of 3,3-dimethyl-9-oxatricyclo[5.2.1.0^{1,6}]decan-5-one (3a)



^1H NMR (300 MHz, CDCl_3): δ 3.89 (d, $J = 5.9$ Hz, 1H), 3.61 (d, $J = 5.9$ Hz, 1H), 3.17 (t, $J = 2.9$ Hz, 1H), 2.48 (broad s, 1H), 2.14 (s, 2H), 2.10 (d, $J = 0.6$ Hz, 1H), 1.77 (dd, $J = 3.1, 7.4$ Hz, 1H), 1.6 (dd, $J = 1.6, 7.4$ Hz, 1H), 1.19 (s, 3H), 1.10 (s, 3H) ppm. MS (EI): $m/z = 180.1(5)$.

2-oxatricyclo[5.4.0.0^{1,5}]undecan-8-one (2c).

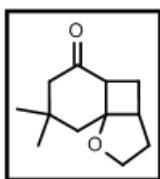
According to the general procedure, 12.3 mg (0.074 mmol) of 5,5dimethyl-3-(2-Propenyloxy)-2-cyclohexen-1-one and 35.8 mg of 4,4-dimethoxybenzophenone (0.148 mmol, 2 equ.) dissolved in 2 ml of acetonitrile and injected within the Dwell Device at a flow rate of 60 μl . Min^{-1} that corresponds to 19 mins of irradiation gave 96% (NMR yield) of 2-oxatricyclo[5.4.0.0^{1,5}]undecan-8-one



^1H NMR (300 MHz, CDCl_3): δ 4.16 (ddd, $J = 1.2, 8, 9$ Hz, 1H), 4 (ddd, $J = 9, 15, 9$ Hz, 1H), 2.83 (dd, $J = 7, 11.5$ Hz, 1H), 2.71 (dt, $J = 5, 8$ Hz, 1H), 2.56-2.46 (m, 1H), 2.32-2.20 (m, 1H), 2.16-1.65 (m, 8 H) ppm. ^{13}C NMR (75MHz, CDCl_3): δ 212.3, 87.4, 66.8, 49.3, 40, 39.1, 31.4, 31.2, 24.2, 19.6 ppm. MS (EI): $m/z = 166.2$

10,10-dimethyl-2-oxatricyclo[5.4.0.0^{1,5}]undecan-8-one (2d).

According to the general procedure, 14.4 mg (0.074 mmol) of 5,5dimethyl-3-(2-Propenyloxy)-2-cyclohexen-1-one and 35.8 mg of 4,4-dimethoxybenzophenone (0.148 mmol, 2 equ.) dissolved in 2 ml of acetonitrile and injected within the Dwell Device at a flow rate of 230 μl . Min^{-1} that corresponds to 5 mins of irradiation gave 97% (NMR yield) of 10,10-dimethyl-2-oxatricyclo[5.4.0.0^{1,5}]undecan-8-one (2b).

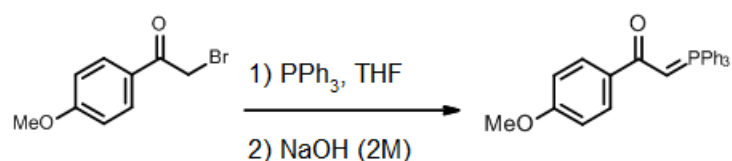


^1H NMR (300 MHz, CDCl_3): δ 4.12 (ddd, $J = 1.5, 7.8, 9.2$ Hz, 1H), 3.81 (ddd, $J = 9.1, 10.9, 5.4$ Hz, 1H), 2.87 (ddd, $J = 11.3, 6.6, 1.7$ Hz, 1H), 2.52-2.44 (m, 1H), 2.34 (ddd, $J = 12.9, 9.1, 6.6$ Hz, 1H), 2.31-2.16 (m, 2 H), 2 (d, 14.5 Hz, 1H),

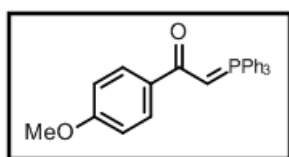
1.82-1.69 (m, 3H), 1.39 (dd, 12.3, 5.4 Hz, 1H), 1.09 (s, 3 H), 1 (s, 3 H) ppm. ^{13}C NMR (75MHz, CDCl_3): δ 211.1, 88.2, 66.6, 53.2, 49, 45.8, 42.8, 33.3, 32.1, 30.5, 28.3, 24.8 ppm. MS (EI): $m/z = 194.4$.

Using photoredox catalysis under visible light irradiation

Synthesis of 1-(4-methoxy-phenyl)-2-(triphenyl- λ -phosphoranylidene) ethanone (**1g**).

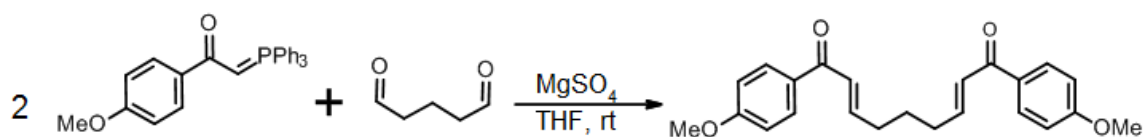


Triphenylphosphine (7 g, 26 mmol) was added to a solution of 4- methoxyphenacyl bromide (6 g, 26 mmol) in THF (50 mL) under nitrogen atmosphere at rt overnight. The solvent is concentrated under reduced pressure. The crude is then washed with diethylether and filtered. The residue is dissolved in an aqueous solution of dichloromethane H_2O 1.5/ 1 CH_2Cl_2 and 100 ml of NaOH (2M) is added and the mixture is stirred rigorously for 2 hours. The desired product is extracted using CH_2Cl_2 (3×100 ml). The collected dichloromethane is washed with a saturated brine solution, dried over MgSO_4 . The evaporation of the solvent under low pressure will give a solid (9.6 g, 90% yield)



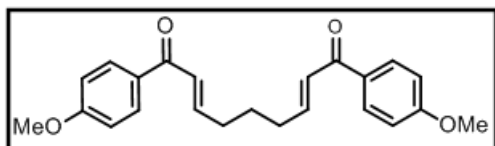
^1H NMR (300 MHz, CDCl_3): δ 7.95-7.88 (m, 2H), 7.75-7.66 (m, 6H), 7.55-7.51 (m, 3H) 7.50-7.41 (m, 6H), 6.89.75-6.81 (m, 2H), 4.34 (d, $J = 24.7$ Hz, 1H), 3.81 (s, 3H).

Synthesis of 1,9-bis-(4-methoxy-phenyl)-nona-2,7-diene-1,9-dione (**1f**)



Using Wittig reaction, the formed product (6.25 g, 15 mmol) will react with glutaraldehyde

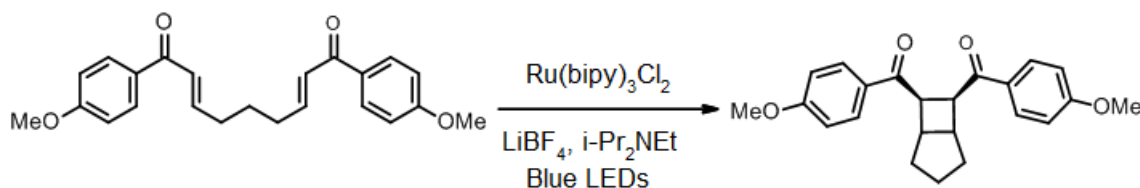
(solution 50% wt, 0.77g, 3.85 mmol) when dissolved in dichloromethane in the presence of MgSO₄. The mixture is stirred overnight at room temperature, then purified by flash chromatography using ethyl acetate/cyclohexane (1:3) as an eluent. A yellow solid is obtained (2.6 g, 95% yield).



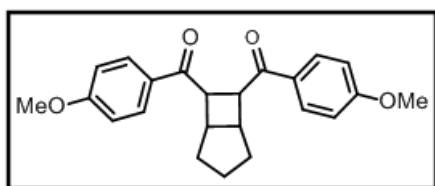
¹H NMR (300 MHz, CDCl₃): δ 7.98-7.91 (m, 4H), 7.1-6.88 (m, 8H), 3.87 (s, 6H) 2.39 (q, 7.2 Hz, 4H), 1.78 (p, 7.4 Hz, 2H). ¹³C NMR (75MHz, CDCl₃):

δ 189.1, 163.6, 147.8, 131.1, 130.9, 126.3, 114.0, 55.7, 32.3, 27 ppm.

General procedure for irradiation under flow conditions using blue LEDs (2g).



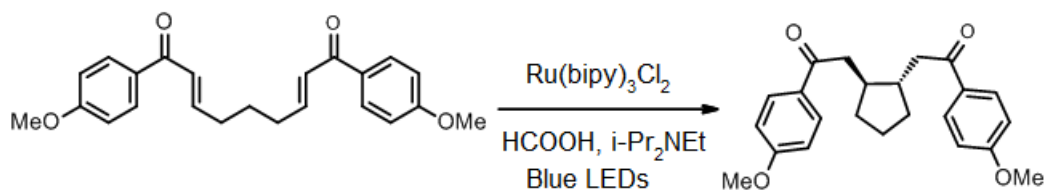
The reaction mixture is prepared by having a solution of the bisenone (33 mg, 90 μmol), Ru(bpy)₃Cl₂•6H₂O (3.38 mg, 5 mol %), LiBF₄ (17 mg, 2 equ), and i-Pr₂NEt (23 mg, 2 equ) in acetonitrile (3 mL). The solution was then degassed using three freeze-pump-thaw cycles under nitrogen in the dark. The solution was then injected into the microreactor which is illuminated by the blue LEDs for a range of irradiation times. Upon completion of the reaction, the solvent was removed by rotary evaporation, and the residue was purified by chromatography on a silica gel column with eluent ethyl acetate/cyclohexane, 1:4



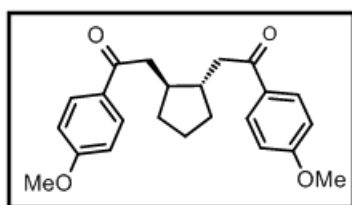
¹H NMR (300 MHz, CDCl₃) δ 7.74 (d, J = 9.0 Hz, 4H), 6.83 (d, J = 9.0 Hz, 4H), 3.81 (s, 6H), 3.20 (m, 2H), 2.02 (m, 2H), 1.83 (ddd, J = 13.5, 5.3, 1.9 Hz, 2H), 1.69

(m, 2H); ¹³C NMR (75 MHz, CDCl₃) δ 197.3, 162.9, 129.9, 129.6, 113.6, 55.3, 48.1, 39.1, 32.5, 25.3

General procedure for reductive cyclization (2f)

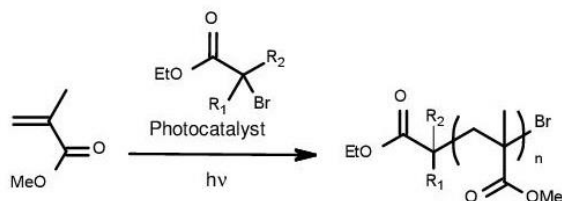


The bisenone (1 equiv), $\text{Ru}(\text{bipy})_3\text{Cl}_2 \cdot 6\text{H}_2\text{O}$ (0.025 eq), HCO_2H (5 eq), $i\text{-Pr}_2\text{NEt}$ (10 eq), and acetonitrile (0.05 M) are added together and degassed in the dark using three freeze/pump/thaw cycles under nitrogen. The solution was then injected into the microreactor illuminated by the blue LEDs for different irradiation times. Upon completion of the reaction, the solvent was removed in vacuo and the residue purified by column chromatography on silica gel. (2:3 ethyl acetate, cyclohexane). The % of conversion was determined using ^1H NMR.



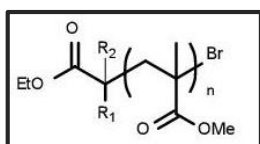
^1H NMR (300 MHz, CDCl_3) δ 7.93 (dt, $J = 9.0, 2.2$ Hz, 4H), 6.92 (dt, $J = 8.9, 2.1$ Hz, 4H), 3.86 (s, 6H), 3.13 (dd, $J = 16.1, 4.8$ Hz, 2H), 2.87 (dd, $J = 16.1, 8.5$ Hz, 2H), 2.15 (m, 2H), 1.96 (m, 2H), 1.62 (m, 2H), 1.27 (m, 2H); ^{13}C NMR (75 MHz, CDCl_3) 198.8, 163.3, 130.4, 130.3, 113.7, 55.4, 43.6, 41.9, 32.5, 23.7;

Photoinduced Atom Transfer Radical Polymerization (ATRP)



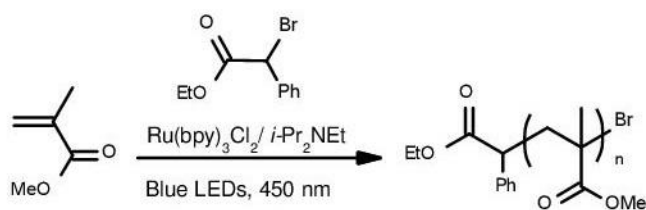
General procedure of ATRP in batch

A Schlenk flask was charged with DMF (2. mL, 50% v/v vs monomer) and photocatalyst (2 μmol) w/o ligand. The flask was sealed with rubber septum and was purged with nitrogen for 20 min to remove the oxygen. The monomer methyl methacrylate (2 mL, 18.8 mmol) that was freshly passes over alumina was then added to the flask by using a syringe under protection of nitrogen. The flask was degassed by three vacuum/N₂ refilling cycles to remove the oxygen. Then the initiator EBPA (82 μL, 0.5 mmol) w/o iPr₂NEt (1 mmol) were added under protection of nitrogen. Then, the flask was irradiated with LEDs for six hours. An aliquot was analyzed by ¹H NMR to determine the % of conversion of methyl methacrylate to Poly (methyl methacrylate). The formed polymer was then precipitated in methanol, filtered and dried under vacuum over the night. A solution of 6 mg/ml in THF was prepared from the dry polymer to be analyzed by GPC. Note that when using Na₂Eosin Y catalyst, two additional initiators EBiB (82 μL, 0.5 mmol) and EBPMPA (0.13g, 0.5 mmol) were also assessed.



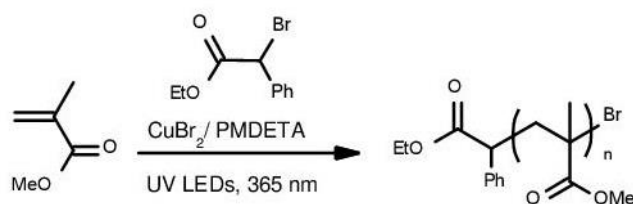
Poly (methyl methacrylate): ¹H NMR (300 MHz, CDCl₃): 3.72 (br s, 3H), 1.94-2.04 (m, 2H), 1.00 (t, J = 7.2 Hz, 3H). ¹³C NMR (75 MHz, CDCl₃): 177.7, 54.4, 51.8, 45.0, 17.0.

ATRP using Ru(bpy)₃Cl₂·6H₂O catalyst illuminated by blue LEDs in batch



Following the general procedure, DMF (2. mL, 50% v/v vs monomer) and Ru(bpy)₃Cl₂·6H₂O (1.5 mg, 2 μmol) were placed in the Schlenk flask that was purged with nitrogen for 20 min to remove the oxygen. The monomer methyl methacrylate (2 mL, 18.8 mmol) that was freshly passes over alumina was then added to the flask that was degassed by three vacuum/N₂ refilling cycles. Then, *i*-Pr₂NEt (170 μL, 1 mmol) and EBPA (82 μL, 0.5 mmol) were added under protection of nitrogen. The flask was later irradiated with blue LEDs (50 W, 4500 lumens) for six hours. ¹H NMR of the crude indicated a 51% of conversion. A solution of 6 mg/ml in THF was prepared from the precipitated and dried polymer to be analyzed by GPC.

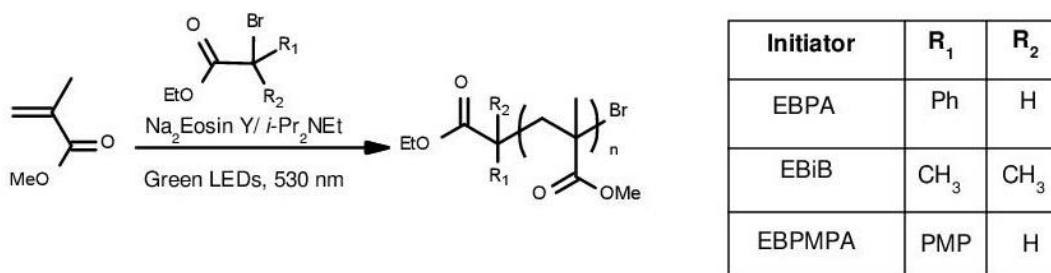
ATRP using CuBr₂/PMDETA illuminated by UV LEDs in batch



Following the general procedure, DMF (2. mL, 50% v/v vs monomer), CuBr₂ (4.18 mg, 18.7 μmol) and the ligand PMDETA (39 μL, 0.18 mmol) were placed in the Schlenk flask that was purged with nitrogen for 20 min to remove the oxygen. The monomer methyl methacrylate (2 mL, 18.8 mmol) that was freshly passes over alumina was then added to the flask that was degassed by three vacuum/N₂ refilling cycles. Then, EBPA (82 μL, 0.5 mmol) was added under protection of nitrogen. The flask was later irradiated with UV LEDs B (365

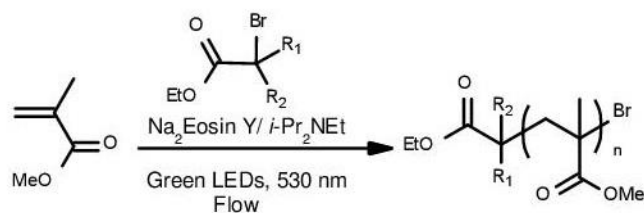
nm, 3 W cm⁻², 100% power) for six hours. ¹H NMR of the crude indicated a 78% of conversion. A solution of 10 mg/ml in THF was prepared from the precipitated and dried polymer to be analyzed by GPC.

ATRP using Na₂Eosin Y catalyst illuminated by green LEDs in batch:



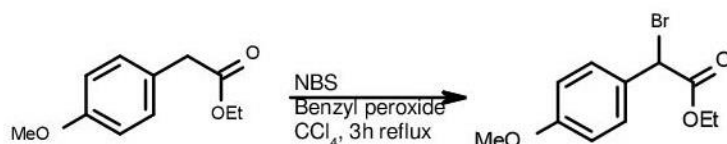
Following the general procedure, DMF (2. mL, 50% v/v vs monomer) and Na₂Eosin Y (1.4 mg, 2 μmol) were placed in the Schlenk flask that was purged with nitrogen for 20 min to remove the oxygen. The monomer methyl methacrylate (2 mL, 18.8 mmol) that was freshly passes over alumina was then added to the flask that was degassed by three vacuum/N₂ refilling cycles. Then, iPr₂NEt (170 μL, 1 mmol) and EBPA (82 μL, 0.5 mmol) were added under protection of nitrogen. The flask was later irradiated with green LEDs (50 W, 4500 lumens) for six hours. ¹H NMR of the crude indicated a 56% of conversion. Replacing EBPA by EBiB (82 μL, 0.5 mmol) and EBPMPA (0.13g, 0.5 mmol) gave a 54% and 50 % conversion respectively. A solution of 6 mg/ml in THF was prepared from each of the three precipitated and dried polymer to be analyzed by GPC.

ATRP using $\text{Na}_2\text{Eosin Y}$ catalyst illuminated by green LEDs in flow:



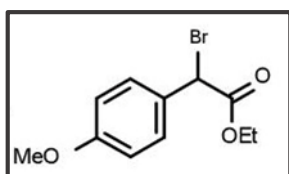
Using the same composition as that in the batch conditions, $[\text{MMA}]: [\text{Initiator}]: [\text{Na}_2\text{Eosin Y}]: [i\text{Pr}_2\text{NEt}] = 200:5:0.02:10$ and $\text{MMA}: \text{DMF} = 1:1$ (v/v), for every run, 4 mL of the reaction mixture was injected within the lab designed microfluidic reactor (FEP tubing, i.d. 800 μm) that was placed in direct contact with the green LEDs. The irradiation time was varied depending on the flow rate that was adjusted by the syringe pump. For each of the three initiators, EBPA, EBiB and EBMPMA, 6 points that correspond to six different irradiation times were performed. For each point the % of conversion was determined by ^1H NMR and the polymers were precipitated, filtered, dried and stored in THF for further analysis by GPC. Note that working under oxygen free conditions was insured, even during the transfer of the reaction mixture from the Schlenk tube to the syringe. The variation of the % of conversion of each polymer versus the irradiation time was used to plot the kinetic curves of ATRP in flow.

Synthesis of ethyl 2-bromo-2-(4-methoxyphenyl) acetate



A mixture of ethyl (4-methoxyphenyl) acetate (5g, 0.025 mmol), N-bromosuccinimide (4.894g, 0.0275 mmol) and benzoyl peroxide (25 mg) in CCl_4 was refluxed for 3h and then allowed to stand overnight to precipitate any dissolved succinimide. The mixture was then

filtered and concentrated to give dark yellow oil in quantitative yield.

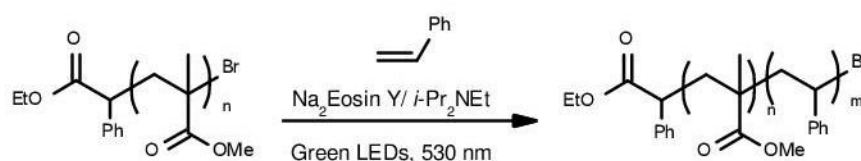


^1H NMR (300 MHz, CDCl_3): δ 7.47 (2H, d, $J = 15$ Hz), 6.85 (2H, d, $J = 15$ Hz), 5.32 (1H, s), 4.20 (2H, q, $J = 14.0$ Hz), 3.77 (3H, s), 1.25 (3H, t, $J = 16.5$ Hz) ppm. ^{13}C NMR (300 MHz, CDCl_3): δ 168.32, 160.17, 130.00, 127.72, 114.11, 62.29, 55.23, 46.73, 13.83. MS (EI): 273.0.

Preparation of a PMMA macroinitiator:

EBPA (82 μL , 0.5 mmol), $i\text{Pr}_2\text{NEt}$ (170 μL , 1 mmol) and $\text{Na}_2\text{Eosin Y}$ (1.4 mg, 2 μmol) were added to a solution of MMA in DMF (4 mL, 1:1 v/v) placed in a Schlenk tube. The solution was degassed by three Freeze-Pump-Thaw cycles then transferred into the syringe that was connected to the lab designed reactor (FEP tubing, i.d. 800 μm). The solution was pumped into the flow system, irradiated by Green LEDs (50 W, 4500 Lumens), at a flow rate of 30 $\mu\text{L}\cdot\text{min}^{-1}$ (irradiation time = 1 hour). The resulting conversion was 52%. The polymer was purified by precipitation in methanol. The resulting macroinitiator was dried overnight, and characterized by GPC to give a macroinitiator of $M_n = 13000$, and $M_w/M_n = 1.417$.

Chain Extension of PMMA macroinitiator with Styrene:



PMMA macroinitiator (0.24 g, 0.02 mmol), $i\text{Pr}_2\text{NEt}$ (35 μL , 0.2 mmol) and $\text{Na}_2\text{Eosin Y}$ (0.3 mg, 0.43 μmol) were combined to a solution of styrene (450 μL , 4 mmol) in 2.5 mL DMF. The solution was degassed by three Freeze-Pump-Thaw cycles then transferred into the syringe that was connected to the lab designed reactor (FEP tubing, i.d. 800 μm). The solution was pumped into the flow system, irradiated by Green LEDs (50 W, 4500 Lumens),

at a flow rate of 10 $\mu\text{L}\cdot\text{min}^{-1}$ (irradiation time = 3 hours). The formed polymer was precipitated, filtered and dried overnight before its analysis by ^1H NMR and GPC.

Polymerization of MMA with Dark Periods

EBPA (164 μL , 1 mmol), $i\text{Pr}_2\text{NEt}$ (340 μL , 2 mmol) and Eosin Y (2.8 mg, 4 μmol) were added to a solution of MMA in DMF (8 mL, 1:1 v/v) placed in a Schlenk tube. The solution was degassed by three Freeze-Pump-Thaw cycles then transferred into the syringe that was connected to the lab designed reactor (FEP tubing, i.d. 800 μm).

The mixture was irradiated for 3 disrupted hours; after each 60 minutes of irradiation, the solution was kept in dark under argon for 2 hours. For every cycle (1 hour “LEDs on”, 2 hours “LEDs off”) two samples of 1 mL each were taken for analysis at the beginning and the end of the “LEDs off” period. During the “LEDs on” period, the solution was pumped into the irradiated flow system at a flow rate of 30 $\mu\text{L}\cdot\text{min}^{-1}$. The six samples that were taken periodically were precipitated in methanol, filtered and dried overnight for analysis by GPC and NMR.

Calculation of degree of conversion by ^1H NMR

The degree of conversion can be determined gravimetrically. The mass of the formed polymer after precipitation, filtration and drying is measured. The ratio of conversion will be the measured mass over the sum of the masses of the monomer and the initiator added. The mass of the initiator can be neglected (Equation 7.2).

$$\% \text{ conversion} = \frac{m \text{ polymer}}{m \text{ monomer} + m \text{ initiator}} \times 100 \quad \text{Equation 7.2}$$

It can also be determined using ^1H NMR spectroscopy. In this case, the ^1H spectrum of the crude prior to any treatment is analyzed. The crude will include the polymer and the

remaining monomer so the % conversion will be determined by the integration of to a peak that corresponds to the same protons of the monomer and the polymer. For example the methoxy (-OCH₃) peak of the monomer methyl methacrylate and those of the methoxy (-OCH₃) but of the polymer. Usually, the peaks of the polymer are broad so can be easily distinguished from the monomer's peaks (Equation 7.3).

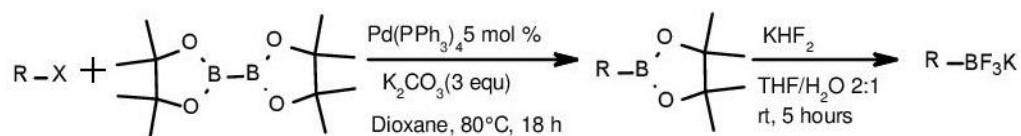
$$\% \text{ conversion} = \frac{I \text{ polymer}}{I \text{ monomer} + I \text{ polymer}} \times 100 \quad \text{Equation 7.3}$$

Note that the peaks included in the equation should correspond to the same of number of protons for both the monomer and the polymer or else further calculation should be done. This method is more precised especially that loss of polymer during precipitation and filtration can be excluded (Equation 6.4).

$$\% \text{ conversion} = \frac{\frac{I \text{ polymer}}{nH \text{ polymer}}}{\frac{I \text{ monomer}}{nH \text{ monomer}} + \frac{I \text{ polymer}}{nH \text{ polymer}}} \times 100 \quad \text{Equation 7.4}$$

C-C and C-O bond formation using photoredox catalysis in flow

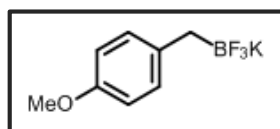
General procedure for the synthesis of trifluoroborates



Alkyl chloride/bromide (3 mmol) was dissolved in 30 mL of anhydrous dioxane along with bis(pinacolato)diboron (3.6 mmol, 1.2 equ.), K₂CO₃ (9 mmol, 3 equ) and the catalyst Pd(PPh₃)₄ (0.05 mmol, 5 mol %). The reaction mixture was heated till 80°C at reflux for 18 h. The reaction mixture was transferred to a separatory funnel to be extracted by diethyl ether (3 ×30 mL). The organic phase collected was then washed with brine, dried over MgSO₄, concentrated *in vacuo* and dissolved in 10 mL of THF. KHF₂ (18 mmol, 6 equ) was dissolved in 5 mL of H₂O and added drop by drop to the THF solution. The obtained mixture was stirred vigorously at room temperature for 5 hours followed by concentration *in vacuo*. The residue obtained was then dissolved in hot acetone that is later filtered and removed under reduced pressure. The resulting white solid was collected by filtration and washed several times with hot ether. The structure of the formed trifluoroborate was confirmed by NMR in acetone-d₆.

Potassium trifluoro (4-methoxybenzyl) borate (1h)

According to the general procedure (1.482 g, 6 mmol), KHF₂ aq. (2.8 g, 36 mmol, H₂O 10 mL) and THF (20 mL) afford Potassium trifluoro (4-methoxybenzyl) borate as a white solid (684 mg, 95%).

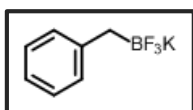


¹H NMR (300 MHz, acetone- d₆) δ: 7.17-7.20 (m, 4H), 7.04-7.06 (m, 1H), 2.55-2.59 (m, 2H), 0.46-0.52 (m, 2H) ppm. ¹³C NMR (75

MHz, acetone- d₆) δ: 149.4, 128.7, 128.6, 125.1, 33, 22.5 ppm.

Potassium trifluoro benzylborate (1i)

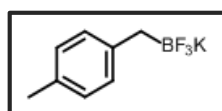
According to the general procedure, benzyl bromide (356 μ L, 3 mmol) bis(pinacolato)diboron (0.914g, 3.6 mmol), K_2CO_3 (1.24 g, 9 mmol), $Pd(PPh_3)_4$ (39.3 mg, 0.05 mmol) in 30 mL dioxane followed by adding, KHF_2 aq. (1.4 g, 18 mmol, H_2O 5.0 mL) and THF (10 mL) afford potassium trifluoro benzylborate as a white solid (404 mg, 68% yield).



1H NMR (300 MHz, acetone- d_6): δ 7.12-6.98 (m, 4 H), 6.89-6.81 (m, 1 H), 1.62 (br s, 2 H) ppm. ^{13}C NMR (75 MHz, acetone- d_6): δ 148, 129.8, 127.9, 122.9 ppm.

Potassium trifluoro (4-methylbenzyl) borate (1j)

According to the general procedure, 4-methylbenzyl bromide (0.555g, 3 mmol) bis(pinacolato)diboron (0.914g, 3.6 mmol), K_2CO_3 (1.24 g, 9 mmol), $Pd(PPh_3)_4$ (39.3 mg, 0.05 mmol) in 30 mL dioxane followed by adding, KHF_2 aq. (1.4 g, 18 mmol, H_2O 5.0 mL) and THF (10 mL) afford potassium trifluoro(4-methylbenzyl)borate as a white solid (483 mg, 76% yield).

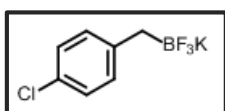


1H NMR (300 MHz, acetone- d_6): δ 6.95-6.86 (m, 3 H), 6.72-6.65 (m, 1 H), 2.19 (s, 3H), 1.59 (br s, 2 H) ppm. ^{13}C NMR (75 MHz, acetone- d_6): δ 143.9, 132.1, 129.7, 128.9, 21.1 ppm.

Potassium trifluoro(4-chlorobenzyl)borate (1k)

According to the general procedure, 4-chlorobenzyl chloride (0.483g, 3 mmol) bis(pinacolato)diboron (0.914g, 3.6 mmol), K_2CO_3 (1.24 g, 9 mmol), $Pd(PPh_3)_4$ (39.3 mg, 0.05 mmol) in 30 mL dioxane followed by adding, KHF_2 aq. (1.4 g, 18 mmol, H_2O 5.0 mL) and THF (10 mL) afford potassium trifluoro(4-chlorobenzyl)borate as a white solid

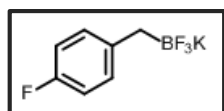
(565 mg, 81% yield).



^1H NMR (300 MHz, acetone- d_6): δ 7.09-7.01 (m, 4 H), 1.61 (br s, 2 H) ppm. ^{13}C NMR (75 MHz, acetone- d_6): δ 146.6, 131.4, 128.5, 128.0 ppm.

Potassium trifluoro(4-fluorobenzyl)borate (**1l**)

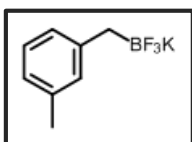
According to the general procedure, 4-fluorobenzyl bromide (0.567g, 3 mmol) gbis(pinacolato)diboron (0.914g, 3.6 mmol), K_2CO_3 (1.24 g, 9 mmol), $\text{Pd}(\text{PPh}_3)_4$ (39.3 mg, 0.05 mmol) in 30 mL dioxane followed by adding, KHF_2 aq. (1.4 g, 18 mmol, H_2O 5.0 mL) and THF (10 mL) afford potassium trifluoro(4-fluorobenzyl)borate as a white solid (479 mg, 74% yield).



^1H NMR (300 MHz, acetone- d_6): δ 7.02-6.94 (m, 2 H), 6.72-6.63 (m, 2 H), 1.51 (br s, 2 H) ppm. ^{13}C NMR (75 MHz, acetone- d_6): δ 146.3, 130.9, 130.8, 114.4 ppm.

Potassium trifluoro(3-methylbenzyl)borate (**1m**)

According to the general procedure, 3-methylbenzyl bromide (0.555g, 3 mmol) gbis(pinacolato)diboron (0.914g, 3.6 mmol), K_2CO_3 (1.24 g, 9 mmol), $\text{Pd}(\text{PPh}_3)_4$ (39.3 mg, 0.05 mmol) in 30 mL dioxane followed by adding, KHF_2 aq. (1.4 g, 18 mmol, H_2O 5.0 mL) and THF (10 mL) afford potassium trifluoro(3-methylbenzyl)borate as a white solid (566 mg, 89% yield).



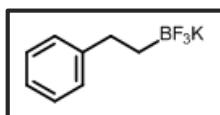
^1H NMR (300 MHz, acetone- d_6): δ 6.95-6.86 (m, 3 H), 6.72-6.65 (m, 1 H), 2.19 (s, 3H), 1.59 (br s, 2 H) ppm. ^{13}C NMR (75 MHz, acetone- d_6): δ 144.5, 129.8, 126.9, 122.8, 20.7 ppm.

For the trifluoroborates **1n**, **1p**, **1q**, **1s** and **1t**, the boronic acid pinacol ester was purchased

instead of the alkyl bromide/halide. Thus the synthesis involves only the addition of KHF_2 to the boronic acid pinacol ester.

Potassium (2-phenylethyl) trifluoroborate (1n)

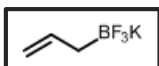
According to the general procedure pinacol ester (0.862 g, 3.03 mmol), KHF_2 aq. (1.4 g, 18 mmol, H_2O 5 mL) and THF (10 mL) afford potassium (2-phenylethyl)trifluoro Borate as a white solid (274 mg, 43%).



^1H NMR (300 MHz, acetone- d_6) δ : 7.17-7.20 (m, 4H), 7.04-7.06 (m, 1H), 2.55-2.59 (m, 2H), 0.46-0.52 (m, 2H) ppm. ^{13}C NMR (75 MHz, acetone- d_6) δ : 149.4, 128.7, 128.6, 125.1, 33, 22.5 ppm.

Potassium allyl trifluoroborate (1p)

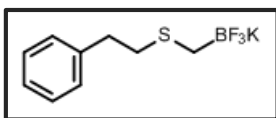
According to the general procedure pinacol ester (0.501 g, 3. mmol), KHF_2 aq. (1.4 g, 18 mmol, H_2O 5 mL) and THF (10 mL) afford potassium allyl trifluoroborate as a white solid (287mg, 65%).



^1H -NMR (300 MHz, acetone- d_6) δ 5.94 (ddt, $J = 17.1, 10.0, 7.9$ Hz, 1H), 4.68 (dd, $J = 17.1, 1.3$ Hz, 1H), 4.57 (dd, $J = 10.0, 2.3$ Hz, 1H), 1.24-1.11 (m, 2H); ^{13}C -NMR (75 MHz, acetone- d_6) δ 143.0, 110.1 ppm.

Potassium phenethylthiomethyl trifluoroborate (1q)

According to the general procedure (0.789 g, 6 mmol), KHF_2 aq. (2.8 g, 36 mmol, H_2O 10 mL) and THF (20 mL) afford Potassium trifluoro (4-methoxybenzyl) borate as a white solid (671 mg, 92% yield).



^1H NMR (300 MHz, DMSO- d_6) δ 7.22 (m, 2H), 7.15 (m, 3H), 2.75 (m, 2H), 2.53 (m, 2H), 1.32 (q, $J = 5.5$ Hz, 2H) ppm. ^{13}C NMR (75 MHz, DMSO- d_6) δ 141.5, 128.4, 128.2, 125.8, 36.0, 35.6, 22.3 ppm.

Potassium tertiary butyl trifluoroborate (1s)

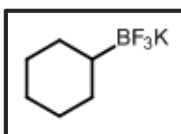
According to the general procedure (0.549 g, 3. mmol), KHF_2 aq. (1.4 g, 18 mmol, H_2O 5 mL) and THF (10 mL) afford potassium tertiary butyl trifluoroborate as a white solid (313 mg, 64%).



^1H NMR (300 MHz, acetone d_6): δ 0.73 (s, 9H) ppm; ^{13}C NMR (100 MHz, acetone d_6): δ = 27.9 ppm.

Potassium cyclohexyl trifluoroborate (1t)

According to the general procedure (0.627 g, 3. mmol), KHF_2 aq. (1.4 g, 18 mmol, H_2O 5 mL) and THF (10 mL) afford potassium cyclohexyl trifluoroborate as a white solid (400mg, 73%).

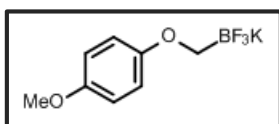


^1H NMR (300 MHz, DMSO- d_6): δ : 1.55 (m, 3H), 1.47 (m, 2H), 1.03 (m, 3H), 0.88 (m, 2H), -0.02 (br, 1H) ppm. ^{13}C NMR (75 MHz, DMSO- d_6): δ : 28.9, 28.4, 27.7 ppm.

Potassium (p-methoxyphenoxy)methyltrifluoroborate (1o)

A 100 mL 2-neck round-bottom flask was charged with NaH (60% dispersion in mineral oil) (0.608 g, 15 mmol, 3equ) and 25 mL of dry THF. p-methoxyphenol (1.87 g, 15 mmol, 3.0 eq.) was added drop wise to the suspension via syringe at 0 °C under N_2 . The mixture was stirred for 15 min and then allowed to warm to rt for 30 min. bromomethyltrifluoroborate (1.02 g, 5.0 mmol, 1.0 eq.) was added to mixture in one portion at 0 °C. The reaction mixture was stirred at rt for 3 days. The mixture was quenched by adding saturated aq. KHF_2 (4.5 M). The reaction mixture was stirred at rt for 30 min, and then the suspension was concentrated and dried in vacuo. The crude solid was extracted with hot acetone and washed with CH_2Cl_2 . The pure compound was dried in vacuo and obtained as a white solid.

The product was obtained in 34% yield (0.418 g, 1.7 mmol) as a white solid.

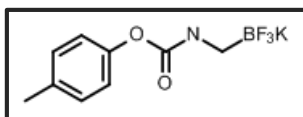


^1H NMR (300 MHz, DMSO- d_6): δ 6.76 (s, 2H), 6.76 (s, 2H), 3.66 (s, 3H), 2.88 (brs, 2H) ppm. ^{13}C NMR (75 MHz, DMSO- d_6): δ 156.2,

151.9, 114.3, 114.2, 55.3 ppm.

Potassium (4-methylphenoxy)carbonylaminomethyltrifluoroborate (1r)

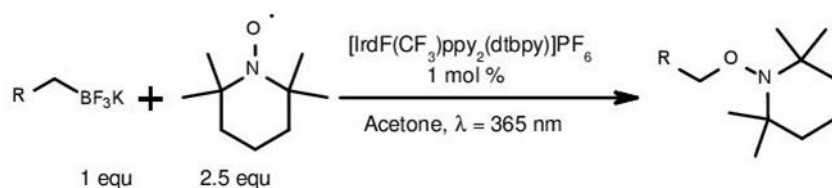
Freshly prepared KHMDS (11% in toluene, ca. 0.5 M) (10mL) in dry THF (10 mL) was added drop wise to a solution of 2-(chloromethyl)-4,4,5,5-tetramethyl-1,3,2-dioxaborolane (0.919 g, 5.16 mmol) in dry THF (10 mL) at -78°C . After stirring for 15 min, the cooling bath was removed and the mixture was stirred at rt for an additional 2 h. Then dry MeOH (0.4 mL) was added at 0°C . After stirring at 0°C for an additional 2 h, p-tolylchloroformate (1.81 g, 10.6 mmol) was added. The reaction was warmed to rt by removing the ice bath and stirring for 24 h. The reaction mixture was concentrated under reduced pressure to remove the THF and toluene. The residue was diluted with MeOH (10 mL) and cooled to 0°C before addition of a saturated solution of KHF_2 (1.55 g, 20.0 mmol). The mixture was stirred at 0°C for 30 min, then dried in vacuo. The residue was dissolved in hot acetone and filtered. After the solvent was removed, the residue was washed with Et₂O and dried under in vacuo. The product was obtained in 51% yield (0.712 g, 2.63 mmol) as a white solid.



^1H NMR (300 MHz, DMSO- d_6 , rt) δ 7.12 (d, $J = 7.6$, 2H), 6.91 (d, $J = 7.6$ Hz, 2H), 5.66 (brs, 2H), 2.27 (s, 3H), 1.97 (m, 2H) ppm.

^{13}C NMR (75 MHz, DMSO- d_6 , rt) δ 155.1, 149.4, 133.2, 129.3, 121.4, 20.3 ppm.

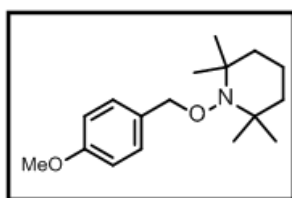
General procedure for the photocatalytic synthesis of oxyanimated products in flow



A potassium trifluoroborate (50 μmol), TEMPO (2.5 eq., 125 μmol), $[\text{Ir}(\text{dF}(\text{CF}_3)\text{ppy})_2(\text{bpy})](\text{PF}_6)$ (0.5 mg, 1 mol%), and 1,3,5-trimethoxybenzene (1 eq., 50 μmol) as an internal standard are mixed in 1.5 mL of acetone. The reaction mixture was degassed by freeze-pump-thaw cycle. The degassed solution was transferred into the syringe and injected into the Mikroglas Dwell Device that is irradiated by the UV LEDs of irradiance 200 $\text{mW}\cdot\text{cm}^{-2}$. The collected irradiated mixture was concentrated by *vacuo* to be dissolved in CDCl_3 and analyzed by ^1H NMR.

1-(4-Methoxybenzyloxy)-2,2,6,6-tetramethylpiperidine (2h)

According to general procedure, TEMPO (39 mg, 0.25 mmol), $[\text{Ir}(\text{dF}(\text{CF}_3)\text{ppy})_2(\text{bpy})](\text{PF}_6)$ (1 mg, 1 mol %), trifluoroborate potassium salt (59 mg, 0.1 mmol) and acetone (3 mL) for irradiation of UV LEDs in flow for 2.5 minutes afford 2c as a pale yellow oil (27.2 mg, 98%) after purification with column chromatography on silica gel (hexane/EtOAc = 20:1).

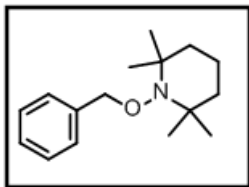


^1H NMR (300 MHz, CDCl_3 , rt): δ 7.33 (d, $J = 8.4$ Hz, 2 H), 6.92 (d, $J = 8.4$ Hz, 2 H), 4.78 (s, 2 H), 3.85 (s, 3 H), 1.70-1.31 (m, 6 H), 1.30 (s, 6 H), 1.18 (s, 6 H). ^{13}C NMR (75 MHz, CDCl_3 , rt): δ 158.4, 129.0, 128.5, 113.0, 77.8, 59.3, 54.7, 39.1, 32.6, 19.7, 16.5.

1-Benzyloxy-2,2,6,6-tetramethylpiperidine (2i)

According to general procedure, TEMPO (39 mg, 0.25 mmol), $[\text{Ir}(\text{dF}(\text{CF}_3)\text{ppy})_2(\text{bpy})](\text{PF}_6)$ (1 mg, 1 mol %), trifluoroborate potassium salt (19.8 mg, 0.1 mmol) and acetone (3 mL) for

irradiation of UV LEDs in flow for 45 minutes to afford 2a as a colorless oil (22 mg, 89 % yield) after purification with column chromatography on silica gel (hexane/EtOAc = 20:1). Spectral data are in agreement with the literature.

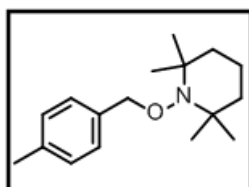


^1H NMR (300 MHz, CDCl_3 , rt): δ 7.38-7.27 (m, 5 H), 4.83 (s, 2 H), 1.70-1.49 (m, 6 H), 1.26 (s, 6 H), 1.16 (s, 6 H). ^{13}C NMR (75 MHz, CDCl_3 , rt): δ 138.4, 128.3, 127.6, 127.4, 78.9, 60.1, 39.9, 33.2, 20.4,

17.3.

1-(4-Methylbenzyloxy)-2,2,6,6-tetramethylpiperidine (2j)

According to general procedure, TEMPO (39 mg, 0.25 mmol), $[\text{Ir}(\text{dF}(\text{CF}_3)\text{ppy})_2(\text{bpy})](\text{PF}_6)$ (1.0 mg, 1 mol %), trifluoroborate potassium salt (21 mg, 0.1 mmol) and acetone (3 mL) for irradiation of UV LEDs in flow for 20 minutes afford 2b as a pale yellow oil (25.7 mg, 99 % yield) after purification with column chromatography on silica gel (hexane/EtOAc = 20:1).

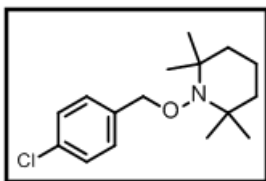


^1H NMR (300 MHz, CDCl_3 , rt): δ 7.30 (d, $J = 7.6$ Hz, 2 H), 7.20 (d, $J = 7.6$ Hz, 2 H), 4.82 (s, 2 H), 1.70-1.38 (m, 6 H), 1.30 (s, 6 H), 1.18 (s, 6 H). ^{13}C NMR (75 MHz, CDCl_3 , rt): δ 136.1, 134.3, 128.1, 126.8,

77.8, 59.1, 38.9, 32.3, 20.4, 19.4, 16.3.

1-(4-Chloro-benzyloxy)-2,2,6,6-tetramethylpiperidine (2k)

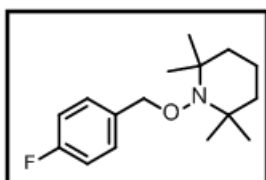
According to general procedure, TEMPO (39 mg, 0.25 mmol), $[\text{Ir}(\text{dF}(\text{CF}_3)\text{ppy})_2(\text{bpy})](\text{PF}_6)$ (1 mg, 1mol %), trifluoroborate potassium salt (21.8 mg, 0.1 mmol) and acetone (3 mL) for irradiation of UV LEDs in flow for 80 minutes afford 2c as a pale yellow oil (10.7 mg, 38%) after purification with column chromatography on silica gel (hexane/EtOAc = 20:1).



^1H NMR (300 MHz, CDCl_3 , rt): δ 7.31-7.26 (m, 4 H), 4.79 (s, 2 H), 1.70-1.30 (m, 6 H), 1.24 (s, 6 H), 1.15 (s, 6 H). ^{13}C NMR (75 MHz, CDCl_3 , rt): δ 136.7, 132.9, 128.6, 128.3, 77.9, 59.9, 39.7, 33.0, 20.2, 17.0.

1-(4-fluorobenzoyloxy)-2,2,6,6-tetramethylpiperidine (2l)

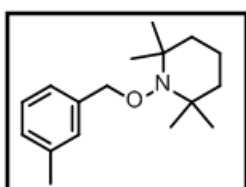
According to general procedure, TEMPO (39 mg, 0.25 mmol), $[\text{Ir}(\text{dF}(\text{CF}_3)\text{ppy})_2(\text{bpy})](\text{PF}_6)$ (1 mg, 1 mol %), trifluoroborate potassium salt (21.5 mg, 0.1 mmol) and acetone (3 mL) for irradiation of UV LEDs in flow for 80 minutes afford 2c as a pale yellow oil (23.9 mg, 90%) after purification with column chromatography on silica gel (hexane/EtOAc = 20:1).



^1H NMR (300 MHz, CDCl_3): δ 7.02-6.94 (m, 2 H), 6.72-6.63 (m, 2 H), 4.79 (s, 2 H), 1.7-1.3 (m, 6H), 1.24 (s, 6H), 1.12 (s, 6H) ppm. ^{13}C NMR (75 MHz, CDCl_3): δ 146.3, 130.9, 130.8, 114.4, 77.9, 59.9, 39.7, 33, 20.2, 17 ppm.

1-(3-methylbenzoyloxy)-2,2,6,6-tetramethylpiperidine (2m)

According to general procedure, TEMPO (39 mg, 0.25 mmol), $[\text{Ir}(\text{dF}(\text{CF}_3)\text{ppy})_2(\text{bpy})](\text{PF}_6)$ (1 mg, 1 mol %), trifluoroborate potassium salt (21.1 mg, 0.1 mmol) and acetone (3 mL) for irradiation of UV LEDs in flow for 40 minutes afford 2c as a pale yellow oil (25.6 mg, 98%) after purification with column chromatography on silica gel (hexane/EtOAc = 20:1).

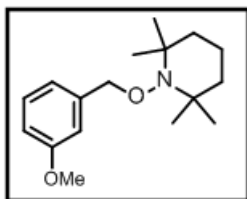


^1H NMR (300 MHz, CDCl_3): δ 6.95-6.86 (m, 3 H), 6.72-6.65 (m, 1 H), 4.82 (s, 2 H), 2.19 (s, 3H), 1.7-1.3 (m, 6H), 1.24 (s, 6H), 1.12 (s, 6H) ppm. ^{13}C NMR (75 MHz, CDCl_3): δ 144.5, 129.8, 126.9, 122.8,

77.9, 59.9, 39.7, 33, 20.2, 20.7, 17 ppm

1-(3-methoxy-benzyloxy)-2,2,6,6-tetramethylpiperidine (2o)

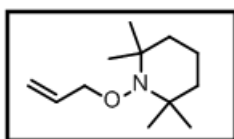
According to general procedure, TEMPO (39 mg, 0.25 mmol), [Ir(dF(CF₃)ppy)₂(bpy)](PF₆) (1 mg, 1 mol %), trifluoroborate potassium salt (21.5 mg, 0.1 mmol) and acetone (3 mL) for irradiation of UV LEDs in flow for 90 minutes afford 2c as a pale yellow oil (15.2 mg, 67%) after purification with column chromatography on silica gel (hexane/EtOAc = 20:1).



¹H NMR (300 MHz, CDCl₃): δ 6.95-6.86 (m, 3 H), 6.72-6.65 (m, 1 H), 4.82 (s, 2 H), 3.65 (s, 3H), 1.7-1.3 (m, 6H), 1.24 (s, 6H), 1.12 (s, 6H) ppm. ¹³C NMR (75 MHz, CDCl₃): δ 144.5, 129.8, 126.9, 122.8, 77.8, 59.3, 54.7, 39.1, 32.6, 19.7, 16.5 ppm.

1-(allyloxy)-2,2,6,6-tetramethylpiperidine (2p)

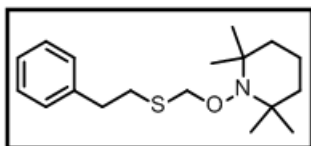
According to general procedure, TEMPO (39 mg, 0.25 mmol), [Ir(dF(CF₃)ppy)₂(bpy)](PF₆) (1 mg, 1 mol %), trifluoroborate potassium salt (14.7 mg, 0.1 mmol) and acetone (3 mL) for irradiation of UV LEDs in flow for 40 minutes afford 2c as a pale yellow oil (14.8 mg, 75%) after purification with column chromatography on silica gel (hexane/EtOAc = 20:1).



¹H NMR (300 MHz, CDCl₃) δ 5.94 (ddt, J = 17.1, 10.0, 7.9 Hz, 1H), 4.68 (dd, J = 17.1, 1.3 Hz, 1H), 4.75 (s, 2 H), 4.57 (dd, J = 10.0, 2.3 Hz, 1H), 1.7-1.3 (m, 6H), 1.24 (s, 6H), 1.12 (s, 6H) ppm; ¹³C NMR (75 MHz, CDCl₃) δ 143.0, 110.1, 76.5, 57.9, 53.8, 39.5, 31.8, 19.3, 16.8 ppm

1-(phenethylthiomethyl)-2,2,6,6-tetramethylpiperidine (2q)

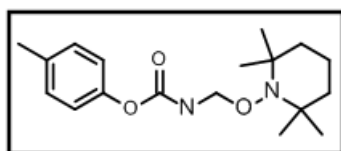
According to general procedure, TEMPO (39 mg, 0.25 mmol), [Ir(dF(CF₃)ppy)₂(bpy)](PF₆) (1 mg, 1 mol %), trifluoroborate potassium salt (25.7 mg, 0.1 mmol) and acetone (3 mL) for irradiation of UV LEDs in flow for 60 minutes afford 2c as a pale yellow oil (8.6 mg, 28%) after purification with column chromatography on silica gel (hexane/EtOAc = 20:1).



^1H NMR (300 MHz, DMSO- d_6) δ 7.22 (m, 2H), 7.15 (m, 3H), 4.82 (s, 2 H), 2.53 (m, 2H), 1.32 (q, $J = 5.5$ Hz, 2H), 1.7-1.3 (m, 6H), 1.24 (s, 6H), 1.12 (s, 6H) ppm. ^{13}C NMR (75 MHz, DMSO- d_6) δ 141.5, 128.4, 128.2, 125.8, 78.9, 60.1, 39.9, 36.0, 33.2, 22.3, 20.4, 17.3 ppm.

1-((4-methylphenoxy)carbonylaminoethyl)-2,2,6,6-tetramethylpiperidine (2r)

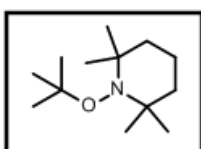
According to general procedure, TEMPO (39 mg, 0.25 mmol), $[\text{Ir}(\text{dF}(\text{CF}_3)\text{ppy})_2(\text{bpy})](\text{PF}_6)$ (1 mg, 1 mol %), trifluoroborate potassium salt (26.9 mg, 0.1 mmol) and acetone (3 mL) for irradiation of UV LEDs in flow for 80 minutes afford 2c as a pale yellow oil (11.2 mg, 35 %) after purification with column chromatography on silica gel (hexane/EtOAc = 20:1).



^1H NMR (300 MHz, CDCl_3) δ 7.12 (d, $J = 7.6$, 2H), 6.91 (d, $J = 7.6$ Hz, 2H), 4.9 (s, 2H), 2.27 (s, 3H), 1.97 (m, 2H) 1.7-1.3 (m, 6H), 1.24 (s, 6H), 1.12 (s, 6H) ppm. ^{13}C NMR (75 MHz, CDCl_3) δ 155.1, 149.4, 133.2, 129.3, 86, 59.3, 54.7, 39.1, 32.6, 19.7, 16.5, 20.3 ppm

1-tert-Butoxy-2,2,6,6-tetramethylpiperidine (2s)

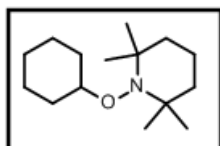
According to general procedure, TEMPO (39 mg, 0.25 mmol), $[\text{Ir}(\text{dF}(\text{CF}_3)\text{ppy})_2(\text{bpy})](\text{PF}_6)$ (1 mg, 1 mol %), trifluoroborate potassium salt (16.5 mg, 0.1 mmol) and acetone (3 mL) for irradiation of UV LEDs in flow for 6 hours afford 2c as a colorless oil (8.5 mg, 40 %) after purification with column chromatography on silica gel (hexane/EtOAc = 20:1).



^1H NMR (300 MHz, CDCl_3): δ 1.63-1.58 (m, 6 H), 1.27 (m, 9 H), 1.25 (s, 6 H), 1.19 (s, 6 H). ^{13}C NMR (75 MHz, CDCl_3): δ 77.4, 58.0, 37.6, 32.8, 30.8, 27.4, 18.4, 15.0.

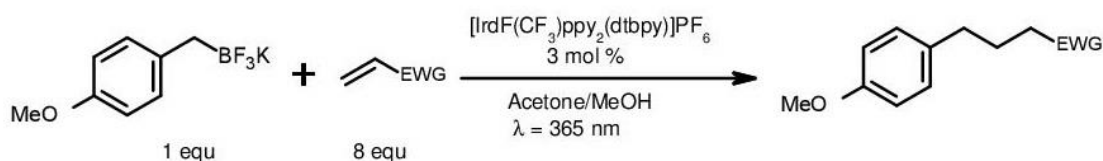
1-Cyclohexyloxy-2,2,6,6-tetramethylpiperidine (2t)

According to general procedure, TEMPO (78 mg, 0.5 mmol), [Ir(dF(CF₃)ppy)₂(bpy)](PF₆) (2 mg, 1 mol %), trifluoroborate potassium salt (38 mg, 0.2 mmol) and acetone (6 mL) for irradiation of UV LEDs in flow for 6 hours afford 2c as a colorless oil (12 mg, 25%) after purification with column chromatography on silica gel (hexane/EtOAc = 20:1).



¹H NMR (300 MHz, CDCl₃, rt): δ 3.64-3.57 (m, 1 H), 2.10-2.06 (m, 2 H), 1.77-1.75 (m, 2 H), 1.70-1.20 (m, 12 H), 1.12 (s, 12 H). ¹³C NMR (75 MHz, CDCl₃): δ 81.5, 59.3, 40.1, 34.3, 32.6, 25.7, 24.8, 19.9, 17.1.

Photocatalytic synthesis of 1,4-addition products in flow

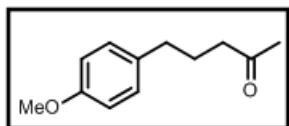


Potassium trifluoro (4-methoxybenzyl) borate (28.5 mg, 125 μmol), H[Ir(dF(CF₃)ppy)₂(bpy)](PF₆) (1.5 mg, 3 mol %), 1,3,5-trimethoxybenzene (21 mg, 125 μmol) and as an internal standard and a Michael acceptor (1 mmol, 8 equ) were added to acetone (1.50 mL) and MeOH (0.5 mL). The reaction mixture was degassed by freeze-pump-thaw cycle to be then transferred into a syringe. The mixture was then injected into the Mikroglas Dwell Device that was irradiated by UV LEDs (200 mW.cm⁻²). The collected irradiated mixture was concentrated by vacuo, re-dissolved in CDCl₃ and analyzed by ¹H NMR

5-(*p*-Methoxyphenyl)-2-pentanone (4a)

According to general procedure, [Ir(dF(CF₃)ppy)₂(bpy)](PF₆) (1.5 mg, 3 mol %), methyl vinyl ketone (70 mg, 1 mmol), potassium trifluoro(*p*-methoxybenzyl)borate (21 mg, 0.125

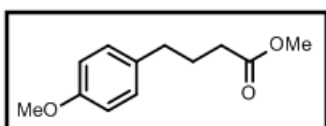
mmol), acetone (1.5 mL) and MeOH (0.5 mL) for irradiation of UV LEDs in flow for 30 minutes afford **4a** as a colorless oil (21.7 mg, 90 % yield) after purification with column chromatography on silica gel (hexane/EtOAc = 10:1). Spectral data are in agreement with the literature.



$^1\text{H NMR}$ (300 MHz, CDCl_3): δ 7.08 (d, $J = 9.4$ Hz, 2 H), 6.83 (d, $J = 9.4$ Hz, 2 H), 3.79 (s, 3 H), 2.56 (t, $J = 7.2$ Hz, 2 H), 2.42 (t, $J = 7.2$ Hz, 2 H), 2.11 (s, 3 H), 1.91-1.83 (m, 2 H). $^{13}\text{C NMR}$ (75 MHz, CDCl_3): δ 209.0, 158.0, 133.8, 129.5, 113.9, 55.4, 42.9, 34.2, 30.1, 25.6.

Methyl 4-(*p*-methoxyphenyl)butanoate (**4b**)

According to general procedure, $[\text{Ir}(\text{dF}(\text{CF}_3)\text{ppy})_2(\text{bpy})](\text{PF}_6)$ (1.5 mg, 3 mol %), methyl acrylate (100 mg, 1 mmol), potassium trifluoro(*p*-methoxybenzyl)borate (21 mg, 0.125 mmol), acetone (1.5 mL) and MeOH (0.5 mL) for irradiation of UV LEDs in flow for 30 minutes afford **4b** as a colorless oil (14.8 mg, 57 % yield) after purification with column chromatography on silica gel (hexane/EtOAc = 20:1). Spectral data are in agreement with the literature.



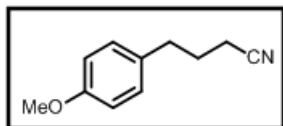
$^1\text{H NMR}$ (300 MHz, CDCl_3): δ 7.09 (dd, $J = 6.8, 2.0$ Hz, 2 H), 6.83 (dd, $J = 6.8, 2.0$ Hz, 2 H), 3.78 (s, 3 H), 3.66 (s, 3 H), 2.59 (t, $J = 7.2$ Hz, 2 H), 2.32 (t, $J = 7.2$ Hz, 2 H), 1.96-1.88 (m, 2 H).

$^{13}\text{C NMR}$ (75 MHz, CDCl_3): δ 174.1, 158.1, 133.6, 129.5, 114.0, 55.4, 51.6, 34.3, 33.5, 26.8.

4-(*p*-methoxyphenyl)butyronitrile (**4c**)

According to general procedure, $[\text{Ir}(\text{dF}(\text{CF}_3)\text{ppy})_2(\text{bpy})](\text{PF}_6)$ (1.5 mg, 3 mol %), acrylonitrile (53 mg, 1 mmol), potassium trifluoro(*p*-methoxybenzyl)borate (21 mg, 0.125 mmol), acetone (1.5 mL) and MeOH (0.5 mL) for irradiation of UV LEDs in flow for 15

minutes afford **4c** as a colorless oil (20 mg, 94 % yield) after purification with column chromatography on silica gel (hexane/EtOAc = 10:1). Spectral data are in agreement with the literature.



$^1\text{H NMR}$ (300 MHz, CDCl_3): δ 7.10 (dd, $J = 6.8, 2.0$ Hz, 2 H), 6.86 (dd, $J = 6.8, 2.0$ Hz, 2 H), 3.79 (s, 3 H), 2.72 (t, $J = 7.2$ Hz, 2 H), 2.30 (t, $J = 7.2$ Hz, 2 H), 1.99-1.91 (m, 2 H). $^{13}\text{C NMR}$ (75 MHz, CDCl_3): δ 158.5, 131.8, 129.5, 119.6, 114.2, 55.4, 33.6, 27.2, 16.4.

References:

1. Rohatgi-Mukherjee, K., *Fundamentals of photochemistry*. 1978: New Age International.
2. Laurino, P., *Photochemical transformations in continuous flow devices*. 2011, Diss., Eidgenössische Technische Hochschule ETH Zürich, Nr. 19754, 2011.
3. Wazzan, N., *Cis-trans isomerisation of azobenzenes studied by NMR spectroscopy with in situ laser irradiation and DFT calculations*. 2009.
4. Montalti, M., et al., *Handbook of photochemistry*. 2006: CRC press.
5. Cambié, D., et al., *Applications of Continuous-Flow Photochemistry in Organic Synthesis, Material Science, and Water Treatment*. Chemical Reviews, 2016.
6. Nugent, W.A. and J.M. Mayer, *Metal-ligand multiple bonds: the chemistry of transition metal complexes containing oxo, nitrido, imido, alkylidene, or alkylidyne ligands*. 1988: Wiley-Interscience.
7. Lever, A., *Charge transfer spectra of transition metal complexes*. Journal of Chemical Education, 1974. **51**(9): p. 612.
8. Vogler, A. and H. Kunkely, *Photoreactivity of metal-to-ligand charge transfer excited states*. Coordination chemistry reviews, 1998. **177**(1): p. 81-96.
9. Trommsdorff, H., *Über Santonin*. Annalen der Pharmacie, 1834. **11**(2): p. 190-207.
10. Cannizzaro, S. and F. Sestini, *Ricerche sulla Santonina*. 1873.
11. Ciamician, G. and P. Silber, *Chemische lichtwirkungen*. Berichte der deutschen chemischen Gesellschaft, 1901. **34**(2): p. 1530-1543.
12. Eaton, P.E. and T.W. Cole, *The cubane system*. Journal of the American Chemical Society, 1964. **86**(5): p. 962-964.
13. Corey, E. and S. Nozoe, *Total synthesis of α -caryophyllene alcohol*. Journal of the American Chemical Society, 1964. **86**(8): p. 1652-1653.
14. Wender, P. and J. Howbert, *Synthetic studies on arene-olefin cycloadditions: total synthesis of (+)- α -cedrene*. Journal of the American Chemical Society, 1981. **103**(3): p. 688-690.
15. Metzger, H., et al., *Photo-Nitrosierung und-Oximierung gesättigter Kohlenwasserstoffe*. Angewandte Chemie, 1959. **71**(7): p. 229-236.
16. Fors, B.P. and C.J. Hawker, *Control of a living radical polymerization of methacrylates by light*. Angewandte Chemie International Edition, 2012. **51**(35): p. 8850-8853.
17. Prier, C.K., D.A. Rankic, and D.W. MacMillan, *Visible light photoredox catalysis with transition metal complexes: applications in organic synthesis*. Chemical reviews, 2013. **113**(7): p. 5322-5363.
18. Narayanam, J.M. and C.R. Stephenson, *Visible light photoredox catalysis: applications in organic synthesis*. Chemical Society Reviews, 2011. **40**(1): p. 102-113.
19. Yoon, T.P., *Visible light photocatalysis: The development of photocatalytic radical ion cycloadditions*. ACS catalysis, 2013. **3**(5): p. 895-902.
20. Koike, T. and M. Akita, *Visible-light radical reaction designed by Ru- and Ir-based photoredox catalysis*. Inorganic Chemistry Frontiers, 2014. **1**(8): p. 562-576.
21. Prier, C.K., D.A. Rankic, and D.W.C. MacMillan, *Visible Light Photoredox Catalysis with Transition Metal Complexes: Applications in Organic Synthesis*. Chemical Reviews, 2013. **113**(7): p. 5322-5363.
22. Knowles, J.P., L.D. Elliott, and K.I. Booker-Milburn, *Flow photochemistry: Old light through new windows*. Beilstein journal of organic chemistry, 2012. **8**(1): p. 2025-2052.
23. Noblelight, H. *High and Low Pressure UV Mercury Vapour Lamps*. 2013; Available from: https://www.heraeus.com/en/hng/products_and_solutions/lamps_for_optics_and_analytics/mercury_lamps.aspx.
24. Company, S.N.E.U., *Rayonet Reactor*. 2013.
25. Limited, P.S.E., *Falling film reactors*. 2014.

26. Baxendale, I.R., et al., *A flow process for the multi-step synthesis of the alkaloid natural product oxomaritidine: a new paradigm for molecular assembly*. *Chemical communications*, 2006(24): p. 2566-2568.
27. Baxendale, I.R., et al., *Multistep synthesis using modular flow reactors: Bestmann–Ohira reagent for the formation of alkynes and triazoles*. *Angewandte Chemie International Edition*, 2009. **48**(22): p. 4017-4021.
28. Mason, B.P., et al., *Greener approaches to organic synthesis using microreactor technology*. *Chemical reviews*, 2007. **107**(6): p. 2300-2318.
29. Ehrfeld, W., V. Hessel, and V. Haverkamp, *Microreactors*. 2000: Wiley Online Library.
30. Köhler, J., et al., *Digital reaction technology by micro segmented flow—components, concepts and applications*. *Chemical Engineering Journal*, 2004. **101**(1): p. 201-216.
31. Su, Y., et al., *Photochemical transformations accelerated in continuous-flow reactors: basic concepts and applications*. *Chemistry—A European Journal*, 2014. **20**(34): p. 10562-10589.
32. Aillet, T., et al., *Accurate measurement of the photon flux received inside two continuous flow microphotoreactors by actinometry*. *International Journal of Chemical Reactor Engineering*, 2014. **12**(1): p. 257-269.
33. Jamali, A., et al., *A batch LED reactor for the photocatalytic degradation of phenol*. *Chemical Engineering and Processing: Process Intensification*, 2013. **71**: p. 43-50.
34. Su, Y., V. Hessel, and T. Noël, *A compact photomicroreactor design for kinetic studies of gas-liquid photocatalytic transformations*. *AIChE Journal*, 2015. **61**(7): p. 2215-2227.
35. Feehs, R.H., *Photochemical apparatus and process*. 1971, Google Patents.
36. Strike, D., et al., *Glucose measurement using a micromachined open tubular heterogeneous enzyme reactor (MOTHER)*. *Microsystem Technologies*, 1994. **1**(1): p. 48-50.
37. Watts, P. and S.J. Haswell, *The application of micro reactors for organic synthesis*. *Chemical Society Reviews*, 2005. **34**(3): p. 235-246.
38. Albin, A. and M. Fagnoni, *Handbook of synthetic photochemistry*. 2009: John Wiley & Sons.
39. Fukuyama, T., et al., *Adventures in inner space: Microflow systems for practical organic synthesis*. *Synlett*, 2008(2): p. 151-163.
40. Shvydkiv, O., et al., *Microphotochemistry: a reactor comparison study using the photosensitized addition of isopropanol to furanones as a model reaction*. *Photochemical & Photobiological Sciences*, 2011. **10**(9): p. 1399-1404.
41. Shvydkiv, O., et al., *From conventional to microphotochemistry: Photodecarboxylation reactions involving phthalimides*. *Organic letters*, 2010. **12**(22): p. 5170-5173.
42. Shvydkiv, O., et al., *Photosensitized addition of isopropanol to furanones in a 365 nm UV-LED microchip*. *Photochemical & Photobiological Sciences*, 2010. **9**(12): p. 1601-1603.
43. Coyle, E.E. and M. Oelgemöller, *Micro-photochemistry: photochemistry in microstructured reactors. The new photochemistry of the future?* *Photochemical & Photobiological Sciences*, 2008. **7**(11): p. 1313-1322.
44. Ciana, C.-L. and C.G. Bochet, *Clean and easy photochemistry*. *CHIMIA International Journal for Chemistry*, 2007. **61**(10): p. 650-654.
45. Hessel, V., S. Hardt, and H. Löwe, *Micro Chemical Process Engineering*. 2004, Wiley-VCH, Weinheim.
46. Jähnisch, K., et al., *Chemistry in microstructured reactors*. *Angewandte Chemie International Edition*, 2004. **43**(4): p. 406-446.
47. Hessel, V., et al., *Laminar mixing in different interdigital micromixers: I. Experimental characterization*. *AIChE Journal*, 2003. **49**(3): p. 566-577.
48. Hessel, V., H. Löwe, and F. Schönfeld, *Micromixers—a review on passive and active mixing principles*. *Chemical Engineering Science*, 2005. **60**(8): p. 2479-2501.
49. El Moctar, A.O., N. Aubry, and J. Batton, *Electro-hydrodynamic micro-fluidic mixer*. *Lab on a Chip*, 2003. **3**(4): p. 273-280.
50. Kralj, J.G., H.R. Sahoo, and K.F. Jensen, *Integrated continuous microfluidic liquid–liquid extraction*. *Lab on a Chip*, 2007. **7**(2): p. 256-263.

51. Baumann, M., et al., *Fully automated continuous flow synthesis of 4, 5-disubstituted oxazoles*. *Organic letters*, 2006. **8**(23): p. 5231-5234.
52. Hartman, R.L., et al., *Distillation in microchemical systems using capillary forces and segmented flow*. *Lab on a Chip*, 2009. **9**(13): p. 1843-1849.
53. Losey, M.W., M.A. Schmidt, and K.F. Jensen, *Microfabricated multiphase packed-bed reactors: characterization of mass transfer and reactions*. *Industrial & engineering chemistry research*, 2001. **40**(12): p. 2555-2562.
54. Hartman, R.L., et al., *Multistep microchemical synthesis enabled by microfluidic distillation*. *Angewandte Chemie International Edition*, 2010. **49**(5): p. 899-903.
55. Incorporated, C. *Corning® Advanced-Flow™ G1 Photo Reactor*. 2014 2014 [cited 2014 March 2014]; Available from: <https://www.corning.com/media/worldwide/global/documents/G1%20Photo%20Reactor%20Product%20Brochure.pdf>.
56. Lu, H., M.A. Schmidt, and K.F. Jensen, *Photochemical reactions and on-line UV detection in microfabricated reactors*. *Lab on a Chip*, 2001. **1**(1): p. 22-28.
57. Wootton, R.C., R. Fortt, and A.J. de Mello, *A microfabricated nanoreactor for safe, continuous generation and use of singlet oxygen*. *Organic process research & development*, 2002. **6**(2): p. 187-189.
58. Fukuyama, T., et al., *Quick execution of [2+ 2] type photochemical cycloaddition reaction by continuous flow system using a glass-made microreactor*. *Chemistry Letters*, 2004. **33**(11): p. 1430-1431.
59. Conradi, M. and T. Junkers, *Efficient [2+ 2] photocycloadditions under equimolar conditions by employing a continuous UV-flow reactor*. *Journal of Photochemistry and Photobiology A: Chemistry*, 2013. **259**: p. 41-46.
60. Zhang, Y., et al., *Peptide Fragment Coupling Using a Continuous-Flow Photochemical Rearrangement of Nitrones*. *Angewandte Chemie International Edition*, 2013. **52**(15): p. 4251-4255.
61. Lefebvre, Q., M. Jentsch, and M. Rueping, *Continuous flow photocyclization of stilbenes—scalable synthesis of functionalized phenanthrenes and helicenes*. *Beilstein journal of organic chemistry*, 2013. **9**(1): p. 1883-1890.
62. Tiwari, D.K., R.A. Maurya, and J.B. Nanubolu, *Visible-Light/Photoredox-Mediated sp³ C—H Functionalization and Coupling of Secondary Amines with Vinyl Azides in Flow Microreactors*. *Chemistry—A European Journal*, 2016. **22**(2): p. 526-530.
63. Talla, A., et al., *Metal-Free Photocatalytic Aerobic Oxidation of Thiols to Disulfides in Batch and Continuous-Flow*. *Advanced Synthesis & Catalysis*, 2015. **357**(10): p. 2180-2186.
64. Jachuck, R. and V. Nekkanti, *Continuous photopolymerization of n-butyl acrylate using a narrow channel reactor*. *Macromolecules*, 2008. **41**(9): p. 3053-3062.
65. Oelgemoeller, M., *Highlights of photochemical reactions in microflow reactors*. *Chemical Engineering & Technology*, 2012. **35**(7): p. 1144-1152.
66. Lévesque, F. and P.H. Seeberger, *Continuous-Flow Synthesis of the Anti-Malaria Drug Artemisinin*. *Angewandte Chemie International Edition*, 2012. **51**(7): p. 1706-1709.
67. Kuhn, H., S. Braslavsky, and R. Schmidt, *Chemical actinometry (IUPAC technical report)*. *Pure and Applied Chemistry*, 2004. **76**(12): p. 2105-2146.
68. Berns, R.S., *Billmeyer and Saltzman's principles of color technology*. 2000: Wiley New York.
69. Fischer, E., *Temperature Dependence of Photoisomerization Equilibria. Part I. Azobenzene and the Azonaphthalenes*. *Journal of the American Chemical Society*, 1960. **82**(13): p. 3249-3252.
70. Leighton, W.G. and G.S. Forbes, *Precision actinometry with uranyl oxalate*. *Journal of the American Chemical Society*, 1930. **52**(8): p. 3139-3152.
71. Volman, D. and J. Seed, *The photochemistry of uranyl oxalate*. *Journal of the American Chemical Society*, 1964. **86**(23): p. 5095-5098.

72. Hatchard, C. and C.A. Parker. *A new sensitive chemical actinometer. II. Potassium ferrioxalate as a standard chemical actinometer.* in *Proceedings of the Royal Society of London A: Mathematical, Physical and Engineering Sciences*. 1956. The Royal Society.
73. Lee, J. and H. Seliger, *Quantum yield of the ferrioxalate actinometer.* The Journal of Chemical Physics, 1964. **40**(2): p. 519-523.
74. Wegner, E.E. and A.W. Adamson, *Photochemistry of complex ions. III. Absolute quantum yields for the photolysis of some aqueous chromium (III) complexes. Chemical actinometry in the long wavelength visible region.* Journal of the American Chemical Society, 1966. **88**(3): p. 394-404.
75. Szychliński, J., et al., *Complementary study on the use of the potassium Reinecke's salt as a chemical actinometer.* Analyst, 1989. **114**(6): p. 739-741.
76. Wintgens, V., L.J. Johnston, and J. Scaiano, *Use of a photoreversible fulgide as an actinometer in one-and two-laser experiments.* Journal of the American Chemical Society, 1988. **110**(2): p. 511-517.
77. Bandara, H.M.D. and S.C. Burdette, *Photoisomerization in different classes of azobenzene.* Chemical Society Reviews, 2012. **41**(5): p. 1809-1825.
78. Rau, H., *Spectroscopic properties of organic azo compounds.* Angewandte Chemie International Edition in English, 1973. **12**(3): p. 224-235.
79. Hartley, G., *The cis-form of azobenzene.* Nature, 1937. **140**: p. 281.
80. Beharry, A.A. and G.A. Woolley, *Azobenzene photoswitches for biomolecules.* Chemical Society Reviews, 2011. **40**(8): p. 4422-4437.
81. Bléger, D., et al., *o-Fluoroazobenzenes as readily synthesized photoswitches offering nearly quantitative two-way isomerization with visible light.* Journal of the American Chemical Society, 2012. **134**(51): p. 20597-20600.
82. Brown, E.V. and G.R. Granneman, *Cis-trans isomerism in the pyridyl analogs of azobenzene. Kinetic and molecular orbital analysis.* Journal of the American Chemical Society, 1975. **97**(3): p. 621-627.
83. Tamai, N. and H. Miyasaka, *Ultrafast dynamics of photochromic systems.* Chemical Reviews, 2000. **100**(5): p. 1875-1890.
84. Bandara, H.D. and S.C. Burdette, *Photoisomerization in different classes of azobenzene.* Chemical Society Reviews, 2012. **41**(5): p. 1809-1825.
85. Lednev, I.K., et al., *Femtosecond Time-Resolved UV-Visible Absorption Spectroscopy of trans-Azobenzene in Solution.* The Journal of Physical Chemistry, 1996. **100**(32): p. 13338-13341.
86. Cattaneo, P. and M. Persico, *An abinitio study of the photochemistry of azobenzene.* Physical Chemistry Chemical Physics, 1999. **1**(20): p. 4739-4743.
87. Wazzan, N.A., P.R. Richardson, and A.C. Jones, *Cis-Trans isomerisation of azobenzenes studied by laser-coupled NMR spectroscopy and DFT calculations.* Photochemical & Photobiological Sciences, 2010. **9**(7): p. 968-974.
88. Monti, S., G. Orlandi, and P. Palmieri, *Features of the photochemically active state surfaces of azobenzene.* Chemical Physics, 1982. **71**(1): p. 87-99.
89. Fujino, T., S.Y. Arzhantsev, and T. Tahara, *Femtosecond/Picosecond Time-Resolved Spectroscopy of *trans*-Azobenzene: Isomerization Mechanism Following $S_{22}(\pi,\pi^*) \rightarrow S_{00}$ Photoexcitation.* Bulletin of the Chemical Society of Japan, 2002. **75**(5): p. 1031-1040.
90. Dou, Y., et al., *Detailed mechanism of trans-cis photoisomerization of azobenzene studied by semiclassical dynamics simulation.* Molecular Physics, 2009. **107**(2): p. 181-190.
91. Wei-Guang Diao, E., *A New Trans-to-Cis Photoisomerization Mechanism of Azobenzene on the $S_1(n,\pi^*)$ Surface.* The Journal of Physical Chemistry A, 2004. **108**(6): p. 950-956.
92. Talaty, E.R. and J.C. Fargo, *Thermal cis-trans-isomerization of substituted azobenzenes: a correction of the literature.* Chemical Communications (London), 1967(2): p. 65-66.

93. Asano, T., et al., *Temperature and pressure dependences of thermal cis-to-trans isomerization of azobenzenes which evidence an inversion mechanism*. Journal of the American Chemical Society, 1981. **103**(17): p. 5161-5165.
94. Nerbonne, J.M. and R.G. Weiss, *Elucidation of the thermal isomerization mechanism for azobenzene in a cholesteric liquid crystal solvent*. Journal of the American Chemical Society, 1978. **100**(18): p. 5953-5954.
95. Zimmerman, G., L.-Y. Chow, and U.-J. Paik, *The Photochemical Isomerization of Azobenzene*. Journal of the American Chemical Society, 1958. **80**(14): p. 3528-3531.
96. Gauglitz, G., *Azobenzene as a convenient actinometer for the determination of quantum yields of photoreactions*. Journal of Photochemistry, 1976. **5**(1): p. 41-47.
97. Gauglitz, G. and S. Hubig, *Azobenzene as a convenient actinometer: evaluation values for UV mercury lines and for the N2 laser line*. Journal of Photochemistry, 1981. **15**(3): p. 255-257.
98. Gauglitz, G. and S. Hubig, *Chemical actinometry in the UV by azobenzene in concentrated solution: A convenient method*. Journal of Photochemistry, 1985. **30**(2): p. 121-125.
99. Siampiringue, N., et al., *The cis → trans photoisomerization of azobenzene: an experimental re-examination*. Journal of Photochemistry, 1987. **37**(1): p. 185-188.
100. NNAJI, N.J., J.U. ANI, and A.M. EKWONU, *THE SOLUTION OF REVERSIBLE FIRST ORDER REACTION EQUATION REVISITED*. Acta Chim. Pharm. Indica, 2013. **3**(3): p. 212-218.
101. Carruthers, W., *Cycloaddition reactions in organic synthesis*. Vol. 8. 2013: Elsevier.
102. Woodward, R. and T.J. Katz, *The mechanism of the Diels-Alder reaction*. Tetrahedron, 1959. **5**(1): p. 70-89.
103. Nicolaou, K.C., et al., *The Diels–Alder reaction in total synthesis*. Angewandte Chemie International Edition, 2002. **41**(10): p. 1668-1698.
104. Houk, K.N., *Frontier molecular orbital theory of cycloaddition reactions*. Accounts of Chemical Research, 1975. **8**(11): p. 361-369.
105. Fukui, K., et al., *Molecular orbital theory of orientation in aromatic, heteroaromatic, and other conjugated molecules*. The Journal of Chemical Physics, 1954. **22**(8): p. 1433-1442.
106. Houk, K., *Applications of frontier molecular orbital theory to pericyclic reactions*. Academic Press, New York, 1977. **2**: p. 181-271.
107. Fleming, I., *Frontier orbitals and organic chemical reactions*. 1977: Wiley.
108. Dilling, W.L., *Intramolecular Photochemical Cycloaddition of Nonconjugated Olefins*. Chemical Reviews, 1966. **66**(4): p. 373-393.
109. Yoon, T.P., M.A. Ischay, and J. Du, *Visible light photocatalysis as a greener approach to photochemical synthesis*. Nature Chemistry, 2010. **2**(7): p. 527-532.
110. Winkler, J.D., C.M. Bowen, and F. Liotta, *[2+ 2] photocycloaddition/fragmentation strategies for the synthesis of natural and unnatural products*. Chemical reviews, 1995. **95**(6): p. 2003-2020.
111. Bach, T., H. Bergmann, and K. Harms, *Enantioselective Intramolecular [2+ 2]-Photocycloaddition Reactions in Solution*. Angewandte Chemie International Edition, 2000. **39**(13): p. 2302-2304.
112. Ojima, I., *Catalytic asymmetric synthesis*. 2004: John Wiley & Sons.
113. Murov, S. and G.S. Hammond, *Mechanisms of photochemical reactions in solution. LVI. A singlet-sensitized reaction*. The Journal of Physical Chemistry, 1968. **72**(11): p. 3797-3801.
114. Shvydkiv, O., K. Nolan, and M. Oelgemöller, *Microphotochemistry: 4, 4'-Dimethoxybenzophenone mediated photodecarboxylation reactions involving phthalimides*. Beilstein journal of organic chemistry, 2011. **7**(1): p. 1055-1063.
115. Tamura, Y., et al., *Intramolecular photocycloaddition of 3-allyloxy-and 3-allylamino-cyclohex-2-enones: formation of oxa-and aza-bicyclo [2, 1, 1] hexanes*. Journal of the Chemical Society D: Chemical Communications, 1971(19): p. 1167-1167.
116. Tamura, Y., et al., *Photochemical syntheses of 2-aza-and 2-oxabicyclo [2.1. 1] hexane ring systems*. The Journal of Organic Chemistry, 1975. **40**(19): p. 2702-2710.

117. Matlin, A.R., et al., *Intramolecular photocycloaddition reactions of 3-(2-propenoxy) cyclopent-2-en-1-ones and 3-(2-propenoxy) cyclohex-2-en-1-ones*. *The Journal Of Organic Chemistry*, 1992. **57**(17): p. 4632-4638.
118. Mattay, J., et al., *Photoreactions of Enones with Amines—Cyclization of Unsaturated Enones and Reductive Ring Opening by Photoinduced Electron Transfer (PET)*. *Chemische Berichte*, 1992. **125**(9): p. 2119-2127.
119. Baldwin, S.W., *Synthetic aspects of 2+ 2 cycloadditions of α , β -unsaturated carbonyl compounds*. *Org. Photochem*, 1981. **5**: p. 123-225.
120. Brimiouille, R. and T. Bach, *[2+ 2] Photocycloaddition of 3-Alkenyloxy-2-cycloalkenones: Enantioselective Lewis Acid Catalysis and Ring Expansion*. *Angewandte Chemie International Edition*, 2014. **53**(47): p. 12921-12924.
121. Blanco-Ania, D., et al., *Rapid and scalable access into strained scaffolds through continuous flow photochemistry*. *Organic Process Research & Development*, 2015.
122. Dilling, W.L., *Photochemical cycloaddition reactions of nonaromatic conjugated hydrocarbon dienes and polyenes*. *Chemical Reviews*, 1969. **69**(6): p. 845-877.
123. Coates, R.M., P.D. Senter, and W.R. Baker, *Annelative ring expansion via intramolecular [2+ 2] photocycloaddition of α , β -unsaturated γ -lactones and reductive cleavage: synthesis of hydrocyclopentacyclooctene-5-carboxylates*. *The Journal of Organic Chemistry*, 1982. **47**(19): p. 3597-3607.
124. Kalyanasundaram, K., *Photophysics, photochemistry and solar energy conversion with tris (bipyridyl) ruthenium (II) and its analogues*. *Coordination Chemistry Reviews*, 1982. **46**: p. 159-244.
125. Juris, A., et al., *Ru (II) polypyridine complexes: photophysics, photochemistry, electrochemistry, and chemiluminescence*. *Coordination Chemistry Reviews*, 1988. **84**: p. 85-277.
126. Hedstrand, D.M., W.H. Kruizinga, and R.M. Kellogg, *Light induced and dye accelerated reductions of phenacyl onium salts by 1, 4-dihydropyridines*. *Tetrahedron Letters*, 1978. **19**(14): p. 1255-1258.
127. Van Bergen, T., et al., *Chemistry of dihydropyridines. 9. Hydride transfer from 1, 4-dihydropyridines to sp^3 -hybridized carbon in sulfonium salts and activated halides. Studies with NAD (P) H models*. *The Journal of Organic Chemistry*, 1979. **44**(26): p. 4953-4962.
128. Zen, J.M., et al., *An efficient and selective photocatalytic system for the oxidation of sulfides to sulfoxides*. *Angewandte Chemie*, 2003. **115**(5): p. 597-599.
129. Okada, K., et al., *Photosensitized decarboxylative Michael addition through N-(acyloxy) phthalimides via an electron-transfer mechanism*. *Journal of the American Chemical Society*, 1991. **113**(24): p. 9401-9402.
130. Ischay, M.A., et al., *Efficient visible light photocatalysis of [2+ 2] enone cycloadditions*. *Journal of the American Chemical Society*, 2008. **130**(39): p. 12886-12887.
131. Nicewicz, D.A. and D.W. MacMillan, *Merging photoredox catalysis with organocatalysis: the direct asymmetric alkylation of aldehydes*. *Science*, 2008. **322**(5898): p. 77-80.
132. Nagib, D.A., M.E. Scott, and D.W. MacMillan, *Enantioselective α -trifluoromethylation of aldehydes via photoredox organocatalysis*. *Journal of the American Chemical Society*, 2009. **131**(31): p. 10875-10877.
133. Narayanam, J.M., J.W. Tucker, and C.R. Stephenson, *Electron-transfer photoredox catalysis: development of a tin-free reductive dehalogenation reaction*. *Journal of the American Chemical Society*, 2009. **131**(25): p. 8756-8757.
134. Condie, A.G., J.C. González-Gómez, and C.R. Stephenson, *Visible-light photoredox catalysis: Aza-Henry reactions via C–H functionalization*. *Journal of the American Chemical Society*, 2010. **132**(5): p. 1464-1465.
135. Campagna, S., et al., *Photochemistry and photophysics of coordination compounds: ruthenium*, in *Photochemistry and Photophysics of Coordination Compounds I*. 2007, Springer. p. 117-214.

136. Bock, C., et al., *Estimation of excited-state redox potentials by electron-transfer quenching. Application of electron-transfer theory to excited-state redox processes.* Journal of the American Chemical Society, 1979. **101**(17): p. 4815-4824.
137. Pavlishchuk, V.V. and A.W. Addison, *Conversion constants for redox potentials measured versus different reference electrodes in acetonitrile solutions at 25 C.* Inorganica Chimica Acta, 2000. **298**(1): p. 97-102.
138. Baik, T.-G., et al., *A diastereoselective metal-catalyzed [2+ 2] cycloaddition of bis-enones.* Journal of the American Chemical Society, 2001. **123**(27): p. 6716-6717.
139. Yang, J., et al., *Anion Radical [2+ 2] Cycloaddition as a Mechanistic Probe: Stoichiometry- and Concentration-Dependent Partitioning of Electron-Transfer and Alkylation Pathways in the Reaction of the Gilman Reagent $\text{Me}_2\text{CuLi} \ominus \text{Li}^+$ with Bis (enones).* The Journal of organic chemistry, 2004. **69**(23): p. 7979-7984.
140. Wang, L.-C., et al., *Diastereoselective cycloreductions and cycloadditions catalyzed by co (dpm) 2-silane (dpm= 2, 2, 6, 6-tetramethylheptane-3, 5-dionate): mechanism and partitioning of hydrometallative versus anion radical pathways.* Journal of the American Chemical Society, 2002. **124**(32): p. 9448-9453.
141. Roh, Y., et al., *Anion radical chain cycloaddition of tethered enones: Intramolecular cyclobutanation and Diels-Alder cycloaddition.* Organic letters, 2002. **4**(4): p. 611-613.
142. Du, J., et al., *Photocatalytic reductive cyclizations of enones: Divergent reactivity of photogenerated radical and radical anion intermediates.* Chemical Science, 2011. **2**(11): p. 2115-2119.
143. Chandler, C.L. and B. List, *Catalytic, Asymmetric Transannular Aldolizations: Total Synthesis of (+)-Hirsutene.* Journal of the American Chemical Society, 2008. **130**(21): p. 6737-6739.
144. Fournier, F. and M. Fournier, *Transferts d'électrons assistés par les métaux de transition: influence de la nature du cation métallique sur la réduction de composés carbonylés en milieu aprotique.* Canadian journal of chemistry, 1986. **64**(5): p. 881-890.
145. Xu, K., *Nonaqueous liquid electrolytes for lithium-based rechargeable batteries.* Chemical reviews, 2004. **104**(10): p. 4303-4418.
146. Hari, D.P. and B. König, *Eosin Y catalyzed visible light oxidative C–C and C–P bond formation.* Organic letters, 2011. **13**(15): p. 3852-3855.
147. Hari, D.P. and B. König, *Synthetic applications of eosin Y in photoredox catalysis.* Chemical Communications, 2014. **50**(51): p. 6688-6699.
148. Darling, T.R., et al., *Living polymerization: Rationale for uniform terminology.* Journal of Polymer Science Part A: Polymer Chemistry, 2000. **38**(10): p. 1706-1708.
149. Szwarc, M., *Living polymers. Their discovery, characterization, and properties.* Journal of Polymer Science Part A: Polymer Chemistry, 1998. **36**(1).
150. Matyjaszewski, K., *Atom transfer radical polymerization (ATRP): current status and future perspectives.* Macromolecules, 2012. **45**(10): p. 4015-4039.
151. Hansen, N.M.L., S. Hvilsted, and M.C. Gerstenberg, *Synthesis of Amphiphilic Copolymers by Atom Transfer Radical Polymerization.* 2007, Technical University of Denmark Danmarks Tekniske Universitet, Others Andre.
152. Szwarc, M., M. Levy, and R. Milkovich, *Polymerization initiated by electron transfer to monomer. A new method of formation of block polymers1.* Journal of the American Chemical Society, 1956. **78**(11): p. 2656-2657.
153. Beylen, M., et al., *Developments in anionic polymerization — A critical review, in Polysiloxane Copolymers/Anionic Polymerization.* 1988, Springer Berlin Heidelberg: Berlin, Heidelberg. p. 87-143.
154. Hadjichristidis, N., et al., *Anionic polymerization: high vacuum techniques.* Journal of Polymer Science Part A: Polymer Chemistry, 2000. **38**(18): p. 3211-3234.
155. Miyamoto, M., M. Sawamoto, and T. Higashimura, *Living polymerization of isobutyl vinyl ether with hydrogen iodide/iodine initiating system.* Macromolecules, 1984. **17**(3): p. 265-268.

156. Aoshima, S. and S. Kanaoka, *A renaissance in living cationic polymerization*. Chemical reviews, 2009. **109**(11): p. 5245-5287.
157. Braunecker, W.A. and K. Matyjaszewski, *Controlled/living radical polymerization: features, developments, and perspectives*. Progress in Polymer Science, 2007. **32**(1): p. 93-146.
158. Matyjaszewski, K., *General concepts and history of living radical polymerization*. Handbook of Radical Polymerization, 2002: p. 361-406.
159. Vaillard, S., et al., *Encyclopedia of Radicals in Chemistry, Biology and Materials*. C. Chatgililoglu and A. Studer, Wiley, 2012. **2**: p. 1059-1093.
160. Yamago, S. and Y. Nakamura, *Recent progress in the use of photoirradiation in living radical polymerization*. Polymer, 2013. **54**(3): p. 981-994.
161. Matyjaszewski, K. and J. Xia, *Atom transfer radical polymerization*. Chemical reviews, 2001. **101**(9): p. 2921-2990.
162. Georges, M.K., et al., *Narrow molecular weight resins by a free-radical polymerization process*. Macromolecules, 1993. **26**(11): p. 2987-2988.
163. Hawker, C.J., A.W. Bosman, and E. Harth, *New polymer synthesis by nitroxide mediated living radical polymerizations*. Chemical Reviews, 2001. **101**(12): p. 3661-3688.
164. Kato, M., et al., *Polymerization of methyl methacrylate with the carbon tetrachloride/dichlorotris-(triphenylphosphine) ruthenium (II)/methylaluminum bis (2, 6-di-tert-butylphenoxide) initiating system: possibility of living radical polymerization*. Macromolecules, 1995. **28**(5): p. 1721-1723.
165. Gaynor, S.G., J.-S. Wang, and K. Matyjaszewski, *Controlled radical polymerization by degenerative transfer: effect of the structure of the transfer agent*. Macromolecules, 1995. **28**(24): p. 8051-8056.
166. Chiefari, J., et al., *Living free-radical polymerization by reversible addition-fragmentation chain transfer: the RAFT process*. Macromolecules, 1998. **31**(16): p. 5559-5562.
167. Lowe, A.B. and C.L. McCormick, *Reversible addition-fragmentation chain transfer (RAFT) radical polymerization and the synthesis of water-soluble (co) polymers under homogeneous conditions in organic and aqueous media*. Progress in Polymer Science, 2007. **32**(3): p. 283-351.
168. Moad, G., et al. *Synthesis of novel architectures by radical polymerization with reversible addition fragmentation chain transfer (RAFT polymerization)*. in *Macromolecular Symposia*. 2003. Wiley Online Library.
169. Moad, G., E. Rizzardo, and D.H. Solomon, *Selectivity of the reaction of free radicals with styrene*. Macromolecules, 1982. **15**(3): p. 909-914.
170. Mougner, S.-J., et al., *Facile and versatile synthesis of rod-coil poly(3-hexylthiophene)-based block copolymers by nitroxide-mediated radical polymerization*. Journal of Polymer Science Part A: Polymer Chemistry, 2012. **50**(12): p. 2463-2470.
171. Delduc, P., C. Tailhan, and S.Z. Zard, *A convenient source of alkyl and acyl radicals*. Journal of the Chemical Society, Chemical Communications, 1988(4): p. 308-310.
172. Destarac, M., et al., *Xanthates as Chain-Transfer Agents in Controlled Radical Polymerization (MADIX): Structural Effect of the O-Alkyl Group*. Macromolecular Rapid Communications, 2002. **23**(17): p. 1049-1054.
173. Perrier, S. and P. Takolpuckdee, *Macromolecular design via reversible addition-fragmentation chain transfer (RAFT)/xanthates (MADIX) polymerization*. Journal of Polymer Science Part A: Polymer Chemistry, 2005. **43**(22): p. 5347-5393.
174. di Lena, F. and K. Matyjaszewski, *Transition metal catalysts for controlled radical polymerization*. Progress in Polymer Science, 2010. **35**(8): p. 959-1021.
175. Fetters, L., et al., *Connection between polymer molecular weight, density, chain dimensions, and melt viscoelastic properties*. Macromolecules, 1994. **27**(17): p. 4639-4647.
176. Fried, J.R., *Polymer science and technology*. 2014: Pearson Education.
177. Izunobi, J.U. and C.L. Higginbotham, *Polymer molecular weight analysis by 1H NMR spectroscopy*. Journal of Chemical Education, 2011. **88**(8): p. 1098-1104.

178. Stevens, M.P., *Definitions, "Polymer Chemistry: An Introduction"*. Oxford University Press, Inc., Sect, 1999. **1**: p. 6-10.
179. Sibilila, J.P., *A guide to materials characterization and chemical analysis*. 1996: John Wiley & Sons.
180. Chen, A., D. Wu, and C.S. Johnson Jr, *Determination of molecular weight distributions for polymers by diffusion-ordered NMR*. Journal of the American Chemical Society, 1995. **117**(30): p. 7965-7970.
181. Cohen, Y., L. Avram, and L. Frish, *Diffusion NMR spectroscopy in supramolecular and combinatorial chemistry: an old parameter—new insights*. Angewandte Chemie International Edition, 2005. **44**(4): p. 520-554.
182. Karasz, F. and W. MacKnight, *The influence of stereoregularity on the glass transition temperatures of vinyl polymers*. Macromolecules, 1968. **1**(6): p. 537-540.
183. Satoh, K. and M. Kamigaito, *Stereospecific Living Radical Polymerization: Dual Control of Chain Length and Tacticity for Precision Polymer Synthesis*. Chemical Reviews, 2009. **109**(11): p. 5120-5156.
184. Moad, G., et al., *Tacticity of poly (methyl methacrylate). Evidence for a penultimate group effect in free-radical polymerization*. Australian journal of chemistry, 1986. **39**(1): p. 43-50.
185. Cowie, J., *Glass transition temperatures of stereoblock, isotactic and atactic polypropylenes of various chain lengths*. European Polymer Journal, 1973. **9**(10): p. 1041-1049.
186. White, A. and F.E. Filisko, *Tacticity determination of poly (methyl methacrylate)(PMMA) by high-resolution NMR*. Journal of Polymer Science: Polymer Letters Edition, 1982. **20**(10): p. 525-529.
187. Hatada, K., et al., *Two-Dimensional NMR Spectra of Isotactic Poly (methyl methacrylate) Prepared with t-C4H9MgBr and Detailed Examination of Tacticity*. Polymer journal, 1987. **19**(4): p. 425-436.
188. Peng, C.-H., et al., *Mechanism of halogen exchange in ATRP*. Macromolecules, 2011. **44**(19): p. 7546-7557.
189. Lin, C.Y., et al., *Linear-Free Energy Relationships for Modeling Structure–Reactivity Trends in Controlled Radical Polymerization*. Macromolecules, 2011. **44**(19): p. 7568-7583.
190. Golas, P.L., et al., *Catalyst performance in "click" coupling reactions of polymers prepared by ATRP: ligand and metal effects*. Macromolecules, 2006. **39**(19): p. 6451-6457.
191. Xia, J., X. Zhang, and K. Matyjaszewski, *The effect of ligands on copper-mediated atom transfer radical polymerization*. 2000.
192. áO'Dell, R. and S. áP Armes, *First example of the atom transfer radical polymerisation of an acidic monomer: direct synthesis of methacrylic acid copolymers in aqueous media*. Chemical Communications, 1999(14): p. 1285-1286.
193. Shen, Y., H. Tang, and S. Ding, *Catalyst separation in atom transfer radical polymerization*. Progress in polymer science, 2004. **29**(10): p. 1053-1078.
194. Leibfarth, F.A., et al., *External regulation of controlled polymerizations*. Angewandte Chemie International Edition, 2013. **52**(1): p. 199-210.
195. Chen, M., M. Zhong, and J.A. Johnson, *Light-Controlled Radical Polymerization: Mechanisms, Methods, and Applications*. Chemical Reviews, 2016.
196. Magenau, A.J., et al., *Electrochemically mediated atom transfer radical polymerization*. Science, 2011. **332**(6025): p. 81-84.
197. Bortolamei, N., et al., *Controlled aqueous atom transfer radical polymerization with electrochemical generation of the active catalyst*. Angewandte Chemie, 2011. **123**(48): p. 11593-11596.
198. Caruso, M.M., et al., *Mechanically-induced chemical changes in polymeric materials*. Chemical Reviews, 2009. **109**(11): p. 5755-5798.
199. Piermattei, A., S. Karthikeyan, and R.P. Sijbesma, *Activating catalysts with mechanical force*. Nature chemistry, 2009. **1**(2): p. 133-137.

200. Otsu, T. and M. Yoshida, *Role of initiator-transfer agent-terminator (Iniferter) in radical polymerizations: polymer design by organic disulfides as iniferters*. Die Makromolekulare Chemie, Rapid Communications, 1982. **3**(2): p. 127-132.
201. Otsu, T., M. Yoshida, and T. Tazaki, *A model for living radical polymerization*. Die Makromolekulare Chemie, Rapid Communications, 1982. **3**(2): p. 133-140.
202. Tehfe, M.A., et al., *Photopolymerization reactions: On the way to a green and sustainable chemistry*. Applied Sciences, 2013. **3**(2): p. 490-514.
203. Dadashi-Silab, S., M. Atilla Tasdelen, and Y. Yagci, *Photoinitiated atom transfer radical polymerization: Current status and future perspectives*. Journal of Polymer Science Part A: Polymer Chemistry, 2014. **52**(20): p. 2878-2888.
204. Decker, C., *Photopolymerization and ultraviolet curing of multifunctional monomers*. Materials science and technology, 1997.
205. Fouassier, J., X. Allonas, and D. Burget, *Photopolymerization reactions under visible lights: principle, mechanisms and examples of applications*. Progress in Organic Coatings, 2003. **47**(1): p. 16-36.
206. Tsarevsky, N.V. and K. Matyjaszewski, *"Green" atom transfer radical polymerization: from process design to preparation of well-defined environmentally friendly polymeric materials*. Chemical reviews, 2007. **107**(6): p. 2270-2299.
207. Moad, G., E. Rizzardo, and S.H. Thang, *Living radical polymerization by the RAFT process*. Australian journal of chemistry, 2005. **58**(6): p. 379-410.
208. Xia, J. and K. Matyjaszewski, *Controlled/"living" radical polymerization. Homogeneous reverse atom transfer radical polymerization using AIBN as the initiator*. Macromolecules, 1997. **30**(25): p. 7692-7696.
209. Gromada, J. and K. Matyjaszewski, *Simultaneous reverse and normal initiation in atom transfer radical polymerization*. Macromolecules, 2001. **34**(22): p. 7664-7671.
210. Matyjaszewski, K. and N.V. Tsarevsky, *Macromolecular engineering by atom transfer radical polymerization*. Journal of the American Chemical Society, 2014. **136**(18): p. 6513-6533.
211. Jakubowski, W. and K. Matyjaszewski, *Activators Regenerated by Electron Transfer for Atom-Transfer Radical Polymerization of (Meth) acrylates and Related Block Copolymers*. Angewandte Chemie, 2006. **118**(27): p. 4594-4598.
212. Dong, H., W. Tang, and K. Matyjaszewski, *Well-defined high-molecular-weight polyacrylonitrile via activators regenerated by electron transfer ATRP*. Macromolecules, 2007. **40**(9): p. 2974-2977.
213. Matyjaszewski, K., et al., *Zerovalent metals in controlled/"living" radical polymerization*. Macromolecules, 1997. **30**(23): p. 7348-7350.
214. Matyjaszewski, K., et al., *Diminishing catalyst concentration in atom transfer radical polymerization with reducing agents*. Proceedings of the National Academy of Sciences, 2006. **103**(42): p. 15309-15314.
215. Tasdelen, M.A., M. Uygun, and Y. Yagci, *Studies on Photoinduced ATRP in the Presence of Photoinitiator*. Macromolecular Chemistry and Physics, 2011. **212**(18): p. 2036-2042.
216. Ciftci, M., et al., *Photoinitiated ATRP in inverse microemulsion*. Macromolecules, 2013. **46**(24): p. 9537-9543.
217. Taskin, O.S., et al., *Photoinduced reverse atom transfer radical polymerization of methyl methacrylate using camphorquinone/benzhydrol system*. Polymer International, 2014. **63**(5): p. 902-907.
218. Tasdelen, M.A., M. Ciftci, and Y. Yagci, *Visible Light-Induced Atom Transfer Radical Polymerization*. Macromolecular Chemistry and Physics, 2012. **213**(13): p. 1391-1396.
219. Murtezi, E. and Y. Yagci, *Simultaneous photoinduced ATRP and CuAAC reactions for the synthesis of block copolymers*. Macromolecular rapid communications, 2014. **35**(20): p. 1782-1787.
220. Konkolewicz, D., et al., *Visible light and sunlight photoinduced ATRP with ppm of Cu catalyst*. ACS Macro Letters, 2012. **1**(10): p. 1219-1223.

221. Anastasaki, A., et al., *Copper (II)/tertiary amine synergy in photoinduced living radical polymerization: Accelerated synthesis of ω -functional and α, ω -heterofunctional poly (acrylates)*. Journal of the American Chemical Society, 2014. **136**(3): p. 1141-1149.
222. Yang, Q., et al., *Photocatalyzed Cu-Based ATRP Involving an Oxidative Quenching Mechanism under Visible Light*. Macromolecules, 2015. **48**(7): p. 1972-1980.
223. Zhang, G., et al., *Free radical polymerization initiated and controlled by visible light photocatalysis at ambient temperature*. Macromolecules, 2011. **44**(19): p. 7594-7599.
224. Pan, X., et al., *Photoinduced Fe-Based Atom Transfer Radical Polymerization in the Absence of Additional Ligands, Reducing Agents, and Radical Initiators*. Macromolecules, 2015. **48**(19): p. 6948-6954.
225. Nzulu, F., et al., *A dinuclear gold (I) complex as a novel photoredox catalyst for light-induced atom transfer radical polymerization*. Polymer Chemistry, 2015. **6**(25): p. 4605-4611.
226. Ravelli, D. and M. Fagnoni, *Dyes as Visible Light Photoredox Organocatalysts*. ChemCatChem, 2012. **4**(2): p. 169-171.
227. Fukuzumi, S. and K. Ohkubo, *Organic synthetic transformations using organic dyes as photoredox catalysts*. Organic & biomolecular chemistry, 2014. **12**(32): p. 6059-6071.
228. Fukuzumi, S. and K. Ohkubo, *Selective photocatalytic reactions with organic photocatalysts*. Chemical Science, 2013. **4**(2): p. 561-574.
229. Treat, N.J., et al., *Metal-free atom transfer radical polymerization*. Journal of the American Chemical Society, 2014. **136**(45): p. 16096-16101.
230. Miyake, G.M. and J.C. Theriot, *Perylene as an organic photocatalyst for the radical polymerization of functionalized vinyl monomers through oxidative quenching with alkyl bromides and visible light*. Macromolecules, 2014. **47**(23): p. 8255-8261.
231. Liu, X., et al., *Metal-free photoinduced electron transfer-atom transfer radical polymerization (PET-ATRP) via a visible light organic photocatalyst*. Polymer Chemistry, 2016. **7**(3): p. 689-700.
232. Gilmore, K. and P.H. Seeberger, *Continuous flow photochemistry*. The Chemical Record, 2014. **14**(3): p. 410-418.
233. Jachuck, R.J.J. and V. Nekkanti, *Continuous Photopolymerization of n-Butyl Acrylate Using a Narrow Channel Reactor*. Macromolecules, 2008. **41**(9): p. 3053-3062.
234. Wenn, B., et al., *Photo-induced copper-mediated polymerization of methyl acrylate in continuous flow reactors*. Polymer Chemistry, 2014. **5**(8): p. 3053-3060.
235. Kermagoret, A., et al., *Improved photo-induced cobalt-mediated radical polymerization in continuous flow photoreactors*. Polymer Chemistry, 2015. **6**(20): p. 3847-3857.
236. Melker, A., et al., *Continuous flow synthesis of poly (methyl methacrylate) via a light-mediated controlled radical polymerization*. Journal of Polymer Science Part A: Polymer Chemistry, 2015. **53**(23): p. 2693-2698.
237. Selsted, M.E. and H.W. Becker, *Eosin Y: a reversible stain for detecting electrophoretically resolved protein*. Analytical biochemistry, 1986. **155**(2): p. 270-274.
238. Salvador, A. and A. Chisvert, *Analysis of cosmetic products*. 2011: Elsevier.
239. Sabnis, R.W., *Handbook of acid-base indicators*. 2007: CRC Press.
240. Ahluwalia, V. and S. Dhingra, *College practical chemistry*. 2005: Universities Press.
241. Penzkofer, A., A. Beidoun, and M. Daiber, *Intersystem-crossing and excited-state absorption in eosin Y solutions determined by picosecond double pulse transient absorption measurements*. Journal of luminescence, 1992. **51**(6): p. 297-314.
242. Penzkofer, A., A. Beidoun, and S. Speiser, *Singlet excited-state absorption of eosin Y*. Chemical physics, 1993. **170**(1): p. 139-148.
243. Lazarides, T., et al., *Making hydrogen from water using a homogeneous system without noble metals*. Journal of the American Chemical Society, 2009. **131**(26): p. 9192-9194.
244. Neumann, M., et al., *Metal-Free, Cooperative Asymmetric Organophotoredox Catalysis with Visible Light*. Angewandte Chemie International Edition, 2011. **50**(4): p. 951-954.

245. Zou, Y.Q., et al., *Highly efficient aerobic oxidative hydroxylation of arylboronic acids: photoredox catalysis using visible light*. *Angewandte Chemie*, 2012. **124**(3): p. 808-812.
246. Hari, D.P., P. Schroll, and B. König, *Metal-Free, visible-light-mediated direct C–H arylation of heteroarenes with aryl diazonium salts*. *Journal of the American Chemical Society*, 2012. **134**(6): p. 2958-2961.
247. Cantillo, D., et al., *Continuous flow α -trifluoromethylation of ketones by metal-free visible light photoredox catalysis*. *Organic letters*, 2014. **16**(3): p. 896-899.
248. Neumann, M. and K. Zeitler, *Application of microflow conditions to visible light photoredox catalysis*. *Organic letters*, 2012. **14**(11): p. 2658-2661.
249. Zhang, T., et al., *ATRP with a light switch: photoinduced ATRP using a household fluorescent lamp*. *Polymer Chemistry*, 2014. **5**(16): p. 4790-4796.
250. Forrester, A.R., J.M. Hay, and R.H. Thomson, *Organic chemistry of stable free radicals*. 1968: Academic Press New York.
251. Sharma, V. and J.J. Tepe, *Diastereochemical diversity of imidazoline scaffolds via substrate controlled TMSCl mediated cycloaddition of azlactones*. *Organic letters*, 2005. **7**(22): p. 5091-5094.
252. Li, W., et al., *Application of 1H DOSY for facile measurement of polymer molecular weights*. *Macromolecules*, 2012. **45**(24): p. 9595-9603.
253. Sibi, M.P., *Radicals in organic synthesis: applications*. Vol. 2. 2001: Wiley-VCH.
254. Rowlands, G.J., *Radicals in organic synthesis. Part 1*. *Tetrahedron*, 2009. **65**(42): p. 8603-8655.
255. Rowlands, G.J., *Radicals in organic synthesis: part 2*. *Tetrahedron*, 2010. **66**(9): p. 1593-1636.
256. Omae, I., *Applications of organometallic compounds*. 1998: wiley.
257. Suzuki, A., F. Diederich, and P. Stang, *Metal-catalyzed cross-coupling reactions*. by F. Diederich and PJ Stang, Wiley-VCH, Weinheim, 1998: p. 49-97.
258. Darses, S. and J.-P. Genet, *Potassium organotrifluoroborates: new perspectives in organic synthesis*. *Chemical reviews*, 2008. **108**(1): p. 288-325.
259. Chambers, R., H. Clark, and C. Willis, *Some salts of trifluoromethylfluoroboric acid1, 2*. *Journal of the American Chemical Society*, 1960. **82**(20): p. 5298-5301.
260. Vedejs, E., et al., *Conversion of arylboronic acids into potassium aryltrifluoroborates: Convenient precursors of arylboron difluoride lewis acids*. *The Journal of Organic Chemistry*, 1995. **60**(10): p. 3020-3027.
261. Vedejs, E., et al., *Asymmetric memory at labile, stereogenic boron: enolate alkylation of oxazaborolidinones*. *Journal of the American Chemical Society*, 1999. **121**(11): p. 2460-2470.
262. Darses, S., G. Michaud, and J.P. Genêt, *Potassium Organotrifluoroborates: New Partners in Palladium-Catalysed Cross-Coupling Reactions*. *European Journal of Organic Chemistry*, 1999. **1999**(8): p. 1875-1883.
263. Stefani, H.A., R. Cella, and A.S. Vieira, *Recent advances in organotrifluoroborates chemistry*. *Tetrahedron*, 2007. **63**(18): p. 3623-3658.
264. Molander, G.A., *Suzuki with trifluoroboronates*. *Aldrichimica Acta*, 2005. **38**: p. 49.
265. Duret, G., et al., *Boron chemistry in a new light*. *Chemical Science*, 2015. **6**(10): p. 5366-5382.
266. Miyazawa, K., T. Koike, and M. Akita, *Hydroaminomethylation of Olefins with Aminomethyltrifluoroborate by Photoredox Catalysis*. *Advanced Synthesis & Catalysis*, 2014. **356**(13): p. 2749-2755.
267. Fuchter, M. and A.E. Homologation, *In Name Reactions for Homologations-Part I; Li, JJ, Ed.* 2009, Wiley: Hoboken, NJ.
268. Suzuki, A., *Organoborane coupling reactions (Suzuki coupling)*. *Proceedings of the Japan Academy, Series B*, 2004. **80**(8): p. 359-371.

269. Davies, A.G. and B. Roberts, *The autoxidation of optically active 1-phenylethaneboronic acid*. Chemical Communications (London), 1966(10): p. 298-299.
270. Smoum, R., A. Rubinstein, and M. Srebnik, *Noncovalent inhibition of the serine proteases, α -chymotrypsin and trypsin by trifluoro (organo) borates*. Organic & biomolecular chemistry, 2005. **3**(5): p. 941-944.
271. Sorin, G., et al., *Oxidation of Alkyl Trifluoroborates: An Opportunity for Tin-Free Radical Chemistry*. Angewandte Chemie International Edition, 2010. **49**(46): p. 8721-8723.
272. Molander, G.A., V. Colombel, and V.A. Braz, *Direct alkylation of heteroaryls using potassium alkyl- and alkoxymethyltrifluoroborates*. Organic letters, 2011. **13**(7): p. 1852-1855.
273. Liwosz, T.W. and S.R. Chemler, *Copper-Catalyzed Oxidative Heck Reactions between Alkyltrifluoroborates and Vinyl Arenes*. Organic letters, 2013. **15**(12): p. 3034-3037.
274. Koike, T. and M. Akita, *Visible-light-induced photoredox catalysis: an easy access to green radical chemistry*. Synlett, 2013. **24**(19): p. 2492-2505.
275. Baguley, P.A. and J.C. Walton, *Flight from the tyranny of tin: the quest for practical radical sources free from metal encumbrances*. Angewandte Chemie International Edition, 1998. **37**(22): p. 3072-3082.
276. Studer, A. and S. Amrein, *Tin hydride substitutes in reductive radical chain reactions*. Synthesis, 2002(7): p. 835-849.
277. Dalco, P.I., *Redox induced radical and radical ionic carbon-carbon bond forming reactions*. Tetrahedron, 1995. **51**(28): p. 7579-7653.
278. Sibi, M.P. and M. Hasegawa, *Organocatalysis in radical chemistry. Enantioselective α -oxyamination of aldehydes*. Journal of the American Chemical Society, 2007. **129**(14): p. 4124-4125.
279. Yasu, Y., T. Koike, and M. Akita, *Visible Light-Induced Selective Generation of Radicals from Organoborates by Photoredox Catalysis*. Advanced Synthesis & Catalysis, 2012. **354**(18): p. 3414-3420.
280. Dixon, I.M., et al., *A family of luminescent coordination compounds: iridium (III) polyimine complexes*. Chemical Society Reviews, 2000. **29**(6): p. 385-391.
281. Miyazawa, K., et al., *Visible-light-induced hydroalkoxymethylation of electron-deficient alkenes by photoredox catalysis*. Chem. Commun., 2013. **49**(65): p. 7249-7251.
282. Melillo, D., et al., *A practical synthesis of (\pm)-thienamycin*. Tetrahedron Letters, 1980. **21**(29): p. 2783-2786.
283. Bonnaud, B., et al., *1-Aryl-2-(aminomethyl) cyclopropanecarboxylic acid derivatives. A new series of potential antidepressants*. Journal of medicinal chemistry, 1987. **30**(2): p. 318-325.
284. Li, Y., et al., *Alkyl- and aryl-thioalkylation of olefins with organotrifluoroborates by photoredox catalysis*. Organic Chemistry Frontiers, 2015. **2**(4): p. 319-323.
285. Huang, H., K. Jia, and Y. Chen, *Hypervalent Iodine Reagents Enable Chemoselective Deboronative/Decarboxylative Alkenylation by Photoredox Catalysis*. Angewandte Chemie, 2015. **127**(6): p. 1901-1904.
286. Gooßen, L.J., G. Deng, and L.M. Levy, *Synthesis of biaryls via catalytic decarboxylative coupling*. Science, 2006. **313**(5787): p. 662-664.
287. Cui, Z., et al., *Copper-catalyzed decarboxylative alkenylation of *sp*³ C-H bonds with cinnamic acids via a radical process*. Chemical Science, 2012. **3**(9): p. 2853-2858.
288. Tellis, J.C., D.N. Primer, and G.A. Molander, *Single-electron transmetalation in organoboron cross-coupling by photoredox/nickel dual catalysis*. Science, 2014. **345**(6195): p. 433-436.
289. Primer, D.N., et al., *Single-electron transmetalation: An enabling technology for secondary alkylboron cross-coupling*. Journal of the American Chemical Society, 2015. **137**(6): p. 2195-2198.
290. Littke, A.F., C. Dai, and G.C. Fu, *Versatile catalysts for the Suzuki cross-coupling of arylboronic acids with aryl and vinyl halides and triflates under mild conditions*. Journal of the American Chemical Society, 2000. **122**(17): p. 4020-4028.

291. Dreher, S.D., et al., *Efficient Cross-Coupling of Secondary Alkyltrifluoroborates with Aryl Chlorides • Reaction Discovery Using Parallel Microscale Experimentation*. Journal of the American Chemical Society, 2008. **130**(29): p. 9257-9259.
292. Karakaya, I., D.N. Primer, and G.A. Molander, *Photoredox Cross-Coupling: Ir/Ni Dual Catalysis for the Synthesis of Benzylic Ethers*. Organic letters, 2015. **17**(13): p. 3294-3297.
293. Molander, G.A. and B. Canturk, *Preparation of potassium alkoxymethyltrifluoroborates and their cross-coupling with aryl chlorides*. Organic letters, 2008. **10**(11): p. 2135-2138.
294. Hansch, C., A. Leo, and R. Taft, *A survey of Hammett substituent constants and resonance and field parameters*. Chemical Reviews, 1991. **91**(2): p. 165-195.
295. Hansch, C. and A. Leo, *Substituent constants for correlation analysis in chemistry and biology*. 1979: Wiley.
296. Pryor, W.A., et al., *Reactions of the hydrogen atom in solution. VI. Addition of hydrogen atoms to substituted benzenes. Use of the Hammett equation for correlating radical reactions*. Journal of the American Chemical Society, 1973. **95**(21): p. 6993-6998.
297. HÉBerger, K., *Linear free energy relationships in radical reactions. II. hydrogen abstraction from substituted toluenes by Tert-Butyl, Tert-Butoxyl and Tert-Butylperoxyl radicals*. Journal of Physical Organic Chemistry, 1994. **7**(5): p. 244-250.